Numerical Analysis of Adsorption Heat Pump Configurations for Residential Stock Buildings

Zur Erlangung des akademischen Grades eines
DOKTORS DER INGENIEURWISSENSCHAFTEN (Dr.-Ing.)

von der KIT-Fakultät für Maschinenbau des
Karlsruher Instituts für Technologie (KIT)
genehmigte

DISSERTATION

von

M.Sc. Alireza Sadeghlu

Tag der mündlichen Prüfung: 04. August 2026

Hauptreferent:	Prof. Dr. sc. techn. Thomas Koch
Korreferent:	Prof. Dr.-Ing. Peter Schossig
Korreferent:	Dr. rer. nat. Ferdinand P. Schmidt

Karlsruhe Institute of Technology (KIT)
Department of Mechanical Engineering
Dean´s Office
Kaiserstraße 12
76131 Karlsruhe

I declare that I have developed and written the enclosed thesis completely by myself, and have not used sources or means without declaration in the text.

PLACE, DATE

. . . .

(Alireza Sadeghlu)

Acknowledgments

I would like to express my sincere gratitude to Professor Thomas Koch for accepting the supervision of my doctoral thesis after the passing of Professor Robert Stieglitz and for giving me the opportunity to complete my doctoral degree at KIT.

I would also like to thank Professor Peter Schossig for his valuable feedback and support during the final stage of my doctoral examination.

My sincere thanks also go to Dr. Ferdinand Schmidt for his technical support, his valuable advice, and for sharing his knowledge and experience with me throughout this journey.

A very special thank you goes to Dr. Balazs Pritz, who supported me not only as a mentor but also as a brother. His guidance, encouragement, and friendship have meant a great deal to me, both professionally and personally.

I would also like to thank my friends and colleagues for their support, encouragement, and the many good moments we shared during this journey.

Finally, I would like to express my deepest gratitude to my parents and my family for their unconditional love, support, patience, and encouragement throughout my life. Without them, this journey would not have been possible.

Abstract

This work investigates strategies for improving Gas Adsorption Heat Pumps (GAHPs) in the renovation of multi-family buildings in Germany, where efficient heating systems are needed to meet supply temperatures up to 55 °C. Utilizing existing radiators with GAHPs at this temperature could significantly reduce renovation costs. However, the temperature lift achievable with the SAPO-34/water working pair in GAHPs is limited to approximately 30 K, constraining the system's ability to provide the required 55 °C supply temperature through adsorption alone, especially under typical low-temperature source conditions. This limitation impacts the system's capacity to fully satisfy both heating demand and Domestic Hot Water (DHW) preparation. Using a validated numerical model of the GAHP, this thesis accomplishes three key objectives. First, recognizing that the GAHP alone cannot fully meet DHW requirements, this work explores the integration of DHW preparation. The goal is to preheat DHW using the combined effects of the condensing boiler and adsorption processes. The efficiency benefits of this approach are assessed by comparing it to conventional "burner-only" DHW preparation method.

Second, the work examines sensible heat recovery within a single-bed adsorber module designed for the AdoSan project, which focuses on developing GAHP technology for building retrofits. The selected module type features a single heat exchanger that enables both evaporation and condensation processes. The research evaluates how heat recovery can be achieved between these two modes within a single adsorber cycle. Furthermore, it assesses the conditions under which this single adsorber cycle configuration could attain performance levels comparable to the dual adsorber cycle implemented in the AdoSan test bed. These findings contribute to the development of more cost-effective and efficient GAHP systems for building renovations.

Finally, the thesis explores two strategies for achieving a minimum Seasonal Gas Utilization Efficiency (SGUE) of 1.3, using a reference building model and component technologies derived from the AdoSan test bed. The first strategy demonstrates that the target can be achieved through the integration of solar thermal collectors. The second strategy examines the feasibility of meeting the SGUE target without solar thermal support by conducting a sensitivity analysis. This includes improving the performance of the heating system by increasing the maximum desorption temperature of the dual-adsorber cycle GAHP. However, for a dual-adsorber cycle GAHP sized for a nominal power of 40 kW, the analysis indicates that achieving the SGUE of 1.3 is not possible without solar collector support.

Zusammenfassung

Diese Arbeit untersucht Strategien zur Verbesserung von Gas-Adsorptionswärmepumpen (GAHPs) bei der Sanierung von Mehrfamilienhäusern in Deutschland, in denen effiziente Heizsysteme für Vorlauftemperaturen bis 55 °C benötigt werden. Die Nutzung vorhandener Heizkörper mit GAHPs bei dieser Temperatur könnte die Sanierungskosten erheblich senken. Allerdings ist der Temperaturanstieg, der mit dem SAPO-34/Wasser-Arbeitspaar in GAHPs erreicht werden kann, auf etwa 30 K begrenzt, was die Fähigkeit des Systems einschränkt, die erforderliche Vorlauftemperatur von 55 °C allein durch Adsorption bereitzustellen, insbesondere unter typischen Randbedingungen für die Niedertemperaturquelle (Erdsonde). Diese Einschränkung wirkt sich auf die Fähigkeit des Systems aus, sowohl den Heizbedarf als auch die Warmwasserbereitung vollständig zu decken. Unter Verwendung eines validierten numerischen Modells der GAHP verfolgt diese Arbeit drei Hauptziele. Zunächst wird die Integration der Warmwasserbereitung untersucht, da die GAHP allein den Warmwasserbedarf nicht vollständig decken kann. Ziel ist die Vorwärmung des Warmwassers durch die kombinierte Wirkung des Brennwertkessels und des Adsorptionsprozesses. Die Effizienzvorteile dieses Ansatzes werden durch einen Vergleich mit der konventionellen Warmwasserbereitung im reinen Brennerbetrieb bewertet.

Zweitens wird die sinnvolle Wärmerückgewinnung in einem Einbett-Adsorbermodul untersucht, das für das AdoSan-Projekt entwickelt wurde und sich auf die Entwicklung der GAHP-Technologie für die Gebäudesanierung konzentriert. Der gewählte Modultyp verfügt über einen einzigen Wärmetauscher, der sowohl Verdampfungs- als auch Kondensationsprozesse ermöglicht. Ziel der Forschungsarbeiten ist es, zu untersuchen, wie die Wärmerückgewinnung zwischen diesen beiden Prozessen in einem Einadsorber Zyklus erreicht werden kann. Darüber hinaus wird analysiert, unter welchen Bedingungen diese Konfiguration des Einadsorber Zyklus ein Leistungsniveau erreichen kann, das mit dem des im AdoSan-Funktionsmuster implementierten Zweiadsorber Zyklus vergleichbar ist. Diese Ergebnisse tragen zur Entwicklung kostengünstigerer und effizienterer GAHP-Systeme für die Gebäudesanierung bei.

Abschließend untersucht die Arbeit zwei Strategien, um einen minimalen Jahres–Gasnutzungsgrad (SGUE) von 1.3 zu erreichen, basierend auf einem Referenzgebäudemodell und Technologien, die aus dem AdoSan-Teststand abgeleitet wurden. Die erste Strategie zeigt, dass dieses Ziel durch die Integration von solarthermischen Kollektoren erreicht werden kann. Die zweite Strategie prüft die Machbarkeit, das SGUE-Ziel ohne Unterstützung durch Solarthermie zu erreichen, indem eine Sensitivitätsanalyse durchgeführt wird. Diese umfasst die Verbesserung der Heizsystemleistung durch Erhöhung der maximalen Desorptionstemperatur des Zweiadsorber Zyklus-GAHP. Für einen Zweiadsorber Zyklus-GAHP mit einer Nennleistung von 40 kW zeigt die Analyse jedoch, dass eine SGUE von 1.3 ohne Unterstützung durch Solarkollektoren nicht erreicht werden kann.

Nomenclature

Abbreviation / Index

AD	Adsorber
adb	Adsorbate
$ADHX$	Adsorber/Desorber Heat Exchanger
$adsorpt$	all working pair cells
avg	average
BHX	Borehole Heat Exchanger
BRN	Burner
COP	Coefficient Of Performance
CV	Control Volume
DHW	Domestic Hot Water
Dub	Dubinin
EC	Evaporator/Condenser
env	Environment
$fluegas$	Flue Gas
FWS	Fresh Water Station
$GAHP$	Gas Adsorption Heat Pump
gen	Generation
GUE_h	Gas Utilisation Efficiency Heating
HDS	Heat Distribution System
HP	Heat Pump
HT	High Temperature
HTF	Heat Transfer Fluid

HTS High Temperature Source

HX Heat Exchanger

in Inlet

L Stratified Storage Layer

LT Low Temperature

LTS Low Temperature Source

MT Medium Temperature

mt Metal

MTS Medium Temperature Sink

NCV Net Calorific Value

NTU Number of Transfer Units

out Outlet

P pump

$SGUE$ Seasonal Gas Utilisation Efficiency

$SGUE_h$ Seasonal Gas Utilisation Efficiency Heating

SHC Space Heating Circuit

$sorb$ Adsorbent

$Stor$ Storage

tot Total

wf Working Fluid

WHC Water Heating Circuit

$SAPO$-34 Silico-alumino phosphate zeo-type adsorbent

Symbol / Description

$\mathrm{X_{eqi}}$ Adsorption Equilibrium [kg/kg]

α Heat Transfer Coefficient [$\mathrm{W/m^2 \cdot K}$]

$\dot{C}$ Capacity Flow Rate [W/K]

$\dot{H}$ Enthalpy Flow Rate [W]

$\dot{m}$	Mass Flow Rate [kg/s]
$\dot{Q}$	Power [W]
ϵ	Heat Exchanger Effectiveness [-]
η	Efficiency [-]
$\frac{dS}{dt}$	Entropy Change Rate [W/K]
ρ	Density [kg/m^3]
RI	Relative Irreversibility [-]
$\tilde{g}$	Partial Molar Gibbs Enthalpy [J/mol]
$\tilde{h}$	Partial Molar Enthalpy [J/mol]
$\tilde{M}$	Molar Mass [kg/mol]
$\tilde{s}$	Partial Molar Entropy [J/mol $\cdot$ K]
$\tilde{v}$	Partial Molar Volume [m^3/mol]
A	Area [m^2]
A_{Dub}	Dubinin Adsorption Potential [J/mol or J/kg]
C	Heat Capacity [J/K]
c_p	Specific Heat Capacity at Constant Pressure [J/kg $\cdot$ K]
$F_R U_L$	Heat Loss Coefficient [W/m^2 $\cdot$ K]
$F_R(\tau\alpha)$	Maximum Efficiency [-]
G_{Tc}	Critical Solar Irradiation [W/m^2]
G_{tilt}	Solar Irradiation on Tilted Surface [W/m^2]
h	Specific Enthalpy [J/kg]
h_{ads}	Specific Adsorption Enthalpy [J/kg]
H_u	Lower Calorific Value [kWh/m^3]
k_{LDF}	Parameter for Linear-Driving-Force Approach [1/s]
m	Mass [kg]
Nu	Nusselt Number [-]
p	Pressure [Pa]

R	Heat Transfer Resistance [K/W]
R_{const}	Universal Gas Constant [J/mol · K]
Re	Reynolds Number [-]
s	Specific Entropy [J/kg · K]
T	Temperature [°C]
t	time [s]
u	Specific Internal Energy [J/kg]
UA	Overall Heat Conductance [W/K]
W_{Dub}	Specific Adsorbed Volume [m^3/kg]
X	Loading [kg/kg]

Contents

1. Introduction

1.1. Background on Adsorption Heat Pump

The main portion of energy consumption in the building sector in Germany is related to space heating (70 %) and domestic hot water preparation (15 %) [1], with natural gas covering 48.3 % of energy carriers[1]. Despite ongoing efforts to reduce dependence on natural gas, gas-condensing boilers are still widely used in the building sector [4].

In light of the rising need to transition towards renewable energy sources [5–8] for space heating and domestic hot water, and to reduce CO_2 emissions contributing to climate change [9], the current high prices of natural gas [10] may motivate homeowners to complement gas-condensing boilers with thermally driven heat pumps. These heat pumps, which utilize high-temperature heat as a driving source, can transfer heat from low-temperature sources, such as air, near-surface geothermal energy [11], or solar thermal collectors [12], to the medium-temperature sink. While thermally driven heat pumps involve higher initial cost, they offer the potential to reduce natural gas consumption by 20–50 % compared to gas-condensing boilers [12].

Additionally, Compression heat pumps are an alternative to gas condensing boilers. However, they rely on electricity as main energy carrier [13], which could increase the load on the power grid and require costly infrastructure changes. In contrast, thermally driven heat pumps use electrical power only for auxiliary functions such as circulation pumps and control units, making them less dependent on the electrical grid. Although thermally driven heat pumps currently represent a niche technology, they remain relevant in specific applications where compression heat pumps face limitations, such as existing multi-family houses [14].

Two types of thermally driven heat pumps are a**b**sorption and adsorption. A**b**sorption heat pumps use substance pairs like ammonia/water and water/lithium bromide. However, for household applications, A**b**sorption systems face challenges in meeting standards related to toxicity and user acceptance. A**b**sorption takes place in a liquid phase, forming a homogeneous solution that can be pumped through the apparatus. In contrast, adsorption is a surface phenomenon that occurs at the surface of a microporous solid adsorbent, which remains fixed in a reactor and is in close contact with a heat exchanger surface. Adsorption heat pumps use more environmentally friendly working pairs such as silica gel/water and silico-alumino phosphates (SAPOs)/water [15], making them safer for households and less prone to malfunction.

Research on improving thermally driven adsorption heat pumps primarily focuses on two key areas. Firstly, efforts are directed towards integrating the adsorber/desorber,

[1]Other energy carriers include 23.4 % oil, 15.2 % district heating, 7.5 % electricity, and 5.6 % liquid gas, wood/pellets, coal, etc. [2, 3].

condenser, evaporator, and storage systems to enhance efficiency through heat recovery strategies [16, 17]. Secondly, there is a significant emphasis on optimizing the components of adsorption heat pumps based on temperature boundary conditions to improve power density [17].

Power density in adsorption heat pumps is highly influenced by the dynamics of heat and mass transfer within the adsorber/desorber and the associated components [18, 19]. In addressing coupled heat and mass transfer challenges in adsorption processes, it is essential to recognize the diversity of regimes where specific sub-processes, such as adsorption kinetics, can become rate-limiting. Füldner [19] provides a detailed exploration of these varied regimes, offering insights into the conditions under which each process may dominate.

The selection and optimization of adsorbent composites are inherently tied to the working pair of the adsorption system. A primary challenge lies in balancing the often conflicting requirements of thermal conductivity and mass transfer efficiency. Composites with high thermal conductivity are typically very dense, which increases mass transport resistance, whereas those with lower density may enhance mass transport but at the cost of thermal performance. This trade-off is especially pronounced when comparing high-pressure working fluids, such as ammonia, with low-pressure counterparts like water. For instance, activated carbon-based composites designed for ammonia adsorption [20, 21] achieve a level of compactness that is not as feasible with SAPO-34/aluminum composites used in water-based systems.

Moreover, the design of the adsorber heat exchanger (HX) is closely linked with composite development. The method used to integrate the composite material with the heat exchanger, as well as the specific production process, plays a crucial role in determining overall system performance. This thesis examines an approach based on in-situ batch crystallization, where the aluminum support structure undergoes partial transformation within large autoclaves. This method represents a distinct production pathway, initially developed in the Schwieger Laboratory at the University of Erlangen [22], and subsequently scaled up and commercialized by the company Fahrenheit [23–25].

In-situ crystallization shows significant promise for producing high-performance adsorbent composites. However, it presents notable production challenges, particularly regarding scalability and consistency in the crystallization process. These challenges underscore the importance of harmonizing the design of composite materials and the HX to optimize both heat and mass transfer capabilities while meeting the specific requirements of various working pairs.

This thesis aims to evaluate the current state of in-situ crystallization technology at a technical scale (AdoSan [26]) and assess its suitability for new applications, boundary conditions, and cycle concepts.

1.1.1. Adsorber Cycle

Comparing the compression heat pump cycle with the adsorber cycle reveals key differences in their components and operation. A compression heat pump contains a compressor, condenser, expansion valve, and evaporator. In contrast, the adsorber cycle in a Two-Heat-Exchanger Adsorption Heat Pump comprises an Adsorber/Desorber and an Evaporator/Condenser within a sealed casing, as illustrated in Figure 1.1.

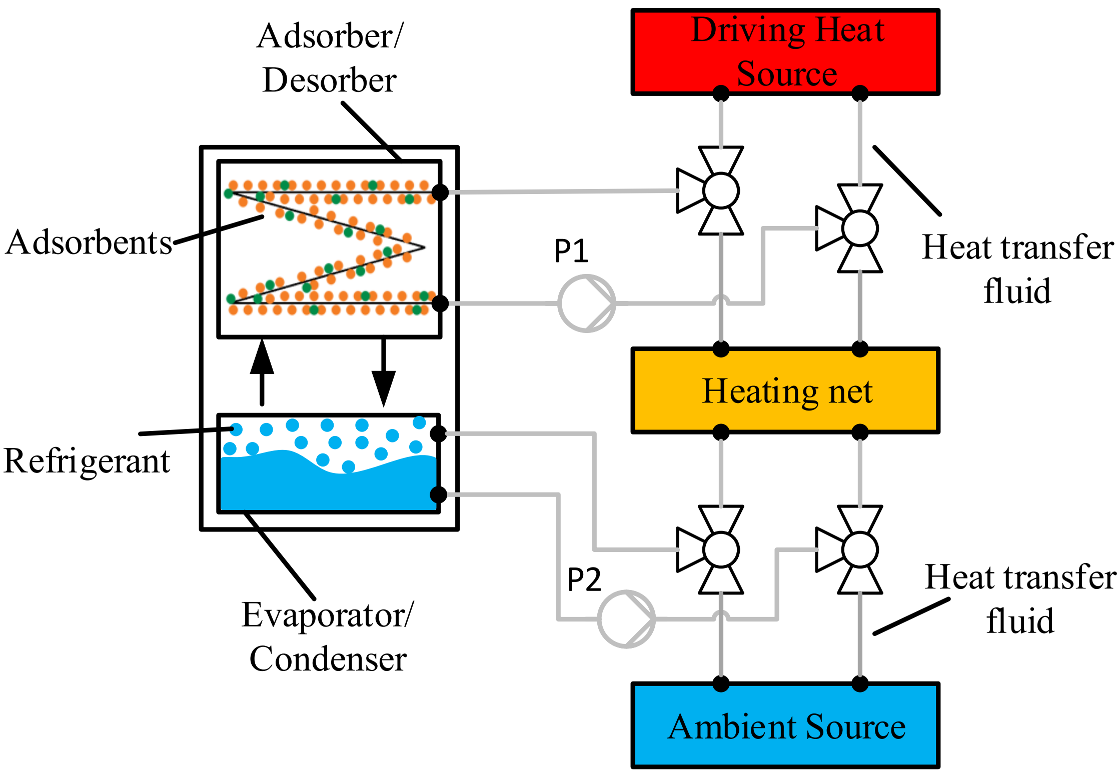

Figure 1.1.: Hydraulic scheme of a two-heat-exchanger adsorption heat pump concept. The driving high source is depicted in red, the medium temperature sink in orange, and the ambient source in blue [27].

The adsorber cycle requires three distinct temperature levels for its basic operation: a high-temperature heat source (drive), a heat sink (heating network), and a low-temperature heat source (ambient heat). Unlike a compression heat pump, which uses electrical power to drive a mechanical compressor, the adsorption heat pump utilizes a high-temperature thermal source to activate a thermal compressor. This process replaces the mechanical compressor with a thermally activated adsorption/desorption process.

Adsorption is a process where vapor-phase molecules of a working fluid attach reversibly to a solid adsorbent. During this process, heat is released (exothermic) as the working fluid bonds with the adsorbent. The adsorption process continues till the adsorbent eventually saturates with the working fluid. In contrast, desorption occurs when heat is applied to the adsorbent, causing the working fluid to detach in an endothermic process.

The heat exchanged between the adsorbed working fluid molecules and the vapor-phase working fluid is known as isosteric adsorption heat [28], a key characteristic of adsorption technology. Adsorption is quantitatively described through a relationship between the adsorbed amount X, which represents the mass ratio of the adsorbed working fluid to the dry adsorbent, and the conditions of pressure (p) and temperature (T), based on specific adsorption models, which is briefly described below.

Langmuir Model [29]: This approach assumes adsorption occurs at independent, identical sites, where molecules attach to a solid surface in a monolayer. This model fits well for cases of gases adsorbed on solid surfaces (like mica and glass), validated by Langmuir's studies [29] with gases like water vapor, nitrogen, and carbon monoxide.

BET Model [30]: Developed by Brunauer, Emmet, and Teller, this model extends Langmuir's approach by considering multilayer adsorption on independent sites. This model applies to various gases (e.g., CO_2, argon) adsorbed on materials like charcoal and silica gel and uses statistical thermodynamics to derive occupancy through ensemble theory and partition functions.

Microporous Adsorption (Dubinin Theory) [31, 32]: For microporous materials, monolayer or multilayer surface adsorption models are inadequate since pore volume—not surface area—is critical. Dubinin's model addresses adsorption in micropores by focusing on the interaction within small pore volumes, offering insights especially for cases where pore size is comparable to the adsorbed molecules.

Considering that microporous adsorption occurs within the adsorber cycle, the cycle description begins with the adsorbent in a cold, saturated state (state 1), initiating the pre-heating process (1-2) in Figure 1.2. During pre-heating, the desorber connects to the driving heat source in Figure 1.3. As heat is supplied, a certain amount of the working fluid is desorbed, leading to an increase in temperature and the corresponding pressure of desorber. Therefore, the pre-heating process within this valveless adsorption module (Figure 1.1) is not isosteric, meaning the pre-heating phase does not occur at a constant loading X_{max}.

The desorbed working fluid then flows to the condenser, where it releases heat, causing the pressure and the corresponding temperature within the condenser to rise from the evaporator pressure to the condenser pressure by the end of the pre-heating process (points 6 to 5 in Figure 1.2), assuming the total heat capacity of the condenser ($\dot{m} \cdot c$), including the metal and heat transfer fluid, is negligible.

Once the desorber reaches point 2 in Figure 1.2 (the minimum desorption temperature), the condenser connects to the heating network as shown in Figure 1.3, initiating the desorption process at the saturated condenser pressure. Desorption process continues until the minimum loading. The constant condenser pressure during desorption is maintained by assuming a very large overall heat transfer coefficient in the condenser, ensuring complete condensation of the desorbed working fluid and rapid heat transfer to the heating network.

In an ideal adsorber cycle, the desorber may also reach the maximum driving source temperature at point 3 in Figure 1.2. This is based on the assumption that the overall heat transfer coefficient between the adsorbent and the heat transfer fluid is very large in the desorber. At point 3 in Figure 1.2, the amount of working fluid per kg of dry adsorbent is $((X_{max} - \Delta X)$-$X_{min})$, which condenses and collects in the condenser space.

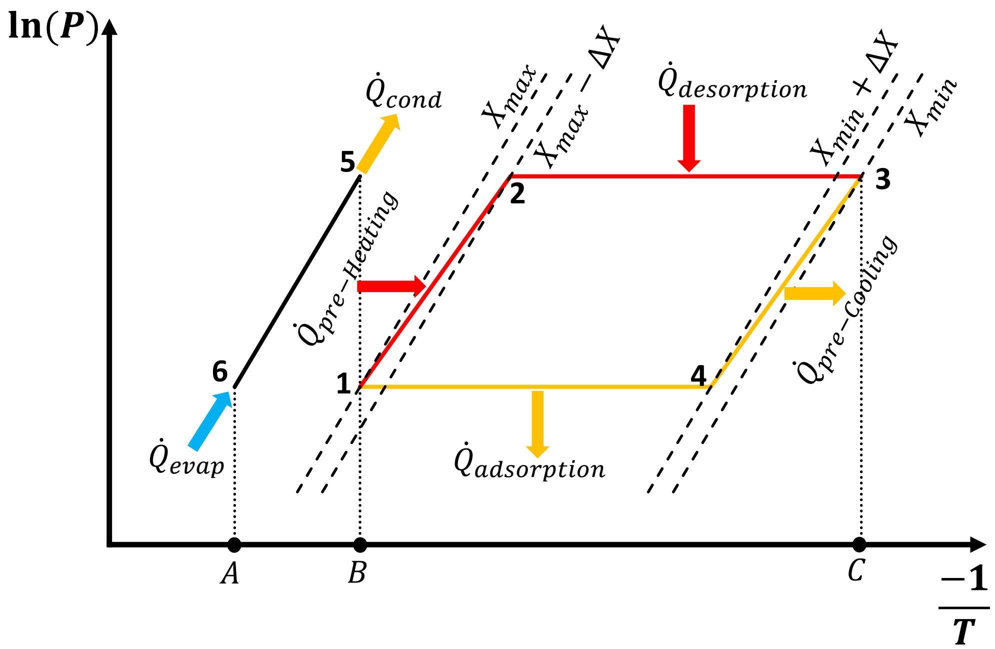

Figure 1.2.: Qualitative scheme of an ideal adsorber cycle on Clausius-Clapeyron diagram. A: $\frac{-1}{T_{\text{Low Temperature level}}}$, B: $\frac{-1}{T_{\text{Medium Temperature level}}}$, and C: $\frac{-1}{T_{\text{High Temperature level}}}$

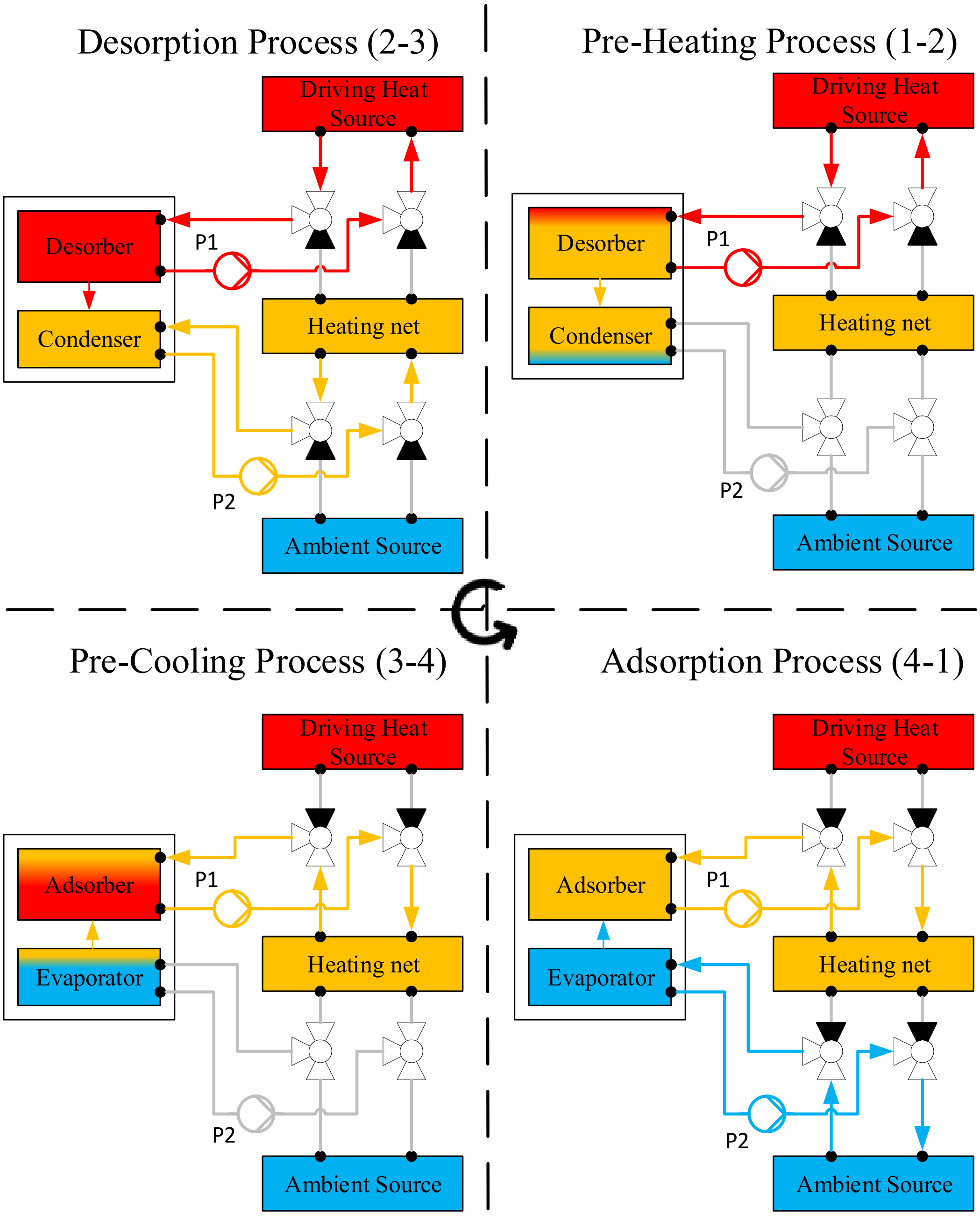

Figure 1.3.: Schematic representation of processes in an adsorber cycle. Blue indicates the low temperature level, orange represents the medium temperature level, and red denotes the high temperature level. Grey lines show the inactive lines.

At point 3 in Figure 1.2, the adsorber connects to the heating network in Figure 1.3, cooling the adsorber and initiating the pre-cooling process. During the pre-cooling process, a certain amount of previously condensed working fluid evaporates in the evaporator. The heat required for evaporation comes from the sensible heat of the remaining working fluid surrounding the evaporator. The pre-cooling process reduces the temperature and pressure of the evaporator from point 5 to point 6 in Figure 1.2 at the end of the pre-cooling process (3–4), assuming the total heat capacity of the evaporator is negligible.

It is worth mentioning that the pre-cooling process is analogous to the throttling process of the refrigerant in vapor compression heat pumps, which occurs in the expansion valve. Thus, the adsorber/desorber in an intermittent adsorption heat pump not only assumes the role of the mechanical compressor but also that of the expansion valve in a vapor compression cycle.

Finally, the adsorption process occurs from point 4 in Figure 1.2, as depicted in Figure 1.3. During this process, the evaporator connects to the ambient heat source to supply heat for evaporation. The evaporated working fluid is then adsorbed in the adsorber, delivering useful heat to the heating network. This process continues at saturated evaporator pressure, assuming a very large overall heat transfer coefficient of evaporator. The heating network temperature can reach the minimum adsorption temperature at point 1 in Figure 1.2, occurring only in the ideal adsorber cycle when the overall heat transfer coefficient in the adsorber is very large. During the adsorption process, (X_{max}-(X_{min} + ΔX)) amount of working fluid per kg of dry adsorbent is evaporated and adsorbed into the adsorbents. Upon reaching point 1 in Figure 1.2, one adsorber cycle is completed and the cycle restarts from point 1 in Figure 1.2 again.

1.1.2. SAPO-34/Water as Working Pair

In a thermally driven adsorption heat pump, the working pair consists of a working fluid (refrigerant) and an adsorbent. Selecting the right working pair for a specific application is crucial in designing adsorption heat pumps [33]. When choosing the working fluid, it should have a high enthalpy of vaporization, reasonable working pressure, low freezing temperature, small molecular size, chemical stability, low toxicity, and low cost [27].

When selecting an adsorbent material, several critical factors must be evaluated. These include water adsorption capacity under operating conditions, regeneration temperature, adsorption/desorption heat, permeability to water vapor diffusion, and intraparticle water adsorption kinetics which means how water interacts with porous materials at a microscopic level. The material should also be stable against mechanical stresses and hydrothermal cycling. Additionally, cost and market availability are important factors [27]. Given these characteristics, water is often chosen as the working fluid in heating applications despite its limitation in applications with temperatures below 0 °C due to the freezing problem in the evaporator.

Extensive research has focused on zeolite-water working pairs due to their non-toxic and environmentally friendly properties [27]. Alumino-silicate zeolites, such as types 4A, 13X, and Y [27, 34], are widely used in commercial applications across various fields, including chemistry and catalysis, because of their strongly hydrophilic nature. This hydrophilicity results in high water vapor adsorption capacity, substantial adsorption/desorption heat, and remarkable structural stability over multiple operating cycles. However, these zeolites require elevated regeneration temperatures (150–300 °C) [35], which restricts their applicability to systems with high-temperature heat sources and significant temperature lifts (around 40 °C or more). Here, “temperature lift” refers to the temperature differential between the evaporator and the condenser, as illustrated by the temperature difference between points 5 and 6 in Figure 1.2.

Advancements in adsorbent materials for low-temperature applications—such as drying, air conditioning, thermal storage, and refrigeration—have prioritized the development of Silico-Aluminophosphates (SAPO) materials, notably SAPO-34. SAPOs are a modified form of Aluminophosphates (AlPOs), distinguished by the inclusion of silica within the AlPO framework, which consists of alternating AlO_2^- and PO_2^+ units, creating a unique lattice structure [36]. The silica incorporation in SAPOs gives them moderate hydrophilicity and enhances water vapor adsorption capacity, which, in turn, allows for lower regeneration temperatures (60–100 °C) and reduced desorption heat compared to conventional adsorbents [37, 38].

Studies on various silico-alumino phosphates (e.g., AlPO-5, AlPO-18, SAPO-34) [15, 39, 40] confirmed their beneficial properties for adsorption cycles. Mitsubishi Plastic Incorporation (MPI) [41] developed and produced novel synthetic functionalized materials, "AQSOA" a type of SAPO, on a pilot scale. The adsorption equilibrium and durability of AQSOA-FAM-Z01 [42] and AQSOA-FAM-Z02 [43] were tested, revealing temperature dependence and S-shaped water vapor adsorption isotherms. These S-shaped isotherms indicate high water exchange capacity at low temperature differences [44]. Additionally, A small hysteresis was observed, with almost no change in adsorption equilibrium after 100,000 cycles, demonstrating the durability of AQSOA for practical use in adsorption heat pumps. However, a general issue with AlPO and SAPO is their high capital cost. This is mainly because the synthesis process is more expensive than that of standard commercial zeolites, and industrial mass production has not yet been established [27].

1.1.3. Review of Adsorption Module Technologies

In the development of adsorption heat pumps, the primary focus has been on increasing the specific power density to create more compact and lightweight units. Central to this effort is the improvement of heat conductance within a adsorber/desorber [45–49]. Consequently, based on the existing type of adsorbents—granules/pellets [50], binder-based coatings [51], and direct crystallization [17, 19, 24]—the research domain of various types of heat exchangers can be categorized into four distinct types: fin-tube, fin-plate, flat tube-fiber structure, and flat tube-lamella.

The simplest design involves a bed of adsorbent grains with an integrated heat exchanger [52]. Enhancing heat conductivity within the adsorber/desorber is crucial for the efficiency of heat pump systems. Methods to improve thermal conductivity include using additives, such as polyaniline composites [37], metal additives [53, 54], and fins within the adsorber/desorber [55]. Additionally, there are two coating techniques used to adhere adsorbents to the heat exchangers, as illustrated in Figure 1.4: ex-situ coating and in-situ coating [22]. In the ex-situ coating method, a binder or glue is used to adhere adsorbents, which are synthesized separately, onto the metal surface of the adsorber/desorber. In contrast, the in-situ coating method, such as the partial support transformation (PST) technique, involves the direct growth of adsorbent crystals on the heat exchanger and into the substrate, necessitating the placement of the heat exchanger in a reaction chamber. Compared to the ex-situ method, the in-situ approach offers enhanced stability [56] and improved compactness. However, thicker adsorbent layers in in-situ coating technique can prevent mass transfer, particularly with water as a working fluid due to low operating pressures. Therefore, solutions such as enlarging the heat exchanger surface area using structures like honeycombs [57], foams [58, 59], or fibers [60] have been proposed.

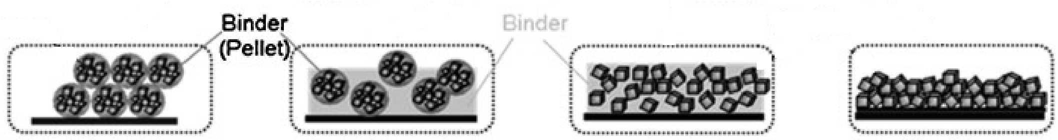

Figure 1.4.: Classification of sorption heat exchanger coating methods based on thermal contact types: from left to right, fixed point bed (point thermal contact), coating (bonded thermal contact), dip coating (bonded thermal contact), and in-situ crystallization (direct thermal contact) [22].

In 2012, a prototype utilizing directly crystallized adsorbent based on PST technique on fiber structures and flat tubes was developed and manufactured by Fraunhofer ISE (Freiburg) / IFAM (Dresden), Fahrenheit GmbH (formerly Sortech AG, Halle / Leipzig) [23]. Subsequently, the initial comprehensive endeavor to model heat and mass transport in directly crystallized fiber structures was undertaken in 2015 by Füldner [19]. Then, in 2016, the first adsorption module based on this technology was assembled through collaboration between Fraunhofer IFAM, Haugg Kühlerfabrik GmbH (Aachen), and Fahrenheit GmbH (formerly Sortech AG) [24].

Wittstadt et al. have developed and experimentally tested a compact adsorption heat pump aimed at increasing power density with specific efficiency [24]. This targeted development pathway resulted in the validated model employed in this research. The adsorption heat pump comprises an adsorber/desorber featuring a flat tube fiber structure, where zeotype silico-alumino phosphate-34 (SAPO-34) is directly crystallized on the fiber structure, and an evaporator/condenser flat tube fiber structure heat exchanger. Their results indicate that the heat and mass transfer resistance in the adsorber/desorber is the limiting factor of the adsorption heat pump. Additionally, Downsizing the Evaporator/Condenser can improve the overall efficiency and compactness of the heat pump [24]. Following these findings, Velte et al. [61] downsized the Wittstadt et al. [24] heat pump by reducing the size of the Evaporator/Condenser to 30 % of the original size, without negatively impacting the output power of the heat pump, as shown in Figure 1.5. The downsized dimension with different cycle control were specifically aimed at integrating the heat pump as a supplement to the widely used wall-hung condensing gas boilers in the European market [61]. However, their results identified the Evaporator/Condenser as the limiting factor of the Velte et al. [61] adsorption heat pump.

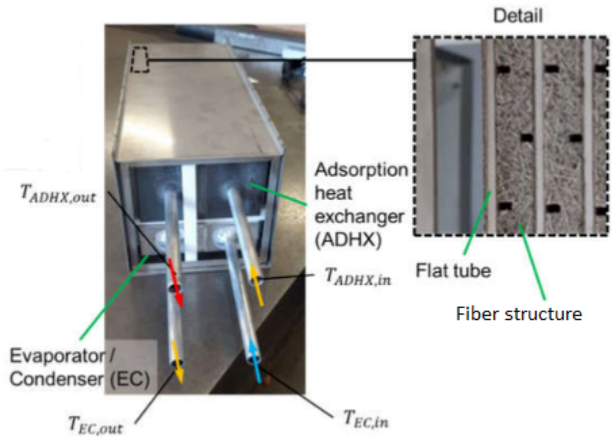

Figure 1.5.: Compact adsorption heat pump module (left) with a detailed view of the fiber heat exchanger (right) [61].

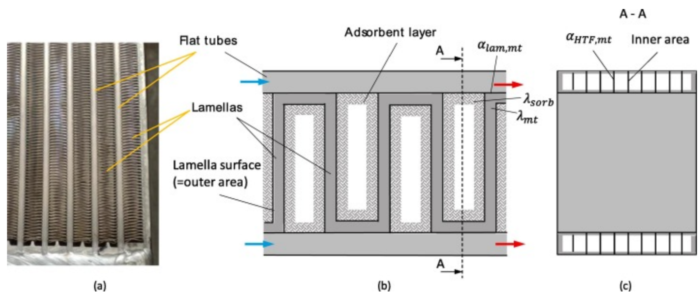

Figure 1.6.: Detailed view of flat-tube lamella heat exchanger [62].

Additionally, A drawback of the fiber structure adsorption heat pump is the severe corrosion of the evaporator/condenser component over long-term stable utilization [62]. Therefore, Velte et al. [62, 63] have experimentally and numerically analyzed adsorption Heat pump with a adsorber/desorber containing a flat tube-lamella heat exchanger Figure 1.6, where SAPO-34 is directly crystallized with the help of the PST technique on the lamella for the adsorber/desorber, and a fin-tube heat exchanger for the evaporator/condenser within a single vacuum chamber. This approach aimed to resolve the production challenges and corrosion issue associated with using fiber-structured heat exchangers.

In this thesis, the numerical model of the complete technical adsorption module–comprising a flat tube-lamella heat exchanger for the adsorber/desorber and a fin-tube heat exchanger for the evaporator/condenser–will be utilized for further analysis. To effectively implement a gas adsorption heat pump using this adsorption module technology, precise sizing of the heat pump is essential. This requires a detailed understanding of the heating demands on the user side.

1.1.4. Heat Demand in Different Stock Buildings

To gain a comprehensive understanding of energy demands in a building, it is necessary to consider various types of building stock in Germany [64]. In 2009, a set of six representative buildings was studied to understand different types of German buildings. These structures accounted for two size categories (SFH: single-family houses with one or two dwellings / MFH: multi-family houses with three or more dwellings) and were categorized into three construction year periods (I – III) based on different levels of energy-saving regulations in Germany. In order to keep the model manageable, the more differentiated construction year classes of the German Building Typology were merged to form the following three building age bands. The initial time frame contains buildings constructed until 1978, predating the first German regulation on thermal protection. The subsequent periods (1979 – 1994 and 1995 – 2009) were selected in alignment with the evolving thermal protection regulations, with multiple updates occurring within each period. This evolution also included the introduction of a more comprehensive energy-saving regulation in 2002 [65].

A large part of German building stock consists of older buildings requiring renovation [66]. In the multi-family housing (MFH) sector, approximately 80 % of buildings are older than 30 years (constructed up to 1987), with around 40 % being older than 60 years [67]. To thoroughly understand the German building stock in the multi-family housing sector, it is recommended to classify it into three distinct categories. Small-sized MFH with less than 3-6 residential units, Medium-sized MFH with 7-12 residential units, and Large-sized MFH with more than 12 residential units [68]. An extensive analysis of buildings reveals that 94 % of the multi-family building stock consists of structures with 3-12 residential units, with a 20 % portion constructed between 1958 and 1968, representing a predominant segment of the German building stock [68].

According to the findings reported by Cischinsky et al. [68] regarding multi family building stock in Germany, a significant portion of the heating demands including Space heating demand and Domestic Hot water in multi-family houses is primarily provided through centralized systems (70 % of cases). The second portion is attributed to district heating. Additionally, Gas serves as the primary energy source for heating, constituting over 56 % of usage, followed by district heating, especially prevalent in large multi-family houses (LMFH).

1.2. Purpose and Objectives of Study

The project consortium "LowEx-Bestand" aimed to enhance heat supply in renovated multi-family existing buildings through heat pumps, heat transfer, and ventilation systems, with a focus on analyzing, developing, and demonstrating solutions to accelerate the market adoption of Low Exergy systems. The consortium operated through three pillars: Analysis, Technology Development, and Demonstration, with Analysis serving as the scientific backbone and Technology Development collaborating with industrial partners to improve technologies. The demonstration projects then implemented and monitored these technologies in renovated multi-family buildings [66].

As part of the technology development efforts, the AdoSan project, outlined in [26], concentrated on advancing a gas adsorption heat pump (GAHP) using SAPO-34 as adsorbent and water as the refrigerant for renovated MFH. The enhancements to the GAHP were made in four stages within this project.

First, Fahrenheit GmbH, an expert in adsorption chillers, developed high-performance fiber-structure adsorber/desorber and sorption module (Adsorber Cycle) and produced operating models.

Second, Haugg GmbH and Fraunhofer IFAM developed production technology for fiber-structure adsorber/desorber, evaporator, and sorption module (Adsorber Cycle).

Third, Hermann Burners and DVGW-EBI developed a gas-flexible burner capable of accommodating up to a 30 % addition of hydrogen (H2).

Fourth, Fraunhofer ISE handled the component dimensioning, hydraulic interconnection of heat exchangers [17], and implementation of control strategies at both the component and device levels of dual adsorber cycle Gas Adsorption Heat Pump [17, 69], while system modeling and simulation tasks were shared between Fraunhofer ISE and KIT.

Consequently, a fully functional test bed with a 40 kW heat capacity, suitable for renovated MMFH, was constructed and tested. This system achieved annual heating coefficients of 1.25-1.3 for a heating net with nominal supply/return temperatures of 55/45 °C, respectively.

Now it is possible to outline the research objectives based on the "AdoSan" project as a part of the "LowEx-Bestand" project in the following subsections.

1.2.1. System-Level Modeling

For heating supply temperatures of up to 55 °C, a significant portion of the existing radiators in the German multi-family building stock could be utilized with a heat pump system, thereby reducing renovation costs [14, 70]. However, the temperature lift (between low temperature source and medium temperature sink) achievable with the SAPO-34/water working pair in GAHPs is constrained to approximately 30 K. As a result, under typical low-temperature source conditions, the adsorption process alone cannot provide the 55 °C supply temperature needed to fully meet heating demand or domestic hot water (DHW) production requirements.

To address this limitation, the system-level design of the adsorption heat pump must incorporate a "direct burner mode" to cover peak loads and satisfy the higher temperature demands. This is especially critical for centralized systems with DHW loads, where a minimum hot water circulation temperature of 55 °C is required to maintain hygiene standards and prevent Legionella growth. In the Adosan project, only space heating demand was addressed. In contrast, the objective of the system-level modeling in this thesis is to integrate the DHW component for the purpose of preheating domestic hot water. While the solution matrix [71] focuses specifically on compression heat pumps, as discussed in chapter 2, the present work extends the analysis to include DHW preheating by utilizing the condensing boiler effect and the sorption process in the GAHP to optimize gas consumption. Furthermore, the performance of DHW preheating will be compared to the conditions under which DHW is prepared exclusively with a burner. Additionally, this study evaluates the capability of efficiently maintaining comfort temperature ranges in both the water heating circuit and the space heating circuit in a medium-sized multi-family house throughout the year. Since heat production is delivered to and heat consumption is drawn from a stratified storage tank, understanding the impact of these components on thermal stratification is essential. This understanding serves as a valuable indicator for interpreting temperature deviations from target temperatures required by heating demands and for assessing system-level control performance. Therefore, the influence of heat production and consumption on thermal stratification will be assessed by balancing entropy, in order to determine which components have the greatest impact on thermal stratification within the storage tank.

1.2.2. Comparative Analysis of System Performance in various Configurations for a Dual Adsorber Cycle Gas Adsorption Heat Pump with low Temperature Heat Sources and Thermal Storage Options

One of the objectives of the AdoSan project [26] is to demonstrate the implementation and achievement of a Seasonal Gas Utilization Efficiency (SGUE) greater than 1.3.

It is important to note that the SGUE, as defined in [72], is the annual ratio of output heat to the input gas energy, as specified in [73]. In contrast, the Seasonal Coefficient of Performance (SCOP) for electrically driven heat pumps, as detailed in [74], is defined as the annual ratio of output heat to input electrical energy. Thus, both SGUE and SCOP serve the same purpose of evaluating system performance, but they differ in the type of energy source they consider.

This research aims to assess various configurations to achieve this objective. Specifically, different hydraulic connections of various components, including a dual adsorber cycle Gas Adsorption Heat Pump, a borehole heat exchanger as a low-temperature heat source, one or two stratified storage tanks, and solar thermal collector, will be evaluated to supply domestic hot water and space heating demand in MFH. Both component-level control strategy, particularly for the Domestic hot water component and solar thermal collector, and system-level control strategy will be considered in this evaluation.

1.2.3. Sensitivity Analysis of a Reference System with Dual Adsorber Cycle Gas Adsorption Heat Pump, Combi-Storage, Ideal Stratifier, and Heat Consumptions

To identify the key parameters affecting the efficiency of the heating system, it is necessary to analyze the impact of boundary conditions, operational parameters, design parameters, and Model properties in each configurations.

1.2.4. Analysis of single adsorber cycle Gas Adsorption Heat Pump with Heat Recovery through Combi-Storage

Enhancing the efficiency of Gas Adsorption Heat Pumps stands as a primary objective within the AdoSan project. Beyond the AdoSan Project, various heat recovery methods, such as the thermal wave cycle [17, 75, 76] and the Stratisorp cycle [16, 77, 78] have shown potential for improving efficiency. Expanding upon the work done in AdoSan, this study advances the research by integrating the single adsorber cycle with a stratified storage tank, aiming to recover sensible heat between the evaporator and condenser. The motivation for this research lies on two reasons. First, a single adsorber cycle heat pump offers potential cost savings over a dual adsorber cycle by requiring only one adsorption module. Second, coupling a single adsorber cycle with stratified storage provides enhanced flexibility and adaptability, as it uses additional degrees of freedom within this heat pump configuration. The main objective of this study is to identify a single adsorber configuration–including both hydraulic scheme and control scheme–that maximize the SGUE while maintaining the same adsorber module and the same adsorbent mass per kilowatt of nominal power of the heat pump as in the AdoSan test bed.

1.3. Thesis structure

Chapter 2 introduces various numerical components, such as the domestic hot water circuit with circulation and the solar thermal circuit, illustrating how renewable energy can be integrated into a building heating system to meet heating demands. The models, reference buildings, and boundary conditions used in this study are based on the LowEx-Bestand [66] research environment, and relevant findings from this framework are referenced to support the modeling choices. Subsequently, a heating system integrating a validated dual adsorber cycle GAHP and Combi-Storage is described. Following that, a heating system integrating a single adsorber cycle GAHP and Combi-Storage is presented to highlight the differences between dual adsorber cycle and single adsorber cycle GAHPs. Four configurations are then explained, providing a detailed description of the implemented control strategy. The subsequent step involves understanding the distinctions between the Reference system and the Base system, along with the calculation of the heating system's efficiency, noting that the Reference system uses a Combi-Storage with a high-temperature burner connected to its top via a heat exchanger to supply the Water Heating Circuit, and includes an additional Water Heating Circuit fed through a Fresh Water Station—features not present in the Base system.

In Chapter 3, entropy balancing is employed to analyze and compare the distribution of thermodynamic losses across components in single adsorber and dual adsorber gas adsorption heat pumps.

In Chapter 4, a detailed analysis of the Reference system is conducted, and the performance of three different configurations is compared against it. Additionally, a sensitivity analysis is performed to identify parameters that significantly impact the Reference system's performance. Finally, the integration of a single adsorber cycle GAHP with Combi-Storage is analyzed in this chapter.

Chapter 5 presents a comprehensive summary of the key results obtained from the dual adsorber cycle GAHP and explores its potential to enhance the performance of Reference system in meeting the heating demands of MFH through parameter variation. Additionally, the chapter provides an in-depth discussion of the heat recovery process between the condenser and evaporator, as well as an analysis of the degrees of freedom within the single adsorber cycle GAHP. This analysis is aimed at evaluating the feasibility of replacing the single adsorber cycle with a dual adsorber cycle GAHP. Chapter 6, on the other hand, outlines potential pathways for future research, providing an outlook for further developments in this area.

2. Technical Description of Building and Heat pump configurations

The use of heat pumps to meet heating demands in Multi-Family Houses (MFHs) requires standardization due to their widespread implementation. To address this, the International Energy Agency (IEA) established a working group (IEA HPP Annex 50) to develop a 'solutions matrix' categorizing different approaches to heat pump utilization in MFHs [71]. Although the solution matrix was developed for compression heat pumps, the boundary conditions are also applicable to gas-driven heat pumps. This classification, illustrated in Figure 2.1, covers a broad spectrum of heating supply methods, ranging from centralized to decentralized compression heat pump installations. The topic of this chapter was specifically addressed in the LowEx-Bestand project [66], which provides a structured framework for classifying these solutions.

2.1. Specification of the Analyzed Building

In Germany, 70 % of the heating requirements in Multi-Family Houses (MFHs) are met through centralized systems, as presented in subsection 1.1.4. Given the dominance of centralized heating, it is essential to highlight its significance in MFHs.

To address research questions regarding heating demands in Medium-sized Multi-Family Houses (MMFHs), this study examines a hybrid heat pump system—a combination of a direct burner and a gas adsorption heat pump—recommended by the solutions matrix [71]. While adsorption heat pumps remain largely in the R&D stage and their labor-intensive production limits scalability for smaller or decentralized units, their economic viability improves with larger systems that achieve significant gas savings. Therefore, this hybrid system is designed to provide both space heating and domestic hot water for the entire building.

Within the LowEx-Bestand project, specific research was conducted to identify representative buildings based on typology [64], age, and heating technology, as well as to define typical renovation scenarios. The findings of this analysis are summarized in [66]. The MMFH selected for this thesis falls under the Building Age Period[1] of 1978–1985 and has been renovated to comply with the Building Energy Law Renovation Standard[2]. Its building envelope characteristics are detailed in [79]. The MMFH consists of 12 apartments with a total conditioned residential area of 908 m² (4 apartments house 1 occupant each, while 8 apartments accommodate 2 occupants each, totaling 20 occupants). To model the heating demand of the MMFH, a load series approach is used, where the building model is

[1] Baualtersperioden (BAP)
[2] Gebäudeenergiegesetz-Sanierung (GEG-Sanierung)

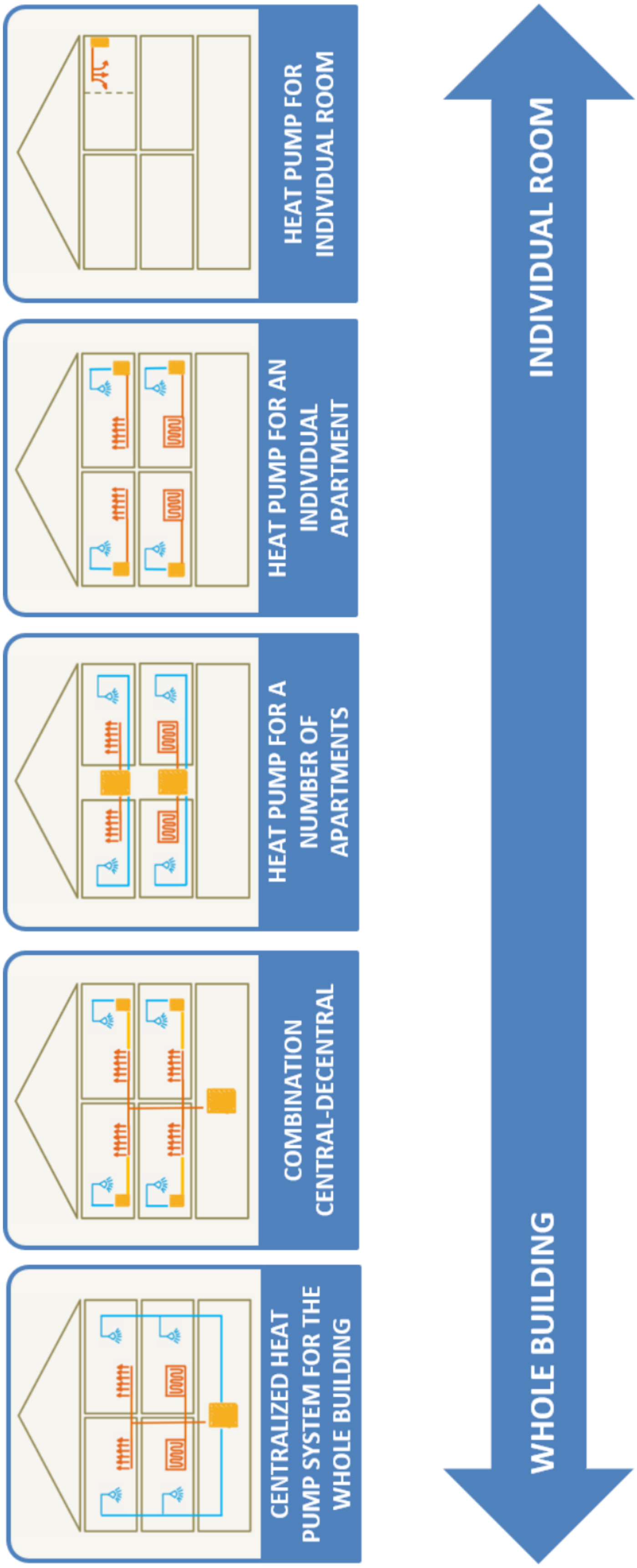

Figure 2.1.: General classification of solutions in multi-family houses, highlighting compression heat pump installations [71].

decoupled from the heating system model. The MMFH has been previously modeled and simulated with ideal heating systems in TRNSYS by colleagues [79], providing load series that serve as boundary conditions for the heating system simulations in this study.

This chapter provides a numerical model description for each component of the studied building's heating system. The numerical models are implemented in Dymola [80], a commercial modeling and simulation environment for Modelica-based models [81]. The resulting nonlinear differential-algebraic equations (DAEs) are then solved using DASSL (Differential Algebraic System Solver), an integration algorithm [82]. This solver employs a variable step-size strategy to adapt the time step during simulation, achieving a balance between accuracy and computational efficiency, particularly in the presence of stiffness or rapidly changing dynamics.

2.1.1. Description of Building Components

An essential part of the heating system model is the representation of heat exchangers. As shown in Figure 2.7, the heat exchangers used in Fresh Water Station, High-Temperature Source Heat exchanger, Medium-Temperature Sink Heat Exchanger, and Low-Temperature Source Heat exchanger are modeled using the ϵ-NTU (effectiveness-Number of Heat Transfer Units) method [83]. In equation (2.1), $\dot{\mathrm{Q}}$ represents the heat flow rate between two hydraulic circuits, denoted as 1 and 2, while $\dot{\mathrm{C}}_1$ and $\dot{\mathrm{C}}_2$ signify the heat capacity rates on sides 1 and 2, respectively.

$$\dot{Q} = \dot{C}_1 \cdot (T_{1,\mathrm{in}} - T_{1,\mathrm{out}}) = \dot{C}_2 \cdot (T_{2,\mathrm{out}} - T_{2,\mathrm{in}}) \tag{2.1}$$

The effectiveness, defined in equation (2.2), quantifies the ratio of the heat flow rate to the maximum possible heat flow rate. $\dot{\mathrm{C}}_{\mathrm{min}}$ denotes the minimum heat capacity rate among the two heat transfer fluids.

$$\epsilon = \frac{\dot{Q}}{\dot{Q}_{\mathrm{max}}} \tag{2.2}$$

$$\dot{Q}_{\mathrm{max}} = \dot{C}_{\mathrm{min}} \cdot (T_{1,\mathrm{in}} - T_{2,\mathrm{out}}) \tag{2.3}$$

The Number of Heat Transfer Units is expressed as the ratio of the overall heat conductance to the minimum capacity flow rate, as depicted in equation (2.4).

$$\mathrm{NTU} = \frac{UA}{\dot{C}_{\mathrm{min}}} \tag{2.4}$$

$$\mathrm{C}^* = \dot{C}_{\mathrm{min}}/\dot{C}_{\mathrm{max}} \tag{2.5}$$

For a counterflow heat exchanger, the relation between NTU and effectiveness is defined by equation (2.6).

$$\epsilon = \frac{1 - \exp -NTU(1 - \mathrm{C}^*)}{1 - \mathrm{C}^* \cdot \exp -NTU(1 - \mathrm{C}^*)} \tag{2.6}$$

To size the heat exchangers in this study, the only adaptable parameter when utilizing the ϵ-NTU method is the UA value. Thus, Three approaches are employed.

Firstly, constant UA values are utilized, sourced from [66], which offer the best fit between experimental and simulated results for Low-Temperature Source heat exchanger (HX_LT) and Medium-Temperature Sink Heat Exchanger (HX_MTS), as detailed in Figure 2.7.

Secondly, the logarithmic mean temperature difference is applied by using known inlet, outlet temperatures, along with nominal demand power of the Domestic hot water profile which is explained in subsubsection 2.1.2.2:

$$\dot{Q} = UA \cdot \underbrace{\frac{\Delta T_2 - \Delta T_1}{\ln\left(\frac{\Delta T_2}{\Delta T_1}\right)}}_{\text{LMTD}} \tag{2.7}$$

Here, $\dot{Q}$ represents the nominal demand power in Domestic hot water consumption, while ΔT_1 and ΔT_2 indicate the temperature differences between inlet and outlet flows on each side of the heat exchanger.

Thirdly, due to the lack of detailed design parameters and inlet-outlet temperatures, a sensitivity analysis is conducted to illustrate the impact of varying UA values on Seasonal Gas Utilization Efficiency.

As explained in subsubsection 2.2.1.1, the simulated model of the heating system does not consider thermal mass. However, the simulated model in this study includes thermal mass. Therefore, Heat exchangers utilizes the "DryCoilCounterFlow" model, characterized by a counterflow coil with discretization along the flow paths without considering humidity condensation, sourced from the Modelica Buildings library [84]. Each discretized element dynamically models the fluids and solids. The driving force for the heat transfer is the temperature difference between the fluid volumes and the solid.

$$\frac{d(C \cdot T)}{dt} = (hA)_1 \cdot (T_1 - T) + (hA)_2 \cdot (T_2 - T) \tag{2.8}$$

The convective heat transfers, which depend on the mass flow rate, are computed using explicit equations to ensure rapid computational processing and numerical stability, particularly designed for time steps of approximately 10 minutes or longer, while disregarding transient dynamic effects [85, 86]. To calculate the heat capacity, the model make the assumption of equal convective heat transfer coefficients for the two heat transfer fluids, denoted as $hA_1 = hA_2$ [84]. Consequently, Equation (2.8) is modified accordingly:

$$C\frac{dT}{dt} = 2 \cdot (UA)_0 \cdot ((T_1 - T) + (T_2 - T)) \tag{2.9}$$

$$C = 2 \cdot (UA_0) \cdot (t_m) \tag{2.10}$$

Here, UA_0 represents the nominal overall heat conductance, determined through the methodologies outlined earlier. Given UA_0, the heat capacity is calculated using (2.10), where t_m denotes the time constant associated with the metal of the heat exchanger when the metal's behavior is approximated by a lumped thermal mass.

2.1.1.1. Water Heating Circuit

Supplying Domestic Hot Water (DHW) in multi-family houses (MFH) presents two distinct challenges when integrating heat pumps. Firstly, achieving energy-efficient heat generation is hindered by the fact that maintaining high temperature levels with heat pumps often results in reduced efficiency [66]. Secondly, the requirement for high temperatures in central DHW systems, mandated by legal hygiene standards for MFH, particularly concerning Legionella protection, adds another layer of complexity. Within this framework, Figure 2.2 presents four variants of Domestic Hot Water supply with heat pumps. In the first variant,

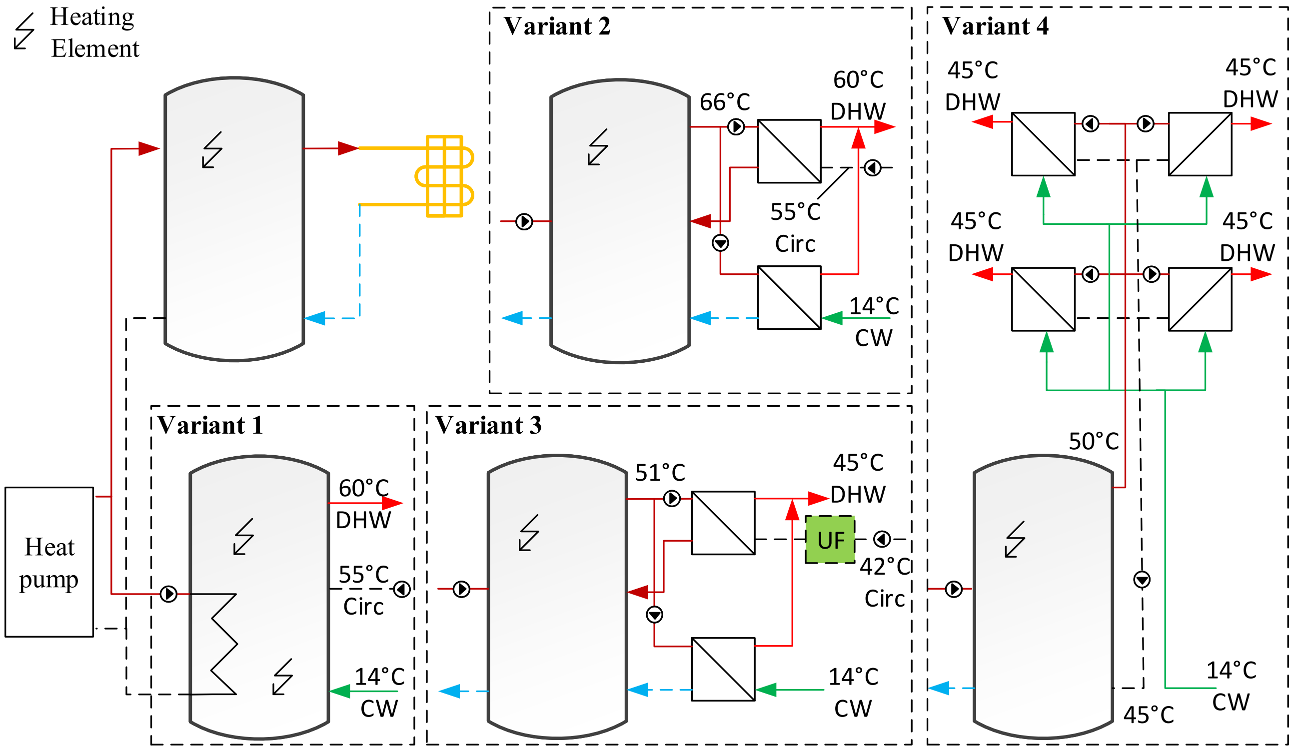

Figure 2.2.: Simplified hydraulic diagram of the heat pump system illustrating space heating via panel radiators and various Domestic Hot Water (DHW) configurations: Variant 1: Central storage water heater with internal heat exchanger (DHW storage). Variant 2: Central domestic hot water heater (Freshwater station) with storage. Variant 3: Inclusion of additional ultrafiltration (UF) in the circulation return bypass. Variant 4: Decentralized domestic hot water heater (apartment stations) with central storage [66].

DHW is supplied using a DHW storage tank equipped with an internal heat exchanger. Variants 2 and 3 employ a fresh water station with a storage tank. Variant 3 incorporates an additional ultrafiltration unit for mechanical Legionella control in the circulation return (bypass operation). According to the manufacturer, this can lower the system temperature in the DHW circuit to nearly the temperature of the drawn water (45 °C). In variant 4, DHW is provided through decentralized fresh water stations (Apartment stations) with a central storage tank. This configuration allows for temperature reduction due to the smaller volumes of DHW-filled pipes [87].

The implementation of thermal insulation regulations on existing building envelopes significantly affects space heating energy demand, potentially reducing it by up to 75 % [66]. This decrease leads to a rise in the relative share of DHW energy consumption in total energy consumption when the DHW temperature level remains unchanged. Consequently, technologies such as ultrafiltration (variant 3) or apartment stations (variant 4) offer a promising opportunity to lower temperature levels in DHW circulation for future-oriented, renewable energy-based heat supply [66]. However, challenges exist concerning ultrafiltration technology and apartment stations in variants 3 and 4, respectively. The inadequate testing of ultrafiltration necessitates regulations to ensure hygienically flawless operation. Additionally, transitioning to a decentralized DHW system presents challenges such as increased construction work, higher investment costs, and a lack of evidence regarding the hygienic safety of such systems.

Considering the gap identified in variant 3 and variant 4, and recognizing that Medium-sized Multi Family Houses (MMFH) represent approximately 70 % of multi-family housing units within the German building stock and commonly utilizing centralized heating systems [68], variant 2 is selected for implementation in the simulation model of this thesis. This decision aims to tackle the challenges associated with ultrafiltration technology and apartment stations, ensuring a more feasible and effective approach to optimizing DHW circulation.

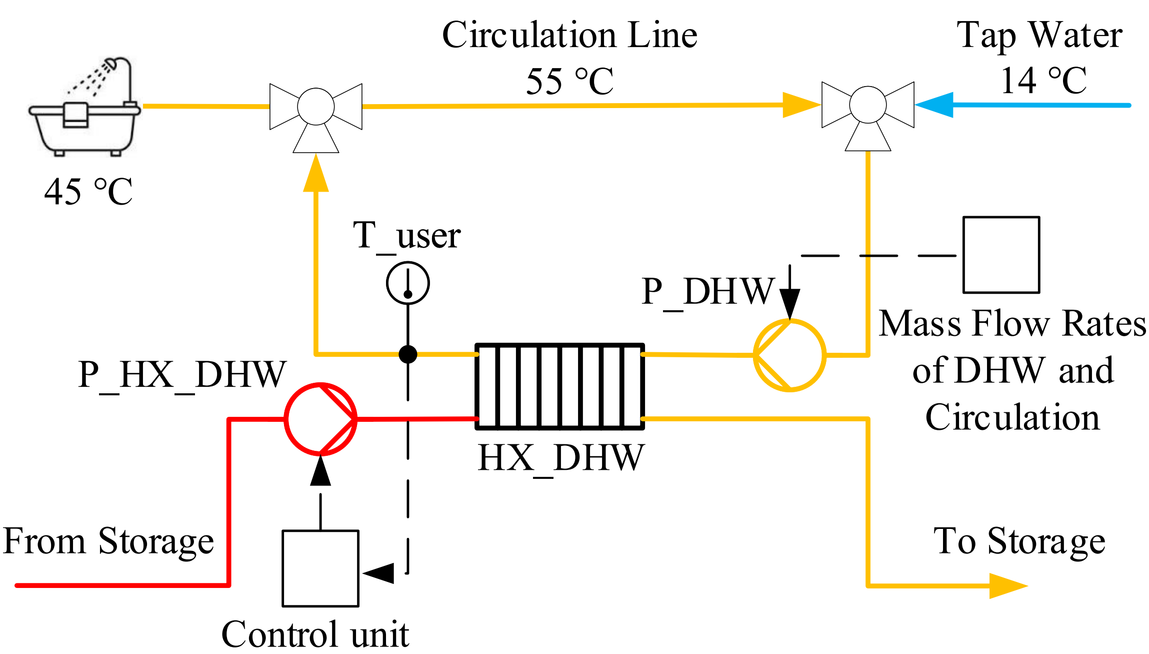

Figure 2.3.: Water heating circuit with circulation line.

Figure 2.3 shows the hydraulic scheme and control strategy of centralized fresh water station. One side of the heat exchanger is connected to the combi-storage, while the other side is connected to the consumption part. On the storage side, the mass flow rate of the pump is regulated by a PI controller with a set point of 60 °C. The measurement point for the controller is the temperature sensor know as T_user. Supply water is taken from the top layer of the combi-storage, where it is almost at 65 °C, and the cooled return water is directed back to the combi-storage using an ideal inserter. This inserter guides the return water to the layer with the closest temperature. On the user side, there are two operational states. First, when the user draws water from the tap, the mass flow rate of the pump is determined by the domestic hot water power profile and the temperature difference between the water supply temperature (14 °C) and the return temperature (60 °C). Subsequently, in the absence of draw-off from the tap, a circulation system is activated. This system circulates cooled return water at 55 °C within the pipe at a rate of 0.015 kg/s. The purpose of this operation is to maintain sanitary conditions, eliminate Legionella bacteria, and reduce waiting times for hot water.

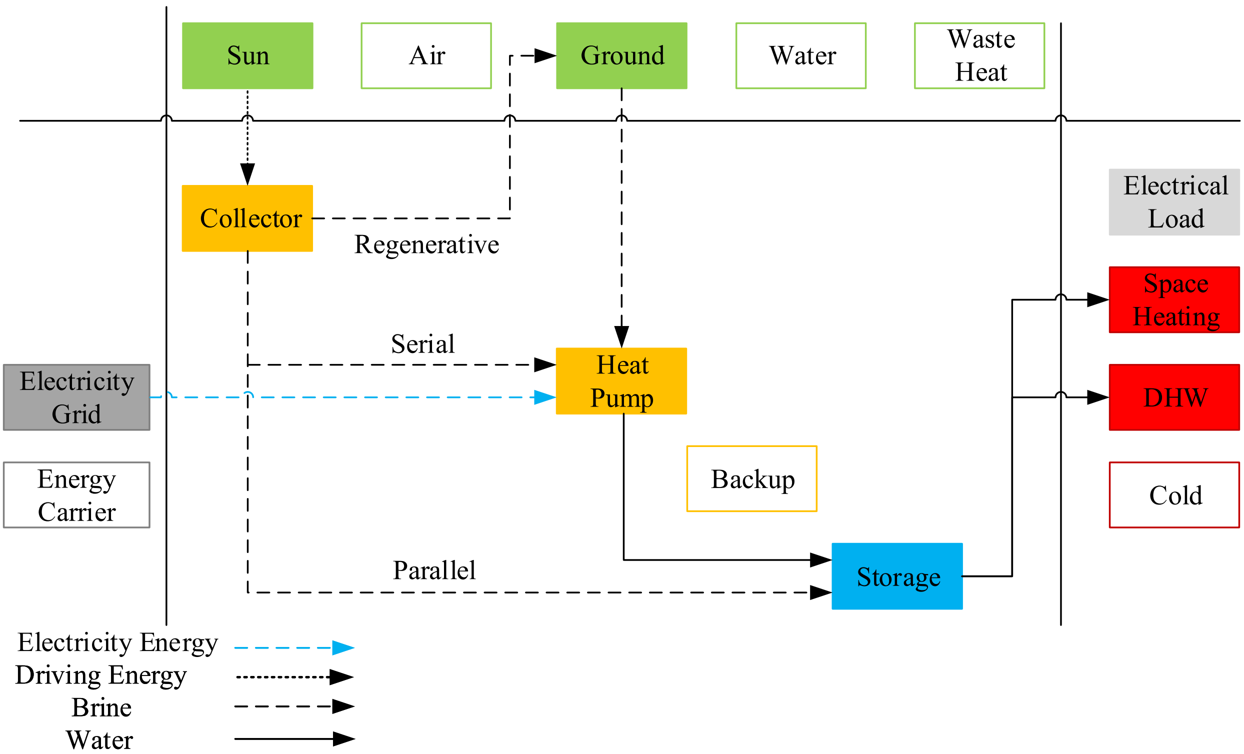

Figure 2.4.: Simplified hydraulic scheme of a ground source heat pump system with an optional solar thermal circuit.

2.1.1.2. Solar Thermal Circuit

The system concept for useful heat production is classified in Figure 2.4, distinguishing between mandatory components (heat pump) and optional component such as the solar thermal collector. It illustrates four combinations. Firstly, the Parallel mode, where the solar thermal collector and heat pump independently supply useful heat to the storage.

Secondly, the Serial mode, where the solar collector serves either exclusively as a low-temperature heat source for the heat pumps, or additionally fulfills that role. Thirdly, the Regenerative mode, where solar energy warms the heat pump's ground heat source. Lastly, there's a combination of these three modes, considering that the Serial mode and/or Regenerative mode do not exclude each other within a system [88].

Based on the case study in this thesis, we opted for the Parallel mode of combination heat pump with solar thermal collector to supply heating demands in a renovated MFH. There are two possible approaches for connecting a solar thermal collector to the stratified storage tank in this system concept: utilizing an internal heat exchanger or an external heat exchanger [89]. Additionally, the return temperature from the solar thermal collector to the stratified storage tank can be regulated using either an internal or external stratification device [89]. Despite the considerable impact of boundary conditions (such as the specific volume flow in solar thermal circuits, the target temperature for domestic hot water production, the operating time of the circulation pump, and the design temperatures for space heating) on system energy savings, Zaß [89] has chosen an external heat exchanger with an ideal inserter due to its consistent results with the findings of Jordan and Vajen [90]. In this research, the hydraulic connection of the solar thermal collector to the combi-storage is considered as an external heat exchanger with an ideal inserter, aiming to address two main questions. Firstly, in scenarios where heat pumps are utilized in densely populated urban areas, the exploitation of air and ground heat sources poses a critical challenge due to limited space availability in inner-city plots. Therefore, the integration of solar thermal collectors with stratified storage systems is being investigated as a potential solution [66]. Secondly, our focus is on achieving a minimum Seasonal Gas Utilization Efficiency (SGUE) of 1.3, in line with one of the objectives outlined in the AdoSan project [26]. To achieve these two objectives, three key parameters need to be calculated.

Firstly, determining the required solar collector area based on the total heating demands for the considered Medium-sized Multi Family House (MMFH) in this reaserch. As illustrated in Figure 2.5, selecting a smaller collector area covers a smaller portion of the total heating demands for MMFH, while a larger area fails to effectively meet these demands. Hence, a solar collector area of 37 m^2 is considered adequate for meeting the heating demands of the MMFH. Based on this, a glazed flat-plate collector manufactured by 'Dimas SA' with the model 'Energy+ARGO 15' is selected for simulation in this study [91, 92].

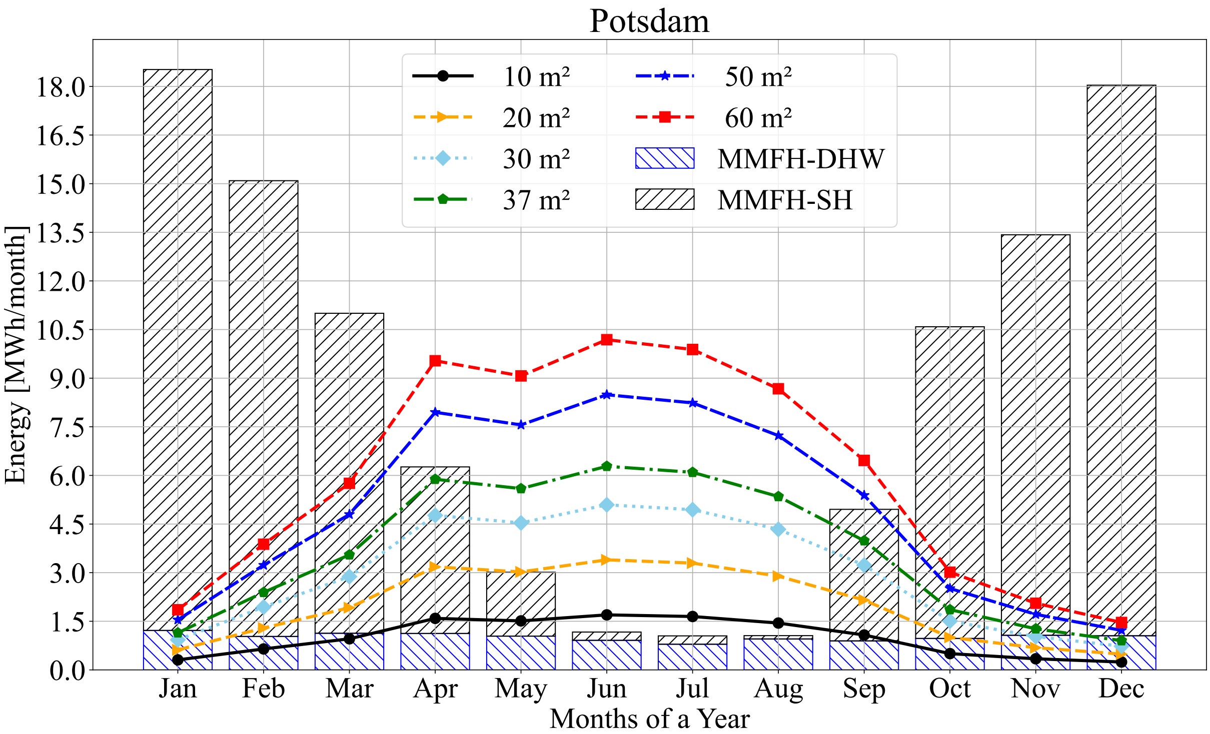

Figure 2.5.: Comparison of monthly space heating and domestic hot water demands in a Medium-sized Multi Family House (MMFH) with annual domestic hot water demand of 11.48 kWh/m^2/year and annual space heating demand of 101.32 kWh/m^2/year, against total solar irradiation across different collector areas on the roof (27 ° inclination [66]) under Potsdam weather conditions.

Secondly, sizing the solar heat exchanger. Based on the technical data sheet, the output power per gross area of the collector named 'Energy+ARGO 15', considering a temperature difference of 10 K between the mean temperature of the collector and the ambient temperature, is reported as 696 W/m^2 [92]. Designing the heat exchanger for an average temperature difference of $a_1 - b_2 = 5$ K [89], resulting in a UA_0 value of 5151 W/K.

Thirdly, determining the mass flow rate of the pumps on both sides of the solar heat exchanger. Typically, lower mass flow rates within the range of 15 to 25 lit/m^2 · h are recommended, while higher mass flow rates between 25 and 45 lit/m^2 · h are also considered [93]. Although higher mass flow rates have the potential to enhance the delivery of the solar thermal power to the storage, it poses a risk of strong mixing despite the ideal inserter [89]. Consequently, a control strategy incorporating two different mass flow rates is considered in this study to balance collector efficiency and mixing risk. In the component-level control strategy for the Solar Thermal Circuit, two pumps are utilized, each with its distinct mass flow rate control mechanism. The pump on the solar collector side adheres to three conditions. Firstly, the critical irradiation of the specific stratified storage layer, associated with the supply line of the heat exchanger on the storage side, is calculated in Equation 2.11 [94] and compared with the total irradiation on a tilted surface.

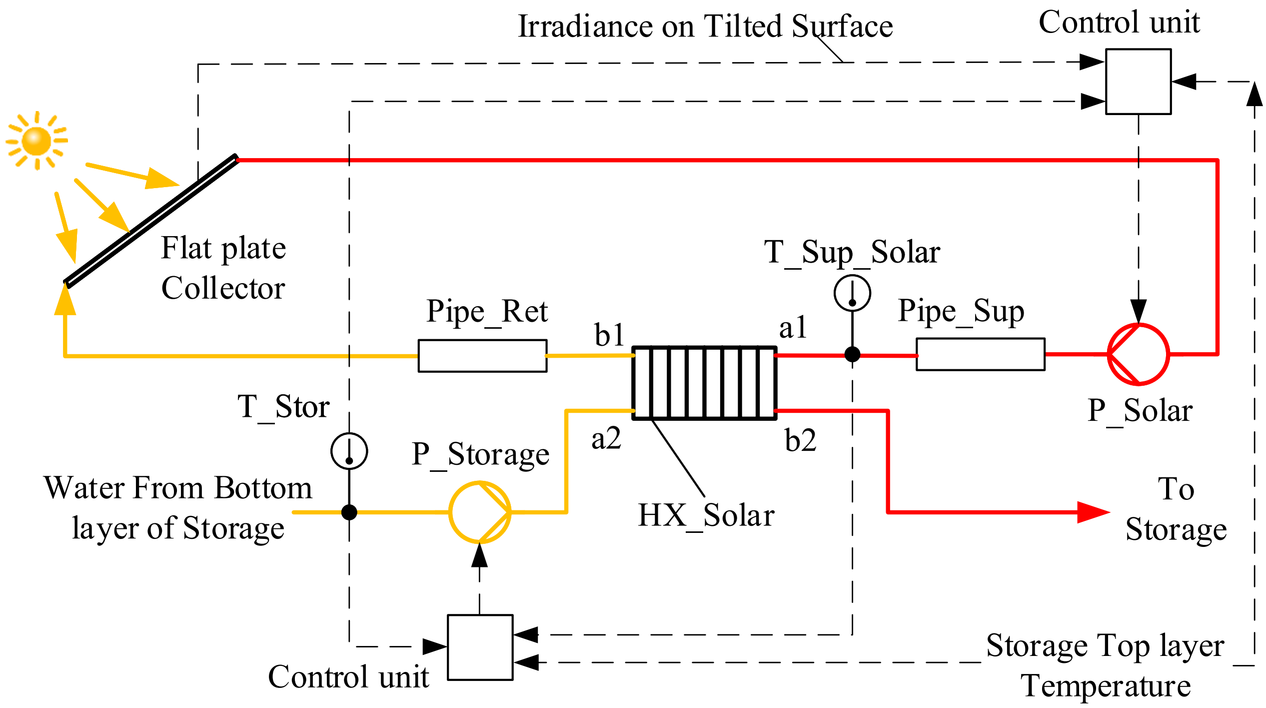

Figure 2.6.: Solar thermal circuit.

$$G_{Tc} = \frac{F_R U_L (T_{in} - T_{env})}{F_R(\tau\alpha)} \tag{2.11}$$

If the total irradiation on the tilted surface exceeds the critical irradiation threshold, the pump activates. Secondly, to harness maximum potential solar power, the pump's mass flow rate doubles when the temperature of the storage's top layer surpasses 70 °C. Finally, a protective measure is implemented during summer to prevent potential harm to the stratified storage tank. When the temperature of the top layer exceeds 95 °C, the pump deactivates.

Similarly, the pump on the storage side operates under a distinct control strategy with two conditions. Firstly, it activates when the water temperature on the flat plate collector side is 2 degrees higher than the supply water temperature to the heat exchanger on the storage side. Secondly, the pump's mass flow rate doubles when the supply water temperature to the top layer surpasses 70 °C.

The solar efficiency, defined here as the gross yield, is calculated under standardized conditions that neglect external influences on the solar input, such as shading from surrounding objects or transient weather conditions. Accordingly, the gross yield is defined as:

$$
\begin{aligned}
\text{yield}_{gross} &= \int_0^{365\times24\times3600} \left(\frac{\text{Supply Power to the Heat Exchanger on the Collector Side}}{\text{Total Solar radiation on Tilted Surface}} \right) dt \\
&= \int_0^{365\times24\times3600} \left(\frac{\dot{Q}_{HX\_Solar}}{G_{Tilt} \cdot A_{Collector}} \right) dt
\end{aligned}
\tag{2.12}
$$

2.1.2. Boundary Conditions

2.1.2.1. Weather Data Set

Simulating a heating system necessitates the availability of at least hourly data to accurately model the behavior of the storage when heat consumption and production are connected to it. However, obtaining hourly climate data that aligns with both long-term monthly averages and standard fluctuations, including realistic statistical distributions for varying weather conditions (like sunny and cloudy situations where irradiance, temperature, humidity, and wind speed correlate), presents a challenge. To address this challenge, two methods are commonly employed [95].

The first method involves the use of the Test Reference Years (TRY) approach, which utilizes measured data from a number of measured years for a specific location to match hourly data with long-term monthly average data. Although the creation of TRY datasets can be expensive and time-consuming, there are instances where free-of-charge data, such as Typical Meteorological Years (TMY), are available [96]. Additionally, measured data ensures the accurate representation of weather fluctuations in the region.

The second method involves the use of weather data generator software, such as METEONORM [97], when actual measured weather data is limited or unavailable for a specific location. These tools employ both physical and statistical approaches to align hourly data with long-term monthly averages. In this study, weather data from two different regions, Potsdam based on the METEONORM dataset [97] and Karlsruhe based on the TMY dataset from 2007-2021 [96], have been employed for three primary purposes. Firstly, these weather datasets contribute to the heating curve, determining the supply and return temperatures for a radiator. The designed heating system should provide these temperature levels based on the outside dry bulb temperature and conditions specified in the VDI 4650-2[73] or DIN EN 12309 [72] standards, with the aim of maintaining the room temperature at a desirable level. Secondly, these weather data are integrated into the building model to assess the impact of irradiation and shading on the power derived from solar radiation. Finally, calculating the amount of irradiation on solar collector.

2.1.2.2. Thermal load Models for Domestic Hot Water and Space Heating

Thermal load modeling for each building is determined based on five available approaches.

First, the Standardized Load Profiles Method: This approach generates average load profiles based on actual measurements and scales them to meet annual energy demands in a building. These profiles are often publicly available and provided by gas and electricity distribution companies.

Second, the Reference Load Profiles Method: A representative annual load profile is selected from measurements, such as those outlined in the VDI 4655 [98] standard. Representative days for various climate conditions are selected from measurements and combined to meet annual energy demands in a building based on specified climate data.

Using reference or standardized load profiles has the drawback of not capturing stochasticity and smoothing effects that appear when many households are simulated together.

Third, Statistical Load Profiles based on measurement: While this method demonstrates good accuracy in predicting the energy usage patterns of known buildings, it encounters difficulties when attempting to predict the behavior of new buildings or account for variations in building dynamics.

Fourth, Physical Models: This model includes lumped energy balance equations alongside physical building properties to compute heat loads. Despite its high accuracy in predicting a building's thermal load, it does not account for user behavior. The benefit of this approach lies in understanding how building materials and control strategies affect thermal comfort and energy consumption, but it requires more information to build the model. The inclusion of additional details in physical models results in increased computation time, model complexity, and thermal nodes within the model.

Fifth, RC-network model: This model is a simplified physical model. DIN EN ISO 13790 [99] presents a commonly utilized calculation method for hourly heat loads, opting for a 5R1C-network representation of the building. This approach provides the opportunity to calculate thermal building loads efficiently while maintaining accuracy comparable to more detailed models, as demonstrated in [100].

To balance accuracy and computational efficiency, and to consider user behavior when calculating energy demand profiles for households, we employ the synPRO model developed by Fischer [101], in addition to a physical model. The synPRO model, which is also used in the LowEx-Bestand project [79], captures the diversity of individual household load profiles as well as their smoothing effects. This makes it particularly well suited for modeling energy demand in multi-family houses.

For the space heating load profiles, a physical model is combined with a behavioral model. This approach takes into account various building physics aspects, including heat losses, solar gains, thermal dynamics, as well as user behavior, which impacts indoor temperature set-points, ventilation rates, and internal gains. Both internal loads and temperature set-points are influenced by user presence and activity, which are generated using the synPRO model. Consequently, the heat demand for space heating is computed following DIN EN ISO 13790 [99], utilizing a 5R2C building model [26]. The resulting energy balance equation is as follows:

$$\dot{Q}_{\mathrm{sh}} = \dot{Q}_{\mathrm{i,ven}} + \dot{Q}_{\mathrm{i,trans}} - \dot{Q}_{\mathrm{g,sol}} - \dot{Q}_{\mathrm{g,int}} - \mathrm{C_m} \cdot \frac{\Delta T_{\mathrm{m}}}{\Delta t} - \mathrm{C_{air}} \cdot \frac{\Delta T_{\mathrm{air}}}{\Delta t} \tag{2.13}$$

In equation (2.13), on the left hand side $\dot{\mathrm{Q}}_{\mathrm{sh}}$ represents required energy for space heating load. On the right hand side, $\dot{\mathrm{Q}}_{\mathrm{i,ven}}$, $\dot{\mathrm{Q}}_{\mathrm{i,trans}}$ show the energy losses through ventilation and transmission, respectively. $\dot{\mathrm{Q}}_{\mathrm{g,sol}}$, $\dot{\mathrm{Q}}_{\mathrm{g,int}}$ signify energy gains through solar radiation and user behavior, respectively. Finally, the last two expressions on the right-hand side of the equation are related to the thermal mass of the building and the air within the building.

Furthermore, for the Domestic Hot water load profiles, the synPRO model has considered three stages. First, synPRO model utilizes data on occupant activities from [102], which categorizes buildings based on socio-economic factors such as age, work schedules, and housing conditions. Next, synPRO model develops probability distributions containing the frequency, start time, and duration of each DHW-consuming activity. Finally, synPRO model employs a stochastic bottom-up approach on the derived probability distribution to generate daily schedules for the use of showers, bath-tubs, and sinks. Accordingly, The energy required for DHW preparation $\dot{Q}_{\mathrm{DHW}}(t)$ at any given time t is determined by typical tapping temperatures $T_{w,h}$, the initial temperature of the incoming cold water $T_{w,c,0}$, and mass flow rates, as provided by Reference [103]. The resulting energy balance equation is

$$\dot{Q}_{\mathrm{DHW}}(t) = \mathrm{f}_{season}(t) \cdot \left[\dot{Q}_{\mathrm{losses}}(t) + \dot{m}(t) \cdot \mathrm{c_w} \cdot (\mathrm{T_{w,h}}(t) - \mathrm{T_{w,c,0}})\right] \tag{2.14}$$

In equation (2.14), f_{season} represents a factor accounting for the variability in cold water temperature and $\dot{Q}_{\mathrm{losses}}(t)$ is circulation losses, while c_w denotes the specific heating capacity of water.

Based on the described modeling approach, the simulation tools generate detailed, time-resolved data for the analyzed building. This includes key building parameters such as the effective thermal mass, as well as hourly load profiles for domestic hot water and space heating over the course of a year. These results form the basis for the subsequent system analysis and performance assessment.

2.1.3. Stratified Storage Tank Model

In stratified thermal storage tanks used in building heating systems, mixing is mainly caused by fluid inflow and outflow at the inlets and outlets. The associated momentum transfer can disturb the thermal stratification. At the same time, buoyancy forces act to stabilize the stratified layers and limit vertical mixing. Therefore, an appropriate representation of both flow-induced mixing and buoyancy effects is required when modeling the thermal behavior of a stratified storage tank. A detailed description of these processes typically requires distributed-parameter models with spatial discretization, which are computationally expensive and difficult to apply in system-level simulations involving multiple components such as heat pumps, domestic hot water and space heating circuits, and control strategies. Consequently, lumped-parameter models are commonly used in building heating applications due to their lower computational complexity.

Baeten et al. proposed a low-order model for hot water storage tanks that incorporates mixing and buoyancy effects, validated against CFD[3] simulations and experimental data [104]. The Baeten et al. model is valid over a range of storage tank sizes and geometries and makes the model suitable for evaluating different system designs or for component sizing using dynamic building energy simulations in an Active Demand Response context, which

[3]Computational Fluid Dynamics

refers to the adjustment of electricity consumption patterns by end-users in response to changes in electricity prices or other incentives.

Subsequently, Prijić developed a stratified storage tank model with integrated rings at KIT and adapted the Baeten et al. one-dimensional mixing model to improve the representation of mixing processes in a Stratisorp system. Prijić demonstrated that a specific diameter at the ring location minimizes the RMSE[4] between experimental and model temperatures, indicating optimal mixing representation. Furthermore, she observed that different mass flow rates require different optimal diameters to achieve minimal RMSE values, suggesting that diameter adjustment alone is insufficient for accurate mixing representation. While she recommended incorporating additional parameters and exploring other adjustment approaches to enhance the correlation for mixing parameters—such as considering mass flow-dependent mixing parameters or conducting CFD simulations for a more accurate model—the study underscores the complexity of accurately modeling mixing processes in Stratisorp system and the need for multifaceted approaches to enhance model precision [105].

Therefore, the numerical stratified storage tank model re-implemented and parametrized by Prijić, based on the Baetens model, has only been partially validated against experimental data and for a limited range of operating conditions. In particular, the model validation does not fully cover the range of mass flow rates and operating regimes required in the present system study, where strongly varying charging and discharging flows occur due to the interaction of heat pumps, domestic hot water demand, and space heating demand. Applying this model would therefore require extrapolation beyond its validated range and could suggest a level of predictive accuracy and technology readiness that cannot be justified at this stage. This limitation represents a weak point of the present study and is explicitly acknowledged.

Given this situation, a simpler stratified storage tank model, characterized by the parameters outlined in Table 2.1, from the Modelica Buildings Library [84] was adopted. This model is based on an ideal plug flow assumption and does not explicitly account for additional mixing mechanisms, except in cases of temperature inversion where buoyancy-driven mixing occurs. While this simplified approach cannot predict the real stratification performance of a storage tank under all operating conditions, it is well suited for a system-level potential analysis. By assuming near-optimal stratification, the model allows the assessment of overall system behavior and performance without introducing uncertain effects from insufficiently validated mixing correlations. Similar modeling approaches are commonly used in stratified storage tank studies, as demonstrated in [106].

Parameter	**unit**	**Value**
Insulation Thickness	cm	12
Insulation Specific Heat Conductivity	$W/m \cdot K$	0.045

Table 2.1.: Stratified storage parameters.

[4] Root Mean Square Error

2.1.3.1. Sizing of Storage

Building on the stratified storage tank model introduced in the previous section, a heating system comprising a DHW circuit and a space heating circuit, including a heat pump and a burner, is considered. Two stratified storage tanks are implemented as separate instances of this model. One storage tank is connected to the DHW circuit and the burner, while the other is connected to the space heating circuit and the heat pump. The sizing of DHW storage is determined by the DHW load profile and the permissible temperature difference (ΔT) in the storage tank. As the DHW load profile is influenced by the number of occupants and their usage patterns, predicting the exact demand is challenging. Consequently, heuristic sizing methods are often employed. According to the heuristic method presented in [107], the required DHW storage capacity is directly related to the number of occupants, as illustrated in equation (2.15). This formula is valid for populations up to 300 individuals. A safety margin S is applied, ranging from 125 % for smaller groups to 105 % for larger groups exceeding 200 individuals.

$$V_{\mathrm{DHW}} \simeq S \cdot 65.0 \cdot n^{0.7} \text{ [l]} \tag{2.15}$$

Fischer [101] has noted that the sizing of space heating storage for air source heat pumps is influenced by several factors, including the characteristics of the heat pump, the thermal inertia of the heat distribution system, and the type of building. His research indicates that the need for larger storage typically arises only under extreme conditions.

In the context of our gas adsorption heat pump, which has a maximum capacity of 17 kW in sorption mode and 50 kW in direct burner mode, the minimum buffer tank size is determined based on the 50 kW installed heat pump capacity, as calculated using equation (2.16) [101]:

$$V_{\mathrm{min,SH}} \simeq 10.0 \cdot \dot{Q}_{\mathrm{HP}} \text{ [l]} \tag{2.16}$$

2.2. Description of Device level for an Gas Adsorption Heat Pump

This section provides a concise overview of the main models and governing equations used in the system simulation. For clarity and readability, many detailed assumptions and model formulations are not discussed here. A comprehensive description of the underlying model assumptions, parameter choices, and validation is provided in Velte's thesis [17]. The following paragraphs therefore focus on the essential characteristics of the applied models and their role within the overall system analysis.

As illustrated in the Figure 2.7, the primary circuit—referred to as the device level in this study—is separated from the secondary circuits, which represent the system level. The numerical model of the GAHP at the device level, excluding the high-temperature source heat exchanger, was developed by Andreas Velte within the AdoSan project [26]. This model was designed to analyze the transient behavior of individual components and their integration into the overall system, where the GAHP supplies the space heating demand of MMFH [79].

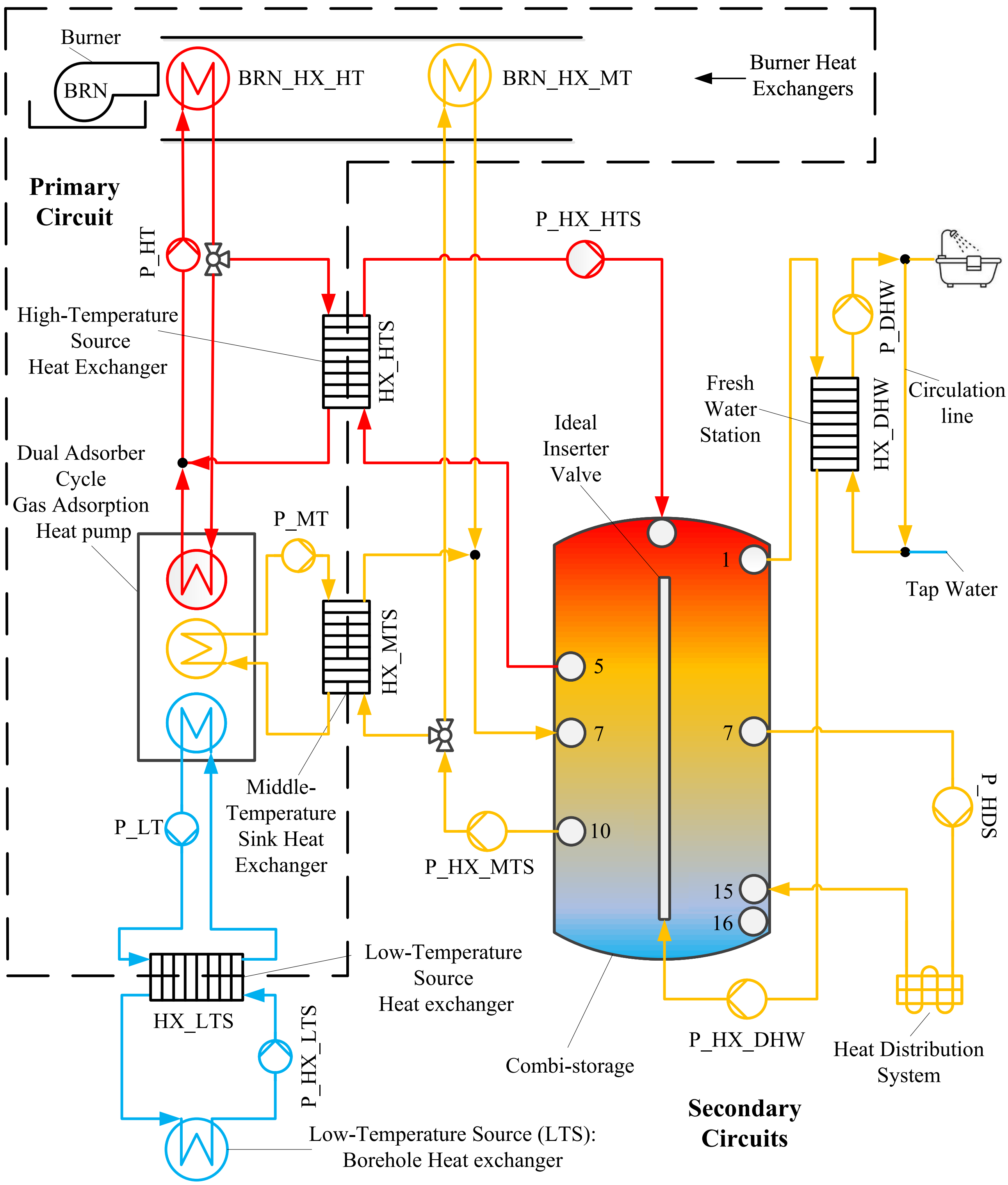

Figure 2.7.: Hydraulic scheme of reference system. Red lines represent water with high temperature; Blue lines show the water with low temperature, and orange lines present water with medium temperature. The details of the symbolic representation of the Dual Adsorber Cycle GAHP are provided in section A.1.

The first law of thermodynamics represents the principle of energy conservation, commonly referred to as the energy balance. The general energy balances for any system undergoing any process can be expressed as [108]:

$$\underbrace{\dot{E}_{\text{in}} - \dot{E}_{\text{out}}}_{\substack{\text{Rate of net energy transfer} \\ \text{by heat, work, and mass}}} = \underbrace{\frac{\mathrm{d}E_{\text{system}}}{\mathrm{d}t}}_{\substack{\text{Rate of change in internal,} \\ \text{kinetic, potential, etc., energies}}} \tag{2.17}$$

The model employs a lumped-parameter approach, using heat and energy balance equations for each relevant solid and fluid domain. The energy balance for heat transfer fluid domains is given in (2.18).

$$\frac{dU_{\text{HTF}}}{dt} = m_{\text{HTF}} \cdot c_{p,\text{HTF}} \cdot \frac{dT_{\text{HTF}}}{dt} + u_{\text{HTF}} \cdot \frac{dm_{\text{HTF}}}{dt} = \sum \dot{H} + \dot{Q}_{\text{HTF,mt}} \tag{2.18}$$

$$\dot{Q}_{\text{HTF,mt}} = \alpha_{\text{HTF,mt}} \cdot A_{\text{HTF,mt}} \cdot (T_{\text{HTF}} - T_{\text{mt}}) \tag{2.19}$$

Here, $\dot{\text{H}}$ represents the incoming and outcoming enthalpy flow rate, and $\dot{\text{Q}}_{\text{HTF,mt}} = f\left(\text{Nu}, \text{Re}, A_{\text{HTF,mt}}\right)$ is the heat flow rate between the heat transfer medium and the metal of the tube [109]. The calculation of the heat transfer coefficient (α) for forced convection is based on the offset-strip-fin correlation, as recommended by Shah et al. [83], for the flat tubes of the adsorber/desorber heat exchanger, and on the correlation suggested by Lanzerath [109] for the round tubes of the EC heat exchanger.

For the solid domains, such as the metal of the heat exchanger, the energy balance is given in (2.20) [109].

$$\frac{dU_{\text{mt}}}{dt} = m_{\text{mt}} \cdot c_{p,\text{mt}} \cdot \frac{dT_{\text{mt}}}{dt} = \dot{Q}_{\text{mt,HTF}} + \dot{Q}_{\text{mt,sorb/wf}} \tag{2.20}$$

$$\dot{Q}_{\text{mt,sorb/wf}} = (UA)_{\text{mt,sorb/wf}} \cdot (T_{\text{mt}} - T_{\text{sorb/wf}}) \tag{2.21}$$

$\dot{\text{Q}}_{\text{mt,sorb/wf}}$ represents the heat flow rate between the metal of the tube and the adsorbent (sorb) if the heat exchanger is adsorber/desorber, or between the metal of the tube and the working fluid (wf) if the heat exchanger is evaporator/condenser. The UA values for the adsorbers, denoted as $\text{UA}_{\text{mt,sorb/wf}}$, are lumped-parameter representations derived from detailed heat and mass transfer models studied extensively at multiple scales, both experimentally and numerically [62]. Furthermore, the combined evaporator-condenser is designed with finned tubes (circular cross section) and is modeled using the energy balance equations (2.18) and (2.20).

Since the ADHX and EC are housed in a single vacuum chamber, no vapor-side valves are required. However, the close proximity of these two heat exchangers results in heat transfer between them, which is accounted for by thermally connecting the ADHX working pair cells and EC working fluid cells as described in Equation 2.22. The overall heat conductance $(UA)_{\text{ADHX,EC}}$ can be estimated from the component energy balances, as demonstrated in [17]. In addition to this coupling, a separate heat transfer path exists due to conductive heat losses through the casing.

$$\dot{Q}_{\mathrm{ADHX,EC}} = (UA)_{\mathrm{ADHX,EC}} \cdot (T_{\mathrm{sorb}} - T_{\mathrm{wf}}) \tag{2.22}$$

The energy balance of the adsorbent domain is provided in equation (2.23) [110]. Here, m_{adb} represents the adsorbate mass, defined as the mass of the working fluid adsorbed / desorbed from the adsorbent, while m_{sorb} represents the adsorbent mass. These quantities are linked through the relation $\mathrm{m_{adb}} = \mathrm{m_{sorb}} \cdot \mathrm{X}$, where X is the actual loading.

$$\frac{dU_{\mathrm{sorb}}}{dt} = u_{\mathrm{adb}} \cdot \frac{d(m_{\mathrm{adb}})}{dt} + \left(m_{\mathrm{adb}} \cdot c_{p,\mathrm{adb}} + m_{\mathrm{sorb}} \cdot c_{p,\mathrm{sorb}}\right) \cdot \frac{dT_{\mathrm{sorb}}}{dt} = \sum \dot{H} + \dot{Q}_{\mathrm{sorb,mt}} \tag{2.23}$$

The change in adsorbate mass $\frac{\mathrm{d(m_{adb})}}{\mathrm{dt}}$ in Equation 2.23, establishes a connection between the energy balance and the mass transfer described by the linear driving force (LDF) approach in equation (2.24). This approach is suitable for describing the adsorbate diffusion mass transfer process in dense, directly crystallized layers of SAPO-34. However, it exhibits certain limitations, particularly during highly dynamic phases characterized by large gradients immediately following transitions between half-cycles, as highlighted by Velte et al. [111]. The LDF parameter $\mathrm{k_{LDF}}$ is dependent on the adsorbate diffusion coefficient, the characteristic thickness of the crystallite layer [17, 111], and is strongly influenced by temperature and loading [112]. For simplicity, this parameter is treated as a constant value in the numerical model.

$$\frac{dX}{dt} = \frac{1}{m_{\mathrm{sorb}}} \cdot \frac{dm_{\mathrm{adb}}}{dt} = k_{\mathrm{LDF}} \cdot \left(X_{\mathrm{eqi}}(p,T) - X\right) \tag{2.24}$$

The internal transport of water vapor within the porous structure of the adsorbent is the underlying physical factor determining these kinetics. In the specific context of adsorption heat pumps, these phenomena—particularly regarding transport regimes such as Knudsen diffusion in micropores—have been extensively investigated and characterized. However, these explicit fluid mechanical aspects are not treated in further detail in this work. Comprehensive theoretical and experimental treatments of these transport mechanisms are available in the established literature, most notably in the doctoral theses of Schnabel [113] and Füldner [19], as well as the collaborative publications resulting from the WasserMOD project [23].

While the LDF model describes the rate of mass transfer, the total capacity of the adsorbent must be defined by the thermodynamic equilibrium. In this research, Dubinin's potential theory is applied to determine the adsorption process in microporous materials [31, 32]. Calculating the equilibrium loading, $\mathrm{X_{eqi}(p,T)}$, requires defining the adsorption potential, $\mathrm{A_{Dub}}$, which depends on both pressure and temperature.

$$A_{\mathrm{Dub}} = -\Delta\tilde{g} \cdot \frac{1}{\tilde{M}_{\mathrm{vap}}} = -(\tilde{\mu}_{\mathrm{adb}} - \tilde{\mu}_{\mathrm{fld}}) \cdot \frac{1}{\tilde{M}_{\mathrm{vap}}} = \frac{R_{\mathrm{const}}}{\tilde{M}_{\mathrm{vap}}} \cdot T \cdot \ln\left(\frac{p_{\mathrm{sat}}(T)}{p}\right) \tag{2.25}$$

The adsorption potential reflects the chemical potential difference between the adsorbate in its free liquid form $\tilde{\mu}_{\mathrm{fld}}$ and the adsorbate adsorbed $\tilde{\mu}_{\mathrm{adb}}$ in micropores. This model assumes that adsorption begins with an initial phase change from gas to liquid, during which energy is released as the adsorbate condenses within the adsorbent's pores, creating the adsorption potential. This potential can be determined using experimentally measured values of pressure and temperature. The saturation vapor pressure curve of the adsorbate $p_{\text{sat}}(T)$ is used for this purpose.

Another important parameter is the specific adsorbed volume, W_{Dub}, which is given in Equation 2.26 as the ratio of the loading to the liquid density of the adsorbate. The liquid density is approximated by the density of liquid water, $\rho_{\text{adb}}(\mathrm{T}) = \rho_{\text{l}}(\mathrm{T})$ [16].

$$W_{\text{Dub}} = \frac{X}{\rho_{\text{adb}}(T)} \tag{2.26}$$

The relationship between loading, pressure, and temperature can be described using the Dubinin formalism through Equation 2.27. This requires a characteristic equation, W(A), derived from empirical data specific to a pair of substances. This framework for describing loading allows the use of various W(A) functions; for example, Schwamberger [16] uses nonlinear regression, whereas Núñez [50] employs fractional rational functions.

$$X_{\text{eqi}}(p,T) = W_{\text{Dub}}(A_{\text{Dub}}(p,T)) \cdot \rho_{\text{adb}}(T) \tag{2.27}$$

Furthermore, the calculation of adsorption enthalpy depends on the adsorption model chosen. Typically, the relationship among pressure, temperature, entropy, and molar volume is derived from an equilibrium condition, where the chemical potentials of the gas and adsorbed phases are equal.

$$\left(\frac{\partial p}{\partial T}\right)_X = \frac{\tilde{s}_{\text{vap}} - \tilde{s}_{\text{adb}}}{\tilde{v}_{\text{vap}} - \tilde{v}_{\text{adb}}} \tag{2.28}$$

Partial molar entropy ($\tilde{\mathrm{s}}$) is defined based on partial molar Gibbs enthalpy ($\tilde{\mathrm{g}}$) and partial molar enthalpy ($\tilde{\mathrm{h}}$)

$$\tilde{s} = -\frac{\tilde{g} - \tilde{h}}{T} \tag{2.29}$$

These expressions are reformulated in Equation 2.30 to maintain the equilibrium condition between the adsorbate and vapor chemical potentials.

$$\left(\frac{\partial p}{\partial T}\right)_X = \frac{\tilde{s}_{\text{vap}} - \tilde{s}_{\text{adb}}}{\tilde{v}_{\text{vap}} - \tilde{v}_{\text{adb}}} = \frac{\tilde{h}_{\text{vap}} - \tilde{h}_{\text{adb}}}{(\tilde{v}_{\text{vap}} - \tilde{v}_{\text{adb}}) \cdot T} \tag{2.30}$$

The "isosteric adsorption enthalpy" [28] reflects the enthalpy difference between the adsorbed and vapor phases for small changes in loading under constant temperature and pressure, even though this process is not strictly isosteric. Assuming ideal gas behavior for the vapor and negligible adsorbate volume compared to vapor volume ($\tilde{v}_{\text{adb}} \ll \tilde{v}_{\text{vap}}$), the adsorption enthalpy ($\Delta\mathrm{h}_{\text{ads}}$) can be estimated using the Clausius-Clapeyron equation, as shown in Equation 2.31.

$$\Delta h_{\text{ads}} = \left(\frac{\partial p}{\partial T}\right)_X \cdot \frac{R_{\text{const}}}{\tilde{M}_{\text{mol,vap}}} \cdot \frac{T^2}{p} \tag{2.31}$$

A comprehensive energy balance in adsorption cycles can be achieved by treating the heat capacity of the adsorbate as a variable parameter. Schwamberger [16, 114] developed an approach to calculate this heat capacity by selecting an integration path aligned with adsorption equilibrium. When applying the standard assumptions for the adsorbate heat capacity typically used within the framework of Dubinin's adsorption model, thermodynamic inconsistencies arise, observed by numerical residuals when integrating the enthalpy over a full adsorption–desorption cycle. To address this, the present numerical model adopts the approach introduced by Schwamberger, which significantly improves thermodynamic consistency. Achieving this consistency requires that the enthalpy of adsorption be computed numerically—using the Clausius–Clapeyron equation without ideal-gas approximations—rather than relying on simplified analytical expressions. Consequently, in this work Dubinin's theory is used solely for parameterizing the adsorption equilibria, while the additional assumptions and approximations commonly associated with Dubinin's model are intentionally not employed.

$$c_{p,\mathrm{adb}}(X,T) = \frac{1}{X} \cdot \int_0^X dX' \cdot \left(\frac{\partial \left(h_{\mathrm{vap}}(p(X',T),T) - \Delta h_{\mathrm{ads}}(X',T) \right)}{\partial T} \right)_{X'} \tag{2.32}$$

According to Equation 2.32, the adsorbate heat capacity is a function of the vapor enthalpy ($\mathrm{h_{vap}}$) and the isosteric adsorption enthalpy ($\Delta\mathrm{h_{ads}}$). Consequently, the heat capacity is inherently tied to the adsorption enthalpy and is ultimately influenced by the selected adsorption model [17].

2.2.1. Dual Adsorber Gas Adsorption Heat Pump

According to the Figure 2.7, the primary circuit includes a burner equipped with two heat exchangers. One of these heat exchangers has dual functions. First, it can be connected to the upper part of the storage through the High-Temperature Source Heat Exchanger, contributing to heating the upper storage part. Second, it can also be linked to the Adsorption Heat Pump, serving as its High-Temperature source. The burner's second heat exchanger cools the flue gas below its dew point to utilize the condensing boiler effect and transfer the recovered heat to the secondary circuit. Additionally, the borehole heat exchanger acts as a low-temperature heat source for the Heat Pump, transferring geothermal power to the evaporator through the Low-Temperature Source Heat Exchanger. Consequently, the output power from the Heat Pump is delivered to the combi-storage through the Medium-Temperature Sink Heat Exchanger.

2.2.1.1. Description of Fraunhofer Institute for Solar Energy Systems (ISE) Model (AdoSan Heat Pump)

The key hardware in a Gas Adsorption Heat Pump (GAHP) is the Adsorber process, as discussed in subsection 1.1.1. To enhance the efficiency and power density of GAHPs, Andreas Velte [17] addressed the dimensioning of the components and the selection of the hydraulic scheme through three distinct steps.

The initial step involves the development of a static heat balance model for the Adsorber Cycle [16, 50]. This model is crucial for determining the potential efficiency under various boundary conditions. This step is particularly efficient due to the limited number of parameters and reduced computation time, making it ideal for evaluating different working pairs for the adsorber/desorber. This evaluation process not only aids in identifying the optimal combination of working fluid and adsorbent for the intended application but also facilitates the calculation of potential heat recovery. Furthermore, it enables the prediction of power density based on the initial dimensions assumed for the adsorber/desorber.

In the second step, a dynamic assessment is conducted to analyze the adsorber/desorber for promising working pair in various hydraulic configurations, including standard cycle [115], cascading cycle [115], Thermal-Wave cycle [75, 76], and Stratisorp cycle [16]. This assessment accounts for all relevant heat and mass transport processes within the adsorber cycle. Since the boundary conditions and cycle type are crucial for optimizing the adsorber cycle, a pre-selection of adsorber cycle is carried out at this stage before further optimization [17]. Based on this pre-selection, the initial geometric design of the adsorber/desorber is optimized by adjusting degrees of freedom such as the adsorbent layer thickness on the fibers, the thickness and porosity of the fibrous structure, the geometry of the flat tubes on the heat-transfer-fluid side, the heat exchanger length, and the number of hydraulic passes, with the aim of maximizing the GAHP's power density.

The third step applies and evaluates the base system–as a heating system incorporating the adsorber cycle–under specific heat-sink characteristics, following the optimization of the adsorber/desorber in the second step. This step demonstrates the integration of the adsorber cycle into a gas heat pump system and examines system efficiency and power density under various GAHP requirements. The predictions made in Velte's work regarding efficiency and power density are robust, as many of the assumptions and parameters were validated through appropriate experiments [17]. However, challenges in manufacturing the adsorber heat exchangers using CAB[5] could not be resolved within the limited resources of the R&D project. As a result, a fallback heat-exchanger design with lower heat and mass transfer performance was selected for the AdoSan project, and all subsequent modeling was based on this revised adsorber design. Consequently, a flat-tube lamella heat exchanger was implemented in the functional GAHP test bed.

Following the development of the Adsorber Cycle, Simon Leisner [69] experimentally validated the dual adsorber cycle GAHP simulation model and refined the classical SorTech/Fahrenheit "delayed-switching" control strategy [116] to improve heat-delivery efficiency. His work focused on the lower four part-load operating points defined in DIN EN 12309-6 [72] and optimized key control parameters, including the maximum desorption temperature, the high-temperature (HT) mass flow during heat recovery, and the temporary bypassing of the low-temperature heat exchanger (LT-HX) during heat recovery. These refinements form the basis of the improved part-load control strategy implemented in the base system. Velte et al. [63] demonstrated that the annual gas utilization efficiency [73] of the base system with a dual adsorber cycle GAHP exceeds 1.3 under favorable boundary conditions—specifically, at supply/return temperatures of 45/35 °C with exhaust air as the low-temperature source. Consequently, one of the primary goals of the AdoSan

[5] controlled-atmosphere brazing

project—developing a GAHP system suitable for MFH renovation based on a highly efficient and powerful Adsorber Cycle—has been achieved for the base system [63]. However, for the reference system in this study, the annual gas utilization efficiency [73] should ideally exceed 1.3 at 55/45 °C, as discussed in Figure 2.7.

Therefore, to understand the heating system at ISE in comparison with the system examined in this research, it is essential to distinguish between the base system and the reference system, as described in subsection 2.4.1. The base system differs from the reference system at both the system and device levels. At the system level, the base system supplies only space heating [26], whereas the reference system provides both space heating and domestic hot water. At the device level, the high-temperature Source Heat Exchanger (HX-HTS) present in the reference system (see Figure 2.7) is not included in the base system. Both systems employ the same Dual adsorber cycle GAHP, comprising two modules, each containing one adsorber/desorber and one evaporator/condenser, housed within two separate casings. The system operates when the supply temperature to the Medium-Temperature Sink Heat Exchanger on the secondary circuit is below 34 °C, and the supply temperature to the Low-Temperature Source Heat Exchanger on the borehole heat exchanger side is above 7 °C, due to the optimal performance of the working pair [63]. The base and reference systems undergo six operational stages, detailed in section A.1 at the device level. The first stage involves desorption in Module 1 and adsorption in Module 2. The second stage is heat recovery. The third stage is direct burner mode, activated when the power delivered through the Medium-Temperature Sink Heat Exchanger cannot meet the required power on the consumption side. This stage continues until the heat pump's output power sufficiently meets the demand. The fourth stage involves desorption in Module 2 and adsorption in Module 1. The fifth stage is heat recovery, followed by the sixth stage of direct burner mode. These stages cycle continuously to meet the space heating demands in Base and Reference system.

2.2.2. Single Adsorber Gas Adsorption Heat Pump

The two different types of adsorption modules are illustrated in Figure 2.8. The valveless module on the left features a single evaporator/condenser heat exchanger (E/C HX) that is externally switched between the low-temperature source loop (when operating as an evaporator) and the medium-temperature sink loop (when functioning as a condenser). In contrast, the right-hand module uses separate heat exchangers and internal vapor valves that operate autonomously via pressure differentials. The use of a valveless adsorption module (left in Figure 2.8) with external switching of the E/C HX in a GAHP necessitates additional sensible heat to change the heat exchanger's thermal mass between evaporator and condenser temperatures; while this leads to a lower COP due to thermal losses (Equation 2.20), the manufacturer selected this configuration for its cost-effectiveness and durability. Consequently, this research focuses on investigating heat recovery strategies to enhance the overall efficiency of this specific module type. To this end, two distinct heat recovery methods are considered:

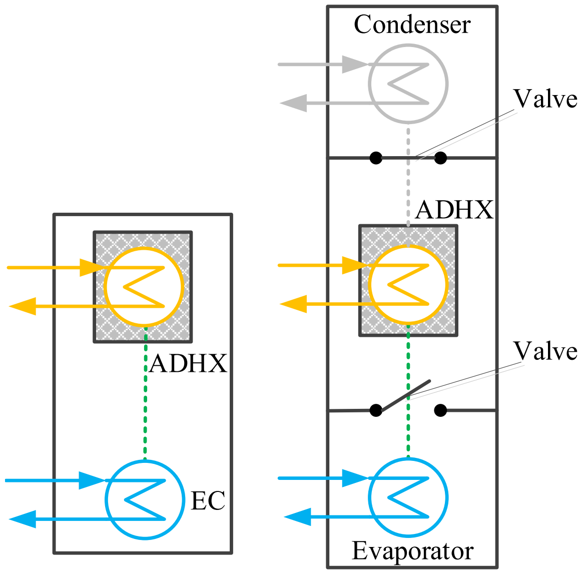

Figure 2.8.: Schematic module comparison of single adsorber cycle during adsorption process: The adsorber/desorber (ADHX) in the right module is connected to separate evaporator and condenser units, with valves positioned between them. In contrast, in the left module, the adsorber/desorber and the combined evaporator/condenser (EC) are placed within the vacuum chamber with no valves between them. (Blue lines indicate the low temperature source loop; orange lines represent the medium temperature sink loop; green dash lines show water vapor; and grey lines denote inactive components [118].)

In dual adsorber cycles, efficient approaches have been developed to partially recover this sensible heat by transferring it between the two E/C heat exchangers within the adsorption modules [117]. In the GAHP prototype designed for the AdoSan project, delayed switching of the return flow is implemented for both the adsorbers and E/C heat exchangers to enable this heat recovery [17, 69, 116].

In single adsorber cycles, however, heat recovery can only be achieved through integrated storage, as no secondary module is available to operate with a phase shift relative to the first module.

Our research group at KIT (led by F. Schmidt) previously developed a single adsorber cycle concept known as “Stratisorp” [16, 119], in which only the adsorber is connected to a stratified storage tank. During the adsorption process, both sensible and sorptive heat from the adsorber is stored in this system, allowing for later utilization during the desorption process. In this configuration, the lowest temperature within the stratified storage, located in the bottom layer, corresponds to the return flow temperature of the heat sink loop. When optimal conditions are met, including effective stratification within the storage, the Stratisorp concept can achieve a heat recovery rate exceeding that of the previously described dual adsorber cycle, thereby enabling higher coefficients of performance (COP) [16]. This approach is especially effective for module designs that include separate evaporator and condenser heat exchangers (illustrated on the right in Figure 2.8). In contrast, with alternative module types (shown on the left), where the evaporator and condenser functions are combined in a single heat exchanger (EC), recovery of sensible heat at temperatures below the heating return flow is not feasible, as the Stratisorp lacks a dedicated storage option for this configuration.

In the single adsorber cycle analyzed in this study, both the adsorber/desorber heat exchanger (ADHX) and the evaporator/condenser heat exchanger (EC HX) are connected to a stratified storage tank. The innovative aspect of this configuration is the use of the lowest section of the stratified storage, as depicted in Figure 2.9, to retain heat at temperatures below the heating return flow, enabling effective heat recovery in both the adsorber and EC loops.

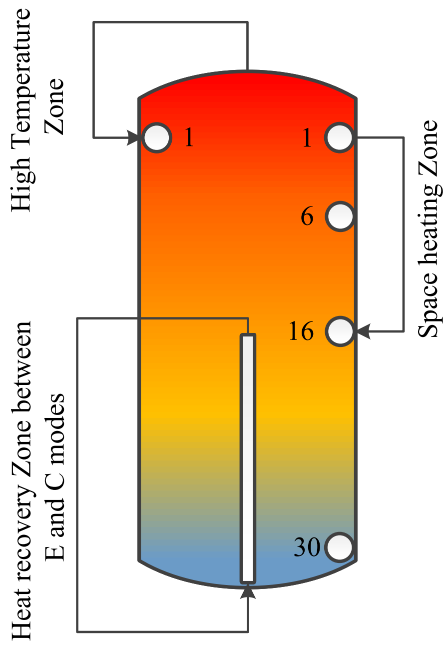

Figure 2.9.: Vertical temperature distribution within the stratified storage tank, illustrating the modified Stratisorp concept with extended low-temperature regions and a dedicated heat recovery section between the evaporator (E) and condenser (C) modes, as well as distinct space heating and high space-heating supply temperature zones.

As part of the AdoSan project a dual adsorber cycle gas absorption heat pump (GAHP) with a nominal heating capacity of 40 kW was calibrated and validated using experimental data (subsubsection 2.2.1.1) under boundary conditions specified in VDI-4650-2 [73]. In this segment of the study, our primary objective is to determine a single adsorber configuration—comprising a hydraulic scheme and control strategy—that maximizes the seasonal gas utilization efficiency (SGUE) while preserving the same adsorber module and adsorbent mass per kW of nominal heat pump power as used in the AdoSan GAHP.

To this end, the single adsorber cycle GAHP is designed with a 20 kW power output, matching both the nominal heating load and burner power. This capacity was selected by halving the initial load in order to avoid scaling the adsorber, thereby ensuring consistency with the already validated model. Additionally, the integration of a stratified storage tank introduces operational flexibility by decoupling the mass flow rates of the adsorber and condenser from the sink flow. This design provides further degrees of freedom for optimizing the operation of the single adsorber cycle GAHP, allowing for enhanced adaptability and potential performance improvements.

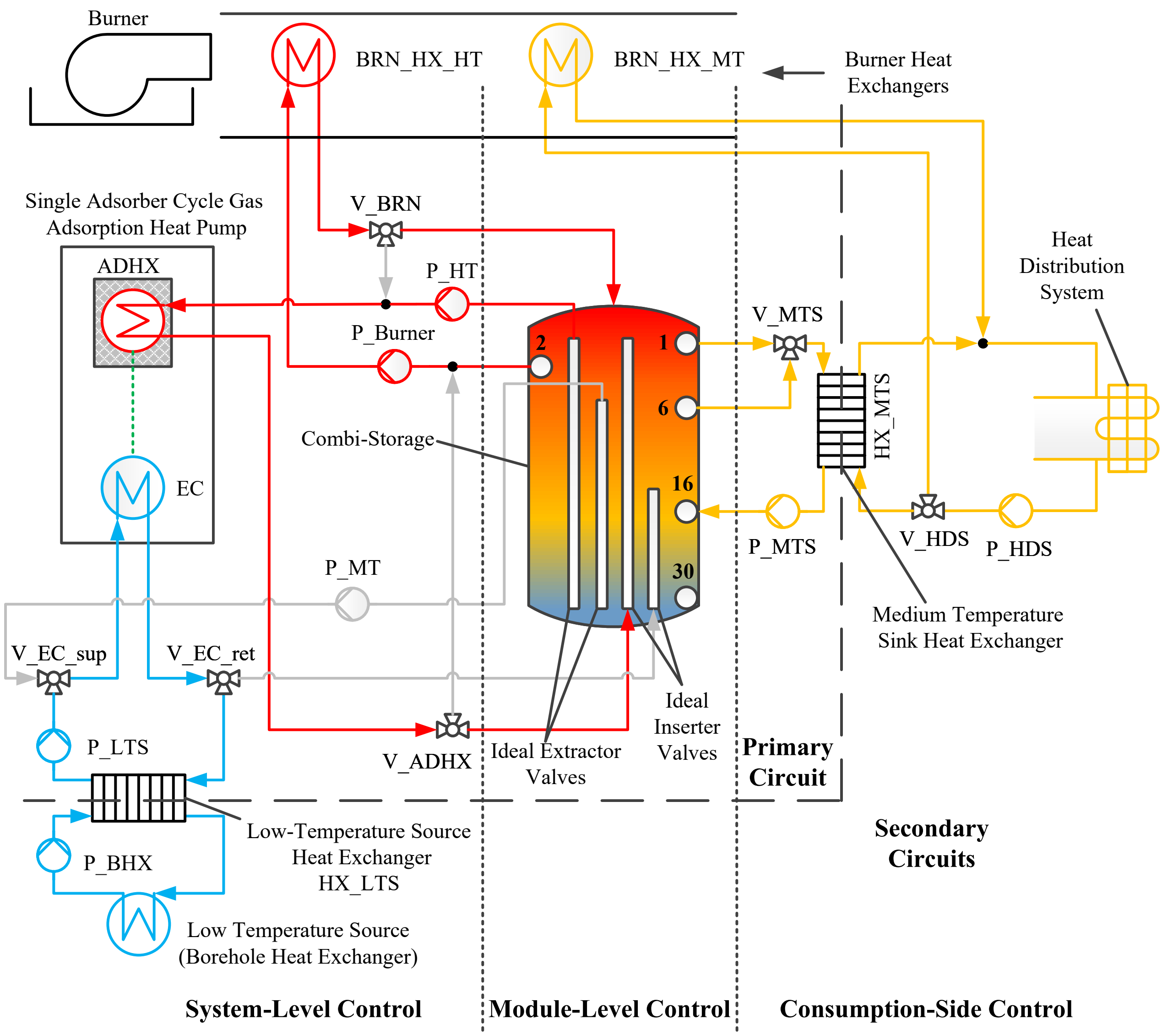

Figure 2.10.: Hydraulic scheme of heating system with single adsorber cycle GAHP. Red lines represent water with high temperature; Blue lines show the water with low temperature; orange lines present water with medium temperature, and grey lines are the deactive mode [118].

As detailed in Figure 2.10, the primary circuit is distinctly isolated from the secondary circuits by the Medium-Temperature Sink Heat Exchanger and the Low-Temperature Source Heat Exchanger. The heating system, which includes the single adsorber cycle GAHP, features a burner with two heat exchangers (BRN_HX_HT and BRN_HX_MT in

Figure 2.10). The first heat exchanger (BRN_HX_HT in Figure 2.10) can be linked either to the adsorber, where it acts as the high-temperature source of the GAHP, or directly to the upper part of the storage, operating in a burner-only mode that bypasses the adsorption module. The burner second heat exchanger (BRN_HX_MT in Figure 2.10), which is required to achieve condensation heat from flue gas, is responsible for cooling the flue gas below the dew point and transferring the extracted heat directly to the secondary circuit (heat sink). It is important to note that storage in Figure 2.10 is an integral part of the heat pump system, which is integrated into its fluid loop. In contrast, in the dual adsorber cycle [26, 62, 63], the storage is typically positioned on the other side of the medium temperature sink heat exchanger, as depicted in Figure 2.7. Therefore, in our single adsorber system, the storage serves a dual role: internal heat recovery within the cycle and buffering for loads. In the primary circuit, a stratified storage is connected to the single-adsorber cycle GAHP through four valves, modelled as ideal valves. In this context, These valves are designed numerically in a way to extract and insert water from specific layers to the adsorber/desorber and the Condenser. Additionally, for switching the connection of evaporator/condenser to stratified storage and borehole heat exchanger as low temperature heat source, two three-way valves (V_EC_sup and V_EC_ret in Figure 2.10) are located in the supply and return lines and operate in the following modes. During desorption process, the two three-way valves (V_EC_sup and V_EC_ret in Figure 2.10) are connected to the stratified storage. In this mode, supply water is extracted from the stratified storage via an ideal extractor and directed to the evaporator/condenser, as described in subsection 2.3.5. Then, the heated water is inserted to the storage through an ideal inserter. At the end of the desorption process, a transition mode from desorption to adsorption occurs. During this transition, the two three-way valves (V_EC_sup and V_EC_ret in Figure 2.10) remain connected to the stratified storage to transfer sensible heat of evaporator/condenser to the stratified storage. This is achieved by changing the evaporator/condenser set point temperature from space heating supply temperature to the storage bottom layer temperature in 180 s intervals, as described in Table 2.2 [118].

Sequence	Time [s]	Set Point (Desorption to Adsorption)	Set Point (Adsorption to Desorption)
1	60	Space Heating Return Temperature	Bottom Layer Temperature
2	60	Bottom Layer Temperature Plus 2 °C	Bottom Layer Temperature Plus 2 °C
3	60	Bottom Layer Temperature	Space Heating Return Temperature

Table 2.2.: Transition modes between desorption and adsorption processes.

Subsequently, during adsorption process, the two three-way valves (V_EC_sup and V_EC_ret in Figure 2.10) connect the evaporator/condenser to the Low-Temperature Source heat exchanger (LTS-HX) to transfer energy from the borehole heat exchanger, within the temperature range of 6 °C to 9 °C [73], to LTS-HX. Finally, at the end of the adsorption process, a transition mode from adsorption to desorption occurs to heat the evaporator/condenser, as described in Table 2.2. During this mode, the two three-way valves (V_EC_sup and V_EC_ret in Figure 2.10) reconnect to the stratified storage in order to raise the evaporator/condenser temperature to the space heating return temperature and recover the stored heat during transition mode from desorption to adsorption [118].

2.3. System Description of the Integral Gas Adsorption Heat Pump in Various Configurations

This section provides a detailed description of each system, where each system is composed of two distinct parts: the heat consumption components and the heat production components, which are interconnected with one or two stratified storage tanks. For the heating system with a dual adsorber cycle GAHP, the heat consumption components include the Space Heating Circuit and Water Heating Circuit, while the heat production components consist of the dual adsorber cycle GAHP and the optional solar thermal circuit. In addition to the heat-pump operating modes, a separate burner-only heat production mode is associated with the high-temperature source of the dual-adsorber cycle GAHP. In this mode, the burner supplies heat directly via a plate heat exchanger, referred to as the High-Temperature Source Heat Exchanger, which connects to the upper part of the stratified storage tank in order to maximize the utilization of the available thermal capacity. Consequently, achieving comfort temperature range in the heat consumption components necessitates careful consideration of the hydraulic scheme of the entire system and control strategies at component-level, module-level, and system-level. In the subsequent sections, the connection of each component to the stratified storage tank is explained. This is followed by a comprehensive discussion of the varied control strategies that have been implemented within the system. Furthermore, it is worth mentioning that a potential limitation of the study pertains to the absence of a validated stratified storage tank with experimental data.

When considering a gas heat pump with one bed adsorber/desorber, the single adsorber cycle GAHP is linked to the Combi-Storage, serving as the heat production component. The heat consumption in the single adsorber cycle GAHP is maintained as a constant load, based on the guidelines provided in VDI 4650-2 [73] and DIN EN 12309-6 [72].

2.3.1. Dual Adsorber Cycle Gas Adsorption Heat Pump with Combi-Storage (Reference system)

The reference system in this study involves the integration of the Domestic Hot Water (DHW) circuit into the AdoSan system, designated as the base system (defined in subsection 2.4.1). The primary objective of selecting this reference system is to evaluate the feasibility of DHW preheating through the utilization of condensing boiler effect and the sorption mode of AdoSan's dual adsorber cycle Gas Adsorption Heat Pump (GAHP). Additionally, this study aims to analyze the sensitivity of various parameters impacting the reference system and to incorporate a solar thermal collector to achieve high system efficiency, in alignment with AdoSan's objective. The description of the Reference system begins by outlining the hydraulic scheme in Figure 2.11. In this scheme, the heat exchanger connecting dual adsorber cycle GAHP to the 16-layer combi storage draws its supply water from layer 10 of the Combi-Storage, and the return hot water is directed to layer 7 of the Combi-Storage. Regarding the low-temperature source circuit of the dual-adsorber cycle GAHP, it features the standard borehole heat exchanger used across all systems, with a depth of 198 m and a diameter of 0.026 m. This heat exchanger is connected to the

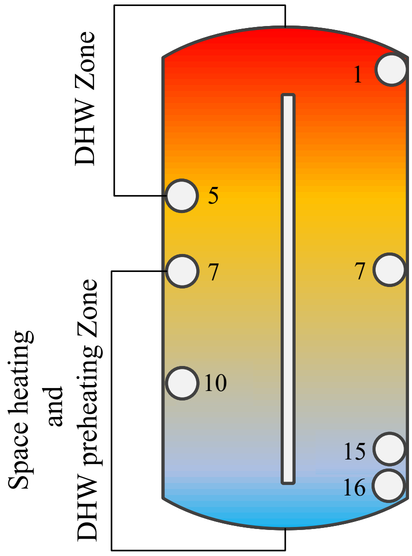

Figure 2.11.: Schematic of the stratified storage tank showing the representative layers and the allocation of layers for domestic hot water (DHW), space heating, and DHW preheating.

evaporator and operates with a constant mass flow rate. Additionally, the heat exchanger that connects the upper part of the Combi-Storage to the burner of dual adsorber cycle GAHP has its supply line connected to layer 5, and the return hot water is connected to the top of the Combi-Storage. Furthermore, the details of operation modes of the dual adsorber cycle GAHP are presented in section A.1.

Regarding the heat consumption components, such as the Water Heating Circuit, the supply water is extracted from layer one of the Combi-Storage and directed to the Water Heating Circuit, while the return water is distributed among the layers of the Combi-Storage using an ideal inserter. In the case of the Space Heating Circuit, the supply water originates from layer 7, and the return water is directed to layer 15 of the Combi-Storage.

As shown in Figure 2.12, there are three hierarchical levels of control for a system, each addressing distinct aspects of control strategies. The first level is the component level, which includes the regulation of pumps' mass flow rates. The water heating circuit with fresh water station is controlled conventionally through on-off control logic and incorporates two effective strategies, without considering circulation [120].

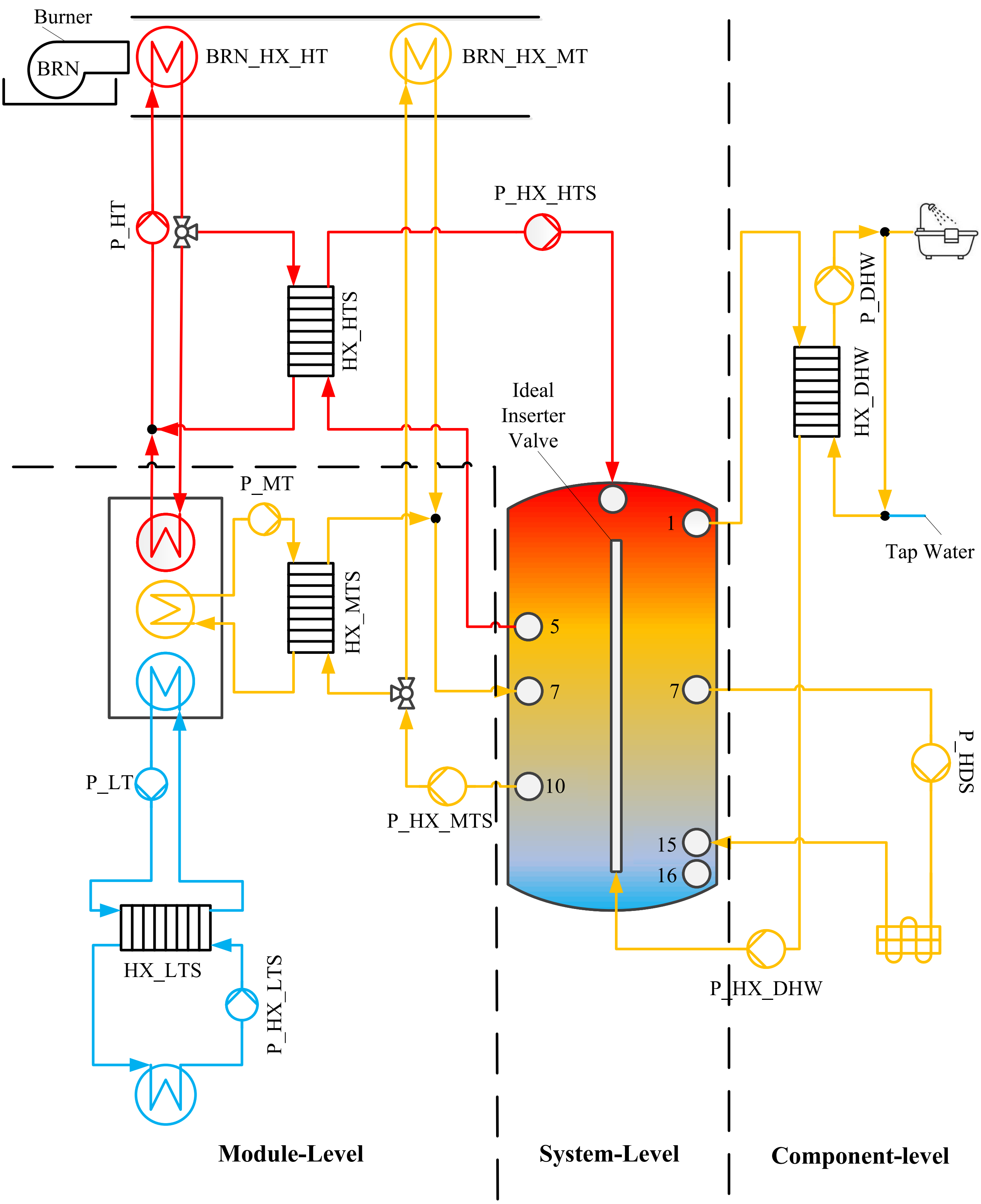

Figure 2.12.: Hydraulic scheme of the reference system illustrating the three control levels. Red lines represent water with high temperature; Blue lines show the water with low temperature, and orange lines present water with medium temperature.

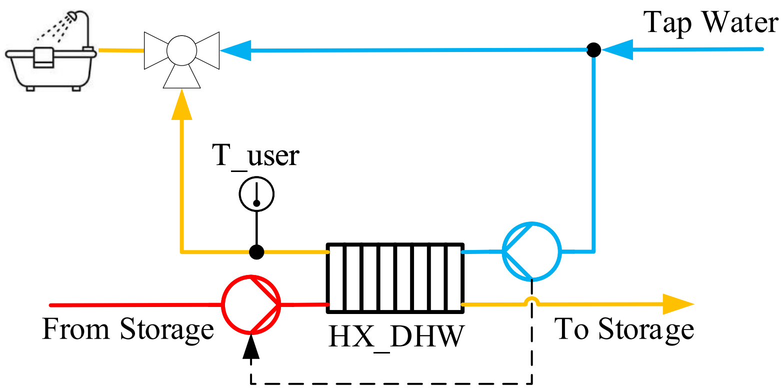

Figure 2.13.: Domestic hot water circuit without circulation A.

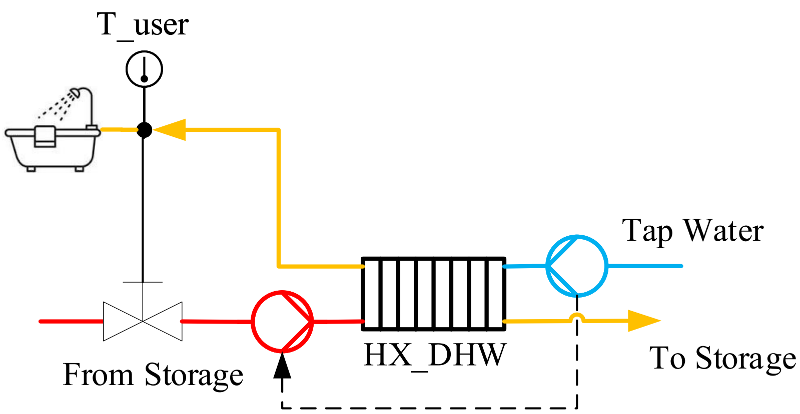

Figure 2.14.: Domestic hot water circuit without circulation B.

First type represents in Figure 2.13, when there is user demand, the storage side pump with a constant mass flow rate activates. On the user side, cold tap water (14 °C) mixes with hot water to supply water at 60 °C to the user. Second type depicts in Figure 2.14, a two-way valve is positioned behind the storage side pump, and the mass flow rate of the two-way valve is controlled based on the user's draw-off temperature sensor. As thermal stratification significantly affects the energy consumption and the quality of domestic hot water (DHW) supply temperature, the first method is not suitable because it creates high mixing inside the stratified storage tank. Additionally, even if the two-way valve modulates smoothly, the on-off nature of the pump can lead to over-heating or under-heating.

The state-of-the-art method for controlling user draw-off temperature in the water heating circuit, presented in Figure 2.3, involves adjusting the mass flow rate of the storage side pump using a PI controller. In this setup, the PI controller is set to maintain a temperature of 60 °C, with the measurement point being a temperature sensor located on the user side. The output of the PI controller is then scaled by the maximum mass flow rate on the user side to ensure that hot water at 60 °C is delivered to the consumer.

The mass flow rate of the Space Heating Circuit pump represents the subsequent component described within the component-level strategy. In this context, the mass flow rate of the pump is governed by a PI controller, with the set point established at 20 °C, and the room temperature serving as the measured parameter. This control strategy mimics the behavior of thermostatic radiator valves, which are not explicitly modeled in the system. Furthermore, the description of the control strategy for heat production circuits comprises two segments: the mass flow rate of each pump on both sides of the heat exchanger (HX_MTS in Figure 2.12) connecting the dual adsorber cycle GAHP to the Combi-Storage, and the mass flow rate of each pump on both sides of the heat exchanger (HX_HTS) connecting the burner to the upper part of the Combi-Storage. In the former case, the pump on the storage side (P_HX_MTS) delivers a mass flow rate equal to that of the pump between the heat exchanger and the GAHP (P_MT), plus an additional 0.1 kg/s. As illustrated in Figure 2.12, this additional flow is directed via the splitting valve to the condensing heat exchanger (BRN_HX_MT) to maintain a constant mass flow rate of 0.1[6] kg/s, ensuring effective utilization of the exhaust gas from the burner. While the mass flow rate of the pump on the dual adsorber cycle GAHP side is governed by module-level control [69], the mass flow rate of each pump on both sides of the heat exchanger (HX_HTS) connecting the burner to the upper part of the Combi-Storage are managed within the system-level control strategy.

The system-level control strategy comprises two main elements: power control of the production circuits and management of valve positions in the ideal inserters.

Regarding power control, the thermal output of the dual-adsorber cycle GAHP is regulated by a PI controller. The controller set point is defined by the supply temperature derived from the heating curve, while the controlled variable is the temperature of layer 7 of the Combi-Storage. The PI controller output is limited by the maximum design burner power of 50 kW. Two heating operating modes are implemented within this framework: (i) an adsorption module heat-pump mode and (ii) a direct burner heat mode, which is activated when the heat provided by the adsorption module is insufficient to maintain layer 7 at its target temperature.

A separate PI controller is employed to regulate the burner power in the domestic hot water (DHW) production circuit. In this case, the set point is fixed at 65 °C, and the measured variable is the temperature of layer 1. The controller output is again scaled between a minimum burner power of 5 kW and a maximum design burner power of 50 kW. The system-level control strategy prioritizes the stability of the DHW supply temperature for the consumer. Consequently, if the temperature in layer 1 drops below 63 °C, the power supply to the Space Heating Circuit is immediately interrupted. This measure ensures that the upper part of the storage remains available to meet DHW demand and guarantees reliable hot water delivery.

In addition, the mass flow rates of the pumps on both sides of the heat exchanger (HX_HTS) connecting the burner to the upper part of the Combi-Storage are controlled at

[6] In principle, the optimal mass flow rate depends on the operating point and would lead to comparable return temperatures from the burner heat exchanger (BRN_HX_MT) and the heat exchanger between the GAHP and the storage (HX_MTS), which would require intra-cycle adjustment of the flow split. However, simulation results indicate that a constant mass flow rate of 0.1 kg/s is sufficient to ensure effective condensation of the exhaust gases, while variations around this value show only limited sensitivity with respect to overall system performance. Consequently, the flow splitting is represented using an idealized valve rather than being modeled explicitly.

the system level. Here, the PI controller output is scaled according to the maximum mass flow rate on the user side of the fresh water station.

With respect to valve control, the system-level control strategy governs the operation of the ideal inserter, which comprises 16 valves corresponding to the individual layers of the Combi-Storage. The control logic ensures that return water is injected into the storage layer whose temperature most closely matches the return water temperature from the domestic hot water system.

2.3.2. Dual Adsorber Cycle Gas Adsorption Heat Pump with Two-Storage

This system is composed of two main storage units: the Water Heating Storage with a capacity of 700 liters and 11 layers, and the Space Heating Storage with a volume of 500 liters and five layers as described in subsubsection 2.1.3.1. The hydraulic scheme in Figure 2.15 consists of two primary segments.

The first segment focuses on hot water preparation for the water heating circuit. It involves connecting the High-Temperature Source Heat Exchanger to the high-temperature source of the dual adsorber cycle GAHP. Here, supply water is drawn from layer 9 of the water heating storage and routed to the High-Temperature Source Heat Exchanger. The resulting heated water is returned to the top of the storage. For consuming hot water, supply water is extracted from layer one of the storage and fed into the water heating circuit. Subsequently, the return water is redistributed within the storage through an ideal inserter.

The second segment addresses the heat demands for the space heating circuit. For producing hot water, supply water is extracted from layer 4 of the space heating storage and sent to the Medium-Temperature Sink Heat Exchanger. After heating, the return hot water is directed to the upper part of the space heating storage. On the consumption side, water is drawn from layer one and sent to the radiator, while the return water from the radiator is guided to the bottom of the space heating storage.

To ensure a comparative analysis, the control strategies—component-level, module-level, and system-level—are consistent with those described in subsection 2.3.1.

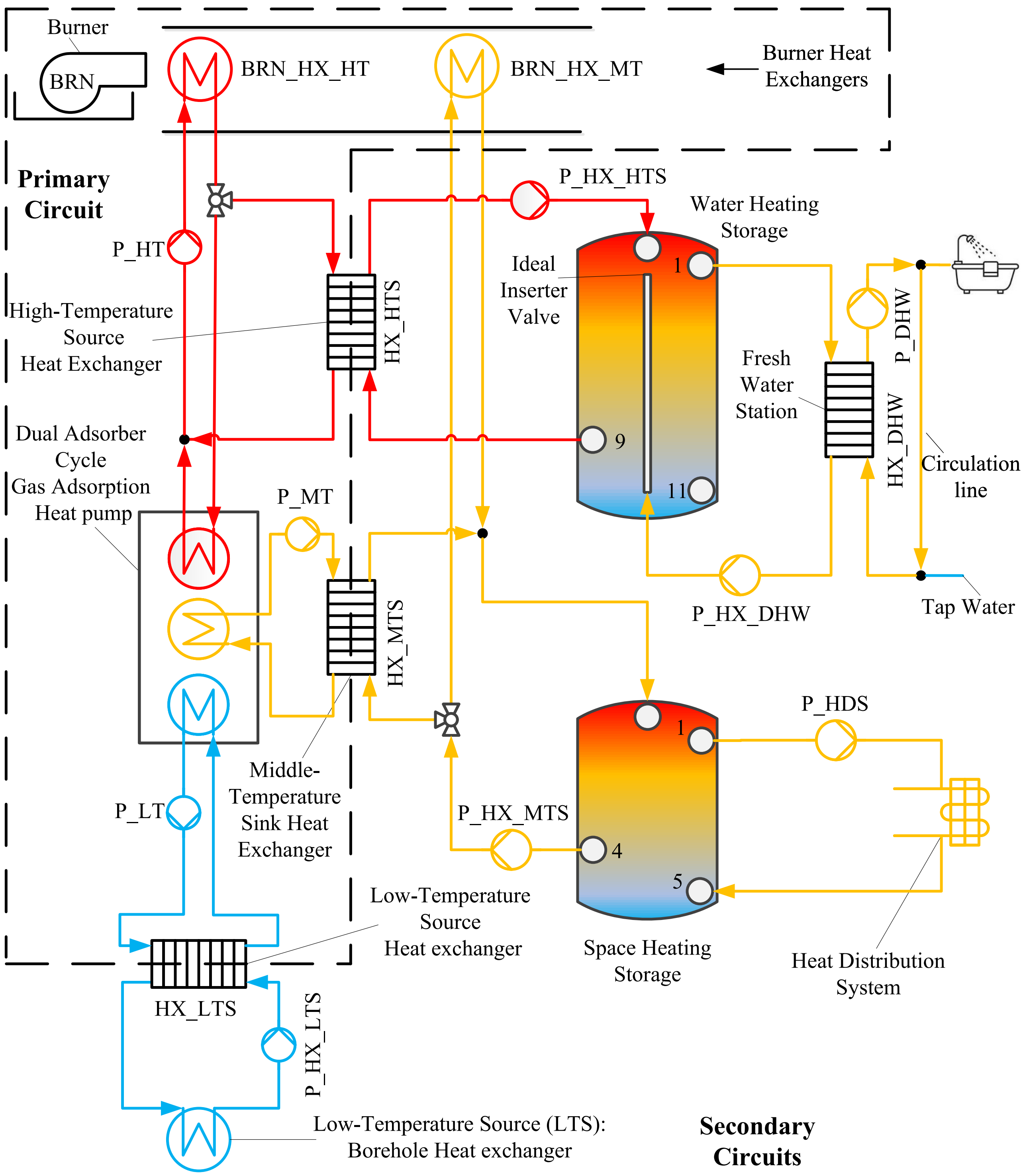

Figure 2.15.: Hydraulic scheme of two-storage system. Red lines represent water with high temperature; Blue lines show the water with low temperature, and orange lines present water with medium temperature.

2.3.3. Dual Adsorber Cycle Gas Adsorption Heat Pump with Combi-Storage and Solar Thermal Circuit

As it is feasible to expand the number of ports within each layer of the stratified storage tank model, the hydraulic configuration in the Combi-Storage Solar Thermal Circuit System (Figure 2.16) remains identical to the combi-storage system in Figure 2.7. Similarly, the control strategy for the three levels—component, module, and system—remains consistent with the combi-storage system, ensuring a comparable analysis with the reference system. However, the integration of the Solar Thermal Circuit with the combi-storage necessitates an examination of additional system-level control strategies and hydraulic connections specific to this component. Regarding the hydraulic connection, water is extracted from bottom layer of the combi-storage and directed into the Solar Thermal Circuit. If the conditions outlined in subsubsection 2.1.1.2 for component-level control strategy of solar thermal circuit are satisfied, the heated return water from the Solar Thermal Circuit is then directed back to the combi-storage through an ideal inserter. In this configuration, both ideal inserters, as shown in Figure 2.16, return water to the layer with closest temperature.

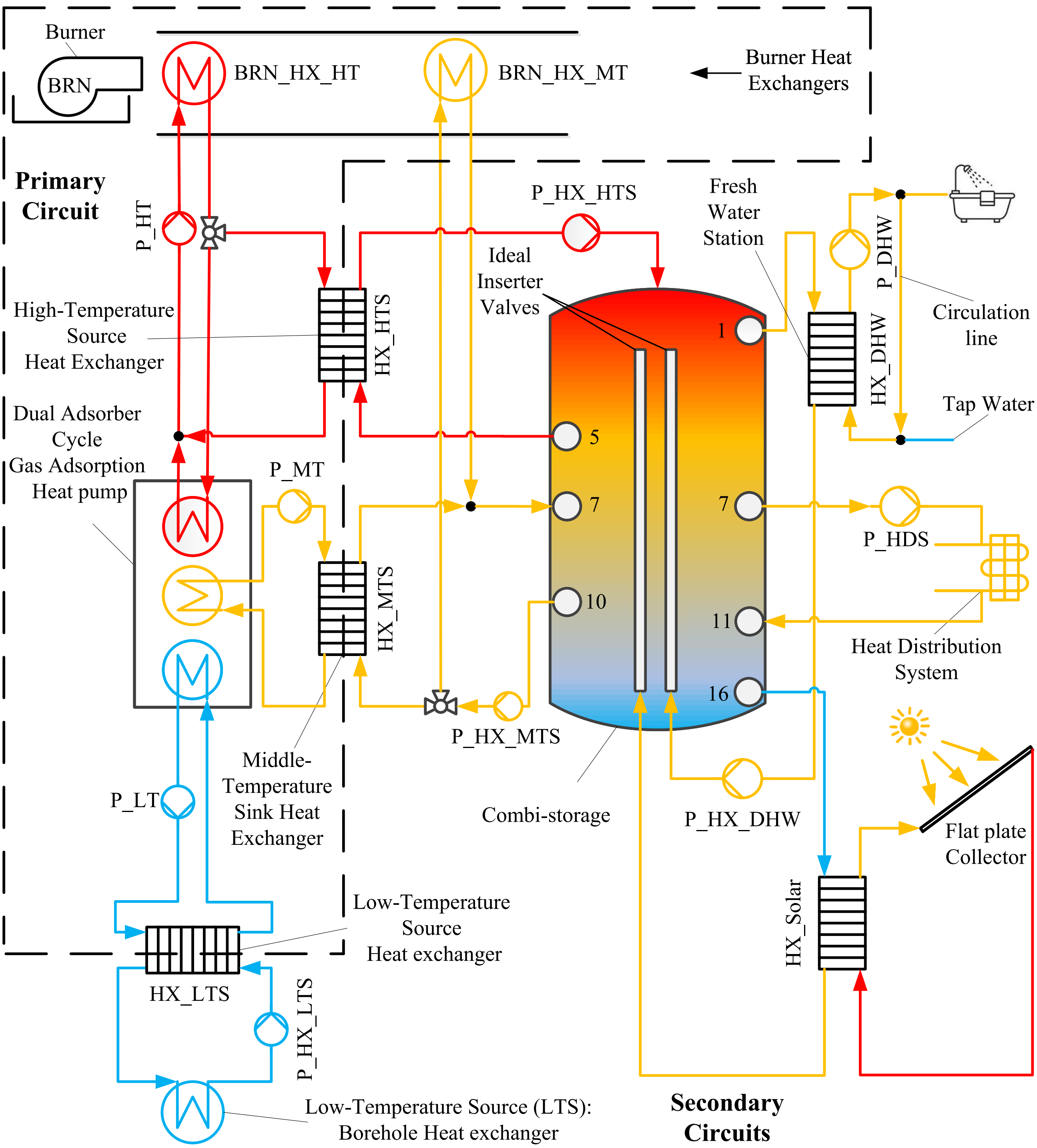

Figure 2.16.: Hydraulic scheme of combi-storage with solar thermal circuit. Red lines represent water with high temperature; Blue lines show the water with low temperature, and orange lines present water with medium temperature.

2.3.4. Dual Adsorber Cycle Gas Adsorption Heat Pump with Two-Storage and Solar Thermal Circuit

There are three key differences between the Two-Storage Solar Thermal Circuit system in Figure 2.17 and the Two-Storage system in Figure 2.15. Firstly, the integration of the Solar Thermal Circuit into either the water or space heating storage. For the space heating storage, supply water is drawn from the bottom layer, while the heated return water is directed to either layer 2 or layer 3. This choice is determined by the component-level control, which selects the layer based on the temperature of layer one. Secondly, for the water heating storage, supply water is taken from layer 11, and the return hot water is directed to either layer 3 or top of the water heating storage. Similar to the space heating storage, the component-level control determines which layer to choose based on layer one's temperature. Thirdly, the system-level control strategy in the Two-Storage system prioritizes supplying power to the space heating circuit when the Solar Thermal Circuit is operational and there is a demand in the space heating circuit. This is implemented using a PI controller, where the measured variable is the room temperature and the setpoint is 20 °C. If the controller output exceeds a small threshold ($\varepsilon = 10^{-1}$), the inlet water to HX_Solar is drawn from the space heating storage. Otherwise, it is supplied from the domestic hot water storage.

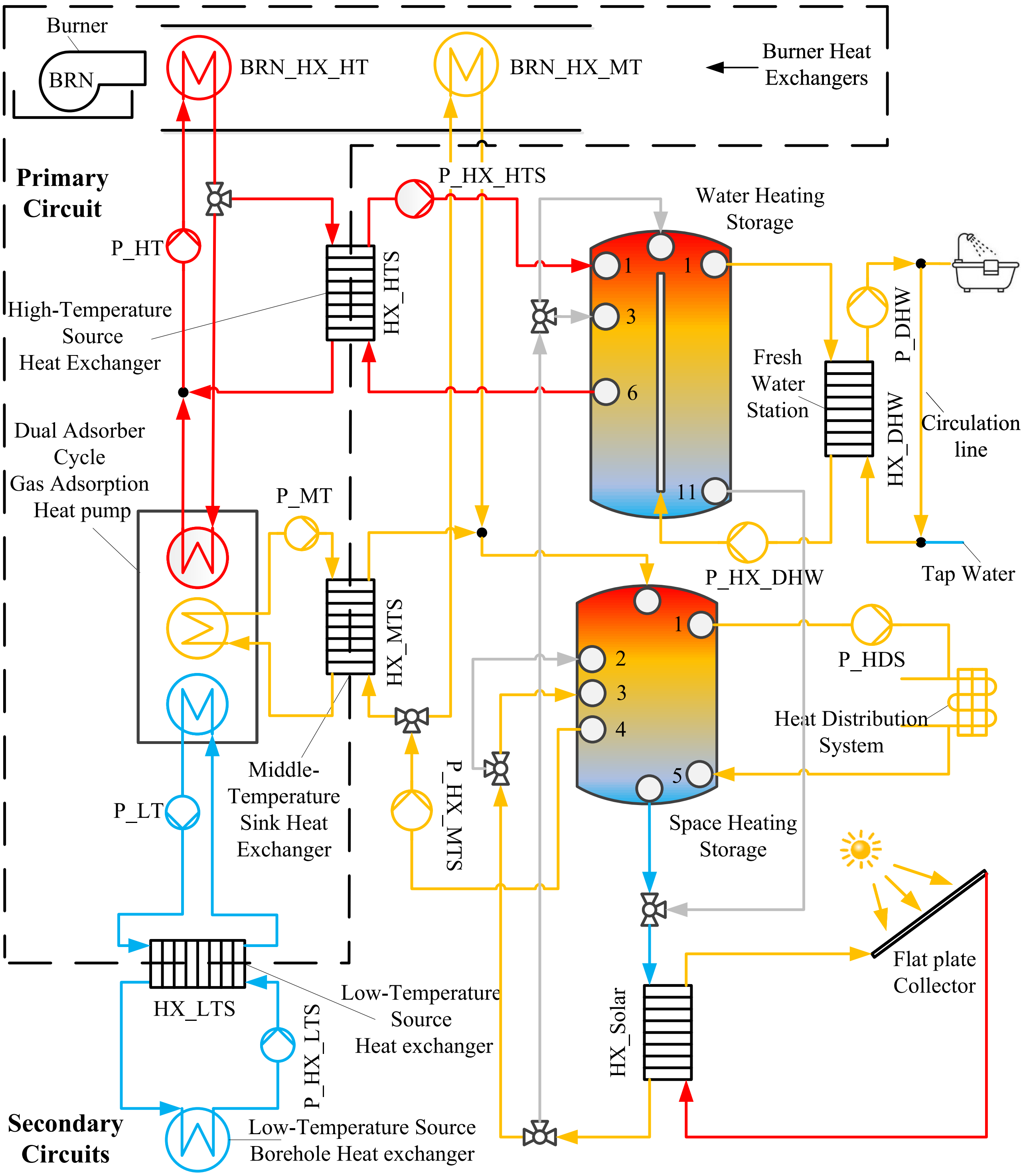

Figure 2.17.: Hydraulic scheme of two-storage with solar thermal circuit. Red lines represent water with high temperature; Blue lines show the water with low temperature, and orange lines present water with medium temperature.

2.3.5. Single Adsorber Cycle Gas Adsorption Heat Pump with Combi-Storage

There are three layered control strategies for the heating system with a single adsorber cycle GAHP, as shown in Figure 2.10. The first layer operates at the component level, controlling certain components, such as the mass flow rate of the pumps (P_HDS and P_MTS), the mixing valve V_MTS with a PI controller, and splitting valve V_HDS. The second layer operates at the module level, switching idealized valves according to temperature criteria. In this context, water is extracted and inserted from specific layers of the stratified storage to manage the adsorption, desorption, and transition processes. The third layer operates at the system level, supervising the mass flow rate of pumps based on module level conditions. It also controls the burner's operation mode, either heating the upper part of the storage to supply space heating demand when the heat pump cannot, or disconnecting from the storage and connect to the desorber to sustain the desorption process [118].

1. **Consumption-Side Control:** The nominal mass flow rate of different components for reference system and single adsorber cycle system are provided in the Table 2.3. The three-way valve, defined as V_MTS in Figure 2.10, is connected to layer 1 and layer 6 of stratified storage to maintain the space heating temperature in comfort range. In this regard, the set point of the PI controller for the V_MTS valve is the supply temperature, which is specified in VDI 4650-2 [73] or DIN EN 12309-6 [72] standards for a renovated building and the measurement point is delivered supply temperature to the space heating circuit. Moreover, the V_HDS valve as shown in Figure 2.10 is controlled to maintain a mass flow rate of 0.1 kg/s in BRN_HX_MT when the burner is active. This is done to achieve the condensing boiler effect despite the high fluid temperatures in the first heat exchanger. The low mass flow rate in BRN_HX_MT is mainly because the efficiency of the reference system is less sensitive to the mass flow fraction [26, 118].

Nominal Mass Flow Rate	Reference GAHP [kg/s]	Single Adsorber Cycle GAHP [kg/s]
Burner	0.67	0.35
Adsorber/Desorber	0.67	0.35
Condenser	0.67	0.5
Evaporator	0.94	0.5
BRN_HX_MT	0.1	0.1

Table 2.3.: Nominal mass flow rate of different components in reference cystem [63] and single adsorber cycle system [118].

2. **Module-Level Control:** At the module-level control strategy, the temperature levels of the ideal extractor used in the supply line of the condenser contain two parts: the desorption mode and the transition modes. During the desorption mode, the extracted water is set to specific temperature levels that match at least the return temperature of the space heating circuit. The supply and return temperature of space heating circuit are specified based on specific representative operating points in Table 2.4, following either VDI 4650-2 [73] or DIN EN 12309-6 [72] standards.

Furthermore, during the burner-assisted desorption phase, when the burner connects to the desorber to complete the desorption process, the temperature level is set to the supply temperature of the space heating circuit. This is mainly because the condenser temperature is a degree of freedom in a single adsorber cycle GAHP as opposed to dual adsorber cycle GAHP. Therefore, a temperature difference ($T_{des} - T_{cond}$) of approximately 40 K, which is defined as temperature thrust, is sufficient for desorption process. This indicates potential for enhancing efficiency by increasing the condenser temperature during the burner-assisted desorption phase [118].

Number	**Part load ratio DIN EN 12309-6 (%)**	Return in °C DIN EN 12309-6	Supply in °C DIN EN 12309-6	**Part load ratio VDI 4650-2 (%)**	Return in °C VDI 4650-2	Supply in °C VDI 4650-2	Borehole heat exchanger inlet in °C
6	**100**	41	55	**100**	45	55	5
5	**73**	37.1	47.6	**63**	37.2	43.4	5
4	**58**	34.7	43.1	**48**	33.8	38.5	6
3	**46**	31.9	38.2	**39**	31.7	35.6	7
2	**31**	29	33.2	**30**	29.6	32.6	8
1	**15**	25.4	27.4	**13**	24.8	26	9

Table 2.4.: The part load ratios and temperature boundary conditions for the secondary hydraulic circuit in Figure 2.10 include supply and return temperatures for the heating system. These temperatures are specified for heating circuit design temperatures of 41/55 °C (according to DIN EN 12309-6 [72]) and 45/55 °C (according to VDI 4650-2 [73]).

The burner-assisted desorption phase is employed at the final stage of each desorption process, irrespective of the load level. This contrasts with the reference system, in which the system-level "direct burner mode" was activated only at high loads, when the sorption cycle could no longer meet the space heating demand effectively [69].

The single adsorber cycle, as shown in left module of Figure 2.8 operates without any internal valve. In the absence of such a valve, the working fluid always flows between adsorber/desorber and evaporator/condenser, even during the supposed isosteric phases of the cycle. This fluid flow is especially pronounced when the temperatures of the two components do not align precisely with the isosteric temperature profile. Therefore, it is important to avoid the loss of cooling capacity through synchronously cooling both the condenser and the desorber during the transition mode from desorption to adsorption. To achieve this, the temperature level of condenser undergoes a series of changes over 180 s (Table 2.2), determined through a trial-and-error approximation, to push warm water from the condenser into the stratified storage [118].

Conversely, during the transition mode from adsorption to desorption, the temperature levels are adjusted to push the cold water from the evaporator into the stratified storage over 180 s (Table 2.2)[118].

Before explaining the ideal extractor valve control logic, which is located on the supply line of the adsorber/desorber, it is important to note that the bottom part of the stratified storage is designated for heat recovery between the evaporator and condenser, which corresponds to the temperature range between the borehole heat exchanger and the space heating circuit return temperature. The middle part of the stratified storage is designated for buffering heat for the sink loop, covering the temperature range between the supply and return temperatures of the space heating circuit. Finally, the top part of the stratified storage is designated for buffering heat above the supply temperature, as shown in the color spectrum of the storage in Figure 2.9. Thus, the module-level control strategy evaluates two distinct conditions through ideal extractor valve to regulate the adsorption and desorption processes within the single adsorber cycle.

In the adsorption process, heat is transferred from the borehole heat exchanger to the evaporator to initiate adsorption by extracting water from the stratified storage to the adsorber. The control system of the ideal extractor checks whether the mean temperature of the adsorbents is at least 2 °C higher than the temperature of the selected layer in the stratified storage. If this condition is met, the valve for the selected layer opens, while the other valves close. This process continues until the control system reaches the set point for the space heating return temperature. The adsorption process continues until the temperature difference between the inlet and outlet of the adsorber is less than 1 °C. At this point, the adsorption process stops, and the transition phase before the desorption phase begins [118].

In the first part of the desorption mode, heat supplies to the desorber from the stratified storage, while the condenser transfers heat to the stratified storage. During this half-cycle, the control system checks if the inlet temperature is at least 2 °C greater than the mean adsorbents temperature. When this condition is satisfied, the selected layer valve opens, and the other valves close. This process continues until the condition reaches the top layer of stratified storage. When the top layer valve opens, and the other valves close, the desorption process starts. Once the 2 °C temperature difference between desorber and first layer is no longer maintained, the desorber is connected to the burner and the desorption process continues until the desorber output temperature exceeds 90 °C. Then, the cycle restarts [118].

Schwamberger [16], building on the Stratisorp concept, extensively investigated the control of adsorber supply temperatures during adsorption and desorption and showed that higher temperature differences lead to increased cycle power. In the present work, a simplified control approach is adopted, with a fixed temperature difference of 2 °C between the adsorber/desorber and the selected storage layer. In principle, a more advanced control strategy could vary this temperature difference as a function of the load fraction. Furthermore, the return water from the condenser and adsorber/desorber is directed to the layer in the stratified storage with the closest temperature through ideal inserters, located in the return line of the adsorber/desorber and condenser heat exchangers.

3. **System-Level Control:** The concept of system-level control is based on the fact that the space heating demand may not be satisfied with the heat pump for high load points. In such cases, the burner operates for an extended period to charge the storage directly. At the system-level control strategy, the burner heats the upper part of the stratified storage when the upper layer temperature is lower than a specific set point temperature. In this process, water is extracted from layer two of the stratified storage, and the return hot water is directed back to the top of the stratified storage. When the extraction index valve reaches the upper layer of the storage, and the layer temperature matches the set point temperature, the burner is shifted from heating the upper part of the stratified storage to the desorber via V_BRN and V_ADHX in Figure 2.10. Furthermore, the system-level control monitors the mass flow rate of adsorber/desorber pump and reduces it only during each of two 180 s transition phases [118].

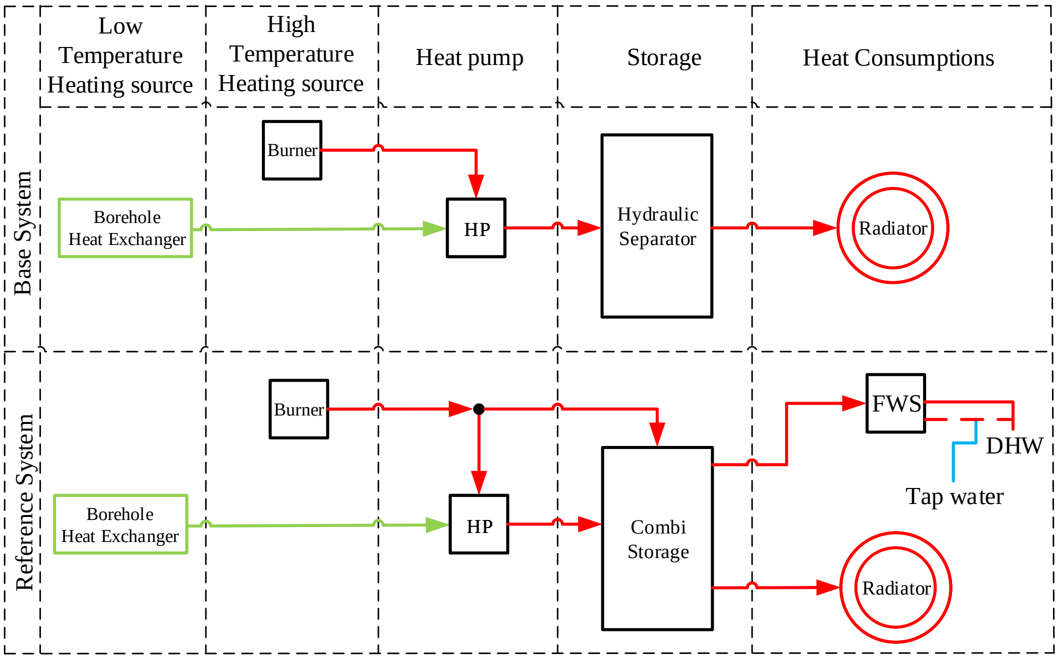

Figure 2.18.: Description of base and reference systems.

2.4. Organization of Simulations

2.4.1. Reference System and Base System

The Base system in Figure 2.18 comprises three heat production components: the Borehole heat exchanger, serving as the low-temperature source for the heat pump; the burner, acting as the high-temperature source for the heat pump; and the dual adsorber cycle Gas Adsorption Heat pump, which operates in three distinct modes: sorption mode, direct burner mode, and heat recovery mode. These modes collectively provide high-temperature water to the Hydraulic Separator. Subsequently, the demand load is supplied to the Space Heating Circuit from the Hydraulic Separator.

The reference system can be viewed as the simplest possible extension of the AdoSan base system to include domestic hot water (DHW) via a Combi-Storage. In this configuration, the Hydraulic Separator is replaced by the Combi-Storage, the high-temperature burner is connected to the top of the storage through a heat exchanger to supply the Water Heating Circuit, and a fresh water station (FWS) is integrated to provide the DHW function through the Combi-Storage.

2.4.2. Annual Simulation

This study addresses two research questions concerning heating systems in renovated Medium-sized Multi Family Houses: firstly, preheating the domestic hot water [71], and secondly, achieving an annual primary energy ratio exceeding 1.3 [26]. In addition, the comparative study of the research project involves three key factors.

A primary focus of this study is the ability of each system configuration to maintain the prescribed comfort temperature ranges for space heating and domestic hot water in a renovated multi-family house over the entire year. This aspect is particularly critical, as thermal comfort is strongly influenced by both the hydraulic system design and the implemented control strategy. One of the objectives is therefore to minimize temperature deviations in all consumption circuits under real operating conditions. To achieve this, dynamic annual simulations are adopted as the principal evaluation methodology. This approach enables a continuous assessment of system behavior under realistic, time-varying boundary conditions, including fluctuating outdoor temperatures and variable user demand. In contrast to assessments based solely on representative operating points defined in VDI 4650 [73] and DIN EN 12309 [72], dynamic simulations subject the control strategy to continuous disturbances arising from weather and load variations. They allow comfort deviations to be evaluated over time rather than only at nominal conditions, capture the transient behavior of thermal storage and stratification, reveal interactions between control loops and operating modes, and enable an assessment of system sensitivity under off-design operation. While standardized representative-point approaches are well suited for ensuring stable and efficient operation at predefined nominal and part-load conditions, they inherently provide robustness only at these discrete states. Consequently, the overall robustness of the heating system—particularly with respect to comfort maintenance, efficiency, and subsystem interaction—can only be reliably assessed using dynamic annual simulations.

Secondly, The Seasonal Gas Utilization Efficiency (SGUE), based on the net calorific value of the fuel gas is a performance indicator for gas adsorption heat pump [72, 73]. Thus, SGUE in equation (2.33) is defined as the ratio of the annual energy delivered to the heat consumption circuits to the annual energy released from the fuel gas during combustion in both burner heat exchangers as shown in Figure 2.7.

$$SGUE = \int_0^{365\times24\times3600} \left(\frac{\dot{Q}_{Stor-SHC} + \dot{Q}_{Stor-WHC}}{\dot{Q}_{H_u}} \right) dt \tag{2.33}$$

$$\dot{Q}_{H_u} = \frac{\dot{Q}_{flueGas,HT}}{\eta_{NCV}(T_{flueGas,HT})} \tag{2.34}$$

$\dot{Q}_{\mathrm{flueGas,HT}}$ in equation (2.34), denotes the heat flow rate supplied by the burner at the high-temperature level. This quantity is prescribed by the GAHP control unit and imposed as a boundary condition on a lumped thermal resistance–capacitance (RC) representation of the burner heat exchanger. Within this thermal model, the flue gas temperature at the high-temperature node, $T_{\mathrm{flueGas,HT}}$, is obtained directly from the simulation by sensing the temperature at the corresponding location in the RC network. This temperature is therefore a time-dependent output of the annual dynamic simulation. The temperature-dependent efficiency $\eta_{\mathrm{NCV}}(\mathrm{T}_{\mathrm{flueGas,HT}})$, based on the net calorific value of methane, is then evaluated point-wise using the correlation provided in section A.4 [63]. At each simulation time step, the instantaneous value of $\eta_{\mathrm{NCV}}(\mathrm{T}_{\mathrm{flueGas,HT}})$ is computed from the simulated flue gas temperature and used to determine the corresponding fuel energy input via

Equation (2.34). Consequently, the annual fuel demand results from the time integration of these instantaneous values, with the simulation inputs being the burner heat flow rate specified by the control strategy and the thermal response of the burner heat exchanger, and the outputs being the flue gas temperature and the associated temperature-dependent efficiency.

The simulated heating system model consists of the Space Heating Circuit, Water Heating Circuit, Gas Adsorption Heat Pump, and Stratified storage tank, as well as two configurations with solar thermal Circuit. The Space Heating circuit is modeled using a detailed building model, as described in subsubsection 2.1.2.2, together with radiator characteristics based on EN 442-2 [63]. The Water Heating circuit is designed for a Medium-sized Multi Family House with 20 occupants, as described in section 2.1. To connect consumption circuits to the Stratified storage tank, sub-models from publicly available libraries for Dymola, such as Buildings-Library [84], AixLib [121], IBPSA [122], SorpLib [123], are used to build a simulation model in this research.

2.4.3. Seasonal Gas Utilization Efficiency

A heating system must adjust both its output power and temperature levels to match the heating load within a building during the heating season, ensuring the maintenance of the building's temperature at a desirable level. In this context, the selection of output power and temperature levels for a heating system relies on various factors, including the outside temperature, the type of radiator in use, and the thermal insulation of the building envelope. To regulate the supply temperature in response to these varying conditions, the heating system in the present simulation is controlled using a standard heating curve. This control approach[7] specifies the required supply temperature as a function of the ambient temperature and represents established practice in radiator-based space heating systems. At lower outdoor temperatures, the heating curve increases the supply temperature to compensate for higher heat losses, while under milder conditions, it reduces the temperature level to avoid unnecessarily high supply temperatures and the associated efficiency losses.

Seasonal Gas Utilization Efficiency (SGUE) [72] is an indicator used to calculate the annual efficiency of a heating system, which in our simulation model is calculated based on the heating curve. To predict SGUE from a limited set of values and focus on the heating system itself and enhancing the heating system control strategy while considering the representative operating points, VDI 4650-2 [73] and DIN EN 12309-6 [72] standards have defined distinct nominal temperature levels and partial loads for buildings in different conditions, such as new, renovated, and old structures.

[7] There are advanced temperature control methods, which adjust in real-time to demand, demonstrate significant potential to reduce supply temperature levels for a substantial portion of the time. For instance, the Fraunhofer Institute for Building Physics (IBP) has shown in their tests on the Wilo Geniax pump that these intelligent control systems can be highly effective [124]. However, implementing such advanced control schemes in existing building renovations presents considerable challenges. New heating systems must be designed to function as direct replacements for older systems to facilitate ease of integration. Consequently, this study does not explore the potential for reducing heating temperatures through time-resolved, room-based demand control

For renovated buildings classified within the 1958–1978 building age class [65], DIN EN 12309-6 [72] prescribes nominal return and supply temperatures of 41/55 °C, whereas VDI 4650-2 [73] uses 45/55 °C, with the five representative temperature points detailed in Table 2.4. Therefore, To predict SGUE of a heating system, the DIN EN 12309-6 [72] standard considers all six representative points throughout the year, including the 100 % operating point, and computes the weighted average. In contrast, VDI 4650-2 [73] utilizes five representative points, excluding the 100 % operating point, and computes the harmonic mean value. The details of these calculation methods are outlined in section A.2.

3. Entropy Balance in different components of the Reference System

Haller et al. [125] demonstrated that the entropy generation from mixing and heat transfer within a stratified storage tank serves as a key performance indicator, referred to as stratification efficiency. This method was applied to six different stratified solar storage systems under three different boundary conditions [126]. The study did not separate the entropy balance of the fresh water station and solar heat exchanger from the entropy balance of the stratified storage. Instead, Haller et al. considered a control volume that includes these heat exchangers within the entropy balance calculation for the stratified storage. The stratification efficiency was evaluated under a 24-hour dynamic simulation for single or double-family houses.

Meunier et al. [127] have shown that the performance of adsorptive refrigeration cycles is inherently less efficient than that of the corresponding Carnot cycle, due to entropy generation. Their analysis indicated that the primary source of entropy generation is the external thermal coupling (similar to R_C in Figure 3.3) between isothermal heat reservoirs and temperature-varying adsorbers, which accounts for approximately 95 % of the total entropy generation in basic uniform temperature cycles.

Schwamberger [16] conducted a detailed calculation of irreversibility in various components of the single adsorber cycle within the Stratisorp cycle, which features distinct evaporator and condenser, and compared it to the same single adsorber cycle in a dual adsorber cycle heat pump. Schwamberger et al. [119] demonstrated that, in a high-temperature Stratisorp system with a thermal oil storage, the entropy generation due to external thermal coupling in the adsorber/desorber of the Stratisorp cycle is significantly lower than that in the dual adsorber cycle heat pump. Moreover, the overall entropy generation in the single adsorber cycle of the Stratisorp cycle, even when accounting for additional entropy generation from mixing in the stratified storage tank, is smaller than the total entropy generation in the dual adsorber cycle heat pump. Although the absolute results are not directly transferable to the present water-based system, their entropy-balancing methodology is applied here.

Current research focuses on entropy balance of each component, including the stratified storage, specific heat exchanger, and single adsorber cycle, utilizing distinct numerical models in contrast to those developed by Schwamberger and Haller.

The entropy balance calculations in this chapter have two primary objectives regarding both dual and single adsorber cycles. First, for the dual adsorber cycle, we aim to characterize the influence of various components on thermal stratification within the stratified storage tank. Second, for the single adsorber cycle, we investigate the feasibility of employing entropy generation as a control mechanism to enhance GAHP performance, focusing on minimizing entropy generation rates associated with mass flow rates.

3.1. Energy and Entropy Balance in Component Level

3.1.1. Storage

The stratified storage is modeled using a fractional plug-flow approach, in which the incoming mass flow is partially transported in a plug-flow-like manner through the storage layers while the remaining fraction is mixed with adjacent layers. This formulation represents an intermediate behavior between ideal plug flow and perfect mixing and is commonly applied in system-level simulations of stratified thermal storage [106]. Due to the discretized, multi-layer representation, the model introduces a certain degree of numerical dissipation, leading to artificial smoothing of temperature gradients and an associated entropy generation that must be distinguished from physical irreversibilities. In contrast, the storage model employed by Schwamberger [16] explicitly accounts for conductive mixing within the storage and convective effects in the vicinity of fluid inlets and outlets. While such mixing and transport mechanisms can be separated explicitly into sequential procedural steps in a MATLAB-based implementation [128], the equation-based formulation used in the present Modelica model does not provide direct access to an intermediate storage temperature state between these processes within a single solver time step [129]. Building on the conceptual description of the storage tank in subsection 2.1.3, the n-layer stratified storage tank, sourced from the Modelica Buildings library [84], is modeled using a discretized control-volume approach (Figure 3.1). Each layer represents a control volume with finite thermal capacitance and dynamically varying temperature, explicitly accounting for the fluid mass in energy storage. Each control volume has three fluid ports: port 1 connects to the adjacent layer above, port 2 to the adjacent layer below, and port 3 allows for extraction or insertion of water from or into the layer by external hydraulic circuits. Water is treated as weakly compressible with temperature-dependent properties but constant density, so volumetric expansion and pressure dynamics are not modeled explicitly. No dedicated expansion vessel is included; instead, pressure reference and volume compensation are handled implicitly via boundary conditions within the hydraulic circuit using source and sink components. Thermal interaction between adjacent layers and heat exchange with the environment are represented by thermal resistances. Assuming layer 1 is the hottest and layer n the coldest, the energy balance of the stratified storage tank can be expressed as follows

$$
\begin{cases}
\text{Storage:} \\
CV_1 : \sum (\dot{m}_{\text{in}} h_{\text{in}})_1 - \sum (\dot{m}_{\text{out}} h_{\text{out}})_1 - \dot{Q}_{1,2} - \dot{Q}_{1,env} = \dfrac{dE_1}{dt} \\
CV_2 : \sum (\dot{m}_{\text{in}} h_{\text{in}})_2 - \sum (\dot{m}_{\text{out}} h_{\text{out}})_2 + \dot{Q}_{1,2} - \dot{Q}_{2,3} - \dot{Q}_{2,env} = \dfrac{dE_2}{dt} \\
\qquad\qquad\qquad\qquad\qquad . \\
\qquad\qquad\qquad\qquad\qquad . \\
\qquad\qquad\qquad\qquad\qquad . \\
CV_n : \sum (\dot{m}_{\text{in}} h_{\text{in}})_n - \sum (\dot{m}_{\text{out}} h_{\text{out}})_n + \dot{Q}_{n-1,n} - \dot{Q}_{n,env} = \dfrac{dE_n}{dt}
\end{cases}
\tag{3.1}
$$

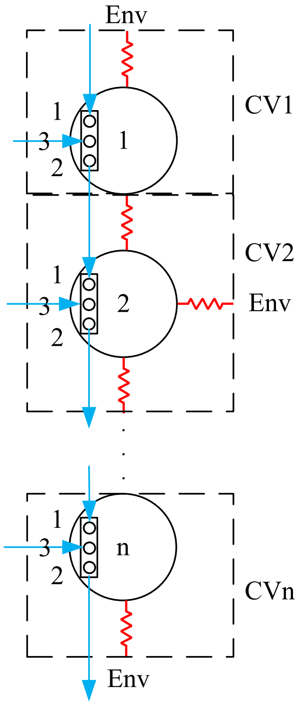

Figure 3.1.: Resistance-Capacitance model with control volumes for a n-layer stratified storage. Each control volume (CV) is equipped with three fluid ports: port 1 connects to the neighboring layer above, port 2 to the neighboring layer below, and port 3 represents external mass flows entering or leaving the storage $\dot{m}_{1,1}$: External flow into CV1, $\dot{m}_{1,3}$: External flow into or out of CV1, $\dot{m}_{1,2}$: Flow out from CV1, $\dot{m}_{2,1}$: Flow into CV2 from CV1, and etc. $\dot{m}_{n,2}$: Flow out of CVn.

The finite temperature difference between each layer with the environment and mass flow rate between layers results in irreversibility in each layer. To calculate the entropy generation rate in each layer, the model shown in Figure 3.1 is divided into n control volumes, namely CV1, CV2, ..., and CVn. The entropy balance for a system undergoing any process can be expressed in terms of the rate as follows [108, 118]:

Rate of net entropy transfer by mass + Rate of net entropy transfer by heat + Rate of entropy generation = Rate of change in the Entropy

$$
\begin{cases}
\text{Storage:} \\
CV_1 : \sum (\dot{m}_{\text{in}} s_{\text{in}})_1 - \sum (\dot{m}_{\text{out}} s_{\text{out}})_1 - \dfrac{\dot{Q}_{1,2}}{T_1} - \dfrac{\dot{Q}_{1,env}}{T_{env}} + \dot{S}_{1,gen} = \dfrac{dS_1}{dt} \\
CV_2 : \sum (\dot{m}_{\text{in}} s_{\text{in}})_2 - \sum (\dot{m}_{\text{out}} s_{\text{out}})_2 + \dfrac{\dot{Q}_{1,2}}{T_1} - \dfrac{\dot{Q}_{2,3}}{T_3} - \dfrac{\dot{Q}_{2,env}}{T_{env}} + \dot{S}_{2,gen} = \dfrac{dS_2}{dt} \\
\quad \vdots \\
CV_n : \sum (\dot{m}_{\text{in}} s_{\text{in}})_n - \sum (\dot{m}_{\text{out}} s_{\text{out}})_n + \dfrac{\dot{Q}_{n-1,n}}{T_n} - \dfrac{\dot{Q}_{n,env}}{T_{env}} + \dot{S}_{n,gen} = \dfrac{dS_n}{dt}
\end{cases}
\tag{3.2}
$$

Here, m represents the mass flow rate, $\dot{Q}$ is the heat transfer rate, $\dot{S}_{gen}$ is the entropy generation rate, and $\frac{dS}{dt}$ signifies the entropy change rate inside each layer. For each control volume CV, the rate of net entropy transfer by mass is given by the difference between the entropy carried by the inlet and outlet flows. When considering the rate of net entropy transfer by heat, it is important to account for the temperature at the boundaries of each control volume. For example, in CV1 the relevant temperature is T1, while in CV2 the boundary temperatures are T1 at the top and T3 at the bottom of the control volume.

The entropy generation equations are solved to quantify the total irreversibilities associated with each control volume in the stratified storage. In the present model, the entropy generation term contains two main contributions: (i) the mass flow exchange between layers, represented through the fractional plug-flow formulation with partial mixing, and (ii) heat transfer between adjacent layers and with the environment, calculated using only the conductive properties of water. Convective effects within each layer or near the inlet/outlet are not explicitly resolved. In contrast, Schwamberger's model [16] separates these contributions more explicitly, including conductive mixing throughout the storage and convective effects near fluid ports, allowing a detailed attribution of entropy generation to different mechanisms. The simplified approach adopted here is justified because, under proper system control that avoids temperature inversions, the contribution of conductive mixing to overall entropy generation is negligible. This choice enables a computationally efficient representation of the storage while capturing the dominant irreversibilities arising from layer-to-layer mass and heat transport.

3.1.2. Fresh Water Station

The fresh water station heat exchanger is modeled using the "DryCoilCounterFlow" model from the Modelica (subsection 2.1.1), configured as a counter flow water–water heat exchanger. Both sides are modeled using constant-property liquid water, and the heat exchanger is discretized into 20 finite elements along the flow paths to capture axial temperature gradients. Heat transfer is purely sensible, assuming single-phase operation with no phase change, no moisture effects, and constant overall heat transfer characteristics, represented by a nominal UA value of 12 kW/K (subsubsection 4.2.2.2). Nominal mass flow rates of 0.224 kg/s, corresponding to the maximum user mass flow rate, and pressure drops of 2 kPa are specified on both sides, while dynamic thermal behavior is represented using first-order time constants for the fluid volumes and the heat exchanger wall. The model assumes ideal counterflow operation with uniform flow distribution and neglects flow-dependent variations of the heat transfer coefficient. The Resistance-Capacitance Model of a heat exchanger is illustrated in Figure 3.2. The model consists of two mixing volumes, labeled as hot side (1) and cold side (3), along with the metal mass, which is represented as a thermal capacitance. Two thermal resistances connect the thermal mass to the mixing volumes, serving as lumped thermal elements for heat convection. Additionally, thermal resistances connecting the mixing volumes and thermal mass to the environment function as lumped thermal elements for transporting heat to the environment without storing it. According to the R-C model, the rate of entropy generation, which arises from constrained temperature differentials and mass flow rate with different temperatures, is determined for each respective control volume.

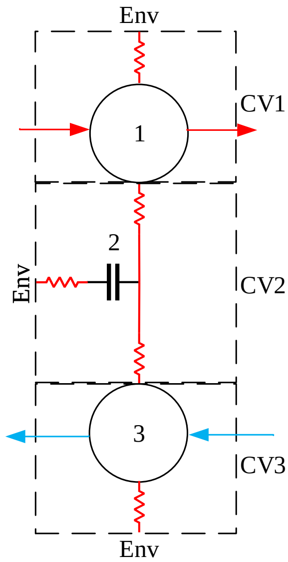

Figure 3.2.: Resistance-Capacitance model with control volumes for a heat exchanger.

$$
\begin{cases}
\text{Heat Exchanger:} \\
CV_1 : \dot{m}_{1,in} * s_{1,in} - \dot{m}_{1,out} * s_{1,out} - \dfrac{\dot{Q}_{1,2}}{T_1} - \dfrac{\dot{Q}_{1,env}}{T_{env}} + \dot{S}_{1,gen} = \dfrac{dS_1}{dt} \\
CV_2 : \dfrac{\dot{Q}_{1,2}}{T_1} - \dfrac{\dot{Q}_{2,3}}{T_3} - \dfrac{\dot{Q}_{2,env}}{T_{env}} + \dot{S}_{2,gen} = \dfrac{dS_2}{dt} \\
CV_3 : \dot{m}_{3,in} * s_{3,in} - \dot{m}_{3,out} * s_{3,out} + \dfrac{\dot{Q}_{2,3}}{T_3} - \dfrac{\dot{Q}_{3,env}}{T_{env}} + \dot{S}_{3,gen} = \dfrac{dS_3}{dt}
\end{cases}
\tag{3.3}
$$

3.2. Entropy Balance in Module level

The Adsorption module is based on the existing implementation by Velte [17]. This work extends the model by incorporating entropy balance equations for heat and mass flows in each control volume, enabling the evaluation of entropy generation and thermodynamic irreversibilities. While the underlying flow and energy balances remain as in the original module, the added entropy balance equations represent the primary contribution of this study to the modeling framework. The RC (Resistance-Capacitance) diagram with Control Volumes shown in Figure 3.3 provides a visual representation of the thermodynamic processes and heat transfer within a module, including one Adsorber and one Evaporator/Condenser located in a single casing. In this diagram, each capacitance represents

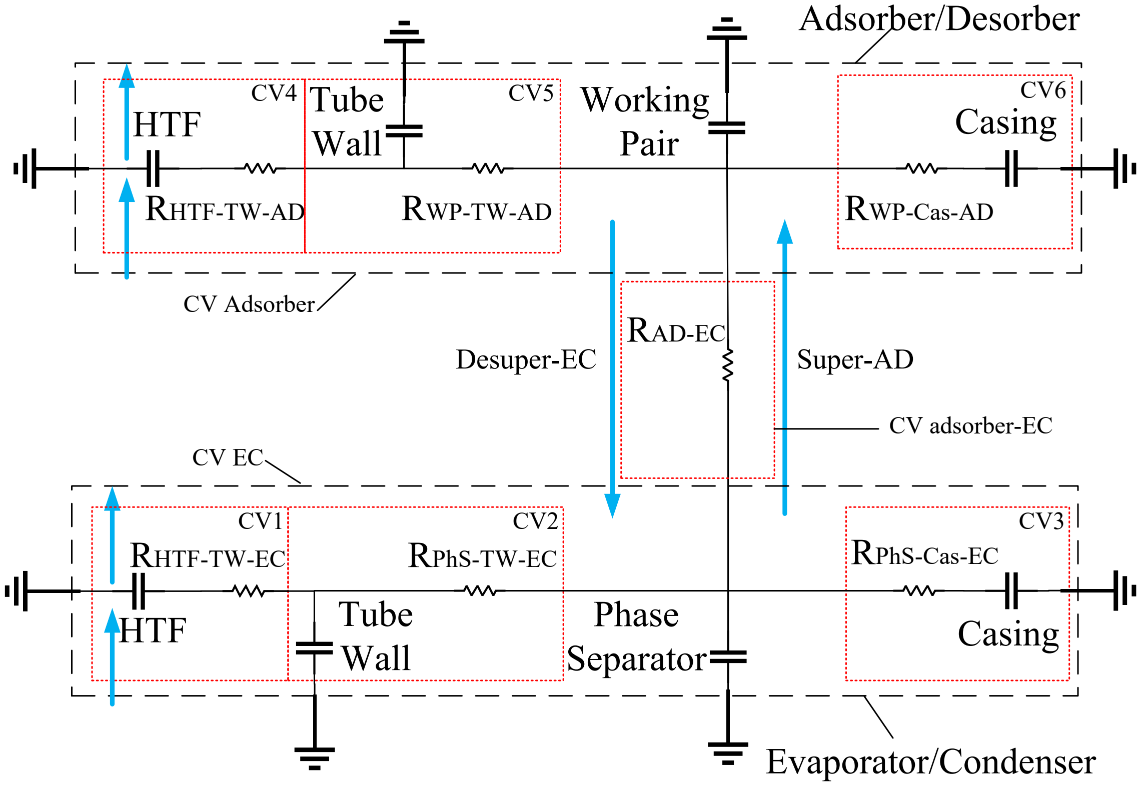

Figure 3.3.: Resistance-capacitance model with control volumes for a single adsorber cycle. Black rectangles indicate the boundaries of the adsorber/desorber and evaporator/condenser components and their control volumes. The red rectangles highlight the irreversibility source in the single adsorber cycle. Blue arrows on the left-hand side show the heat transfer fluid inside the pipes, with the central section illustrating the superheating and desuperheating states of the working fluid [118].

the thermal mass of the materials, and each resistance, as defined in Table 3.1, signifies a specific heat transfer mechanism that includes a combination of radiation, conduction, and convection heat transfer.

The phase separator represents the physical measures implemented in the evaporator design to prevent liquid droplets from entering the adsorber chamber. In the considered system, the evaporator is designed to ensure complete phase separation between liquid and vapor refrigerant by means of gravity separation and controlled vapor flow velocities, such that only saturated vapor is supplied to the adsorber. This assumption is consistent with experimental investigations on evaporator design for adsorption systems, where appropriately designed phase separators and vapor outlets effectively suppress liquid carryover under normal operating conditions. Detailed studies on evaporator geometry, flow behavior, and droplet separation efficiency are reported by Volmer et al. [130], who demonstrated stable evaporator operation with no liquid carryover into the adsorber chamber across a wide range of operating conditions. Based on these findings, the model assumes ideal phase separation and neglects liquid droplet transport into the adsorber chamber.

Symbol	Definition
HTF-TW-EC	Resistance between Heat Transfer Fluid and Tube Wall in the Evaporator/Condenser
PhS-TW-EC	Resistance between Phase Separator and Tube Wall in the Evaporator/Condenser
PhS-Cas-EC	Resistance between Phase Separator and Casing in the Evaporator/Condenser
AD-EC	Resistance between Adsorber/Desorber and Evaporator/Condenser
Desuper-EC	Desuperheat in the Evaporator/Condenser
Super-AD	Superheat in the Adsorber/Desorber
WP-Cas-AD	Resistance between Working Pair and Casing in the Adsorber/Desorber
WP-TW-AD	Resistance between Working Pair and Tube Wall in the Adsorber/Desorber
HTF-TW-AD	Resistance between Heat Transfer Fluid and Tube Wall in the Adsorber/Desorber

Table 3.1.: Different elements of R-C model for a single adsorber cycle.

Three sets of equations are presented below [118], applying the entropy balance for each control volume presented in Figure 3.3. Initially, to define the sign of the entropy transfer rate through heat transfer, we assume that an adsorption process occurs within the module. As a result, the top sign of the entropy transfer rate through heat transfer is associated with the evaporation and adsorption processes, while the bottom sign is linked to the condensation and desorption processes within the module. Additionally, the entropy generation rates for desuperheat and superheat are considered when there is mass flow rate from the adsorber to the evaporator/condenser and from the evaporator/condenser to the adsorber, respectively. In the Modelica implementation, the stream connector ensures that properties are passed in the correct direction based on the local pressure gradient, which automatically enforces the correct flow direction for these entropy calculations.

$$\begin{cases} \text{Evaporator/Condenser:} \\ CV_1 : (\dot{m} * s)_{\text{HTF,in}} - (\dot{m} * s)_{\text{HTF,out}} \mp \dfrac{\dot{Q}_{\text{HTF,Tube Wall}}}{T_{\text{Tube Wall}}} + \dot{S}_{HTF,\text{gen}} = \dfrac{dS_{\text{HTF}}}{dt} \\ CV_2 : \pm \dfrac{\dot{Q}_{\text{HTF,Tube Wall}}}{T_{\text{Tube Wall}}} \mp \dfrac{\dot{Q}_{\text{Tube Wall,Phase Separator}}}{T_{\text{Phase Separator}}} + \dot{S}_{\text{Tube Wall,gen}} = \dfrac{dS_{\text{Tube Wall}}}{dt} \\ CV_3 : \dfrac{\dot{Q}_{\text{Casing,Phase Separator}}}{T_{\text{Phase Separator}}} - \dfrac{\dot{Q}_{\text{Casing,environment}}}{T_{\text{Casing}}} + \dot{S}_{\text{Casing,gen}} = \dfrac{dS_{\text{Casing}}}{dt} \end{cases} \tag{3.4}$$

$$\begin{cases} \text{Between Evaporator/Condenser and Adsorber/Desorber:} \\ CV_{\text{Desuperheat}} : \dot{m}_{\text{AD}} \left(s_{\text{in,AD}} - s_{\text{out,EC}} - (\dfrac{h_{\text{in,AD}} - h_{\text{out,EC}}}{T_{\text{EC}}}) \right) + \dot{S}_{\text{Desuperheat,gen}} = 0 \\ CV_{\text{Superheat}} : \dot{m}_{\text{EC}} \left(s_{\text{in,EC}} - s_{\text{out,AD}} - (\dfrac{h_{\text{in,EC}} - h_{\text{out,AD}}}{T_{\text{AD}}}) \right) + \dot{S}_{\text{Superheat,gen}} = 0 \\ CV_{\text{AD-EC}} : \dfrac{\dot{Q}_{\text{AD,EC}}}{T_{\text{AD}}} - \dfrac{\dot{Q}_{\text{AD,EC}}}{T_{\text{EC}}} + \dot{S}_{\text{AD-EC,gen}} = 0 \end{cases} \tag{3.5}$$

$$\begin{cases} \text{Adsorber/Desorber:} \\ CV_4 : (\dot{m} * s)_{\text{HTF,in}} - (\dot{m} * s)_{\text{HTF,out}} \pm \dfrac{\dot{Q}_{\text{HTF,Tube Wall}}}{T_{\text{Tube Wall}}} + \dot{S}_{HTF,\text{gen}} = \dfrac{dS_{\text{HTF}}}{dt} \\ CV_5 : \mp \dfrac{\dot{Q}_{\text{HTF,Tube Wall}}}{T_{\text{Tube Wall}}} \pm \dfrac{\dot{Q}_{\text{Tube Wall,Working Pair}}}{T_{\text{Working Pair}}} + \dot{S}_{\text{Tube Wall,gen}} = \dfrac{dS_{\text{Tube Wall}}}{dt} \\ CV_6 : \dfrac{\dot{Q}_{\text{Casing,Working Pair}}}{T_{\text{Working Pair}}} - \dfrac{\dot{Q}_{\text{Casing,environment}}}{T_{\text{Casing}}} + \dot{S}_{\text{Casing,gen}} = \dfrac{dS_{\text{Casing}}}{dt} \end{cases} \tag{3.6}$$

To evaluate the relative irreversibility of each component, the entropy generation of the entire module must first be determined. The relative irreversibility is then calculated based on the time-integrated entropy generation rates. Accordingly, Equation 3.9 is applied to the dual-adsorber cycle GAHP configuration, while Equation 3.10 is used for the single-adsorber cycle GAHP. These formulations are derived from the general methodology presented in [131] and adapted here to the specific GAHP configurations considered in this study.

$$\begin{aligned} & CV_{EC} : \\ & (\dot{m} * s)_{\text{HTF,EC,in}} - (\dot{m} * s)_{\text{HTF,EC,out}} + (\dot{m} * s)_{\text{wf,EC,in}} - (\dot{m} * s)_{\text{wf,EC,out}} \\ & + \frac{\dot{Q}_{\text{AD,EC}}}{T_{\text{EC}}} - \frac{\dot{Q}_{\text{Casing,environment}}}{T_{\text{Casing}}} + \dot{S}_{\text{EC,gen}} \\ & = \frac{dS_{\text{HTF}}}{dt} + \frac{dS_{\text{Tube Wall}}}{dt} + \frac{dS_{\text{Phase Separator}}}{dt} + \frac{dS_{\text{Casing}}}{dt} \end{aligned} \tag{3.7}$$

$$
\begin{aligned}
&CV_{Adsorber/Desorber}: \\
&(\dot{m} * s)_{\text{HTF,AD,in}} - (\dot{m} * s)_{\text{HTF,AD,out}} + (\dot{m} * s)_{\text{wf,AD,in}} - (\dot{m} * s)_{\text{wf,AD,out}} \\
&-\frac{\dot{Q}_{\text{AD,EC}}}{T_{\text{EC}}} - \frac{\dot{Q}_{\text{Casing,environment}}}{T_{\text{Casing}}} + \frac{\dot{x}_{adsorpt,avg} * m_{\text{adsorbent}} * h_{\text{ads}}}{T_{adsorpt,avg}} + \dot{S}_{\text{AD,gen}} \\
&= \frac{dS_{\text{HTF}}}{dt} + \frac{dS_{\text{Tube Wall}}}{dt} + \frac{dS_{\text{adsorbent}}}{dt} + \frac{dS_{\text{Casing}}}{dt}
\end{aligned}
\tag{3.8}
$$

$$
RI_{\text{dual,i}} = \frac{\int_{t0}^{t_f} \dot{S}_{i,gen} dt}{\int_{t0}^{t_f} \dot{S}_{tot,gen} dt} = \frac{\int_{t0}^{t_f} \dot{S}_{i,gen} dt}{\int_{t0}^{t_f} (\dot{S}_{AD,gen} + \dot{S}_{EC,gen}) dt}
\tag{3.9}
$$

$$
RI_{\text{single,i}} = \frac{\int_{t0}^{t_f} \dot{S}_{i,gen} dt}{\int_{t0}^{t_f} \dot{S}_{tot,gen} dt} = \frac{\int_{t0}^{t_f} \dot{S}_{i,gen} dt}{\int_{t0}^{t_f} (\dot{S}_{storage,gen} + \dot{S}_{AD,gen} + \dot{S}_{EC,gen}) dt}
\tag{3.10}
$$

4. Performance Analysis of Different Gas Adsorption Heat Pump Configurations

This chapter presents the results of dynamic simulations conducted using the Modelica/Dymola environment[1]. These simulations are based on the component models and governing equations introduced in section 2.2, particularly those describing the adsorption subsystem. The analysis follows the organizational structure established in section 2.4.

The evaluation begins with the reference system described in subsection 2.3.1, consisting of a dual adsorber module coupled with a combi-storage tank. The following analysis focuses on a representative load point for space heating only (i.e., without domestic hot water production). This operating point is characterized by a part-load ratio of 36.33 %, with a heating system supply temperature of 34.3 °C and a return temperature of 30.8 °C. The procedure for determining representative operating points is described in section A.3.

The resulting cycle dynamics are illustrated in the Clausius–Clapeyron diagram in Figure 4.1. While the phases of adsorption, desorption, and transition are clearly identifiable, the plot reveals noticeable pressure deviations from the ideal cycle (subsection 1.1.1). These deviations arise from the dynamic coupling between the adsorber/desorber and the evaporator/condenser (E/C) in a single-adsorber module without internal vapor valves.

Furthermore, the diagram indicates that adsorption ends at approximately 30 °C, which is below the required heating supply temperature of 34.3 °C. This apparent inconsistency can be explained by the transient behavior of the system: the combi-storage tank still provides sufficient thermal energy to maintain the required supply temperature, while gradually cooling during the cycle. In addition, temperature differences across the adsorber heat exchanger contribute to this deviation. Therefore, the system is not in thermodynamic equilibrium at this stage, which must be considered when interpreting the results.

A detailed analysis of the cycle dynamics, including pressure fluctuations and non-equilibrium thermal behavior, is provided in 4.3.

[1] Version 2019 FD01

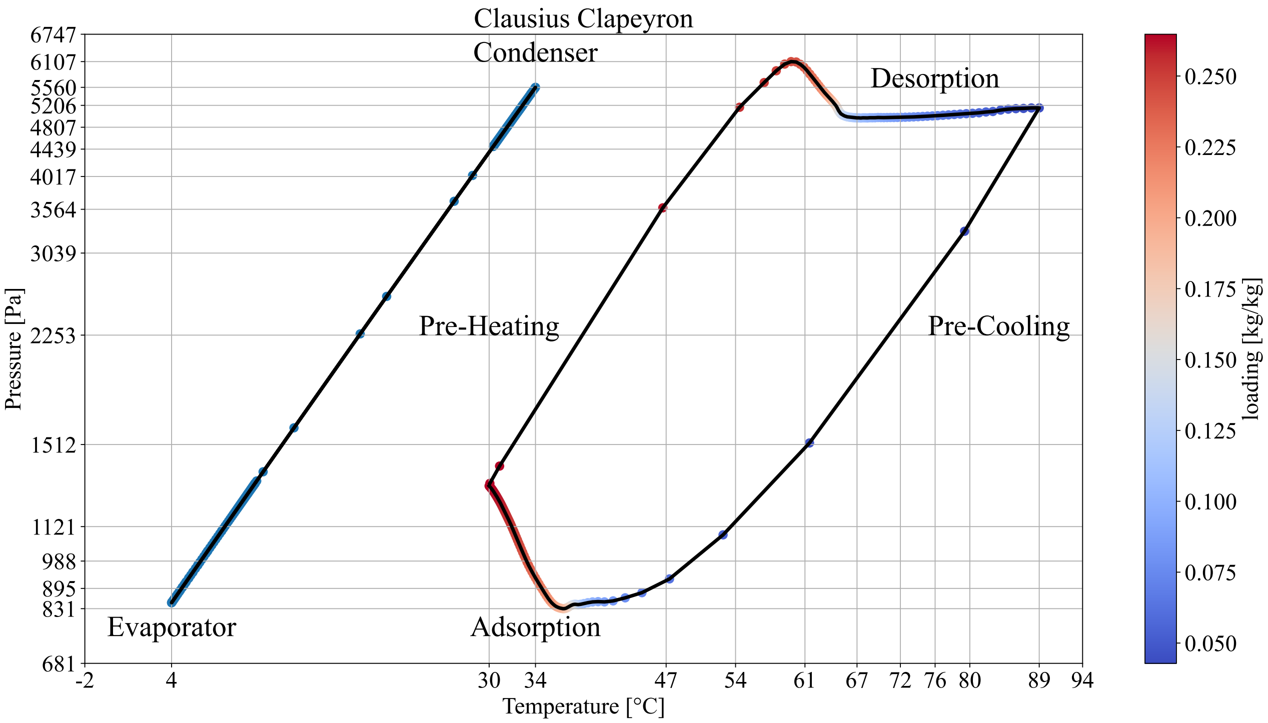

Figure 4.1.: Variation in pressure, temperature, and loading for a working pair in adsorber/desorber (right plot) and variation in pressure vs. temperature in evaporator/condenser on the working fluid side (left plot). This data corresponds to one cycle data extracted from annual simulation of reference system at 36.33 % part load with supply temperature 34.3 °C and return temperature 30.8 °C, with the maximum high-temperature source set at 90 °C.

4.1. Annual Simulation of Various Configurations Integrated with a dual adsorber cycle Gas Adsorption Heat Pump and Medium-sized Multi Family House Demands

4.1.1. Reference System

The heat production, heat consumption, and relevant storage-layer temperatures for both the space heating (SHC) and domestic hot water (DHW) circuits are shown for 29 October between 6:06 and 9:30. This period is extracted from an annual dynamic simulation and represents a characteristic operating window with a part-load ratio of 36.33 % (see section A.3).

While previous studies by Velte[17], Núñez[50], and Schwamberger [16] focus on stationary cycles at fixed operating points, the present work advances this approach by incorporating fully dynamic simulations that capture the impact of stochastic DHW demand and system-level control interactions.

To account for these effects, the system is simulated over a full year, ensuring that all relevant dynamic behaviors and control responses are captured. Representative operating points are then identified in two steps: first, by calculating characteristic load conditions for the given building, system, and climate (see section A.3), and second, by selecting corresponding time periods within the annual simulation that match these conditions. The selected time window shown here therefore reflects a realistic transient system state rather than an idealized stationary cycle, and is used to illustrate the system-level control behavior under representative operating conditions.

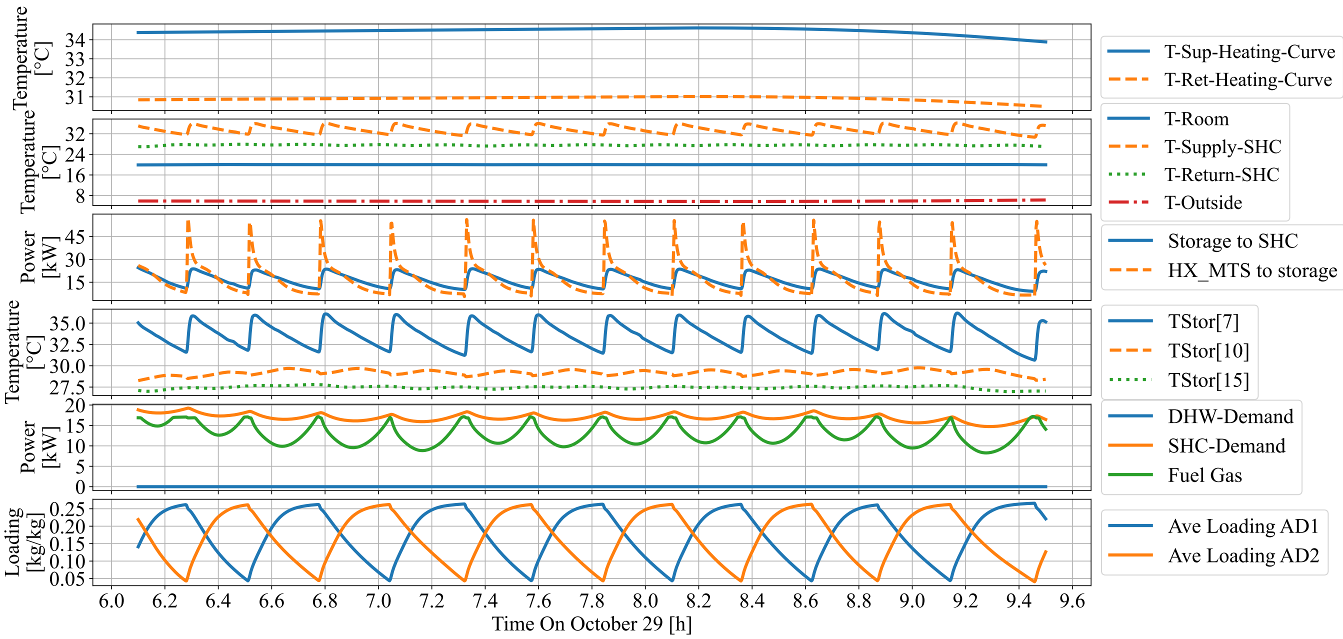

Figure 4.2.: Heat consumption side, heat production side, and relevant storage temperatures for the space heating circuit in the reference system between 6:06 and 9:30 on 29 October.

Following the reference system described in subsection 2.3.1, the SHC results are presented in Figure 4.2. The first subplot displays the heating-curve supply temperature—the setpoint for storage layer 7—alongside the corresponding return temperature. The radiator supply and return temperatures in the second subplot exhibit characteristic periodic oscillations.

The observed temperature peaks (approx. 36 °C) occur shortly after the burner operating at a controlled maximum of 17 kW (subplot 5), despite an absolute installed capacity of 50 kW. These peaks are initiated during the transition phase (heat recovery mode, section A.1), where the system facilitates a rapid thermal transition between the two adsorber modules. During this phase, internal sensible heat is exchanged—with the desorber module pre-cooling and the adsorber module pre-heating—at an instantaneous thermal power magnitude significantly greater than the average output during the standard sorption phase [69]. As the system exits heat recovery and enters the subsequent sorption cycle, the thermal power transferred to the storage reaches its maximum, temporarily exceeding the instantaneous demand of the heating curve.

Once the transition is complete and the burner output modulates downward, the system settles into an adsorption phase, during which both the adsorption heat and condenser heat are released and transferred to the storage. As adsorbent loading increases (subplot 6), the module's heat output gradually declines, causing the supply temperature to drift toward 31 °C until the subsequent switching event.

The resulting alternation between 36 °C and 31 °C yields a time-averaged supply temperature near the target of 34.3 °C. Consequently, the indoor temperature remains stable at 20 °C (subplot 2). The thermal inertia of the radiator network and the high water volume effectively damp these short-term power fluctuations, resulting in a nearly constant return temperature. Finally, the smoother profile of the thermal power extracted from storage layer 7 (subplot 3) compared to the input from the HX_MTS highlights the effective buffering capacity of the stratified storage.

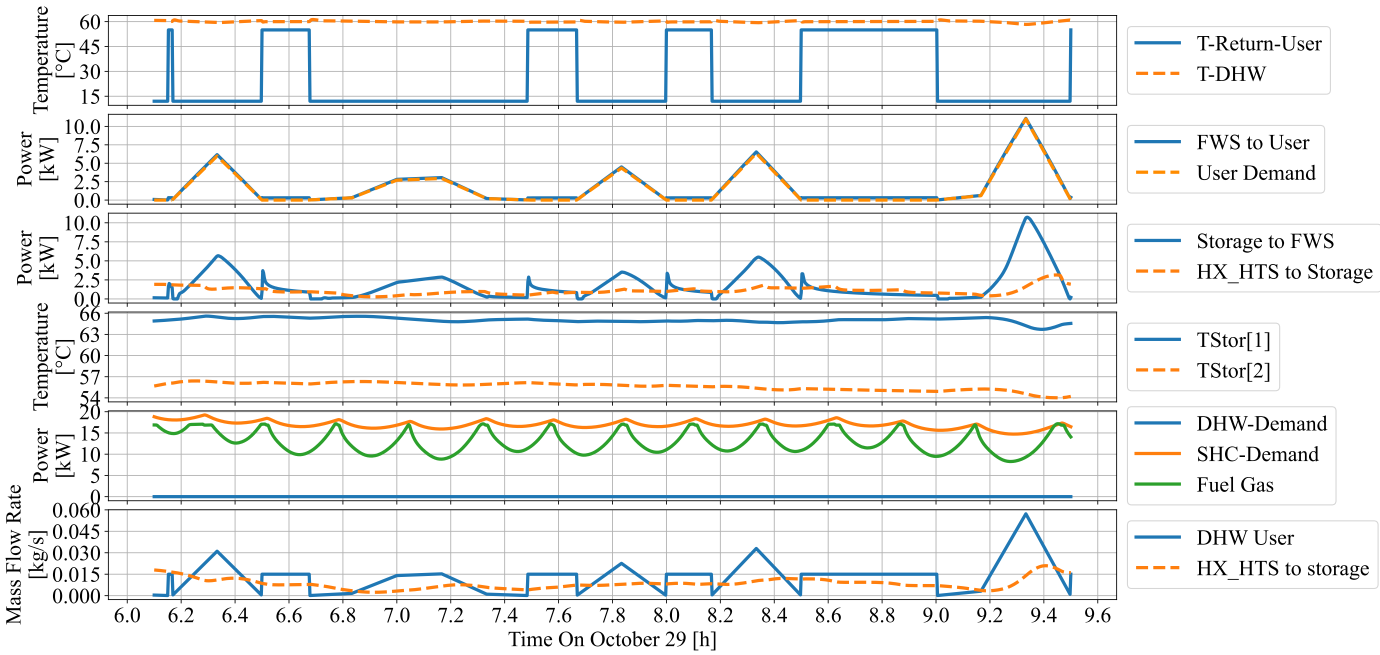

Figure 4.3.: Heat consumption side, heat production side, and relevant storage temperatures for the domestic hot water circuit in the reference system between 6:06 and 9:30 on 29 October.

To address the behavior of the DHW circuit as shown in Figure 4.3, it is essential to distinguish between the hydraulic and thermal response of the Fresh Water Station (FWS).

During periods without tapping, the circulation loop maintains a relatively high and nearly constant return temperature (the "rectangular" plateaus in subplot one) because the pump continuously recirculates water at a fixed setpoint to compensate for pipe heat losses and ensure immediate user comfort. In contrast, the mass flow rate in subplot six follows a triangular profile during tapping events, reflecting the stochastic nature of user demand as taps are opened and closed with varying intensity. The corresponding return temperature appears rectangular because it rapidly drops to a physical lower limit—governed by the cold mains water inlet and the high heat extraction rate within the FWS—and remains at this relatively constant level for the duration of the tap. This divergence in signal shapes effectively illustrates the decoupling between the transient hydraulic demand and the thermal limits of the heat exchanger, where the return temperature is constrained between the circulation setpoint and the cold-water cooling limit.

The user demand power and the thermal power transferred from the Fresh Water Station (FWS) to the user are shown in subplot two. The additional thermal power required during circulation becomes evident in subplot three.

During the considered period, the DHW demand remains zero (subplot five) because the temperature of the upper storage layer stays at approximately 65 °C, as shown in subplot four. Therefore, the required DHW temperature can be ensured without activating a priority mode (subsection 2.3.1). The mass flow rates on both sides of the HX_HTS are regulated by a PI controller (subplot six). This control strategy enables controlled heat transfer to the upper storage layers while the system simultaneously covers the space heating demand. In this way, the high-temperature heat source of the GAHP is effectively utilized without disturbing the overall system balance.

The Power Duration Curve (Figure 4.4) presents a graphical representation of the annual distribution of the supply power[2].

[2]To construct the annual power duration curve shown in Figure 4.4, no additional binning or hourly averaging was applied. The annual simulation was performed in Dymola using the DASSL solver, with output data written at a fixed time step of 10 minutes. The released fuel gas power was extracted directly from this time series. All simulated power values over the full year were then sorted in descending order to obtain the duration curve. After sorting, the horizontal axis was converted from the original simulation time (seconds) to hours to represent the cumulative operating duration over the year. Therefore, each point in the duration curve corresponds to a 10-minute simulation interval, and the curve reflects the full temporal resolution of the annual simulation rather than hourly averaged values.

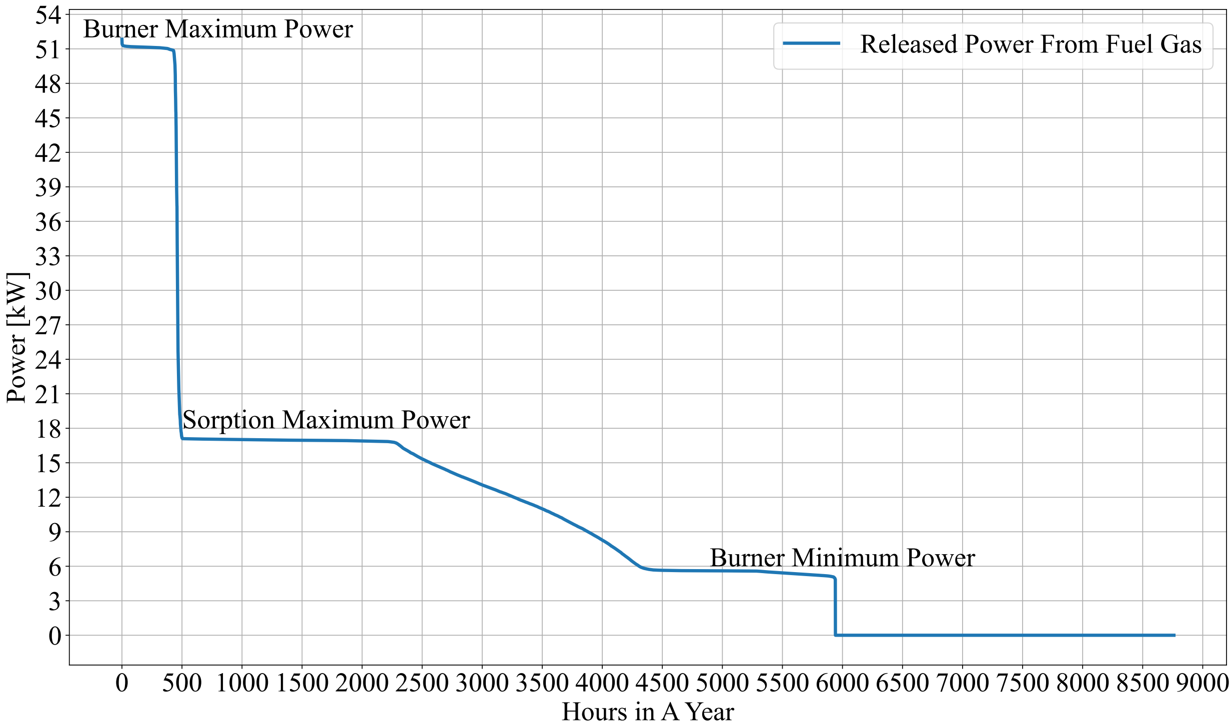

Figure 4.4.: Annual power duration curves in the reference system.

The burner of the dual adsorber cycle Gas Adsorption Heat pump (GAHP) operates in two distinct modes Figure 4.4. The first mode is the direct burner mode, with a maximum burner power output of 50 kW ($\approx 500h/year$). This mode is activated to supply either the priority demand of domestic hot water or space heating demands when the dual adsorber cycle GAHP cannot meet the space heating requirements. In this scenario, the burner adjusts its output power according to the demand, utilizing a control strategy until the power demand in the water heating circuit is satisfied or the dual adsorber cycle GAHP can supply the space heating demands.

The second mode is the sorption mode, with a maximum power output of 17 kW. Depending on the demand power on the consumption side, the burner adjusts the power delivered to the adsorber/desorber to preheat the domestic hot water or to meet space heating demands. Additionally, the burner deactivates when the power demand falls below 5 kW.

It is noteworthy that the output power from the Medium-Temperature Sink Heat Exchanger to the Combi-Storage varies based on the operational modes. In direct burner mode, as detailed in section A.1 in Figure A.3 and Figure A.6, the output power originates from the first burner heat exchanger. However, in sorption mode, as shown in Figure A.1 and Figure A.4, the output power comes from two sources: geothermal power and the combined power from the adsorber and condenser units. Subsequently, the Medium-

Temperature Sink Heat Exchanger output power is combined with the exhaust gas power of second burner heat exchanger and then goes to the combi-storage.

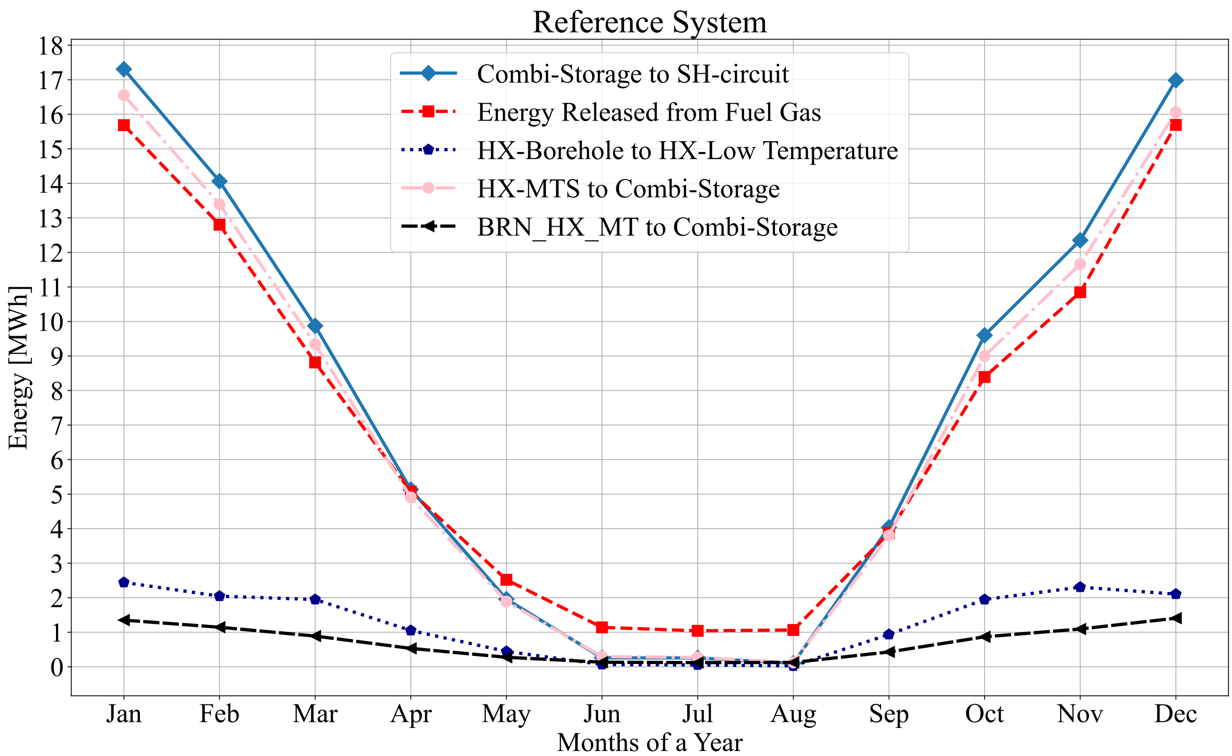

Figure 4.5.: Energy production and consumption of various components over one year in the reference system.

Figure 4.5 presents the energy released from fuel gas and the energy delivered to various components each month over one year. It shows that during the heating season, from January to April and from September to December, the energy consumption in the space heating circuit is higher than the energy delivered from the GAHP through the Medium-Temperature Sink Heat Exchanger to the Combi-Storage. However, by incorporating the energy delivered from the second burner heat exchanger (BRN-HX-MT in Figure 2.7 in subsection 2.3.1), the energy demand in the space heating circuit is met. Additionally, from April to September, the energy released by fuel gas consumption exceeds the space heating energy demands. The surplus gas consumption is utilized for domestic hot water demands, as depicted in Figure 4.6.

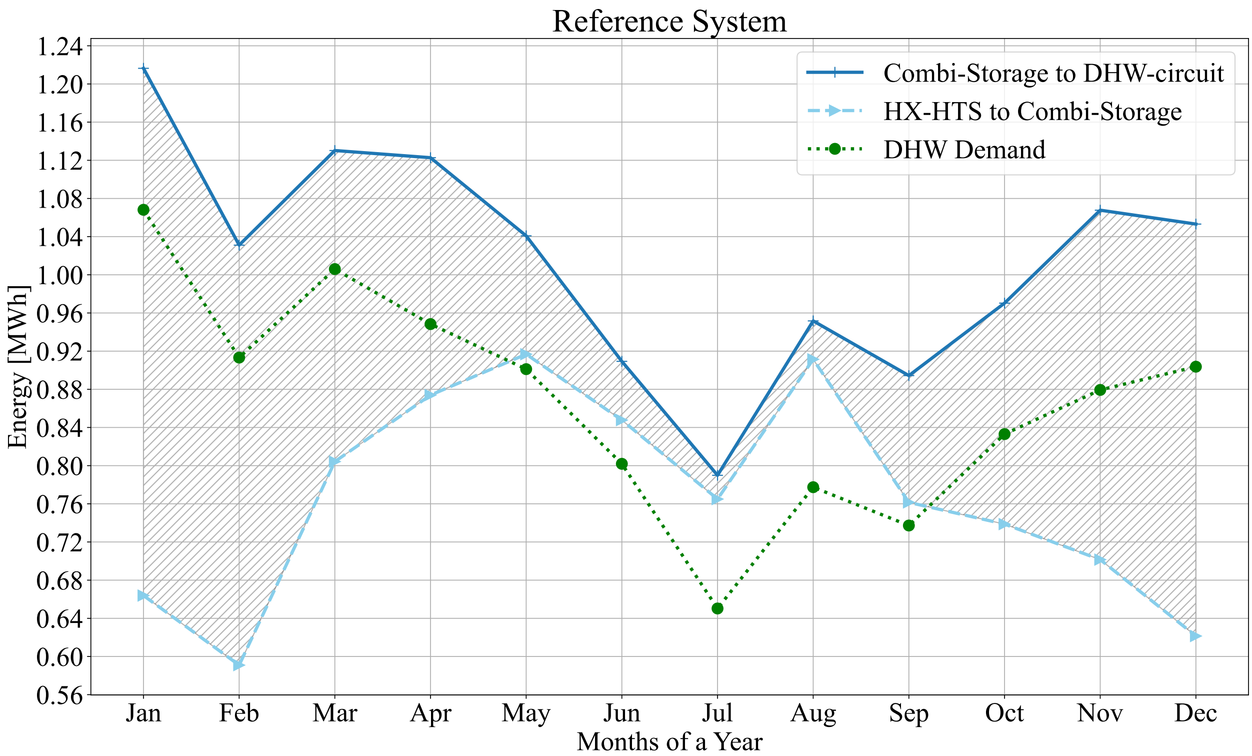

Figure 4.6.: Preheating domestic hot water over one year in the reference system. The shaded area represents the energy gap, filled by the heat pump, between the energy supplied to the domestic hot water (DHW) circuit from storage and the energy delivered to storage by the burner.

Figure 4.6 illustrates the energy delivered from fuel gas consumption to the combi-storage through the High-Temperature Source heat exchanger (sky blue), the energy delivered from combi-storage to the domestic hot water circuit (dark blue), and the domestic hot water energy demands (green). The hatched area indicates that, over the course of the year, energy consumption within the domestic hot water circuit surpasses the energy delivered from the burner to the combi-storage through the High-Temperature Source heat exchanger. This deficit is compensated by the heat contribution of the Gas Adsorption Heat Pump (GAHP) and the integrated condensing effect at the Medium-Temperature level. This underscores a primary research objective: to preheat domestic hot water using the dual adsorber cycle GAHP, thereby reducing the high-temperature thermal load required from the burner. Furthermore, the difference between the energy delivered from the combi-storage to the domestic hot water circuit (dark blue) and the actual domestic hot water demand (green) reflects the energy losses during circulation within the domestic hot water circuit.

The monthly fluctuation of the delivered energy is solely caused by the DHW demand time series used in the simulation. Seasonal variations in circulation losses are not considered in the model.

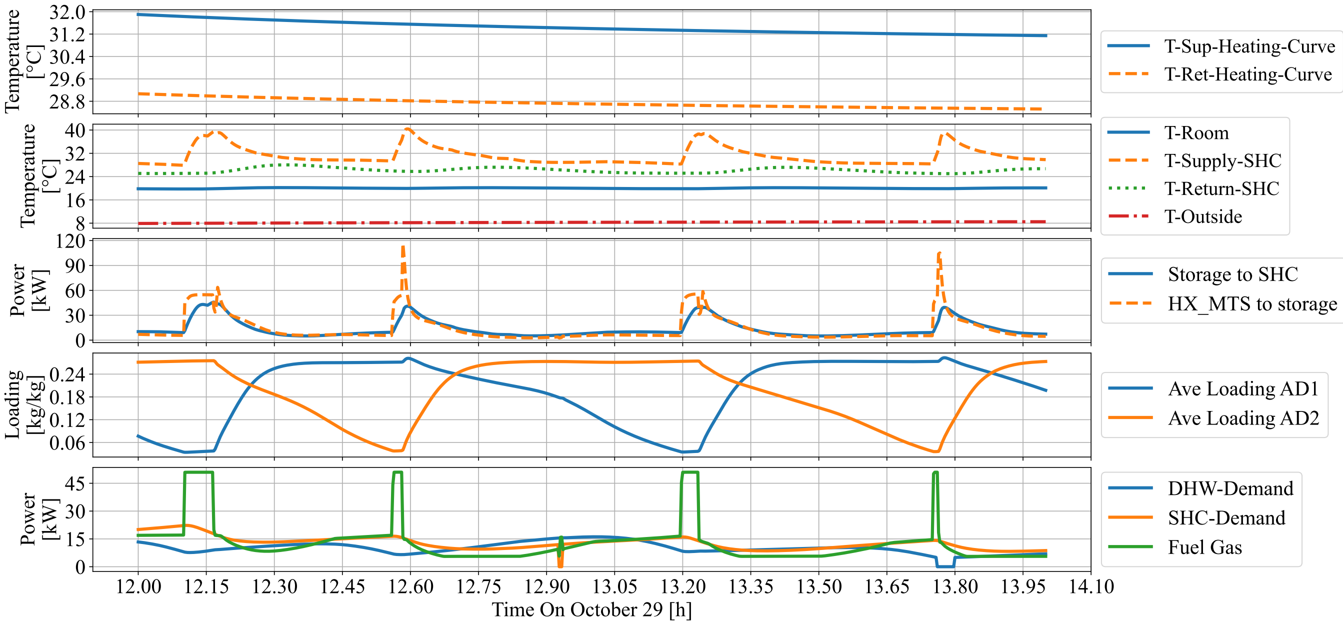

Figure 4.7.: Heat consumption side, heat production side for the space heating circuit in the reference system between 12:00 and 14:00 on 29 October.

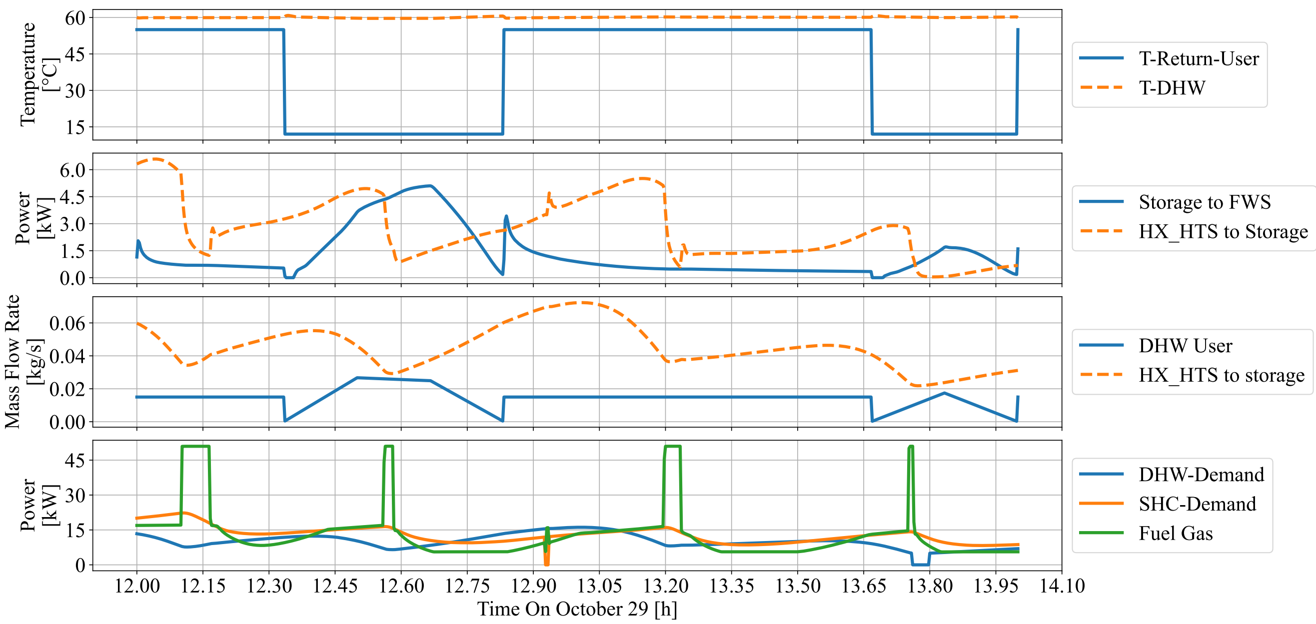

Figure 4.8.: Heat consumption side, heat production side for the domestic hot water circuit in the reference system between 12:00 and 14:00 on 29 October.

The time window between 12:00 and 14:00 on 29 October is selected to explicitly illustrate the switching behavior of the system between space heating (SHC) operation in Figure 4.7 and domestic hot water (DHW) in Figure 4.8.

In Figure 4.7, the first subplot shows the SHC supply and return temperatures defined by the heating curve. The second subplot presents the radiator supply and return temperatures, indicating stable room temperature control at 20 °C when the outdoor temperature is 8 °C. This indicates that the system maintains thermal comfort even during source switching events.

According to the system-level control logic, the fuel gas power shown in subplot 5 modulates between 5 kW and 17 kW during sorption periods. During sorption modes, the continuous variation in adsorber loading (subplot 4) reflects the adsorption–desorption cycle, where the total heat output consists of both adsorption and condenser heat— enhanced by the integrated condensing boiler effect— delivered to storage layer 7 via the HX_MTS. During specific intervals (e.g., between 12:22 and 12:34), the adsorber loading remains constant. In this period, no adsorption or desorption occurs, and the thermal power transferred to the storage consists only of sensible heat recovery. Consequently, no thermal surge occurs at the end of these intervals. In contrast, the highest thermal power peaks (subplot 3) are observed immediately following the heat recovery modes when a new sorption cycle begins. Additionally, In direct burner modes, the system utilizes the installed maximum burner capacity of 50 kW.

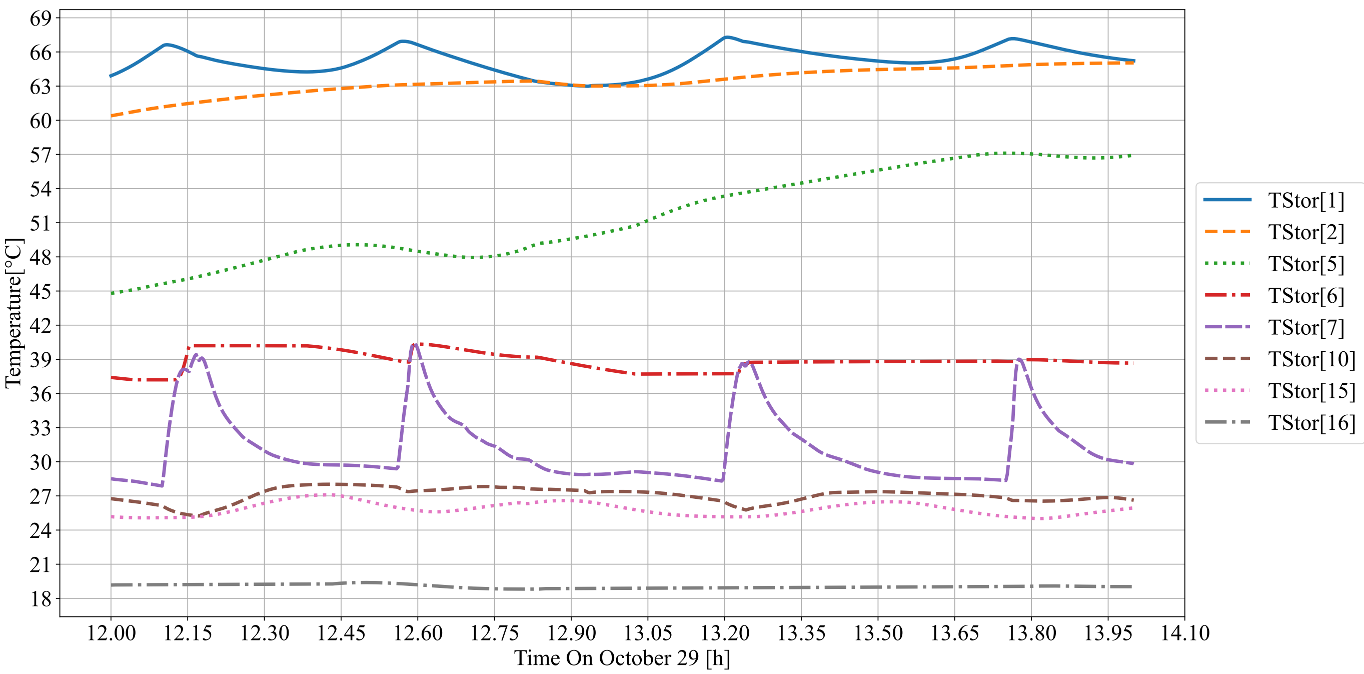

Figure 4.9.: Storage layer temperatures in the reference system between 12:00 and 14:00 on 29 October.

The switching to DHW priority becomes evident when the temperature of the upper storage layer (TStor[1] in Figure 4.9) falls below the safety threshold of 63 °C at approximately 12:56. At this moment, the control strategy interrupts the SHC demand and prioritizes DHW heating. The burner output increases to approximately 16 kW (subplot 5 in Figure 4.8), while the SHC power is reduced to 0 kW. Simultaneously, the mass flow rates on both sides of HX_HTS increase, enhancing heat transfer to the upper storage layers.

It should be noted, however, that a nonzero DHW demand can also occur at higher storage temperatures (e.g., around 12:00), even when TStor[1] is above 63 °C. In this case, the demand is driven by tapping events in the fresh water station rather than by the DHW priority control. As long as the storage temperature remains above the threshold, the system continues parallel operation without interrupting the SHC, and the DHW demand is covered directly from the storage without activating the priority mode.

A key effect during this period is the temperature rise of storage layer 5, which supplies HX_HTS. Its temperature increases from approximately 45 °C to 57 °C. This intermediate temperature increase reduces the required temperature lift to reach the DHW setpoint. As a result, TStor[2] gradually increases from about 60 °C to 65 °C over the considered time window.

This sequence demonstrates the DHW preheating concept: by utilizing the GAHP and condensing effect to elevate intermediate storage temperatures, the system reduces burner stress and enables efficient DHW priority operation while maintaining overall stratification stability.

Figure 4.10 presents the domestic hot water temperatures recorded hourly throughout each day of the year. This carpet plot illustrates that the system-level control strategy effectively maintains the DHW temperature within the comfort range of 58.5 °C to 61.5 °C. According to both the VDI 6023 [132] standard and DIN EN 806-2 [133], the acceptable temperature for domestic hot water to prevent Legionella bacteria is 60 °C for storage and 55 °C for distribution. However, Figure 4.11 which illustrates the frequency distribution of DHW in 1 °C temperature ranges, shows that the circulation temperature in the DHW circuit remains between 53 °C and 54 °C for 20 minutes, and between 54°C and 55 °C for another 20 minutes. These short-term deviations from the standards are not critical, as they are accumulated over different high-demand days throughout the year and therefore do not represent continuous operation at reduced temperatures. As a result, they are not clearly visible in Figure 4.10. Furthermore, a 10-year surveillance study conducted in a district general hospital shows that Legionella-related disease can be effectively controlled by maintaining circulating hot water temperatures above 55 °C together with continuous clinical monitoring [134]. While such systematic surveillance is not feasible in typical household applications, the study provides supportive evidence that strict temperature control alone can significantly reduce health risks, even without complete eradication of Legionella spp. from the hot water system [134]. This is consistent with guidance from the DVGW[3], which reports that Legionella growth slows significantly above 45 °C, is effectively inhibited at 50 °C, and rapid bacterial inactivation occurs at temperatures above 60 °C [135].

[3]Deutscher Verein des Gas- und Wasserfaches

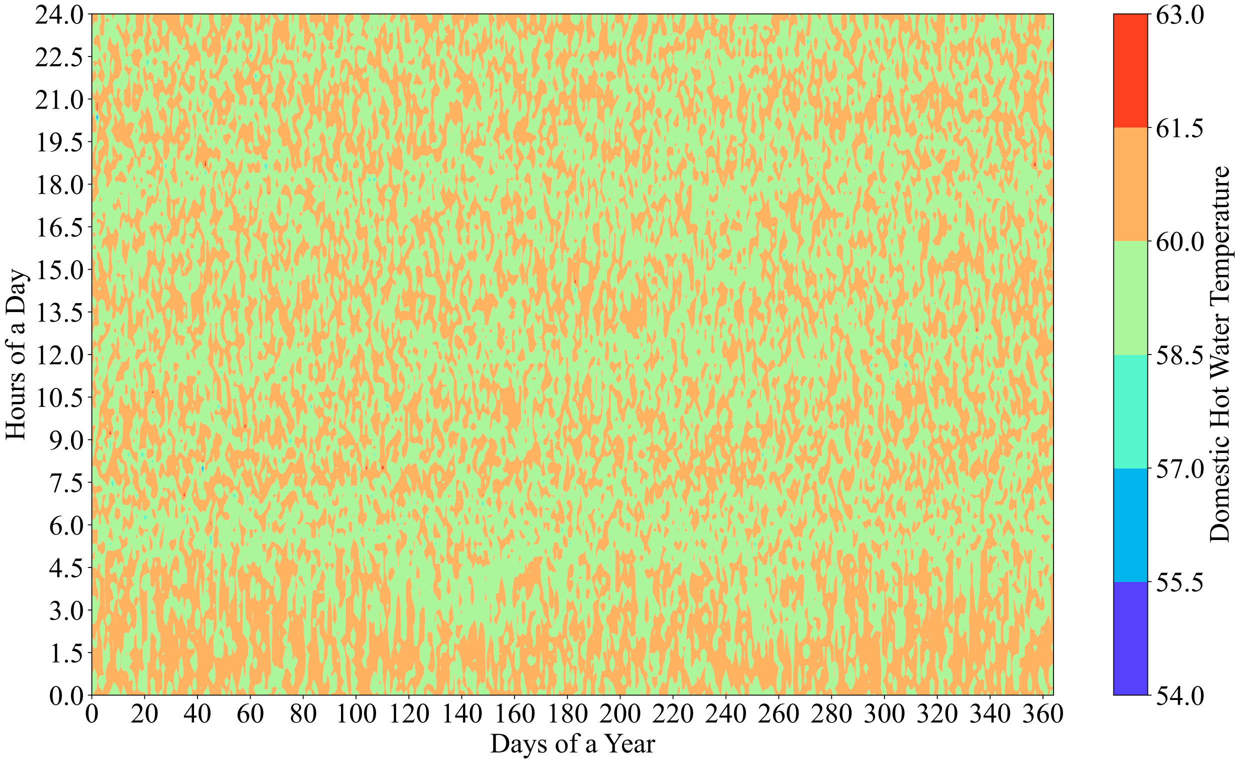

Figure 4.10.: Domestic hot water temperature recorded hourly over one year in the the reference system.

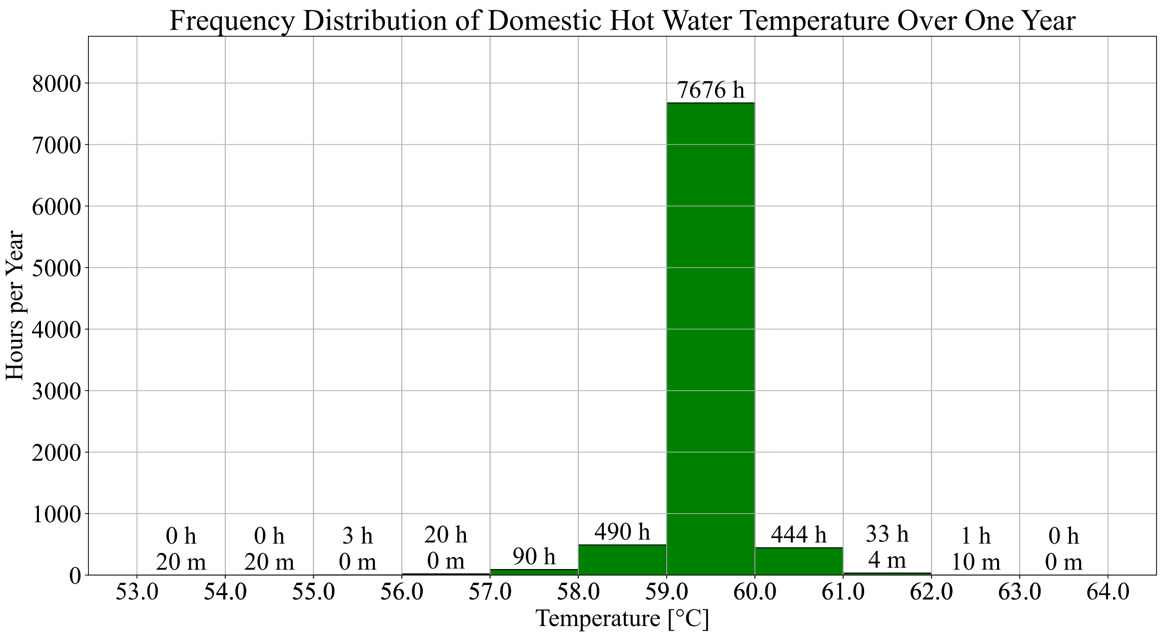

Figure 4.11.: Frequency distribution of domestic hot water temperature in 1 °C temperature bins in the reference system. The hot water supply temperature remains between 58 °C and 61 °C for a total duration of 8610 h (h: hour and m: minute).

Night setback, a control strategy employed to lower indoor temperatures at night to conserve energy, functions by reducing heat losses through a decreased temperature gradient between the interior and exterior of a building. This method allows for energy and cost savings without compromising comfort, particularly in single-family houses [136, 137]. In Swedish district heating systems, implementing night setback typically results in a temperature drop in the evening followed by a morning peak as the system reheats the building to the desired temperature. However, this strategy does not reduce overall heat consumption in modern, well-insulated buildings [138]. Since the renovated medium-sized multifamily house in our simulated model is uniformly heated by a centralized system, applying night setback could cause uneven heating, with some units experiencing excessive cold or heat. Consequently, night setback was excluded from our simulation model.

Figure 4.12 illustrates the hourly deviations of indoor temperature from the comfort range in a medium-sized multi-family house during the coldest days of the year. The data indicates that deviations below the target temperature occur over an 8-month period and typically last no longer than two hours. Thus, the maintained comfort temperature range is considered satisfactory. Figure 4.13 presents the duration within each temperature bin, highlighting the minimum temperature range observed in the annual simulation.

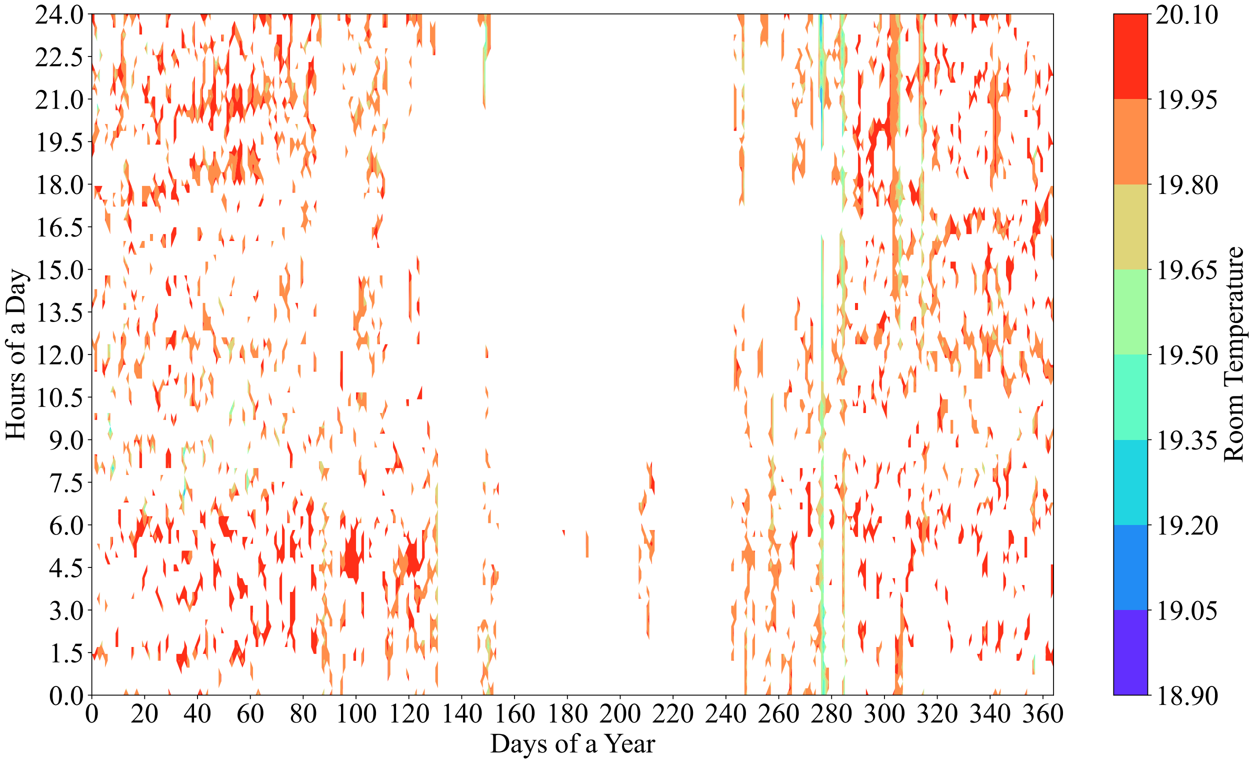

Figure 4.12.: Hourly room temperature over one year in the reference system. White areas indicate temperatures above 20.1 °C.

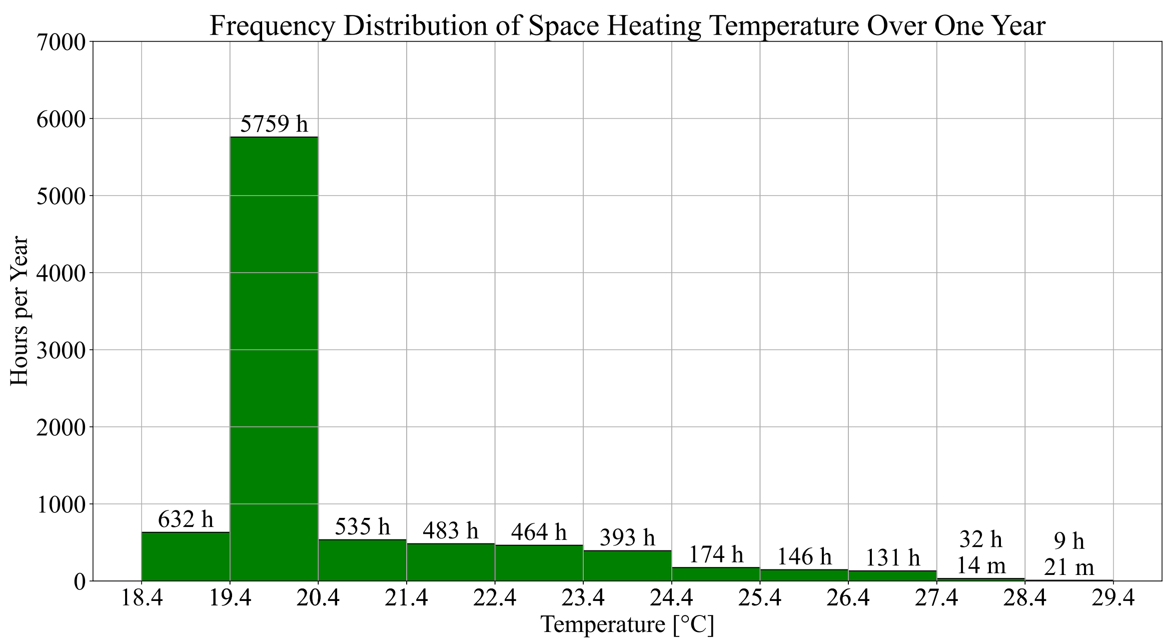

Figure 4.13.: Frequency distribution of room temperature in 1 °C temperature bins in the reference system.

The annual temperature distribution across each layer of the Combi-Storage, which has a volume of 1.2 m^3 as described in subsubsection 2.1.3.1, is detailed in Figure 4.14 for the default 16-layer Reference System. In the system setup, where power is supplied from the High-Temperature Source Heat Exchanger to the Combi-Storage, water is drawn from layer five, and the returning hot water is introduced into the top layer, as indicated by the arrow and annotation in Figure 4.14. For space heating, power is supplied via the Medium-Temperature Sink Heat Exchanger; water is extracted from layer 10 and the heated water is directed into layer 7. For meeting space heating demand within the Space Heating Circuit, water is withdrawn from layer 7, and the return cold water from the Space Heating Circuit is reintroduced into layer 15. Additionally, for the Water Heating Circuit, water is extracted from layer 1 and reintroduced into the Combi-Storage through an ideal inserter to meet demand power.

The discretization into 16 layers is a modeling choice intended to adequately represent the thermal stratification within the combi-storage and to reduce numerical fluctuations in the calculated layer temperatures. The total storage volume and the relative volume fractions of the individual layers, however, correspond to the physical design of the modeled system and can be related to established sizing rules for combi-storages.

Furthermore, the allocation of five layers for domestic hot water (DHW) preparation and four layers for space heating, with one buffer layer (layer 6) separating the space heating from DHW preparation, enhances the preheating efficiency of the DHW preparation using the sorption module of the Gas Adsorption Heat Pump (GAHP).

As DHW preheating is one of the objectives of this thesis, it is essential to examine the impact of eliminating the buffer layer (layer 6) on DHW preheating. Figure 4.15 illustrates the temperature layers and hydraulic connection of the components.

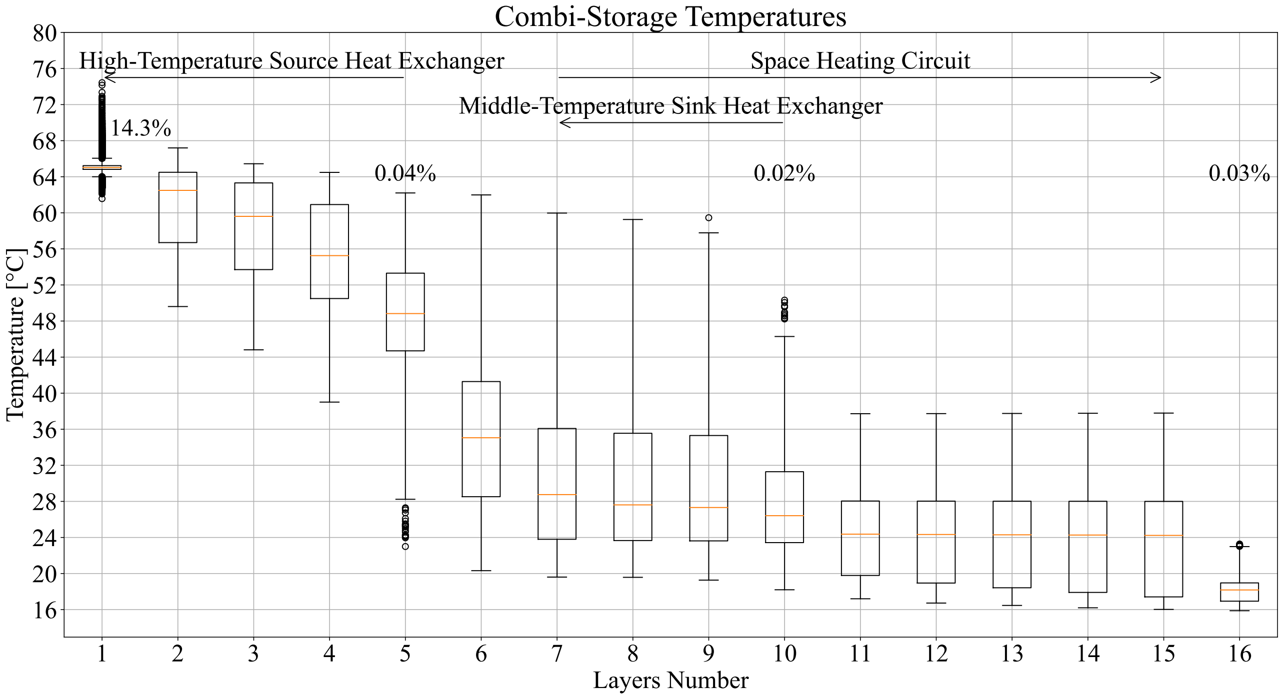

Figure 4.14.: Annual temperatures of storage layers in the reference system. Box plots are based on quartile statistics, where the box represents the interquartile range (IQR = $Q_3 - Q1$) and the line indicates the median. Whiskers are defined as $Q1 - 2 \times$ IQR and $Q3 + 2 \times$ IQR; values outside this range are considered outliers, and their percentage represents the share of transient temperature deviations relative to the total dataset for each layer.

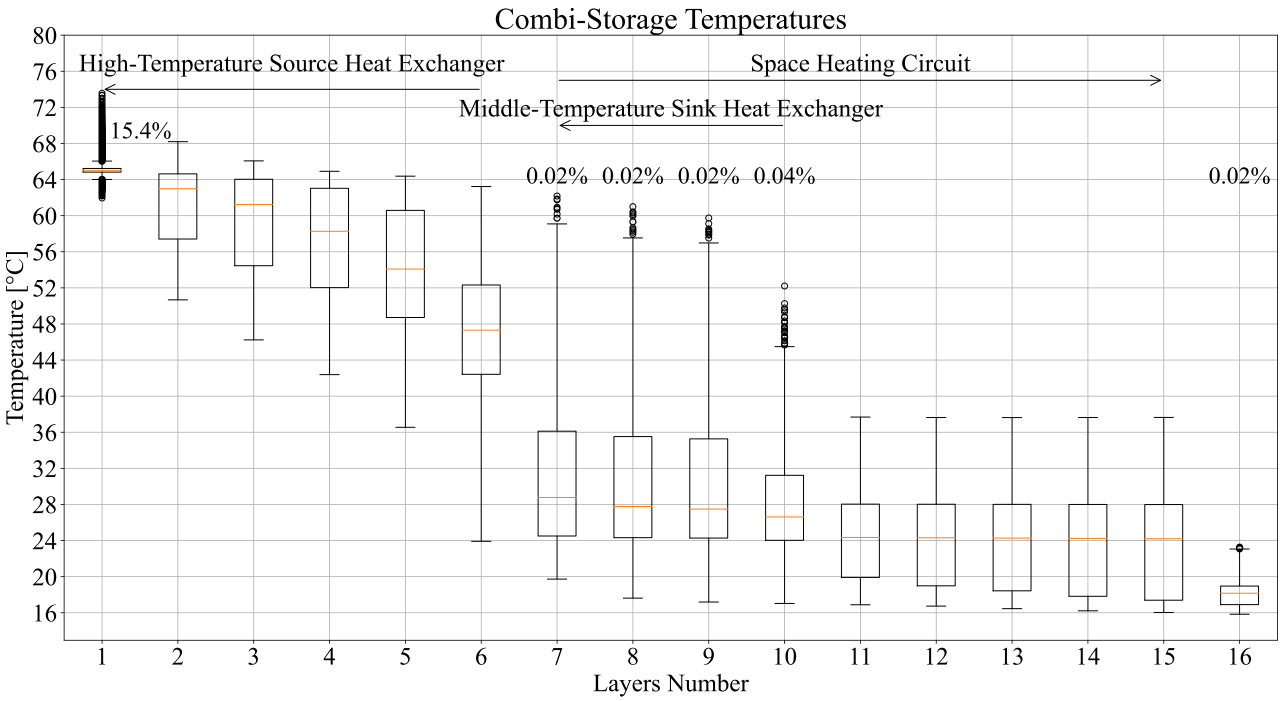

Figure 4.15.: Temperature layers in the reference system without a buffer layer between domestic hot water and space heating preparation. Outliers percentage represents the share of transient temperature deviations relative to the total dataset for each layer.

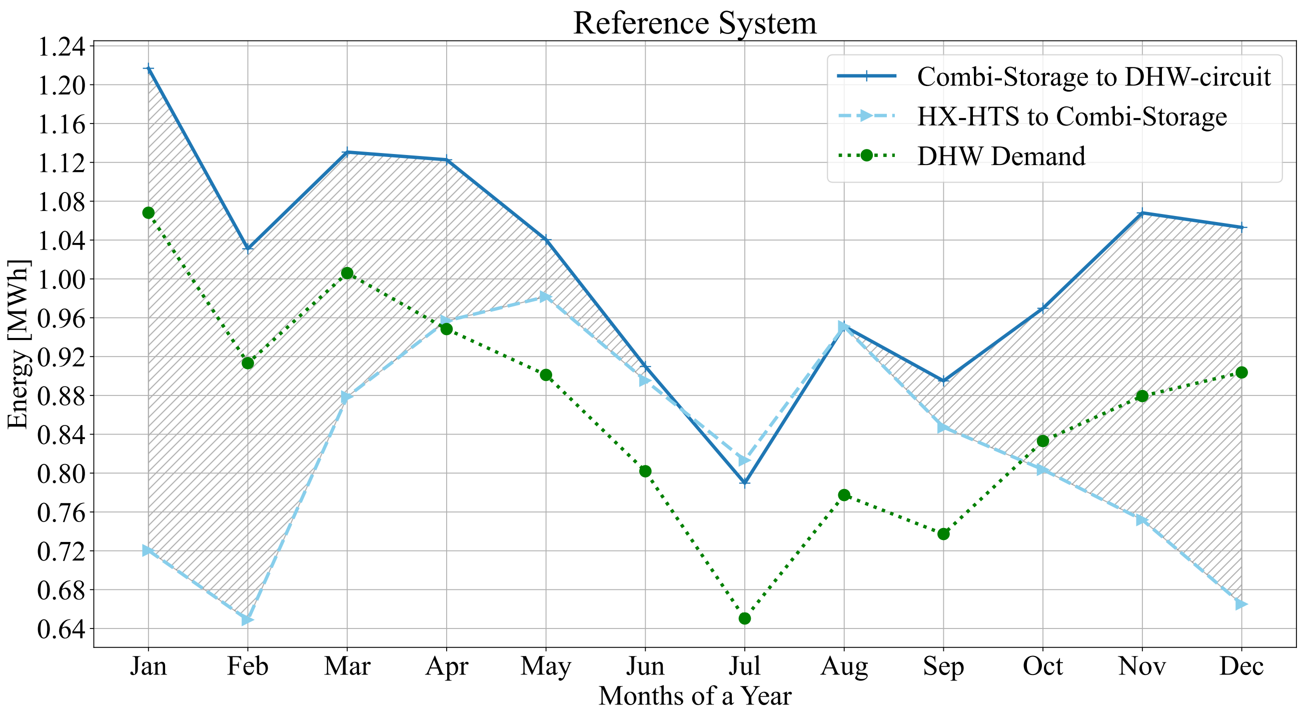

Figure 4.16.: Preheating domestic hot water without buffer layer. The shaded area represents the energy gap, filled by the heat pump, between the energy supplied to the domestic hot water (DHW) circuit from storage and the energy delivered to storage by the burner. The removal of the buffer layer negatively impacts DHW preheating with the heat pump from mid-June to August.

A comparison of Figure 4.16 with Figure 4.6 demonstrates the negative impact on DHW preheating due to the removal of the buffer layer. From mid-June to August, the DHW demand is supplied by the burner.

According to subplot 5 in Figure 4.17, the fuel gas power follows the SHC control strategy. At the end of each adsorption/desorption cycle, the system can enter direct burner mode depending on the current demand and control state, which increases the thermal power supplied to the storage via HX_MTS (subplot 3) and temporarily raises the radiator supply temperature (subplot 2). At the transition through the heat recovery mode, a distinct power spike occurs due to the internal heat exchange between the adsorber modules. After this peak, the system enters a new sorption cycle (subplot 4). The resulting fluctuations in fuel gas power and thermal output reflect the dynamic system-level control.

The decisive effect on storage layer 1, however, is governed by the DHW priority control. As shown in subplot 4 of Figure 4.18, the control strategy ensures that the temperature of layer 1 does not fall below 63 °C. When this threshold is approached, the SHC demand is set to 0 kW and the burner supplies heat directly to the upper storage layer. This results in frequent intra-cycle switching between SHC operation and DHW priority mode.

This behavior indicates that the current control strategy strongly prioritizes maintaining the DHW temperature but leads to repeated switching and increased system dynamics. A possible improvement would be to adapt the control strategy by introducing a wider hysteresis band, predictive control based on anticipated DHW demand, or a smoother modulation of burner power. Such modifications could reduce intra-cycle switching and lead to more stable system operation.

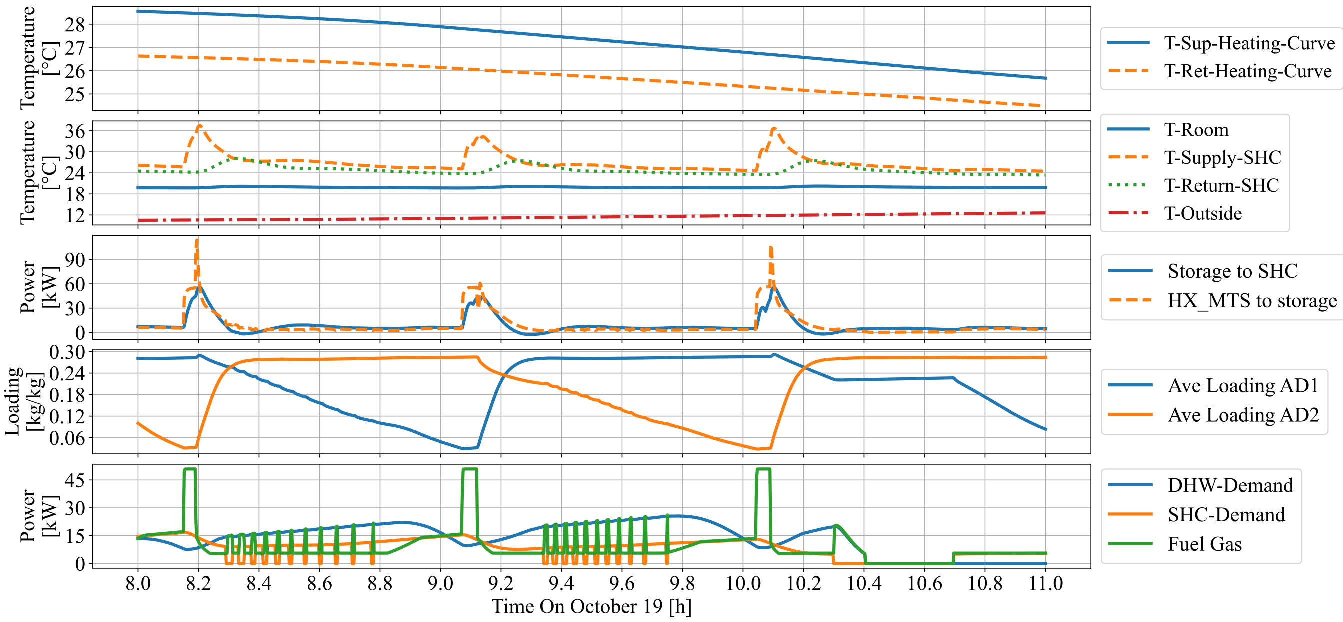

Figure 4.17.: Heat consumption and heat production of the space heating circuit, together with the average adsorber loading in the reference system, between 08:00 and 11:00 on 19 October.

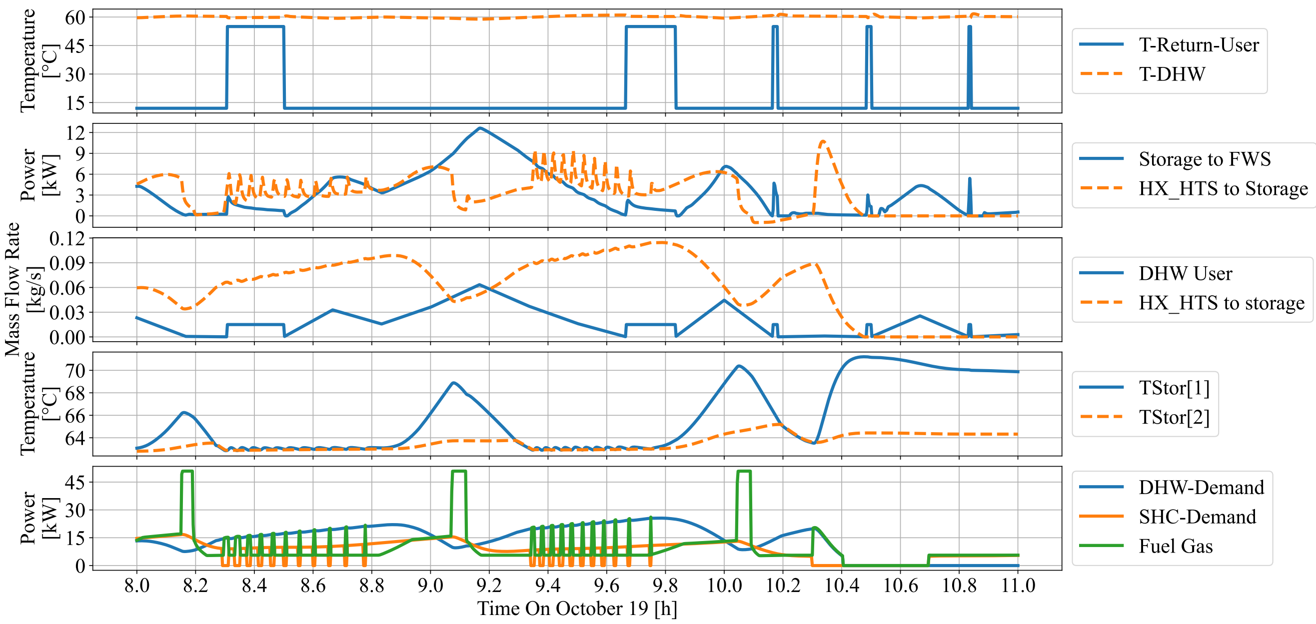

Figure 4.18.: Heat consumption side, heat production side, and relevant storage temperatures for the domestic hot water circuit in the reference system between 8:00 and 11:00 on 19 October.

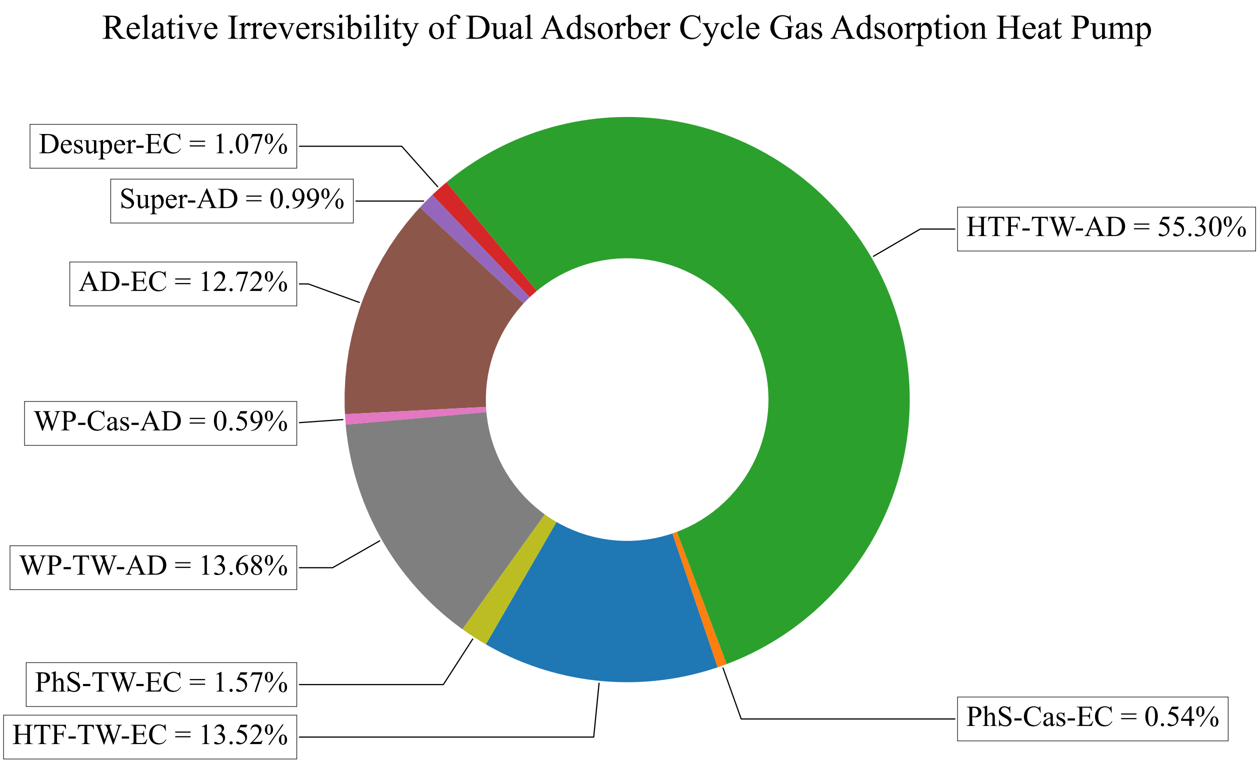

Figure 4.19.: Relative irreversibility of dual adsorber cycle GAHP in the reference system based on annual simulation results.

To identify the source of irreversibility in the dual adsorber cycle GAHP, which causes the highest impact on the thermal stratification of the storage, the relative irreversibility of various elements within the dual adsorber cycle GAHP was assessed. Figure 4.19 reveals that the highest portion of relative irreversibility occurs between the Heat Transfer Fluid and the Tube Wall of the adsorber/desorber (HTF-TW-AD). This finding aligns with Meunier's results, which defined this phenomenon as external thermal coupling between isothermal heat reservoirs and temperature-varying within the adsorber/desorber [127]. Following this, the heat transfer between Working Pair and Tube Wall in the adsorber/desorber(WP-TW-AD) exhibit the second highest portion of irreversibility within dual adsorber cycle GAHP. Additionally, the heat and mass transfer between Heat Transfer Fluid and Tube Wall in the evaporator/condenser (HTF-TW-EC), as well as the heat transfer between the adsorber/desorber and evaporator/condenser (AD-EC) ranks as the third and fourth contributors to high irreversibility within the dual adsorber cycle-GAHP system.

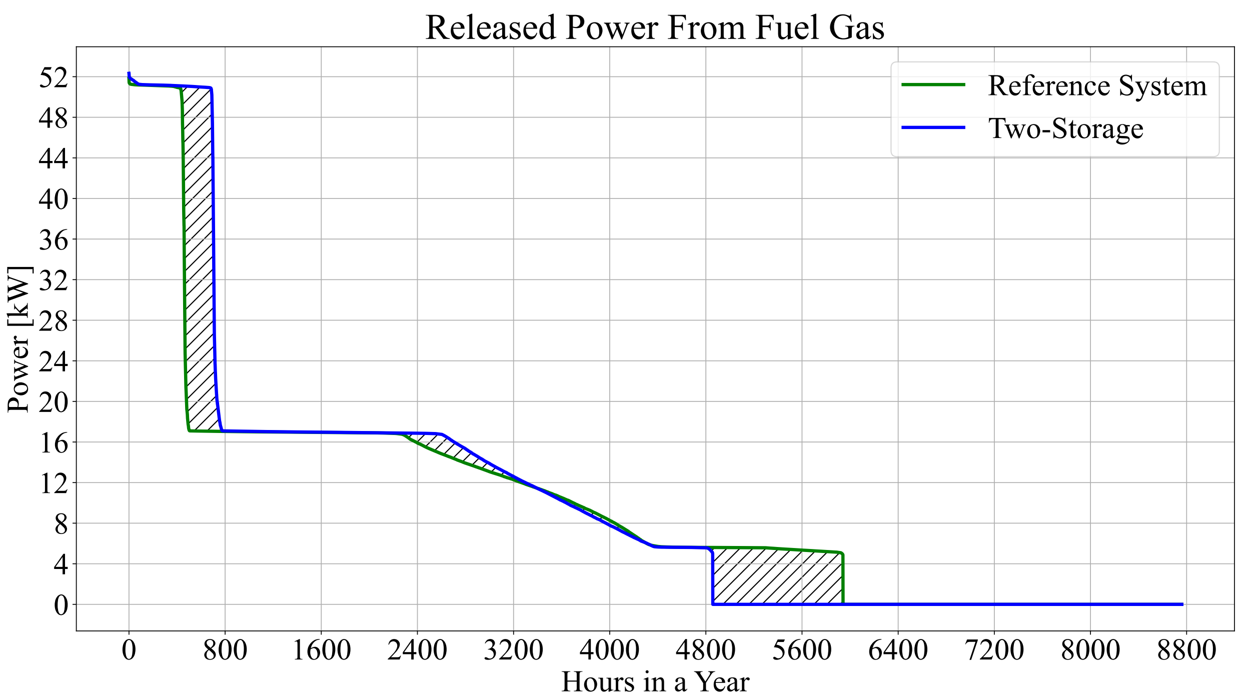

Figure 4.20.: Annual power duration curves for reference system (green line) and two-storage system, highlighting a shift towards sorptive heating at lower power levels in the reference system.

4.1.2. Two-Storage System

The hydraulic scheme of the Two-Storage system is illustrated in Figure 2.15 in subsection 2.3.2. The domestic hot water (DHW) demand is supplied by a 700-liter storage unit, as detailed in subsubsection 2.1.3.1, while the space heating demand is met by a 500-liter storage unit, as outlined in subsubsection 2.1.3.1. As observed in Figure 4.20, the heat generating system in the Two-Storage configuration operates more frequently in direct burner mode compared to the reference system.

Frequent burner mode operation in the Two-Storage system, due to the use of separate storage for DHW preparation and space heating demands, is evident in the monthly energy released from fuel gas, as shown in Plot B of Figure 4.21. The Two-Storage system covers lower demand power with the sorption mode compared to the reference system, as depicted in Figure 4.20. This leads to two effects. First, it delivers slightly less monthly energy from the medium-temperature sink to the space heating storage (Plot D of Figure 4.21). Second, the borehole heat exchanger delivers less monthly energy in the two-storage system, as indicated in plot B of Figure 4.21. Consequently, the Seasonal Gas Utilization Efficiency (SGUE) in the two-storage system (SGUE=1.14) is reduced by 4.9% compared to the reference system (SGUE=1.20).

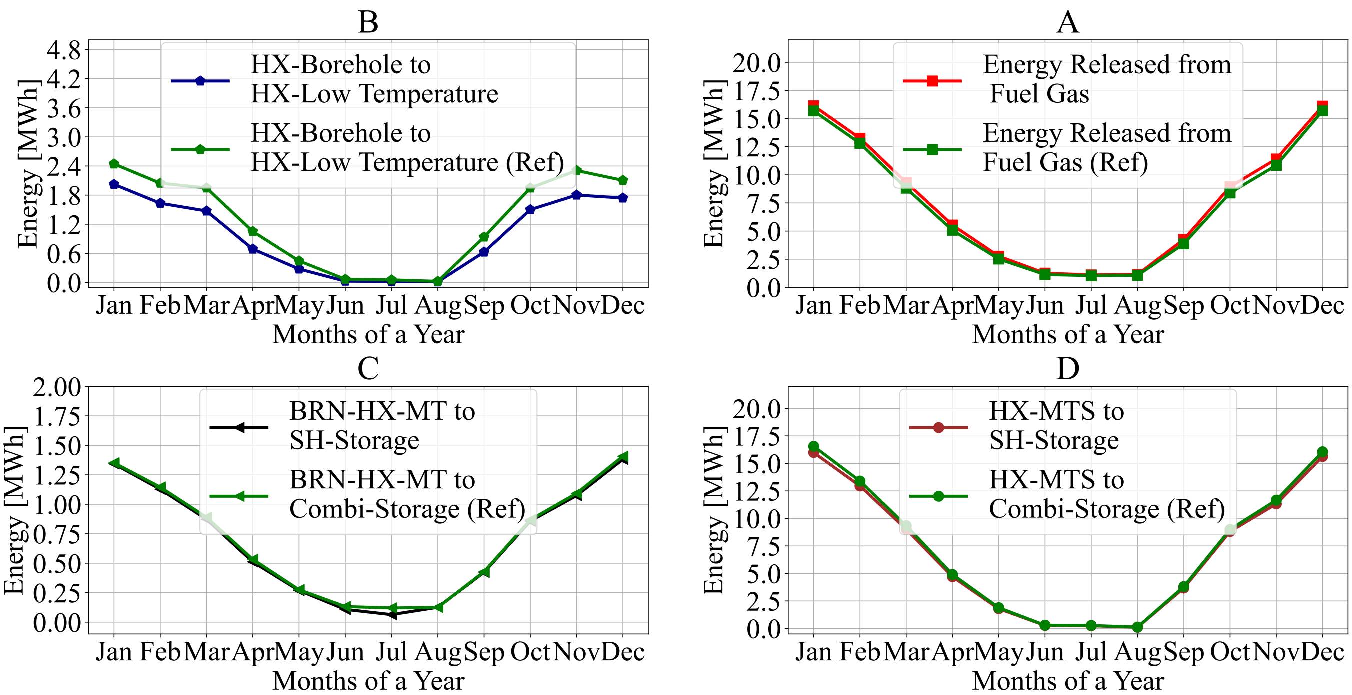

Figure 4.21.: Monthly energy released from fuel gas and monthly energy delivered from various components in the two-storage and reference systems.

Preheating the domestic hot water (DHW) demand through the sorption process is a key objective of this thesis. In the investigated hydraulic configuration, the condensing boiler heat exchanger is intentionally connected only to the space heating storage, while the DHW storage is deliberately heated exclusively by the burner. As a result, both the DHW demand and the heat losses of the separate DHW storage must be fully supplied via the HX_HTS. This configuration allows the effect of sorption-based preheating to be evaluated independently of the trivial condensing boiler contribution. Figure 4.22 therefore compares the DHW preparation in the reference system (low-density hatch pattern), where sorption-based preheating is available, with the two-storage system (high-density hatch pattern), where DHW demand is provided solely in burner mode.

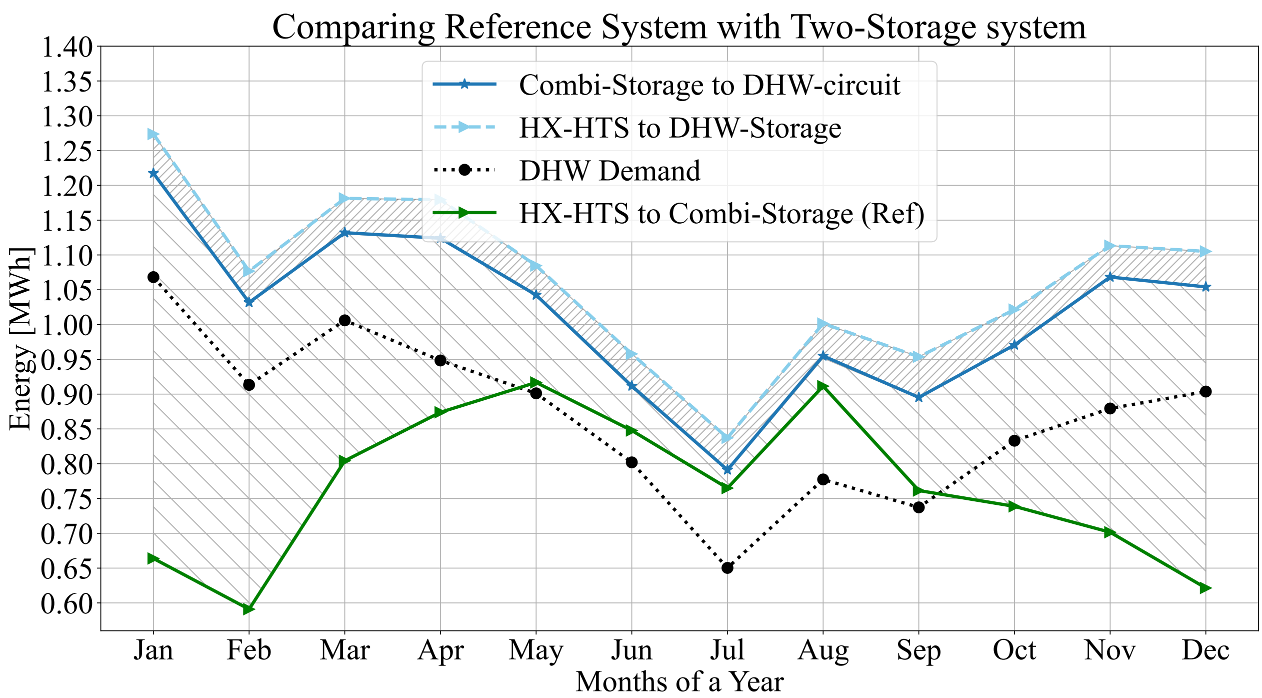

Figure 4.22.: Comparison of DHW preparation in reference system vs. two-storage system.

The detailed temperatures of the storage layers, as well as the DHW and space heating comfort temperature ranges, are provided in the appendix (see section A.5)

4.1.3. Combi-Storage and Solar Circuit System

One of the primary objectives of this thesis is to achieve a minimum Seasonal Gas Utilization Efficiency (SGUE) of 1.3 using a dual adsorber cycle Gas Adsorption Heat Pump (GAHP). To this end, the system configuration has been designed numerically as depicted in Figure 2.16, and the control strategy has been implemented at three different levels, as described in subsection 2.3.3.

An arbitrary operating window on November 23 is selected to evaluate the robustness of the system-level control when integrating solar thermal (ST) energy and GAHP to the storage. This high-resolution analysis illustrates how the system maintains stratification through hydraulic best practices, particularly principles of exergy management, which are typically obscured in aggregated monthly results.

A key requirement for stratified storage operation is the avoidance of mixing effects that disturb the established temperature gradient. By utilizing an ideal inserter for the solar loop return flow, solar energy is introduced into the 16-layer storage at a temperature-matched level, thereby preserving the thermal structure of the tank. This behavior is reflected in the smooth and stable temperature profiles of TStor[5] and TStor[6], even during periods of peak solar power injection.

To preserve the exergy of the upper storage zone, the control strategy also prevents excessive heating of the intermediate layers that could trigger mixing with the domestic hot water (DHW) layer. As shown in the temperature profile (Figure 4.23), TStor[1] remains consistently above the 63 °C threshold, while the solar-influenced intermediate layers (TStor[5-7]) remain below 51 °C, maintaining a clear thermal separation. This temperature stratification ensures that lower-temperature solar gains do not degrade the high-exergy DHW reserves.

Collector efficiency is maximized when the solar loop receives the coldest possible return water. In this configuration, solar supply water is extracted from the lower storage layers, where TStor[16] remains close to 24 °C during solar operation, providing a favorable temperature level for efficient heat transfer from the collector field.

The 16-layer storage also provides an important buffering function that decouples the heat sources and loads. Although the GAHP supplies fluctuating thermal power to the intermediate storage layers (visible in the intermittent peaks of TStor[7]), the heat extraction for the SHC circuit remains stable, maintaining indoor temperatures of approximately 20 °C despite variations in solar availability. This decoupling is further confirmed in Figure 4.24, where the SHC demand (orange line in subplot 5) and the fuel gas power input (green line) indicate that solar energy is prioritized, while the GAHP modulates its output to meet the residual demand. At the same time, the adsorber loading profiles in subplot 4 demonstrate that the internal sorption cycles of AD1 and AD2 remain unaffected by the concurrent solar heat input.

Overall, this detailed temporal analysis confirms that while the SGUE of 1.3 is achievable through solar scaling, the system is supported by a stable and non-conflicting operational strategy that effectively manages the combistorage as a thermal interface between the ST system, the GAHP, and heat consumption.

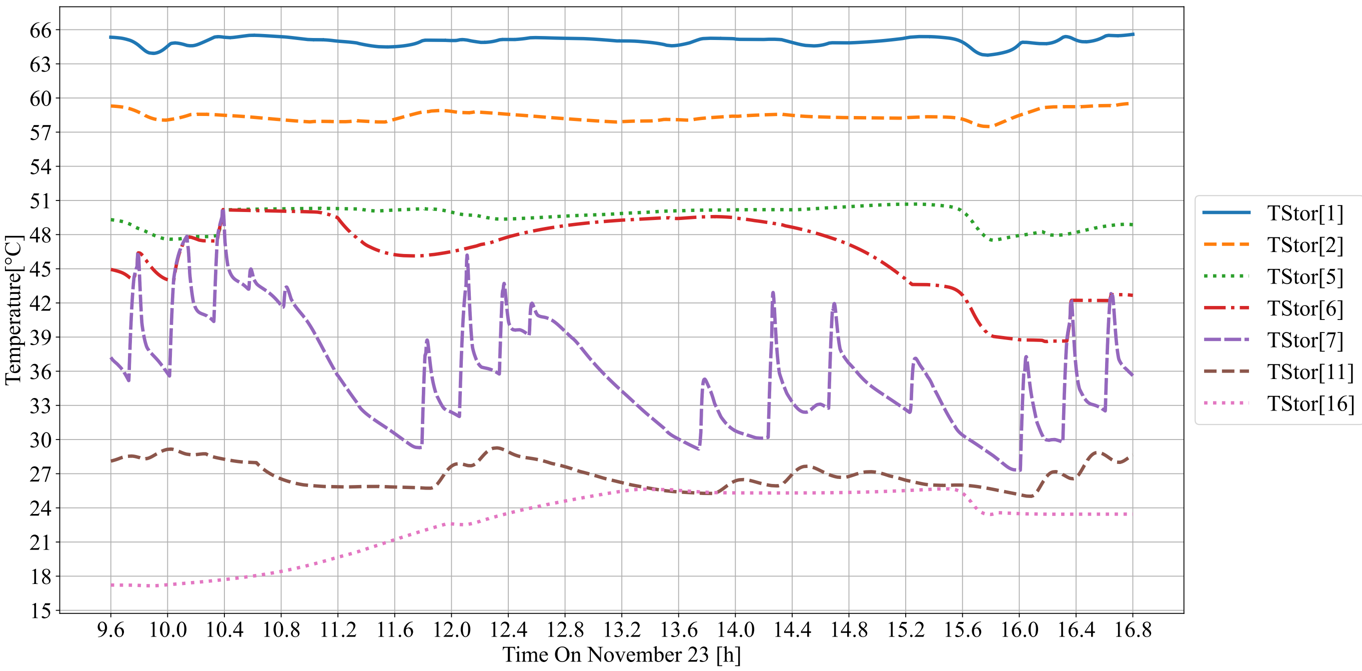

Figure 4.23.: Storage layer temperatures in the combi-storage and solar circuit system between 9:36 and 16:48 on 23 November.

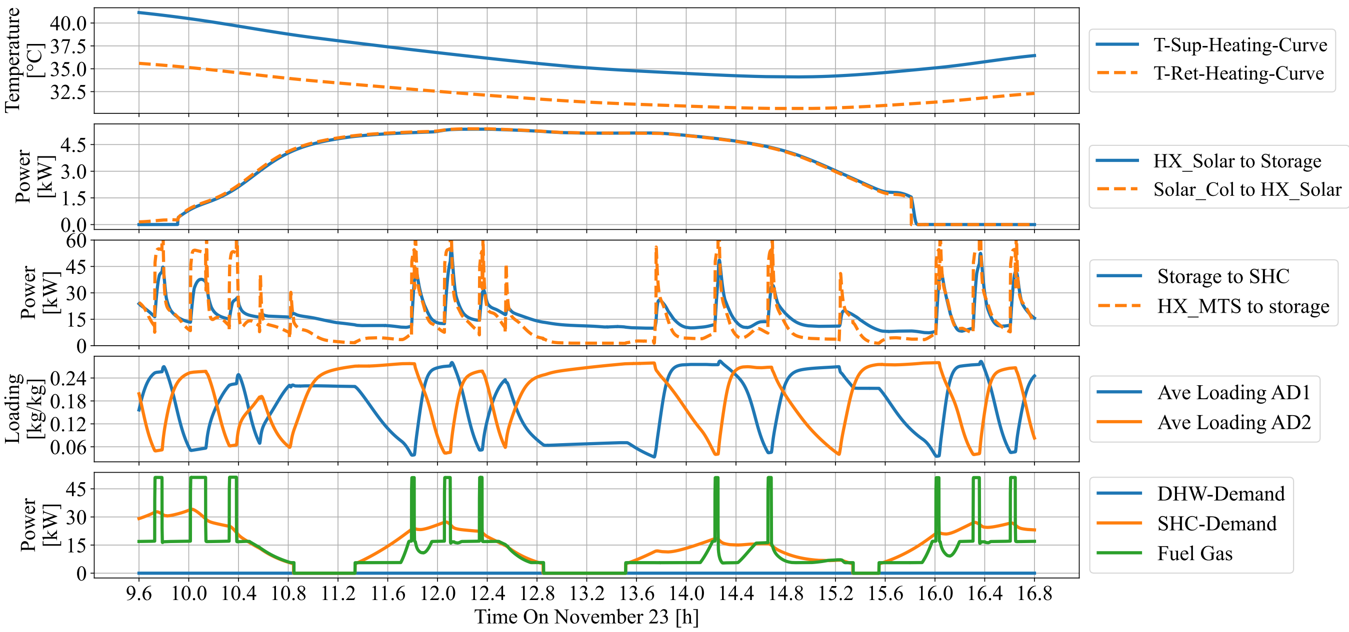

Figure 4.24.: Heat consumption and heat production of the space heating circuit, together with the average adsorber loading in the combi-storage and solar circuit system between 9:36 and 16:48 on 23 November.

Figure 4.25 illustrates that the GAHP in system with solar circuit operates at power levels between 17 kW and 5 kW less frequent than the reference system. Additionally, plot A in Figure 4.26 demonstrates the monthly energy released from fuel gas for the system with the solar thermal circuit relative to the reference system. Consequently, the monthly energy delivered from burner to the combi-storage through High-Temperature Source heat exchanger in the configuration with the solar thermal circuit (represented by the hatch pattern) is less than that of the reference system.

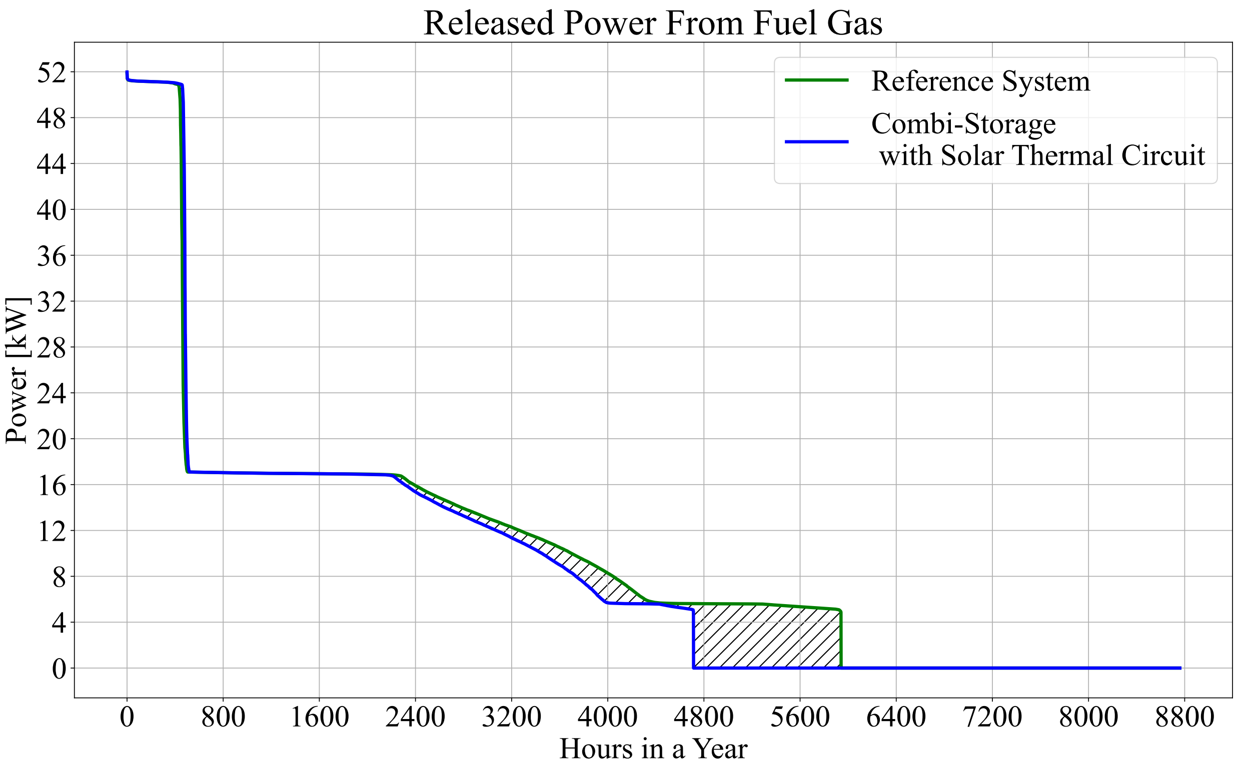

Figure 4.25.: Annual power duration curves for reference system (green line) and combi-storage and solar circuit system, showing that the solar thermal system hardly reduces direct burner operation but significantly decreases the runtime of the adsorption heat pump.

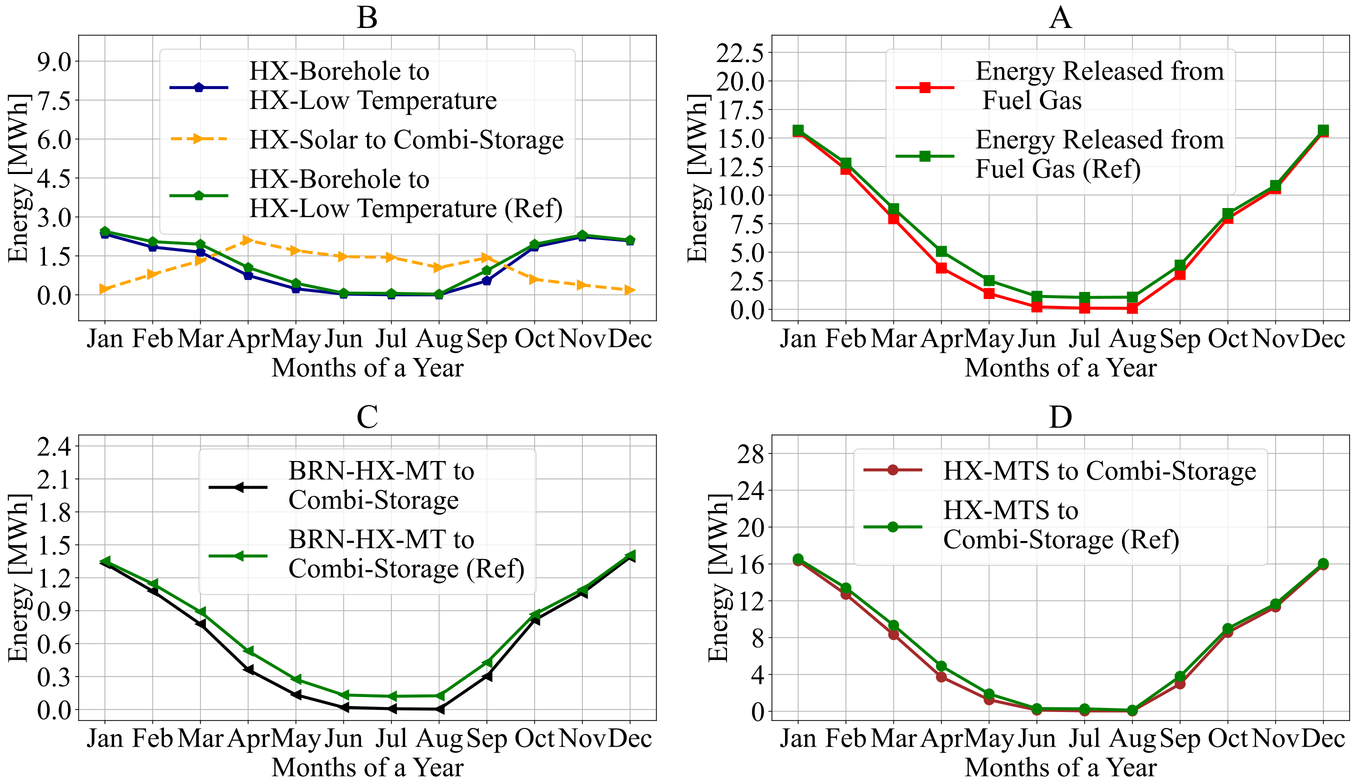

Figure 4.26.: Monthly energy released from fuel gas and monthly energy delivered from various components in reference vs. combi-storage and solar circuit system.

In addition to reduced gas consumption, the less frequent operation of the GAHP in the system with the solar thermal circuit compare to the reference system (as shown in plot D of Figure 4.26) reveals lower monthly delivered energy from both the borehole heat exchanger (plot B) and the secondary burner heat exchanger (plot C), compared to the reference system.

A comparison of the monthly domestic hot water (DHW) energy preparation between the system with the solar thermal circuit and the reference system reveals that the application of the solar thermal circuit increases the preheating DHW area. This effect is illustrated in Figure 4.27, where the impact of the solar thermal circuit and GAHP (low-density hatch pattern) is compared to the effect of only GAHP in the reference system (dense hatch pattern). Consequently, the SGUE for the reference system is 1.20, while the SGUE for the system with the solar thermal circuit is 1.33, reflecting an 11 % increase and achieving the system design goal.

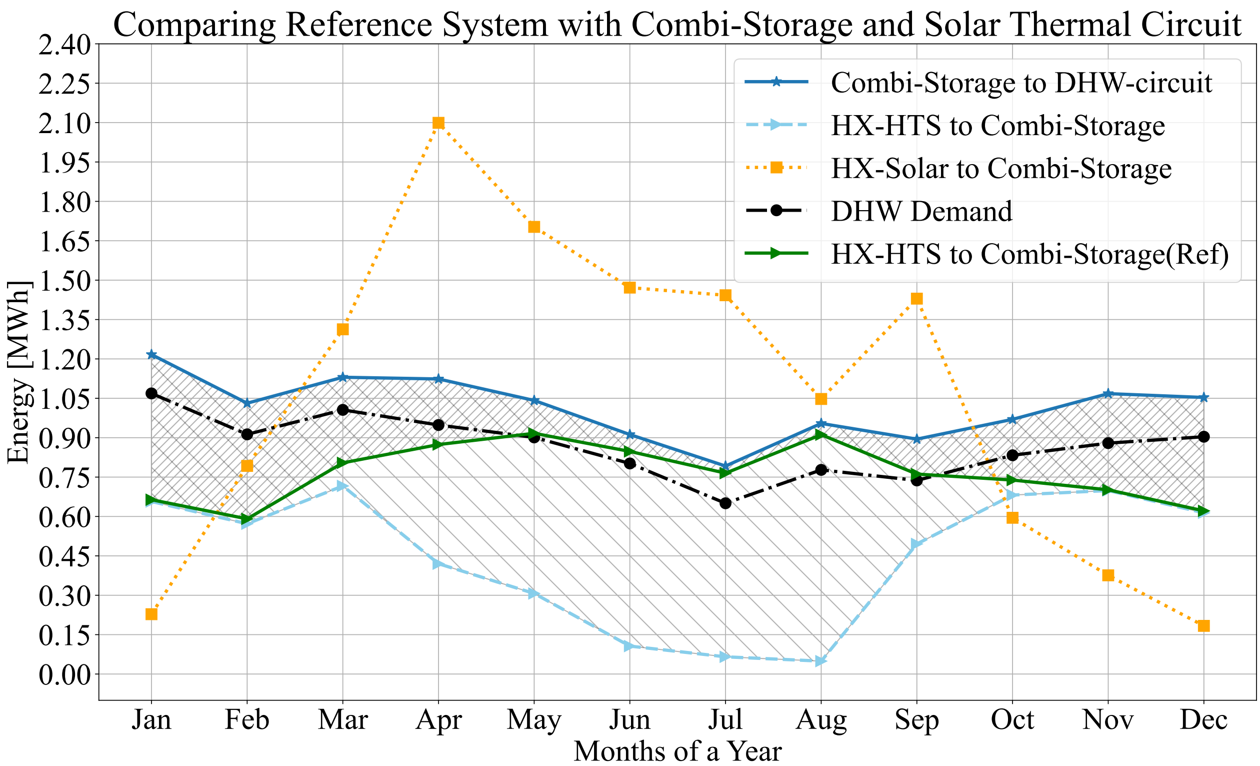

Figure 4.27.: Comparison of DHW preparation in reference system vs. combi-storage and solar circuit system.

A sensitivity analysis was conducted to investigate the influence of the overall heat transfer coefficient–area product (UA value) and the mass flow rates of the pumps on both sides of the solar heat exchanger shown in Figure 2.6. The analysis evaluates their effect on the solar gross yield and the DHW preheating performance. While low-flow operation is often recommended for solar thermal systems with stratified storage tanks to enhance stratification, the results indicate that higher mass flow rates improve the solar utilization in the investigated system configuration. This behavior is related to the specific hydraulic integration and control strategy of the solar loop, which is described in subsubsection 2.1.1.2. The detailed results of this analysis are presented in section A.10.

4.1.4. Two-Storage and Solar Circuit System

The configuration of a system with Two-storage and a solar thermal circuit is depicted in Figure 2.17, with the control strategy detailed across three levels in subsection 2.3.4. When comparing the system with Two-storage and a solar circuit to the reference system in Figure 4.28, it is observed that high gas consumption power is slightly more frequent in the two-storage system with the solar circuit. In contrast, gas consumption power between the maximum sorption power (17 kW) and the minimum burner power (5 kW) is more prevalent in the reference system. Consequently, the Seasonal Gas Utilization Efficiency (SGUE) of the two-storage system with a solar circuit is 8.4 % higher than that of the reference system.

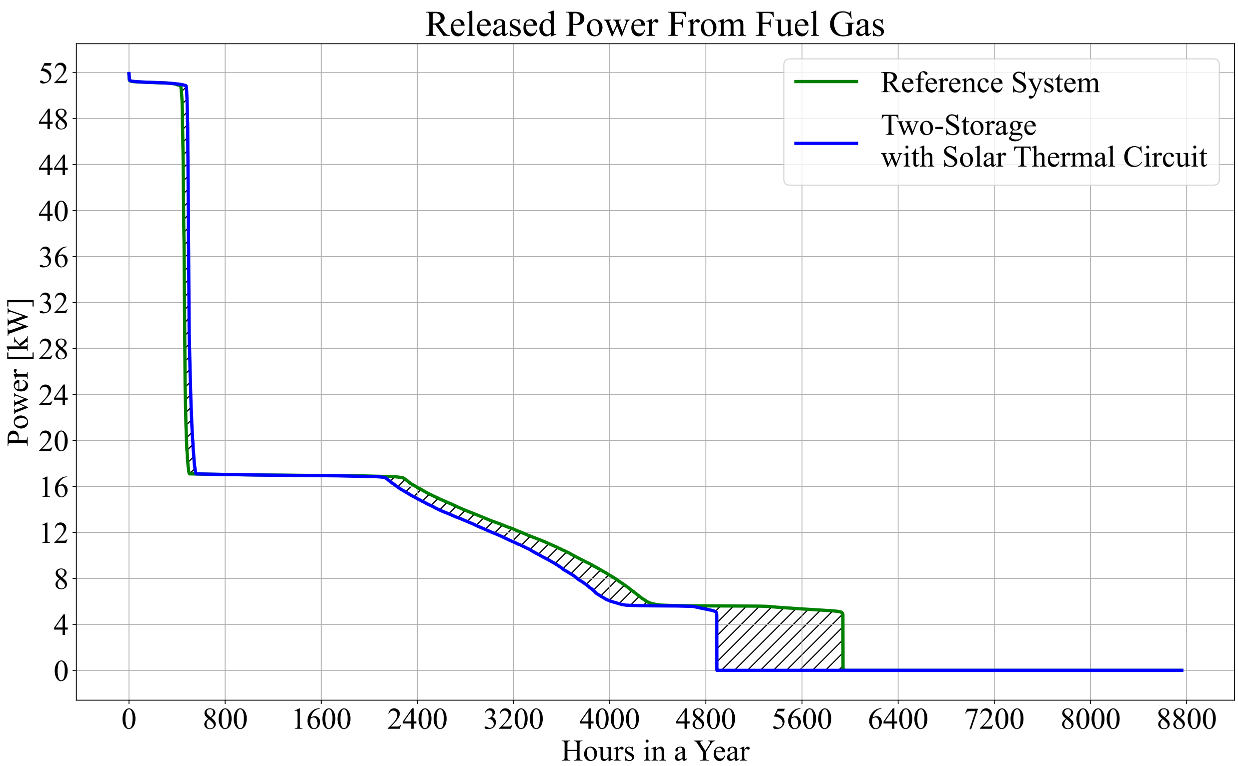

Figure 4.28.: Annual power duration curves for reference system (green line) and two-storage and solar circuit system.

In the two-storage system with a solar thermal circuit, the GAHP is only connected to the space heating storage. Thus, Domestic Hot Water (DHW) preparation relies solely on the burner. Figure 4.29 illustrates that when solar energy is delivered to the water heating storage, gas consumption energy is significantly reduced (as indicated by the less dense hatch pattern).

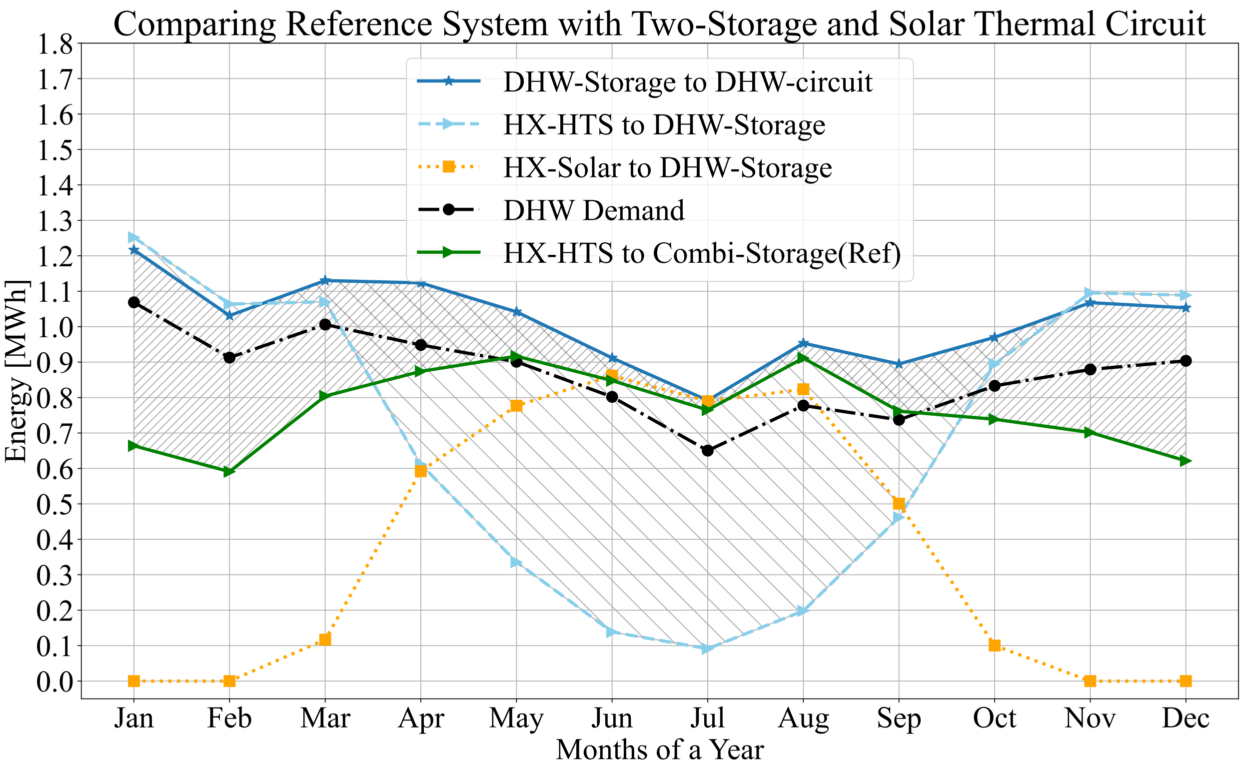

Figure 4.29.: Comparison of DHW preparation in reference system vs. two-storage and solar circuit system.

Monthly solar irradiation, energy delivered, specific solar yield, and annual storage layer temperatures for the studied systems are shown in the appendix (see section A.6).

4.1.5. Comparative System Summary

This section has provided an extensive overview of the annual energy flow for different systems. It includes the energy transfer from low-temperature heat sources to both heat pump and storage, as well as the energy transfer from high-temperature source to heat pump and storage. Furthermore, the energy flow from heat pump to storage and subsequently to heat consumption components has been presented for various systems: the reference system in Figure 4.30, the system with two storage in Figure 4.31, the system with solar thermal circuit and combi-storage in Figure 4.32, and the system with solar thermal circuit and two storage in Figure 4.33. Additionally, energy flow diagrams can serve as an effective verification tool for the numerical simulation. When applying the energy balance to the storage system, no energy deficiency is observed. The energy balance is expressed as: annual inlet energy - annual outlet energy - heat losses = annual change in energy within the storage. A positive value indicates an increase in the thermal energy of the storage's thermal mass.

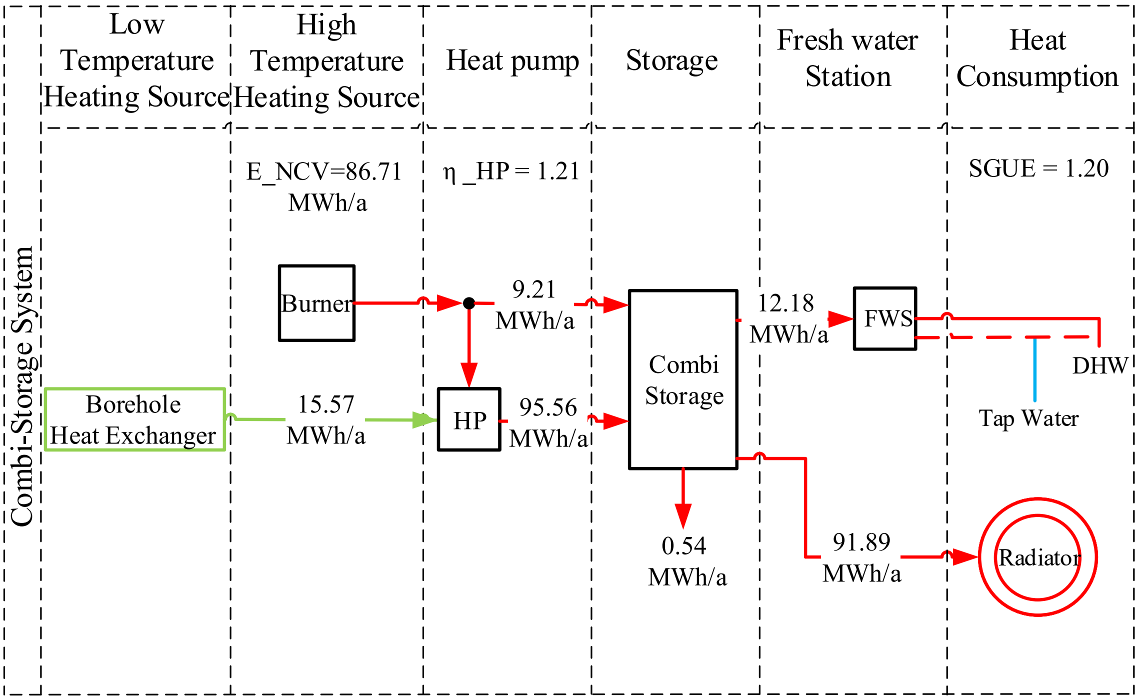

Figure 4.30.: Reference system.

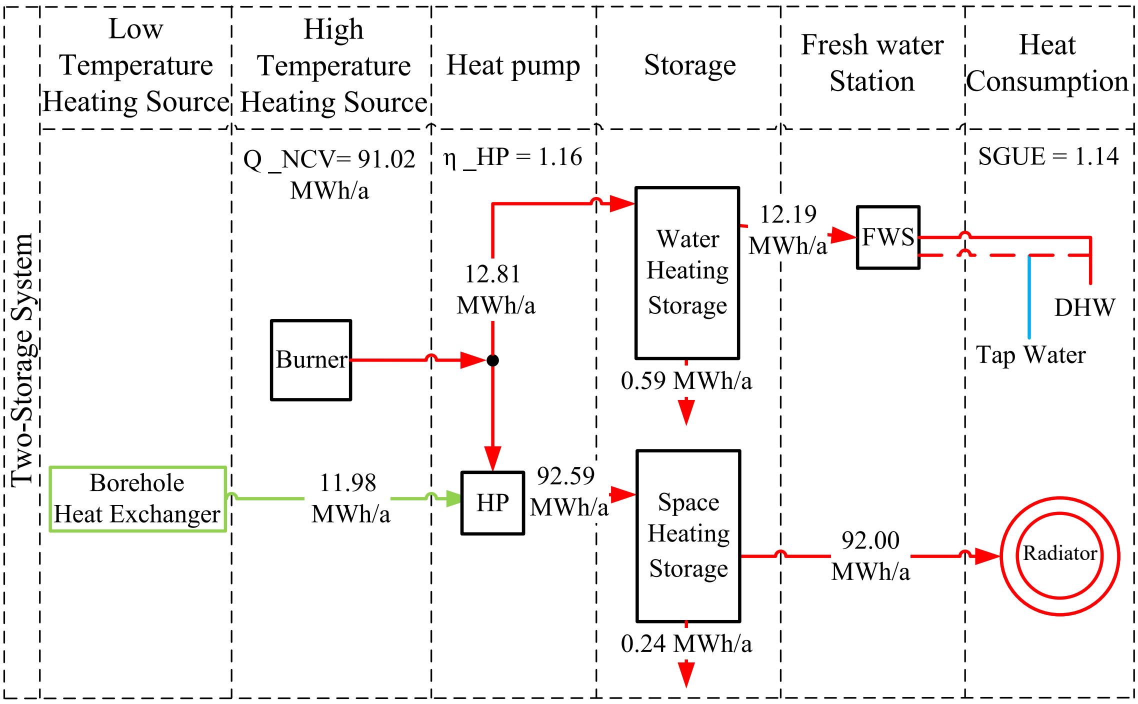

Figure 4.31.: Two-Storage system.

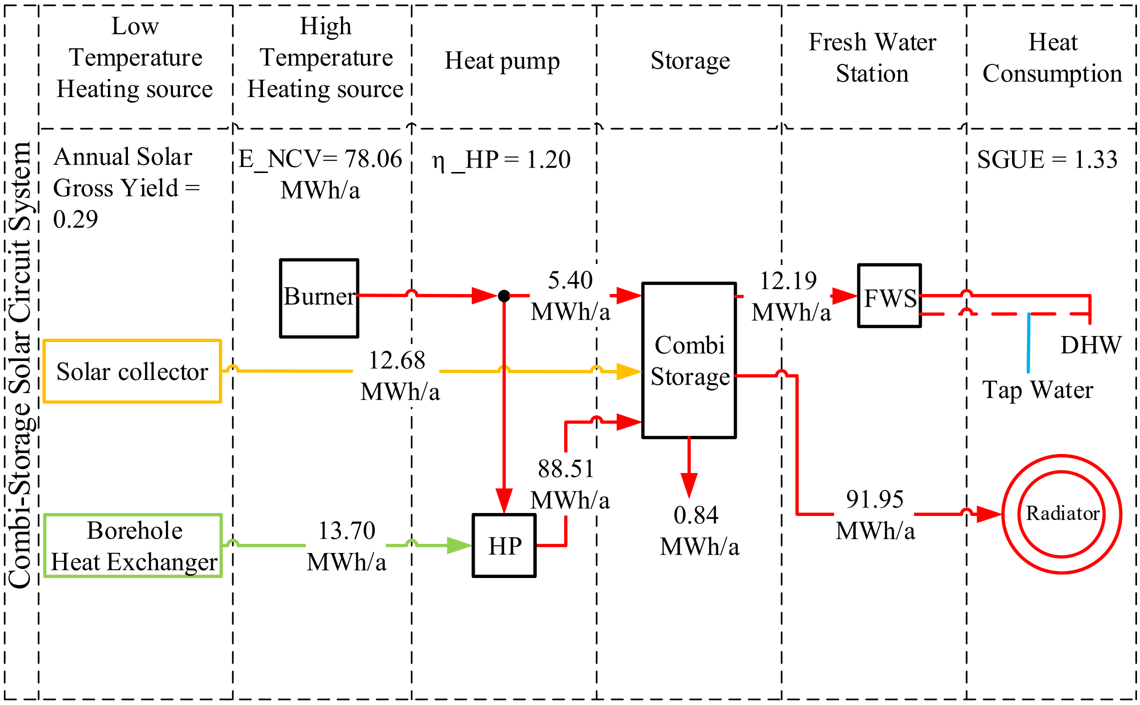

Figure 4.32.: Combi-Storage and solar thermal circuit system.

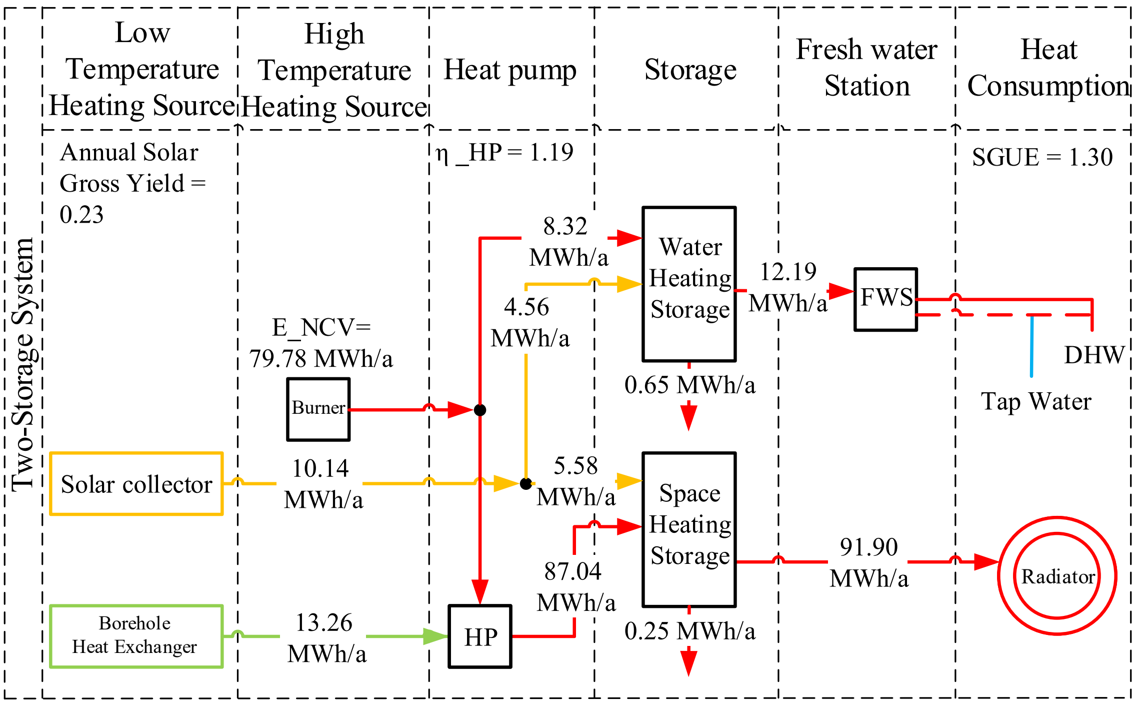

Figure 4.33.: Two-Storage and solar thermal circuit system.

Figure 4.34 presents the Seasonal Gas Utilization Efficiency (SGUE) for the aforementioned systems. The systems incorporating solar thermal circuits address the research question by achieving a minimum SGUE of 1.3. In this regard, the SGUE of combi-system with solar thermal circuit is 2.3 % greater than that of two-storage system with solar thermal circuit.

To enable a consistent comparison, the base system was extended to include domestic hot water (DHW) supply. Since the base system only covers the space heating circuit (SHC), the DHW demand was assumed to be provided by a condensing boiler with a SGUE of 0.94. Combining the SHC performance of the base system (SGUE = 1.21) with the DHW supply results in an overall SGUE of 1.17. Compared to this value, the reference system achieves a slightly higher SGUE of 1.20 (2.5 % improvement) while covering both SHC and DHW demands.

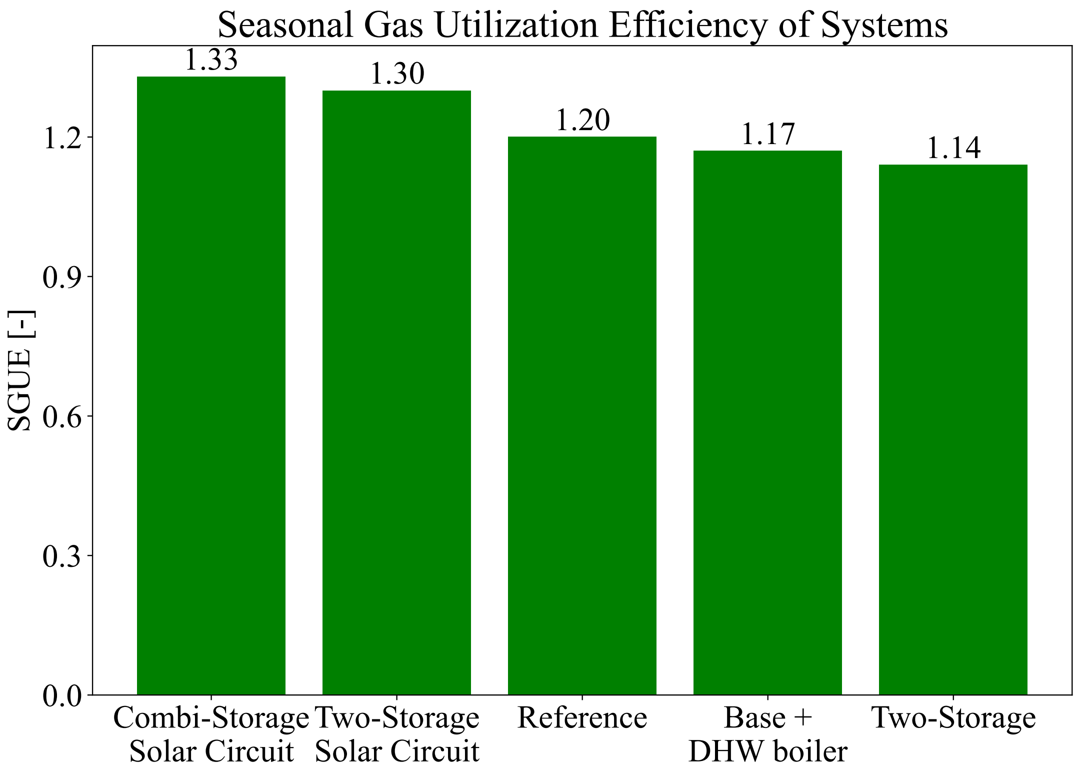

Figure 4.34.: Seasonal gas utilization efficiency of various systems.

For the two solar-assisted configurations, it should be noted that the adopted system balancing approach attributes the useful heat provided by the solar thermal subsystem directly to the overall SGUE. However, the solar thermal system does not increase the thermodynamic efficiency of the gas-fired subsystem itself; instead, it reduces the required operating time and fuel consumption of the gas burner. Consequently, the improvement in SGUE observed in the solar-assisted variants primarily reflects the substitution of gas-derived heat with solar heat rather than an intrinsic efficiency improvement of the gas-based conversion process.

4.2. Sensitivity Analysis of the Reference System

This section analyzes the performance of the reference system with particular focus on the achieved SGUE. A central question is whether the reported SGUE value of 1.3 can be achieved without the contribution of solar thermal energy or whether the solar subsystem plays a decisive role in reaching this performance level. To address this, the following analysis compares the different system variants. A summary of the resulting SGUE values for all investigated cases is presented in Table 4.1 at the end of this section.

4.2.1. Effect of Boundary Conditions

4.2.1.1. Different Weather Data

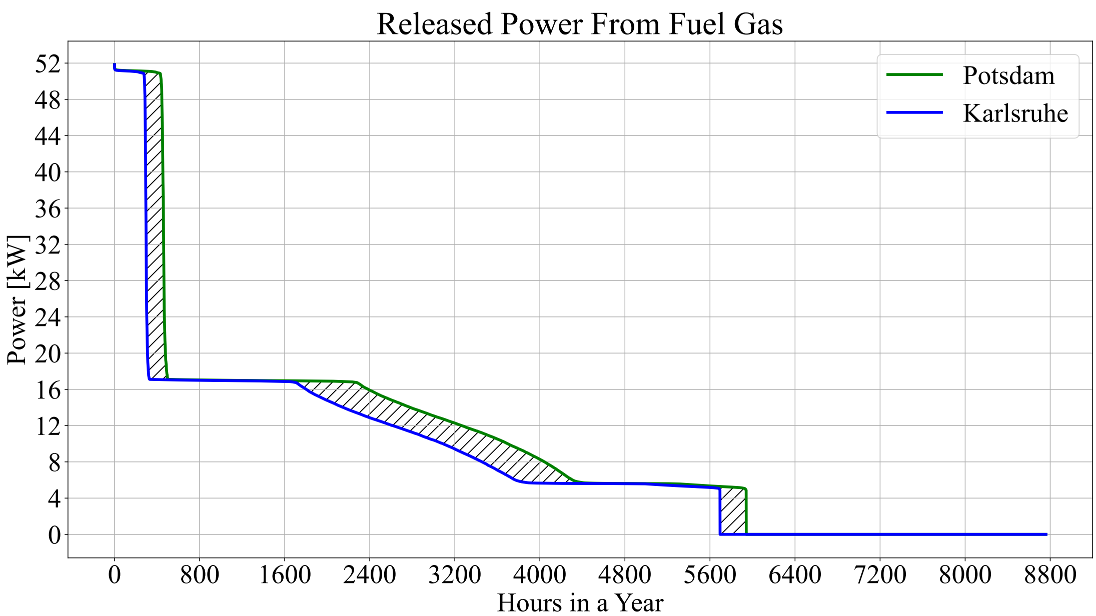

Figure 4.35.: Annual power duration curves for reference system under Potsdam and Karlsruhe weather conditions.

As described in the weather data sets in subsubsection 2.1.2.1, Potsdam weather conditions are used as the default climate for the reference system, while Karlsruhe weather conditions are used to assess the sensitivity of the system to different climatic conditions. Compared to Potsdam, Karlsruhe has a milder climate with lower heating demand during both the winter months and the transitional seasons. This difference in heating load is reflected in the system operation. As shown in Figure 4.35, the GAHP operates less frequently in both direct burner and sorption modes under Karlsruhe weather conditions. Correspondingly, the monthly energy delivered from the combi-storage to the space heating circuit is lower for Karlsruhe, as illustrated in Figure 4.36.

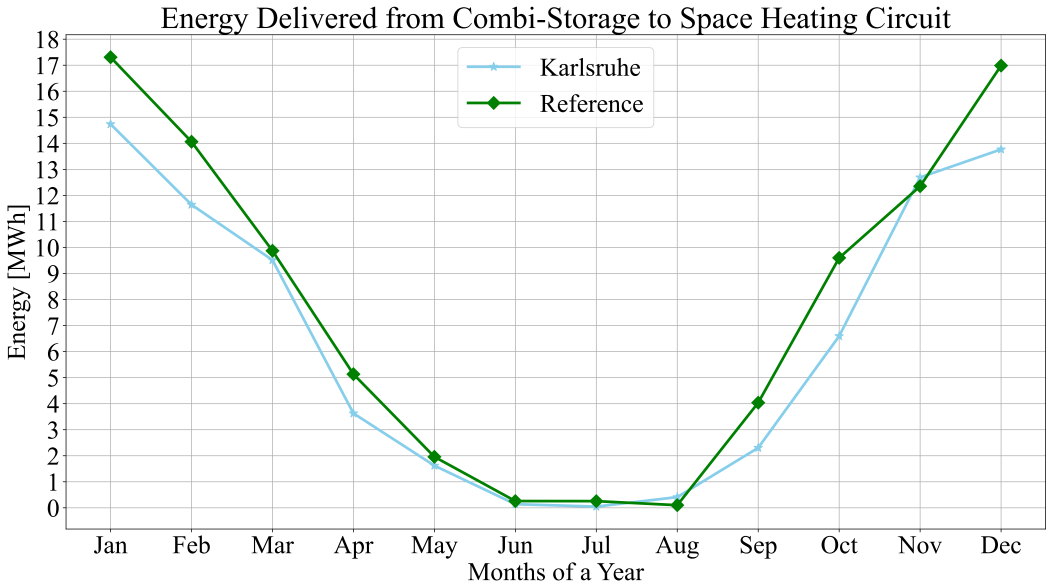

Figure 4.36.: Monthly energy delivered from combi-storage to space heating circuit under Potsdam and Karlsruhe weather conditions.

The comparison between Potsdam and Karlsruhe weather conditions should also be interpreted in the context of the different design outdoor temperatures defined in DIN EN 12831. According to this standard, the design temperature for Potsdam is −14 °C, while for Karlsruhe it is −10 °C, implying that heating systems would typically be sized differently for these locations. In the present study, however, the same system configuration and component sizes are used for both climates to isolate the influence of weather conditions. Consequently, the system is effectively oversized for the Karlsruhe climate. This results in lower average load factors and more frequent cycling, which contributes to the reduced operational hours of the GAHP (Figure 4.35) and the lower space heating demand (Figure 4.36) observed in the results.

DHW preheating under Potsdam and Karlsruhe conditions is shown in the appendix (section A.7).

The monthly energy released from fuel gas is shown in plot A of Figure 4.37 for both weather conditions. Under Karlsruhe weather conditions, the GAHP operates less frequently in sorption mode, which is consistent with the lower space heating demand associated with the milder Karlsruhe climate. It should be noted that the undisturbed ground temperature of the borehole heat exchanger was assumed to be identical for both locations; although in reality the ground temperature in Karlsruhe could be slightly higher than in Potsdam (typically by about 0.5–1 °C), this effect was not considered in the present analysis. Consequently, the borehole heat exchanger supplies slightly less energy to the low-temperature heat exchanger of the GAHP from January to March due to the reduced operation of the sorption cycle, leading to a 1.6 % increase in SGUE for the Karlsruhe case.

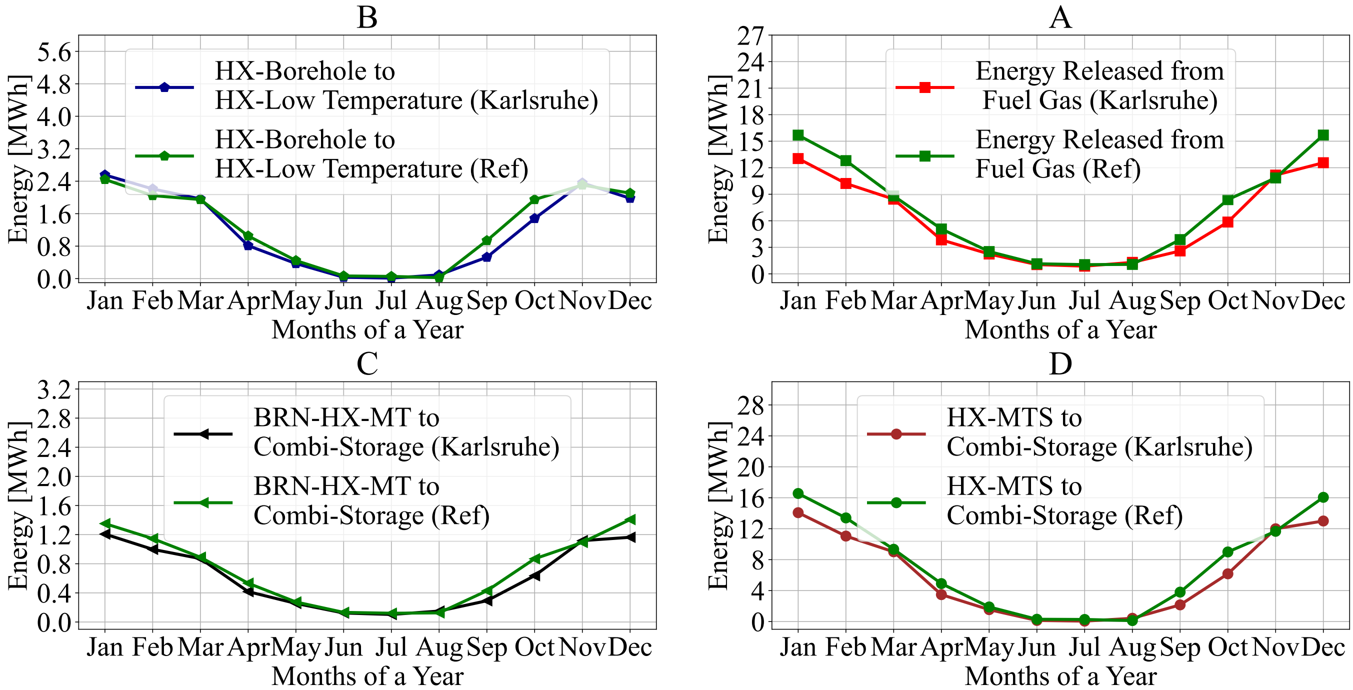

Figure 4.37.: Monthly energy released from fuel gas and monthly energy delivered from various components in reference system under Potsdam and Karlsruhe weather conditions.

4.2.1.2. Impact of Domestic Hot Water Profile

In many simplified building energy models, the domestic hot water (DHW) demand is assumed to be constant throughout the year. In this study, however, the DHW profile is generated using a stochastic load generator based on the methodology developed by Fischer [101], which introduces noticeable seasonal variations in the demand. These variations (as described in subsubsection 2.1.2.2) may reflect behavioral effects represented in the stochastic model, such as occupancy changes during holiday periods. In addition to the useful DHW draw-off, the circulation loop contributes additional thermal demand required to maintain the distribution temperature. From a thermodynamic perspective, it is therefore useful to distinguish between the useful DHW demand (energy required for water heating at the draw-off points) and the circulation heat losses, which represent additional heat input to maintain the loop temperature (e.g. Figure 4.3, subplot 2-3). It should be noted, however, that in the present annual simulation the heat transfer between the circulation pipes and the ambient environment is not explicitly modeled. Consequently, the circulation-related thermal demand represents the heat required to maintain the circulation loop temperature within the system model rather than detailed pipe heat losses to the surroundings.

Furthermore, the sensitivity analysis with increased DHW demand should be interpreted in the context of the adopted scaling approach. Since the stochastic load generator could not be reconfigured to generate a higher demand scenario, the DHW profile was scaled by a factor of 2.5. This method increases the instantaneous draw-off rate during each event while keeping the timing and duration of the events unchanged. Although this preserves the temporal structure of the demand profile, it does not fully represent realistic user behavior, as higher DHW consumption would typically occur through longer draw-off durations or additional events rather than proportionally higher flow rates. Therefore, the scaled scenario should be interpreted as a parametric sensitivity analysis of increased thermal DHW demand, rather than a realistic representation of occupant behavior.

The hydraulic configuration in the reference system with scaled consumption remains unchanged (Figure 4.38). Detailed power, energy, DHW preheating, and comfort temperature distributions for the reference system are provided in the appendix (section A.8).

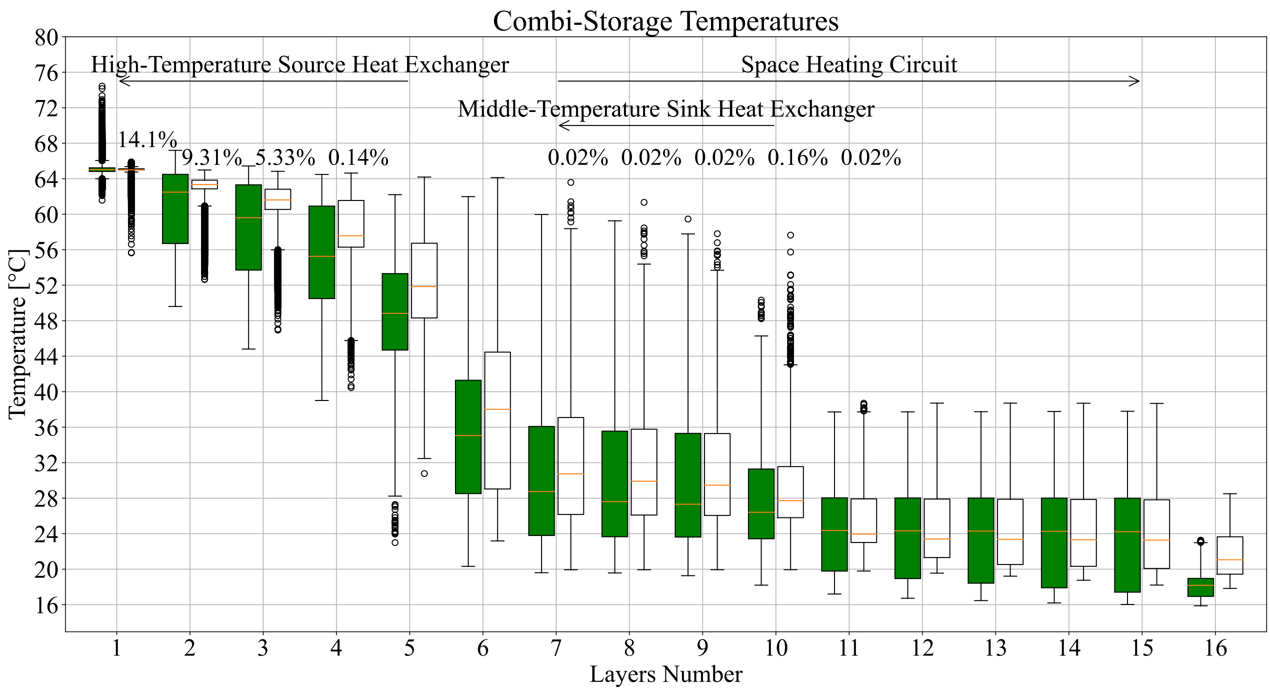

Figure 4.38.: Temperature layers in the reference system (green) and reference system with scaled consumption (factor of 2.5). The outlier percentages indicate the share of transient deviations relative to the total dataset for each layer in the scaled-consumption case.

4.2.2. Effect of Operational Parameters

4.2.2.1. Maximum Desorption Temperature

To analyse the effect of the desorption temperature on the performance of the GAHP, its influence is first evaluated under standardized operating conditions. For this purpose, the system performance is assessed at the operating points defined in VDI 4650-2 [73]. The results for the single adsorber cycle GAHP presented in subsection 4.3.1 show that increasing the desorption temperature from 90 °C to 110 °C leads to a slight improvement in system performance, as indicated by the Seasonal Gas Utilization Efficiency (SGUE). Since the thermodynamic adsorption–desorption mechanism is common to both system configurations, this trend provides an indication of how the desorption temperature may influence the GAHP cycle performance. Based on this assessment at representative operating points, the influence of the desorption temperature on the dual adsorber cycle is subsequently analysed through annual simulations in order to capture the impact of realistic load variations and dynamic operating conditions.

Based on the representative day of 29 October, the loading, SHC and DHW demand power as well as fuel-gas power is shown in Figure 4.39. The reference case corresponds to the AdoSan configuration with a maximum desorption temperature of 90 °C [26]. Increasing the maximum desorption temperature to 110 °C alters the dynamic operation of the GAHP.

As illustrated in subplots 1 and 2, increasing the desorption temperature leads to longer adsorption and desorption phases, thereby reducing the number of completed cycles within the same time period. This change in cycle dynamics is also reflected in the fuel-gas-power profiles (subplots 3 and 4), where the 90 °C case operates within the typical sorption range with a maximum around 17 kW, while the 110 °C case exhibits short peaks of up to approximately 50 kW, indicating periods of direct-burner operation. These peaks can be attributed to the extended desorption half-cycles, which reduce the instantaneous heat supply from the sorption module to the storage and may result in insufficient heating capacity under certain conditions.

Overall, the time-resolved analysis indicates a trade-off between the two operating strategies. At higher sorption powers, the lower desorption temperature appears to be advantageous, as the 110 °C case exhibits pronounced direct-burner peaks due to reduced instantaneous heat supply. At lower power levels, however, the differences between the two cases are less pronounced, and potential advantages of the higher desorption temperature cannot be clearly identified from the present analysis. It should be noted that these results depend on several operational parameters, including control settings, temperature levels, and mass flow rates, which are not fully optimized in this study. In particular, the control strategy is not adapted to the modified desorption temperature, which limits the comparability of the two cases. Nevertheless, the findings indicate that further improvements in system performance are possible through parameter adjustment under varying load conditions. In this context, entropy generation analysis provides a valuable basis for identifying thermodynamic inefficiencies and guiding a more systematic optimization of system operation.

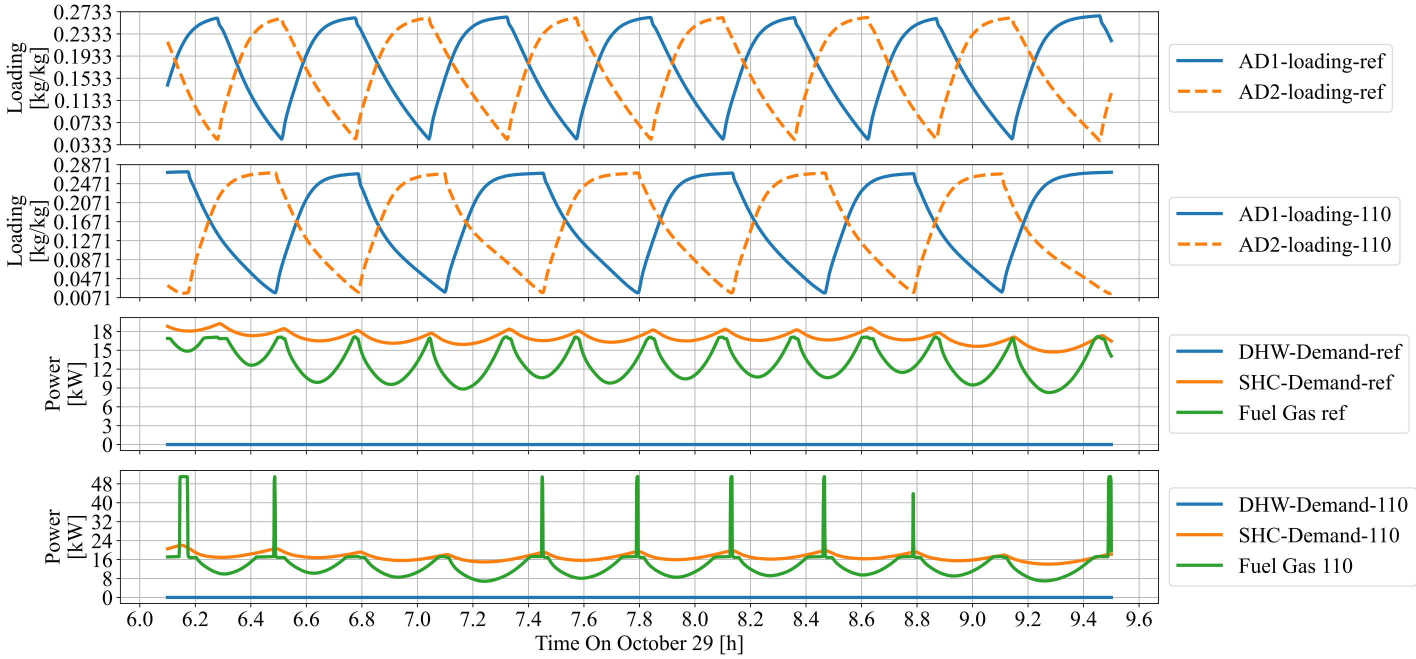

Figure 4.39.: loading, space heating the domestic hot water power demand and fuel gas power in reference system with two maximum desorption temperature: 90 °C (reference) and 110 °C between 6:06 and 9:30 on 29 October.

4.2.2.2. Heat Exchanger Properties

The UA values for the fresh water station and the high-temperature source heat exchanger were determined based on a sensitivity analysis of the Seasonal Gas Utilization Efficiency (SGUE). The analysis revealed that the SGUE is highly sensitive to the fresh water station's UA at lower values, increasing by approximately 1.32 % (from 1.183 to 1.199) across the analyzed range. In contrast, the high-temperature source heat exchanger showed negligible impact, with a maximum SGUE variation of only 0.1 %.

Beyond a UA value of 12 kW/K, both components reached a plateau where further increases yielded diminishing returns and minor numerical fluctuations. Consequently, a UA value of 12 kW/K was selected for both heat exchangers as an optimal balance between thermal performance and computational stability.

4.2.2.3. Using Three Ideal Stratifiers

To investigate the high-resolution dynamics of the system, a representative short-term period on October 29 is analyzed (Figure 4.40). The reference configuration uses three ideal inserters (for the DHW, HX_MTS, and SHC returns in Figure 2.7). These components minimize exergy losses by directing return flows to the storage layer with the most compatible temperature. Figure 4.40 highlights that the adsorption cycles primarily influence the middle-to-lower storage region, specifically layers 7 through 10, while the bottom layers (15 and 16) remain thermally inactive at a constant 17 °C. At 05:48, a temperature drop in Layer 1 indicates the onset of DHW draw-offs, which subsequently triggers the burner and heat transfer to the upper layers. A distinct feature of this simulation is the temperature jump in Layer 6 at 06:00. Although the return flow from the high-temperature source (HTS) is physically directed to Layer 5, the system enters direct burner mode at its maximum capacity of 50 kW at this time. This causes a rapid temperature spike in Layer 7 via the BRN_HX_MT. As TStor[7] rises to exceed TStor[6], the storage model detects a temperature inversion and triggers a mixing event to maintain physical stratification. This numerical mixing causes Layer 6 to jump and synchronize with the temperature of the layer below it. This interaction demonstrates the high sensitivity of the stratified model to peak power inputs and is further supported by the control signals shown in Figure 4.42 and Figure 4.41.

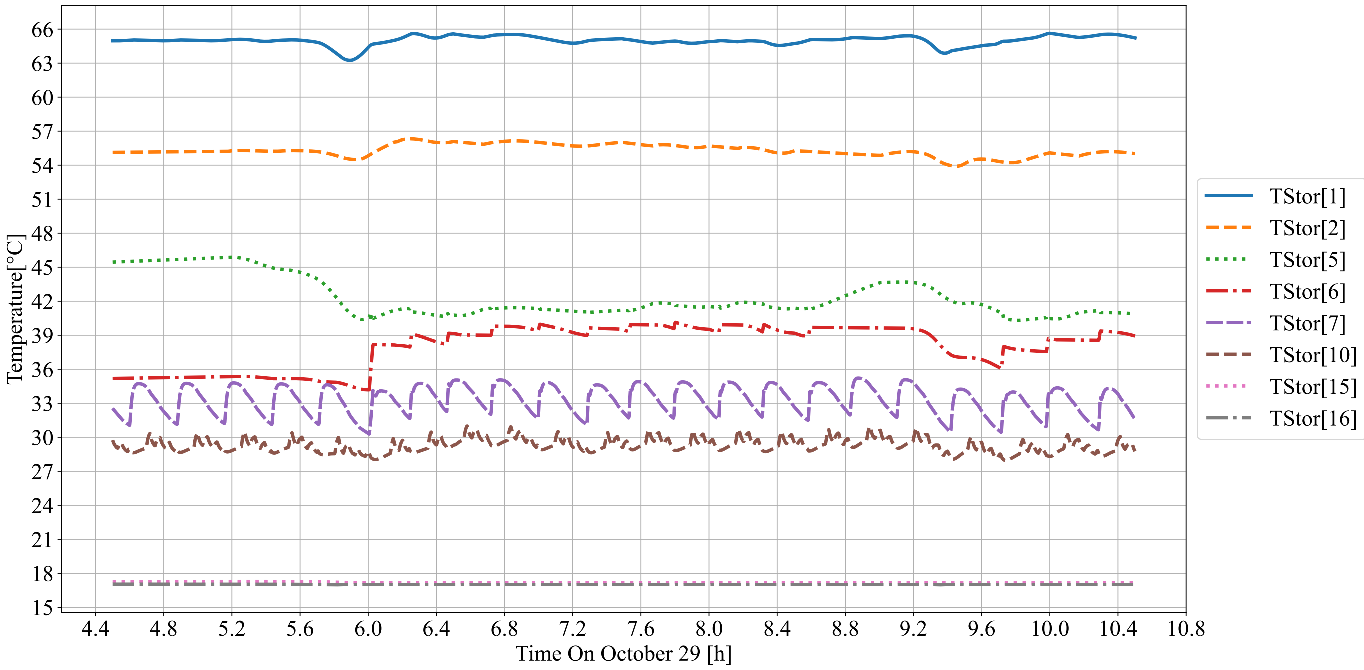

Figure 4.40.: Storage layer temperatures in the reference system with three ideal inserters between 4:30 and 10:30 on 29 October.

An important effect is the increased DHW preheating achieved through the sorption mode of the GAHP in the configuration with three ideal inserters (Figure 4.43). In this context, a higher utilization of borehole energy is observed, primarily during the period from November to March, while the impact on thermal comfort remains negligible. Furthermore, the results show that the five layers of the combi-storage are only marginally utilized in this configuration (Figure 4.44), indicating that the storage volume could be reduced without compromising the required temperature levels in the DHW and space heating circuits.

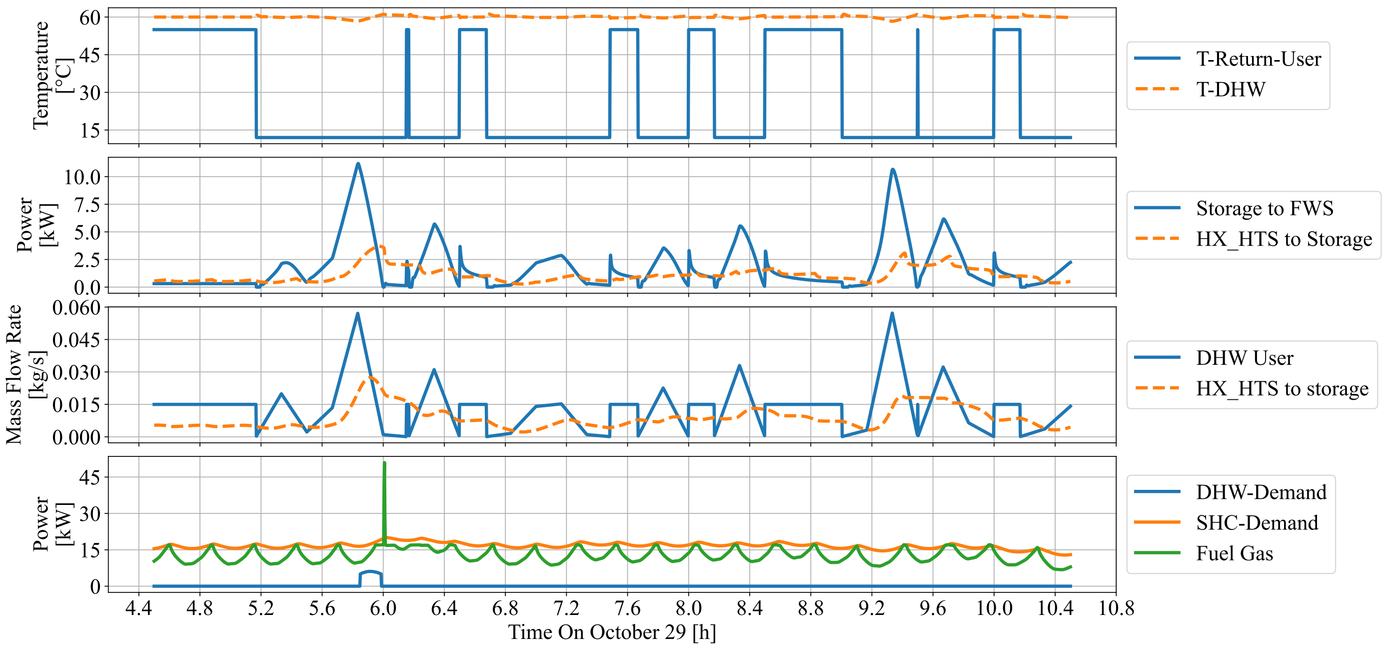

Figure 4.41.: Heat consumption side, heat production side for the domestic hot water circuit in the reference system with three ideal inserters between 4:30 and 10:30 on 29 October.

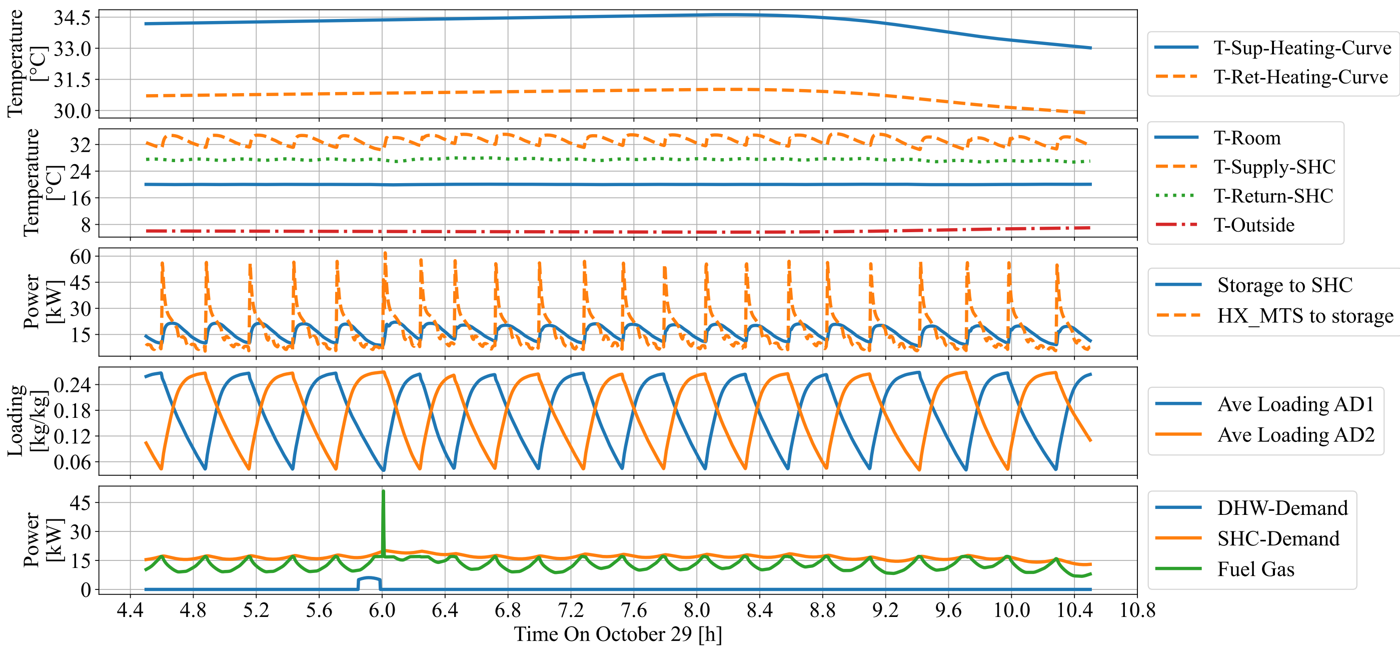

Figure 4.42.: Heat consumption side, heat production side for the space heating circuit in the reference system with three ideal inserters between 4:30 and 10:30 on 29 October.

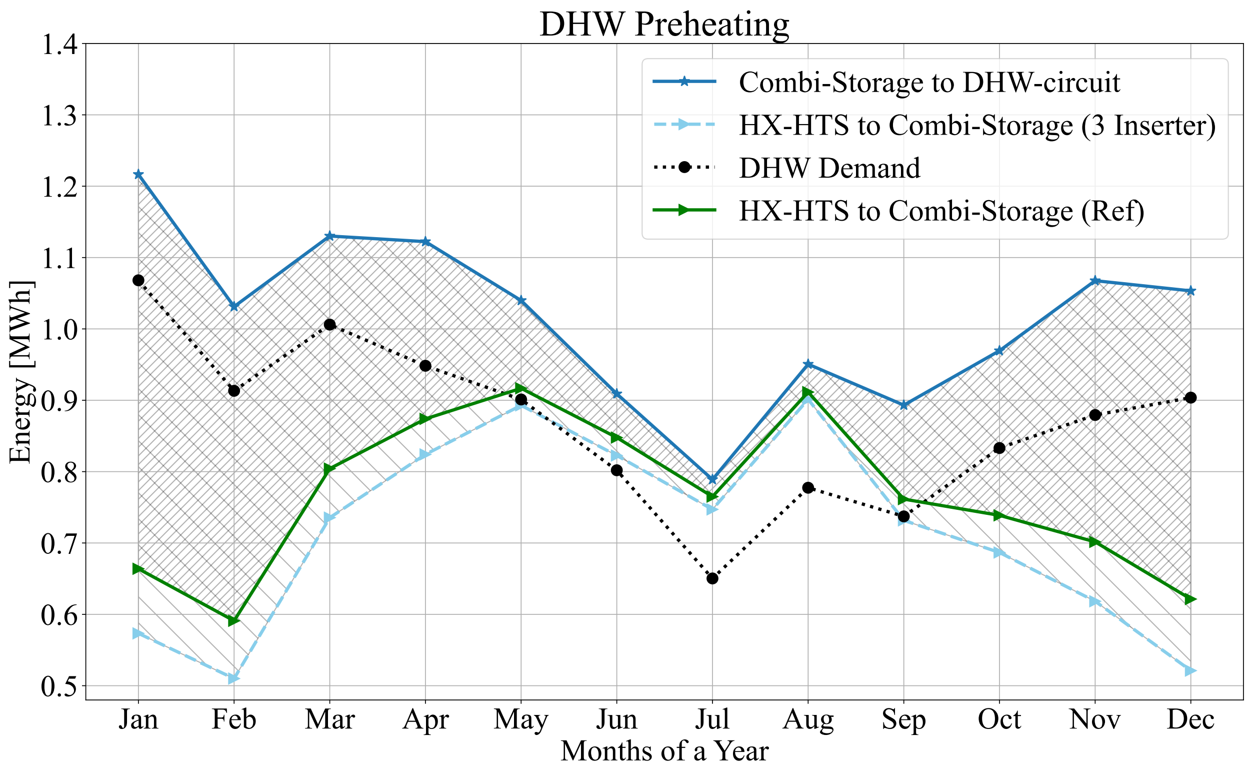

Figure 4.43.: Preheating DHW in reference system with three ideal inserters.

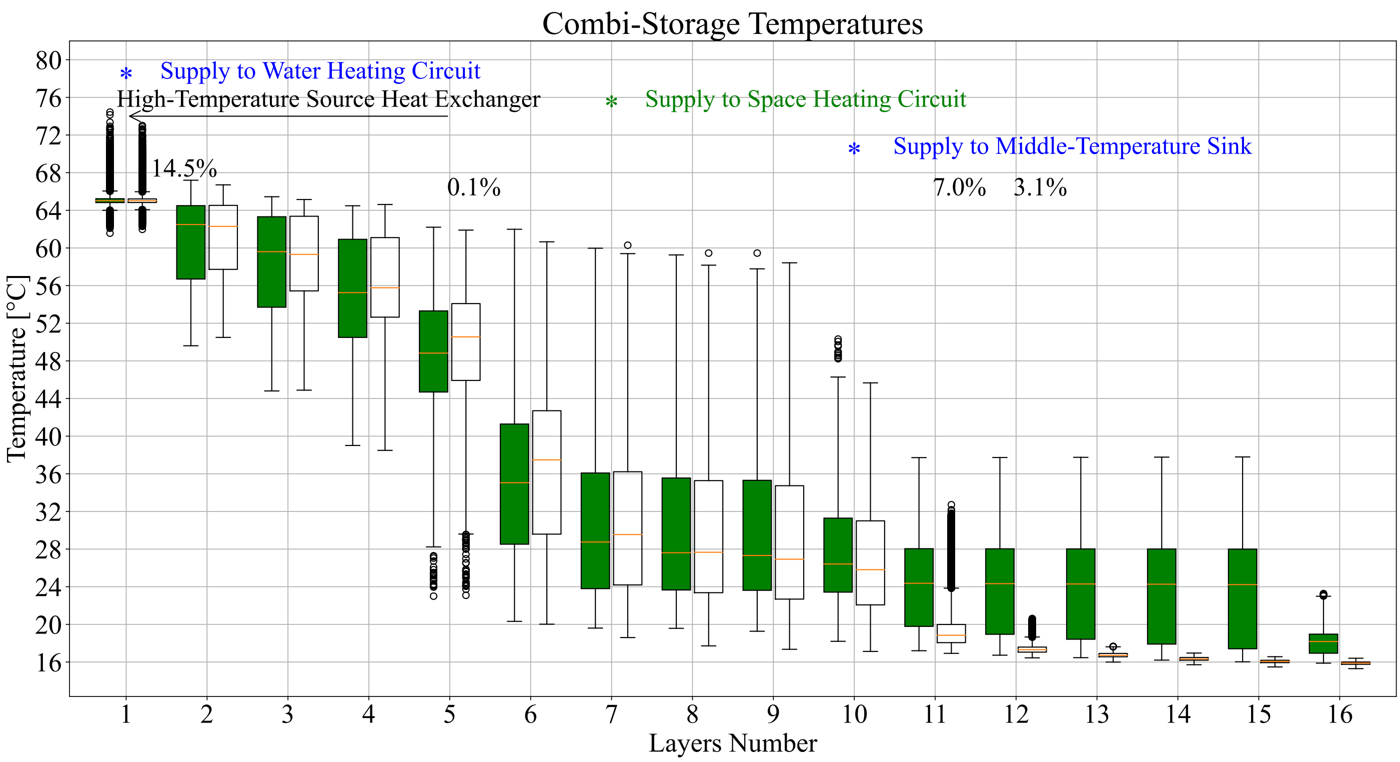

Figure 4.44.: Temperature layers in the reference system (green) and reference system with three ideal inserters. The outlier percentages indicate the share of transient temperature deviations relative to the total dataset for each layer in the three ideal inserters case.

4.2.3. Effect of Model Properties

4.2.3.1. Storage Properties

In this section, the number of layers in the Combi-Storage of the Reference System has been increased from 16 to 32 layers in order to explore the impact of storage properties on system characteristics. To keep power distribution consistent, just like in the 16-layer Reference System, we adjusted the hydraulic connections and system-level control in the system. Given the height of the storage, which is 2.03 meters, the changes in hydraulic connections can be divided into four main parts.

Firstly, power delivery through High-Temperature Source Heat Exchanger to the Combi-Storage. In this configuration, the supply water is extracted from a height of 1.43 meters, and the hot water from the High-Temperature Source Heat Exchanger returns to the top of the storage at 2.03 meters.

Secondly, Power supply within the Water Heating Circuit via 32-layer Combi-Storage. In this part, the supply water is extracted from a height of 1.94 meters, and the return water from the Water Heating Circuit is directed to the Combi-Storage through an ideal inserter.

Thirdly, power delivery from the Medium-Temperature Sink to the Combi-Storage. In this regard, the supply water to the Medium-Temperature Sink Heat Exchanger is extracted from a height of 0.79 meters, and the return hot water is directed to a height of 1.24 meters.

lastly, Power supply within the Space Heating Circuit with Combi-Storage. Here, the supply water is extracted from a height of 1.24 meters, and the return water goes to 0.16 meters.

Furthermore, the system-level control has undergone changes in two aspects.

Firstly, the measurement point for the PI controller regulating the DHW supply power with High-Temperature Heat exchanger to the Combi-Storage has been adjusted from 1 to 2.

Secondly, the measurement point for the PI controller managing the Space heating supply power in conjunction with the Medium-Temperature Sink Heat Exchanger to the Combi-Storage has been shifted from 7 to 13.

Additionally, the priority of the system has been set to the temperature of layer 2 instead of layer 1 in the 16-layer reference system, aiming to supply hot water within the Water Heating Circuit. Subsequently, when the temperature of layer 2 drops below 63 °C, the PI controller responsible for delivering power from the High-Temperature Source Heat Exchanger to the Combi-Storage is activated, while the PI controller related to the space heating supply power from the Medium-Temperature Sink Heat Exchanger to the Combi-Storage is deactivated.

A detailed analysis of the modified hydraulic connections and system-level control for the reference system with 32 storage layers, including their influence on comfort temperature ranges, GAHP operating behavior, and DHW preheating, is presented in section A.9.

In conclusion, Table 4.1 provides an overview of the Seasonal Gas Utilization Efficiency for the reference system and systems with various changes made during the sensitivity analysis. These changes were carried out while considering the system-level control strategy, aiming to improve DHW preheating and minimize temperature deviations in both the space heating and water heating circuits from their respective comfort temperature range.

The table highlights two key points. First, it identifies parameters with the potential for improving system performance beyond the capabilities of the current dual adsorber cycle GAHP technology. Second, it demonstrates that achieving a minimum SGUE of 1.3 is not feasible without a solar collector circuit, since the GAHP system is designed for renovated multi-family houses with 40 kW nominal power output.

N	**System**	**SGUE**
1	16-layer Reference System under Karlsruhe Weather Data	1.218
2	16-layer Reference System Using Three Ideal Inserters	1.213
3	16-layer Reference System with Maximum 110 °C Desorption Temperature	1.208
4	32-layer Reference System	1.203
5	16-layer Reference System	1.199
6	16-layer Reference System under Domestic Hot water Profile Variation	1.146

Table 4.1.: Seasonal Gas Utilization Efficiency (SGUE) comparison between the reference system and systems with various changes conducted during the sensitivity analysis.

4.3. Analysis of Single Adsorber Cycle Gas Adsorption Heat Pump with a Combi-Storage in Representative Points in accordance with standards

The heating system including single adsorber cycle GAHP (Figure 2.10) is simulated within Dymola program over a three-day period using prescribed load points defined in Table 2.4. For each load point, the supply and return temperatures as well as the heating load are fixed and applied as constant boundary conditions throughout the simulation. During this period, multiple cycles are executed until the results stabilize and exhibit periodicity. Periodicity is achieved when the system state at the end of cycle n is equivalent to the state at the end of cycle $n + 1$. A three-day simulation period was generally adequate for achieving equilibration. During the final ten cycles, the fluctuation in Gas Utilization Efficiency (GUE) consistently remained below 0.3 %. Consequently, the final cycle was selected for further analysis and evaluation.

The idealized standard cycle of an adsorption heat pump, as outlined in subsection 1.1.1, comprises two isosteric and two isobaric phases [27]. However, in real systems, perfectly isosteric processes do not occur due to the heat capacity of the metal and the water within the evaporator/condenser [27]. In systems utilizing a module with separate evaporators and condensers, as shown in the right module of Figure 2.8, the switching phases between adsorption and desorption occur with the vapor valves closed and at intermediate pressures. Under these conditions, mass transfer is strongly suppressed, and the switching phases are therefore much closer to isosteric behavior, although not perfectly isosteric due to the thermal inertia of the system. By contrast, in systems with a combined E/C HX and no internal vapor valves, mass transfer continues during the switching phases, resulting in larger deviations from isosteric behavior [27].

In the simulated single adsorber cycle, the process will be described by pre-cooling, which starts at the end of the desorption phase to cool the desorber and condenser, as depicted in Figure 4.45. This pre-cooling is facilitated by the flexibility of connecting the single adsorber cycle GAHP to the stratified storage, allowing the condenser temperature to drop from the supply space heating temperature to the temperature of the storage bottom layer over a 180 s interval, as shown in the second plot of Figure 4.46.

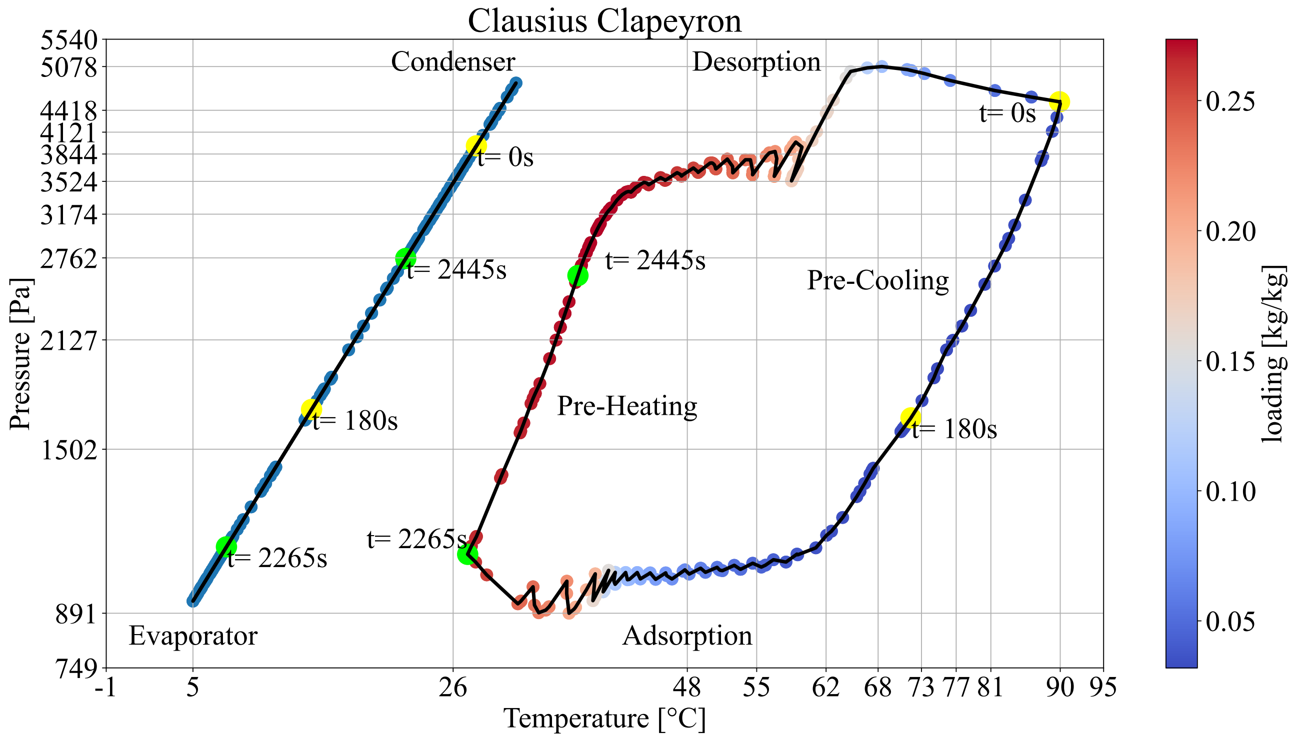

Figure 4.45.: Variation in pressure, temperature, and loading for a working pair in adsorber/desorber (right plot) and variation in pressure vs. temperature in evaporator/condenser on the working fluid side (left plot). This data corresponds to a heating system integrating with a single adsorber cycle GAHP operating at a 13 % part load ratio (refer to Table 2.4) for a cycle, with the maximum high-temperature source set at 90 °C. Timestamps associated with the transition phases are displayed along the curves to link characteristic operating points to the corresponding time series.

Time Point	**Desorber**		**Condenser**	
	Temperature (°C)	**Pressure (Pa)**	**Temperature (°C)**	**Pressure (Pa)**
Start	90	4540	28.7	3946
End	72.1	1660	15.0	1705

Table 4.2.: Desorber and condenser conditions during 180 s transition.

Time Point	**Adsorber**		**Evaporator**	
	Temperature (°C)	**Pressure (Pa)**	**Temperature (°C)**	**Pressure (Pa)**
Start	28	1075	8.4	1101
End	37.9	2612	22.7	2758

Table 4.3.: Adsorber and evaporator conditions during 180 s transition.

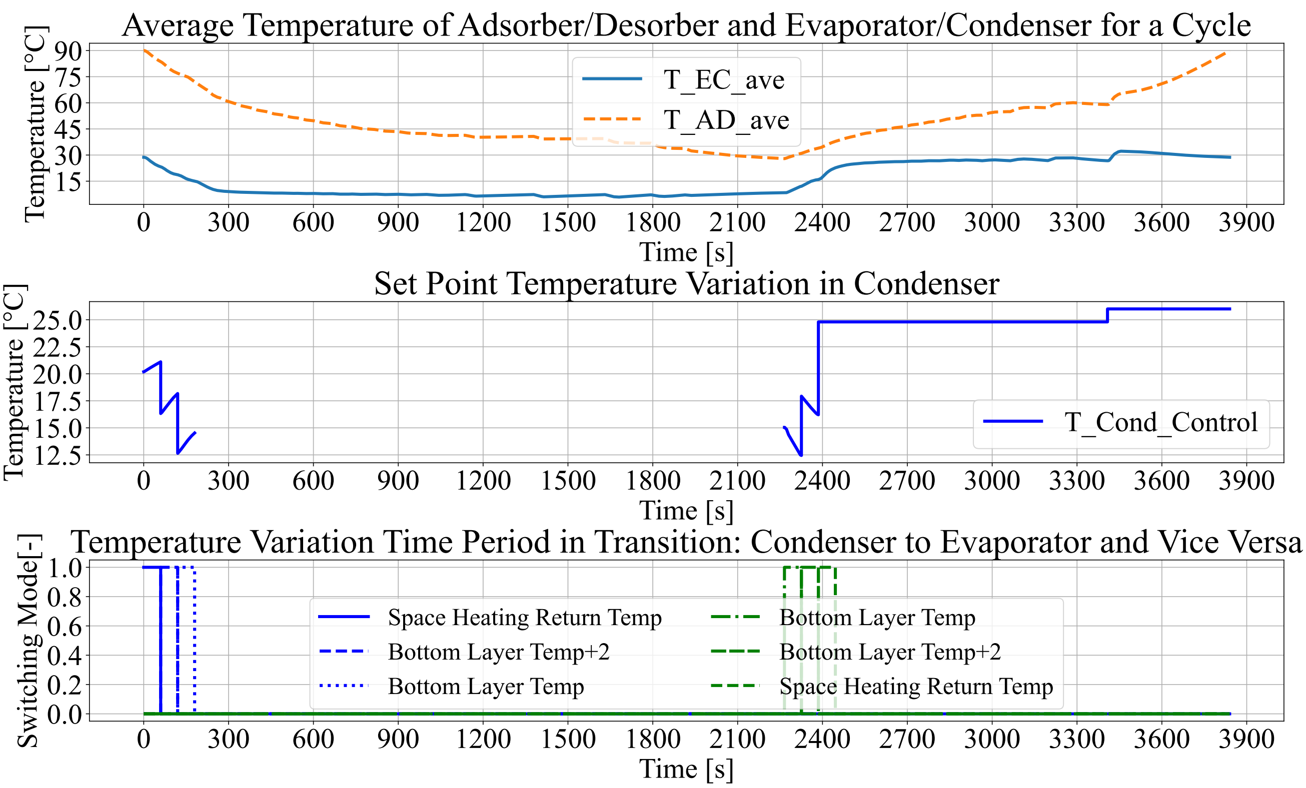

Figure 4.46.: Time series of the average temperatures of the adsorber/desorber and evaporator/condenser, as well as the condenser set point temperatures for the ideal extractor valve in the supply line of the evaporator/condenser, and the activation time period of the valve during transition mode. This data corresponds to a heating system integrating with a single adsorber cycle GAHP operating at a 13 % part load ratio (refer to Table 2.4) for a cycle, with the maximum high-temperature source set at 90 °C.

The pre-cooling process stores the available heat from the condenser in the storage. If this heat is not stored, some of the condensation heat during the next desorption process will be used to achieve the necessary sensible heating of the condenser to reach space heating return temperature. However, by storing and using this heat, a greater amount of condensation heat remains within the useful temperature range, thereby improving the performance.

During pre-cooling, a transition phase of 180 s is applied by extracting water from the storage at 50 % of the nominal Adsorber/Desorber mass flow rate specified in Table 2.3 at subsection 2.3.5. This flow is used to cool the desorber, while the condenser mass flow rate remains unchanged. However, the condenser temperature decreases during this phase, as shown in the second plot of Figure 4.46. The results of the 180 s transition phase, shown in the loading plot of Figure 4.47, indicate that a reduction in adsorbent loading occurs during the first 30 s of pre-cooling. This reduction is caused by the high desorber temperature and the decrease of the condenser supply temperature from the space heating supply level to the space heating return level. Furthermore, Figure 4.45 shows that the pre-cooling process is not fully completed at the end of the 180 s period. After this phase, the condenser is connected to the borehole heat exchanger and further cooled until it reaches the evaporator temperature.

Under ideal isosteric switching conditions, the adsorber and condenser heat exchangers would be cooled synchronously, such that the equilibrium loading remains constant. In the present system, however, the adsorber is cooled more rapidly during pre-cooling, which shifts the equilibrium and initiates adsorption already in this phase. As a consequence, a fraction of the previously condensed working fluid evaporates and is adsorbed by the adsorbent, leading to a further reduction in the condenser temperature [118].

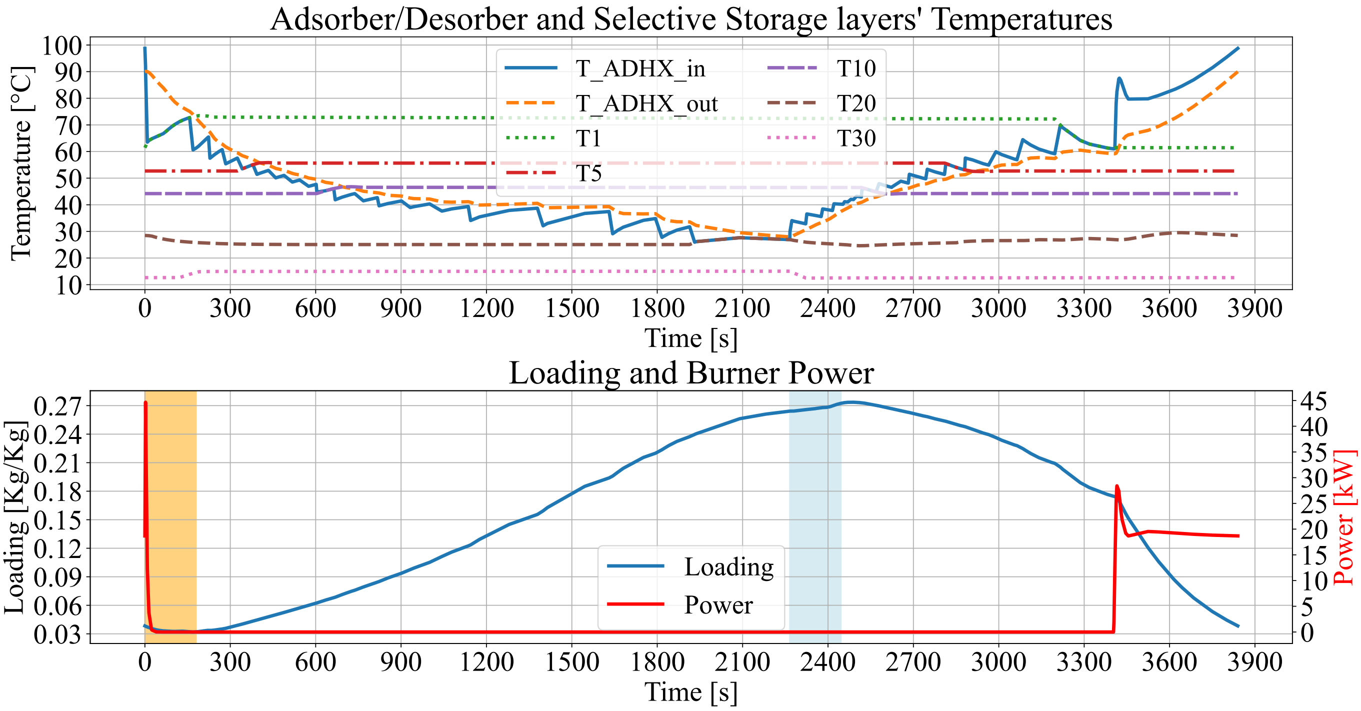

Figure 4.47.: Time series of heat transfer fluid supply and return temperatures for the adsorber/desorber, combi-storage representative layers' temperatures, loading, and burner power. This data corresponds to a heating system integrating with a single adsorber cycle GAHP operating at a 13 % part load ratio (refer to Table 2.4) for a cycle, with the maximum high-temperature source set at 90 °C. The orange and light blue shaded regions indicate two 180s transition phases.

The Coefficient of performance and power density of gas adsorption heat pumps must be balanced as a trade-off [16, 17, 26]. In the single adsorber cycle, additional degrees of freedom arise from the ability to select which layers of the stratified storage are used for heat exchange. As a result, the adsorption process starts with a low adsorption rate, as indicated by the loading plot in Figure 4.47. This low rate is due to the extraction water from a high-temperature layer (T1 in Figure 4.47), which is a compromise for effective heat recovery. Then, inserting water from the lower temperature layer of storage into the adsorber increases the driving temperature between adsorber and stratified storage, subsequently enhancing the rate of adsorption.

The pressure fluctuations observed during the adsorption and desorption phases (Figure 4.45) arise from the dynamic coupling between the adsorber/desorber and the evaporator/condenser (E/C) in a single-adsorber module without internal vapor valves. In this configuration, the vapor space remains permanently connected, such that system pressure is not externally imposed but evolves from the instantaneous balance between adsorption or desorption in the adsorbent and evaporation or condensation in the E/C HX. Due to finite heat transfer rates in both heat exchangers and actively controlled hydraulic boundary conditions, the adsorber/desorber and E/C HX temperatures do not change synchronously. This thermal mismatch leads to transient deviations between the equilibrium pressure of the adsorbent and the saturation pressure of the working fluid, resulting in oscillatory pressure behavior during nominally isobaric phases, described in subsection 1.1.1. The effect is further amplified by the steep, S-shaped adsorption isotherm of the SAPO-34/water working pair, for which small temperature changes induce pronounced variations in loading and vapor mass transfer (Figure 4.48). In the present model, the adsorber is discretized into two serial nodes, which is sufficient for seasonal system-level simulations but leads to sharper, saw-tooth-like pressure variations compared to more spatially resolved models or real systems. For instance, Schwamberger's detailed model employs approximately 100 adsorber nodes [16], yielding significantly smoother pressure trajectories. Consequently, the observed pressure fluctuations should be interpreted as the combined result of physical limitations inherent to single-adsorber systems without vapor valves and numerical effects associated with reduced spatial discretization, rather than as a physical instability or a fundamental design flaw.

During the pre-heating phase, the evaporator temperature must reach the condenser temperature. Thus, the evaporator connects to the storage. A 180 s transition phase occurs by extracting water from storage at 50 % of the nominal Adsorber/Desorber mass flow rate specified in Table 2.3 at subsection 2.3.5 to heat up the adsorber, while the mass flow rate of the evaporator remains unchanged. However, the evaporator temperature levels changes, as shown in Table 2.2. The results of 180 s transition phase, as presented in Table 4.3 and Figure 4.45, show that pre-heating does not conclude at the end of this period. The pre-heating process causes some of the working fluid within the adsorbents desorb and flow to the evaporator, which increases the evaporator temperature to reach the space heating return temperature, explaining why the pre-heating process is not an isosteric process. Figure 4.49 clearly shows that the heat recovery occurs during transition modes between evaporator and condenser in a single adsorber cycle, which is connected to the stratified storage tank. In the first transition mode, the condenser heat is delivered to the storage, resulting the bottom layer temperatures to increase. In contrast, during the second transition mode, cold water is delivered to the storage, resulting in a decrease in the bottom layer temperatures.

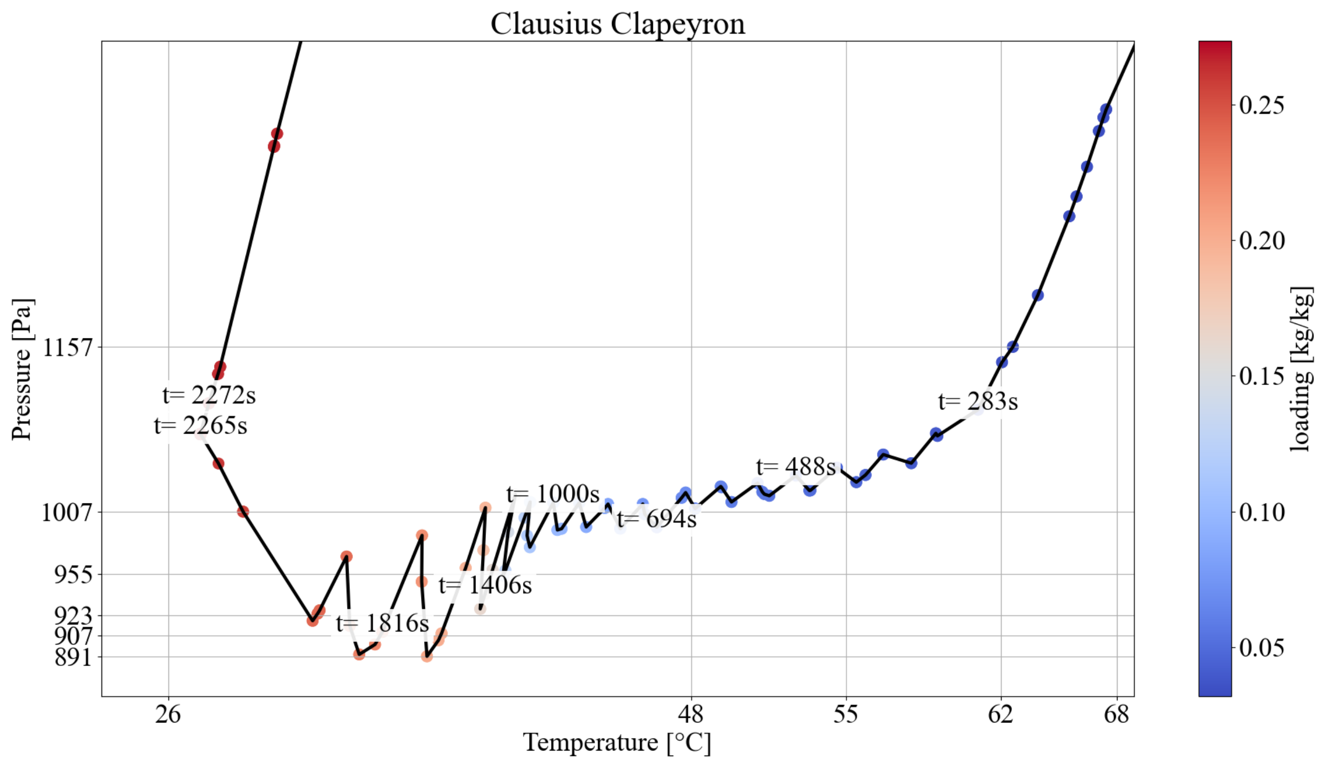

Figure 4.48.: Magnified view of the bottom region of the Clausius–Clapeyron plot shown in Figure 4.45.

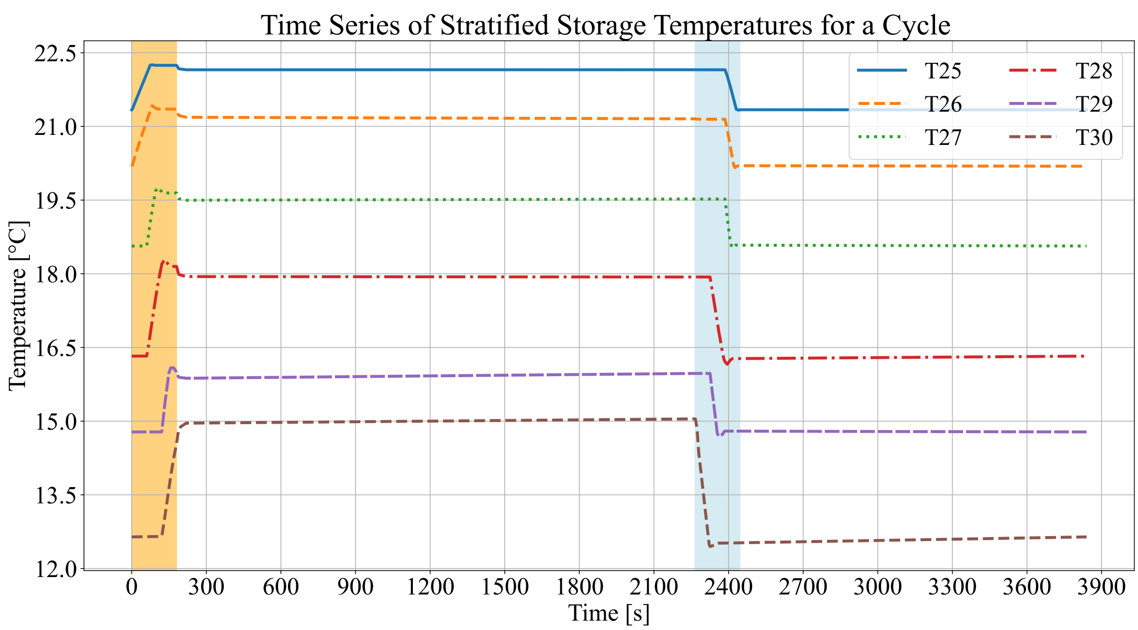

Figure 4.49.: Storage bottom layers temperature and transition mode from condenser to the evaporator (orange shaded area) and from evaporator to the condenser (light blue shaded area). This data corresponds to a heating system integrating with a single adsorber cycle GAHP operating at a 13 % part load ratio (refer to Table 2.4) for a cycle, with the maximum high-temperature source set at 90 °C.

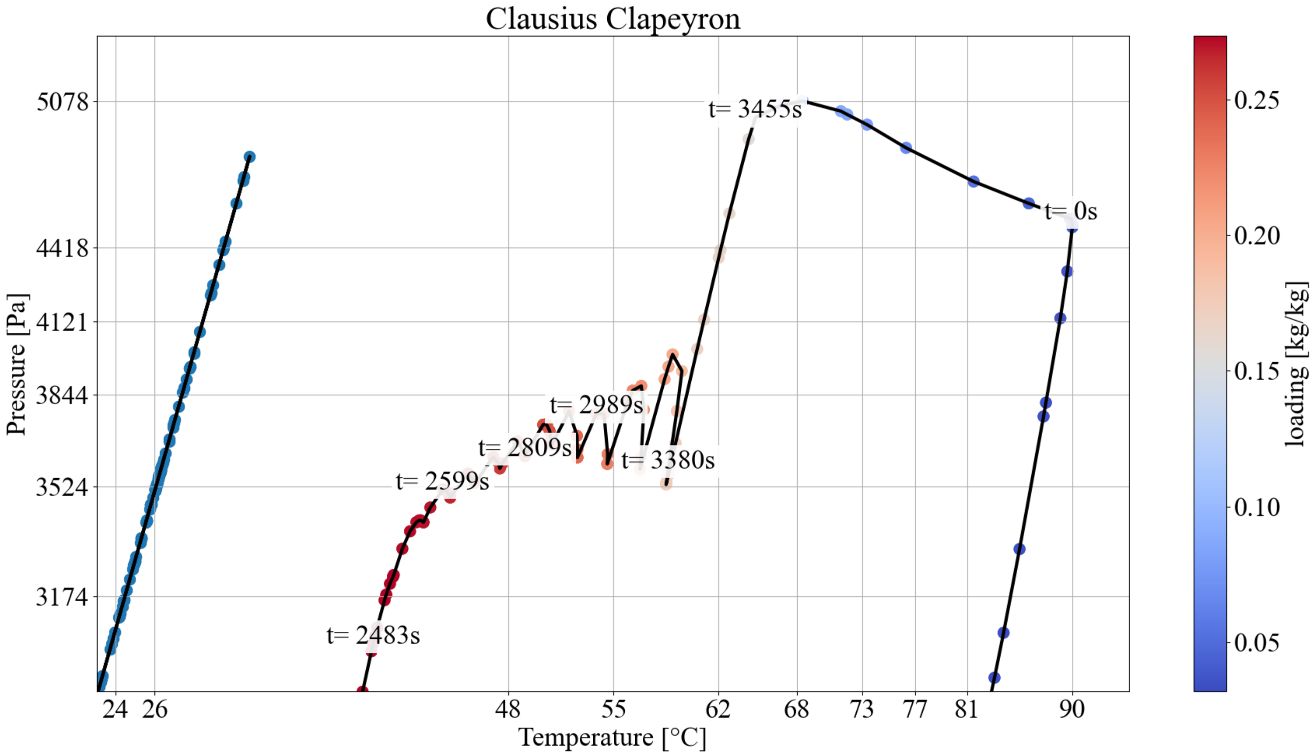

Figure 4.50.: Magnified view of the upper region of the Clausius–Clapeyron plot shown in Figure 4.45.

Similar to the start of the adsorption process, Figure 4.50 shows that at the beginning of the desorption process the pressure in the desorber is temporarily higher than the saturation pressure of the condenser. This behavior is not caused by a delay in the control system. Instead, it results from a rapid decrease in adsorbent loading and from the thermal response of the condenser. The heat transfer rate on the condenser side decreases because the condenser temperature setpoint changes and because the condenser heat exchanger has a finite thermal mass. These effects limit the rate of condensation and therefore delay the pressure reduction in the desorber.

As the extraction index approaches the first layer with the highest temperature, the desorption process requires a higher water temperature to proceed effectively. Consequently, the burner is activated and connected to the desorber, as represented by the red plot in Figure 4.47. This activation results in a noticeable increase in pressure, as demonstrated in Figure 4.50. The connection between the desorber and the burner remains until the desorber outlet temperature reaches 90 °C. At this point, one cycle completes.

When the desorber outlet temperature reaches 90 °C, the burner is switched off and hydraulically connected to the stratified storage by redirecting the mass flow from the adsorber circuit to the storage circuit. As the burner heat exchanger still contains a significant amount of sensible heat, the temperature difference between the burner and the storage water initially induces a high conductive heat transfer rate. This results in a short power peak at the beginning of the cycle, as shown in the burner power time series in Figure 4.47 This transient power peak is therefore transferred to the storage, rather than to the adsorber. Following the module-level control strategy, if the temperature difference between the mean adsorbents temperature and the inlet water temperature is less than 2 °C, the extraction layer is altered. Consequently, the inlet temperature to the adsorber/desorber changes during an adsorber cycle in Figure 4.47. Moreover, the plot shows that the stratified storage layer temperatures increase during adsorption, while they decrease during desorption. It is also evident from Figure 4.47 that the desorption phase is significantly shorter than the adsorption phase, which not only serves as an efficient parameter to maximize COP and power density [139], but is also contrary to the behavior observed in the reference GAHP [63].

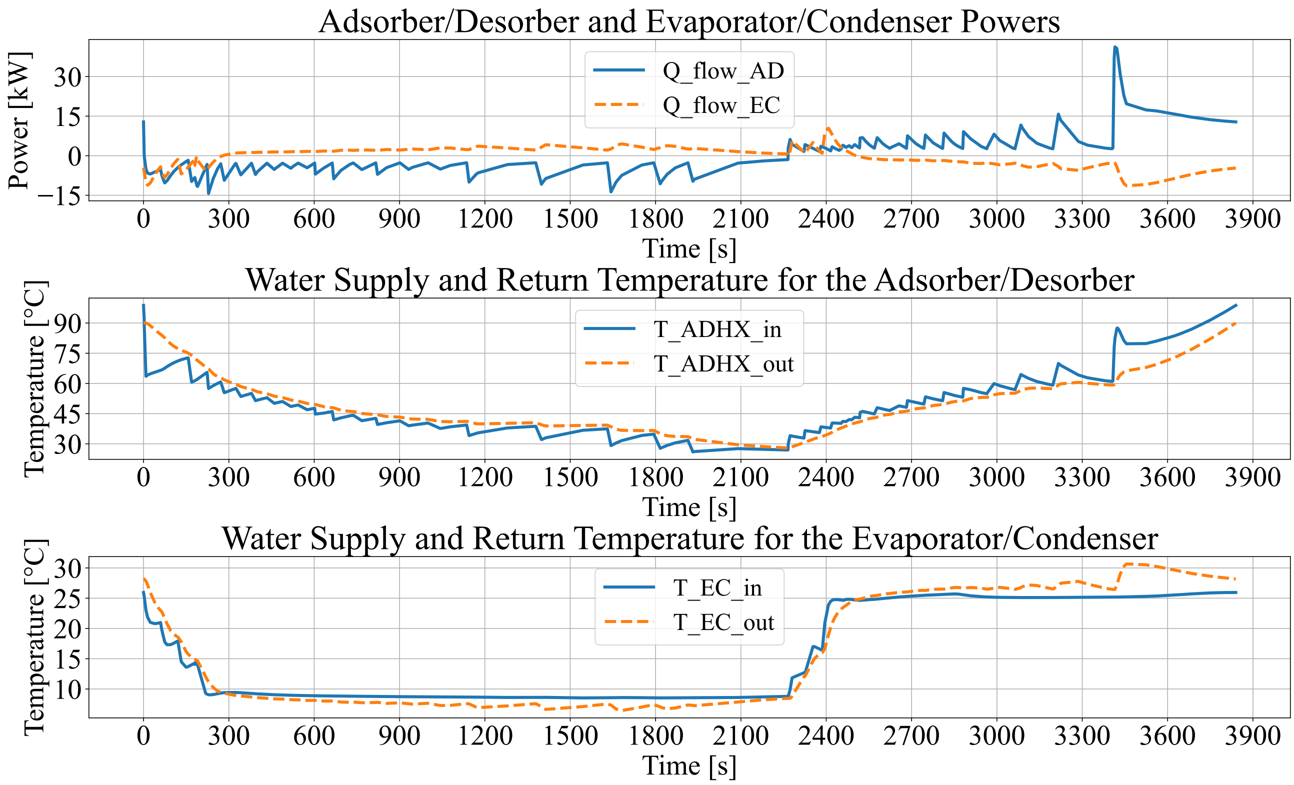

Figure 4.51.: Time series of power, supply, and return temperatures of heat transfer fluid for a module. This data corresponds to a heating system integrating with a single adsorber cycle GAHP operating at a 13 % part load ratio (refer to Table 2.4) for a cycle, with the maximum high-temperature source set at 90 °C.

The adsorber power time series within a cycle is depicted in Figure 4.51. It shows that the first 180 s are associated with the transition mode from the desorption to adsorption process. Subsequently, the adsorption process takes place. Another 180 s, a transition mode from adsorption to the desorption process occurs, followed by the desorption process to complete a cycle processes. In the second plot, the extraction and insertion of water from stratified storage into the adsorber/desorber are presented. Finally, the last plot illustrates the inlet and outlet heat transfer fluid temperature within the evaporator/condenser. The nearly identical inlet and outlet water temperatures at the end of each 180 s transition phase indicate that the stratified storage can no longer provide additional cooling to the evaporator/condenser through the selected hydraulic connections. Consequently, extending the transition period beyond 180 s would not yield further thermal benefit, which justifies the choice of a 180 s duration for the transition phases. The time series

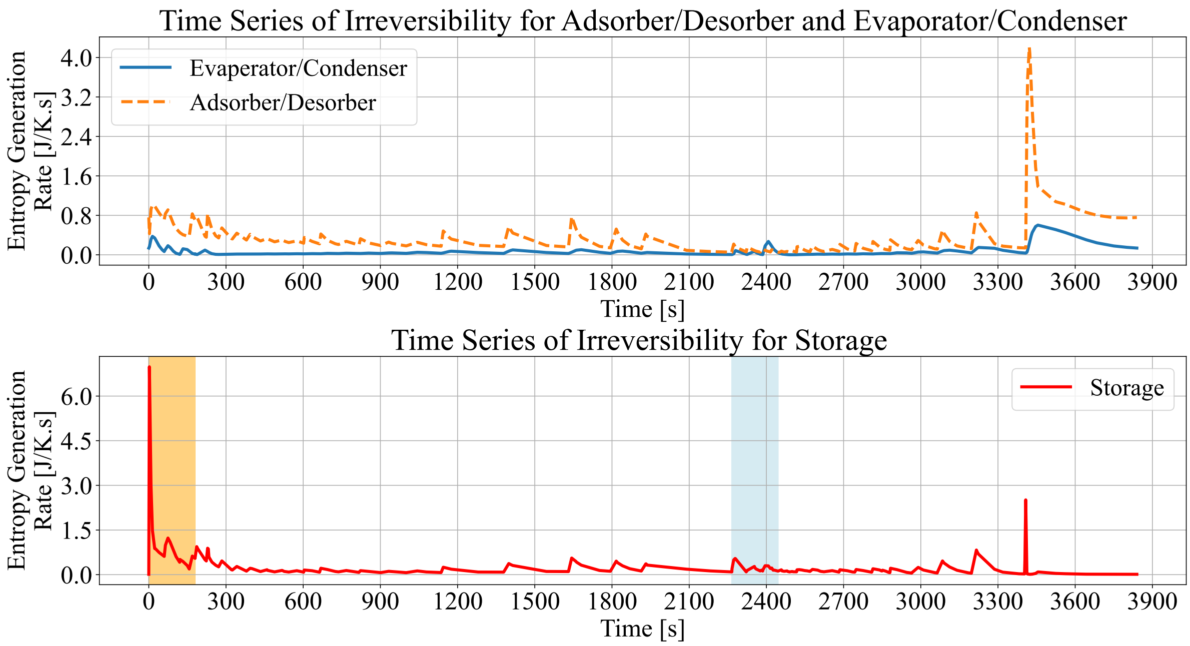

Figure 4.52.: Time series of entropy generation rate within module and storage as well as transition mode from condenser to the evaporator (orange shaded area) and vise versa (blue shaded area). This data corresponds to a heating system integrating with a single adsorber cycle GAHP operating at a 13 % part load ratio (refer to Table 2.4) for a cycle, with the maximum high-temperature source set at 90 °C.

of the entropy generation rate within the adsorber/desorber and storage is presented in Figure 4.52. This representation provides insights into when and where the entropy generation rate is notably high. Figure 4.52 also presents a segment of the control strategy during the transition mode from desorption to adsorption and vice versa. There are two noticeable spikes in the entropy generation rates: the first in the desorber and the second in the storage. The initial plot shows the first spike, which is associated with the activation of the burner and its connection to the desorber. This connection causes a sudden increase in the temperature of the heat transfer fluid in the desorber, resulting in higher entropy generation rate. Furthermore, the second spike at the beginning of a cycle within the combi-storage is linked to the connection of adsorber to the combi-storage at the end of the desorption process. Consequently, the notable temperature difference between desorber and the first layer of the combi-storage results in a higher entropy generation rate at the beginning of the cycle.

As described in the control strategy in subsection 2.3.5, the mass flow rates and temperature levels during the transition phases are adjusted using standard thermal control rules. Entropy-related values are not used directly in the control. However, the resulting system operation shows a reduction in the entropy generation rate in both the adsorber and the stratified storage. This reduction is therefore a consequence of the applied control strategy rather than a design target. The lower entropy generation also supports better thermal stratification in the storage and helps to explain the thermodynamic effects of the chosen control approach. To illustrate the contribution of storage irreversibility in the single-adsorber GAHP cycle, the sources of relative irreversibility are analyzed in Figure 4.53 through Figure 4.56 for the load points defined in VDI 4650-2 [73], as listed in Table 2.4. The analysis reveals that the largest contribution to irreversibility is associated with storage. The second-largest source is attributed to "HTF-TW-AD," which refers to heat and mass transfer within the pipe between the heat transfer fluid and the tube wall in the adsorber/desorber. The third-largest source, "AD-EC," represents heat transfer between the adsorber/desorber and the evaporator/condenser. The fourth-largest contributor, "HTF-TW-EC," corresponds to heat and mass transfer inside the pipe between the heat transfer fluid and the tube wall in the evaporator/condenser. Finally, the fifth-largest portion, "WP-TW-AD," represents heat transfer between the working pair and the tube wall in the adsorber/desorber.

Another key observation from comparing relative irreversibility across various partial load conditions (as shown in Figure 4.53, Figure 4.54, Figure 4.55, and Figure 4.56) is that storage relative irreversibility increases as the partial load rises. This increase can be attributed to the temperature distribution across layers within the storage, as shown in Figure 4.57, Figure 4.58, Figure 4.59, and Figure 4.60. Proper thermal stratification results in reduced storage relative irreversibility. It is important to note that the stratified storage tank is designed to maintain conditions comparable to those in the reference system [26] for accurate comparison with the single adsorber cycle GAHP, and it is not sized to serve as a buffer for hot water preparation and heating. Consequently, these factors contribute to suboptimal thermal stratification, with certain layers exhibiting minimal temperature variation.

Furthermore, comparing the relative irreversibility of the dual adsorber (Figure 4.19) and the single adsorber (e.g. Figure 4.54) reveals that while external temperature coupling losses in the adsorber are reduced in the single adsorber configuration, new irreversibilities—primarily due to storage mixing—are introduced. The tradeoff between these different losses is influenced by component sizing, control parameter selection, and the level of technological advancement, particularly improvements in heat and mass transfer through adsorbent composites. However, due to production constraints, the AdoSan testbed did not incorporate the planned adsorbent composite technology. In a single adsorber cycle, the integration of advanced adsorbent composites enhances heat and mass transfer, leading to shorter cycle times and, consequently, reduced storage mixing. As adsorber technology advances, this tradeoff improves, reinforcing the importance of entropy balancing as a crucial tool for optimizing component sizing and control strategies.

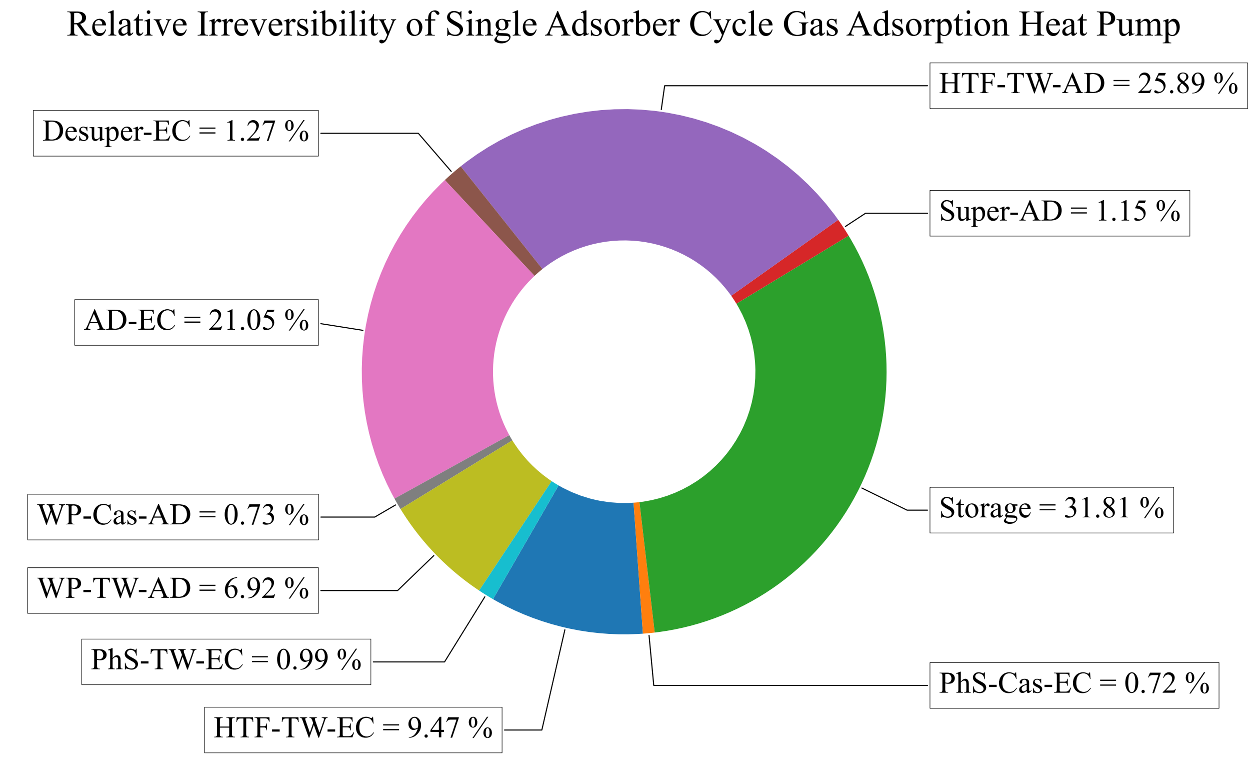

Figure 4.53.: Relative irreversibility for distinct elements within a module. This data corresponds to a heating system integrating with a single adsorber cycle GAHP operating at a 13 % part load ratio (refer to Table 2.4) for a cycle, with the

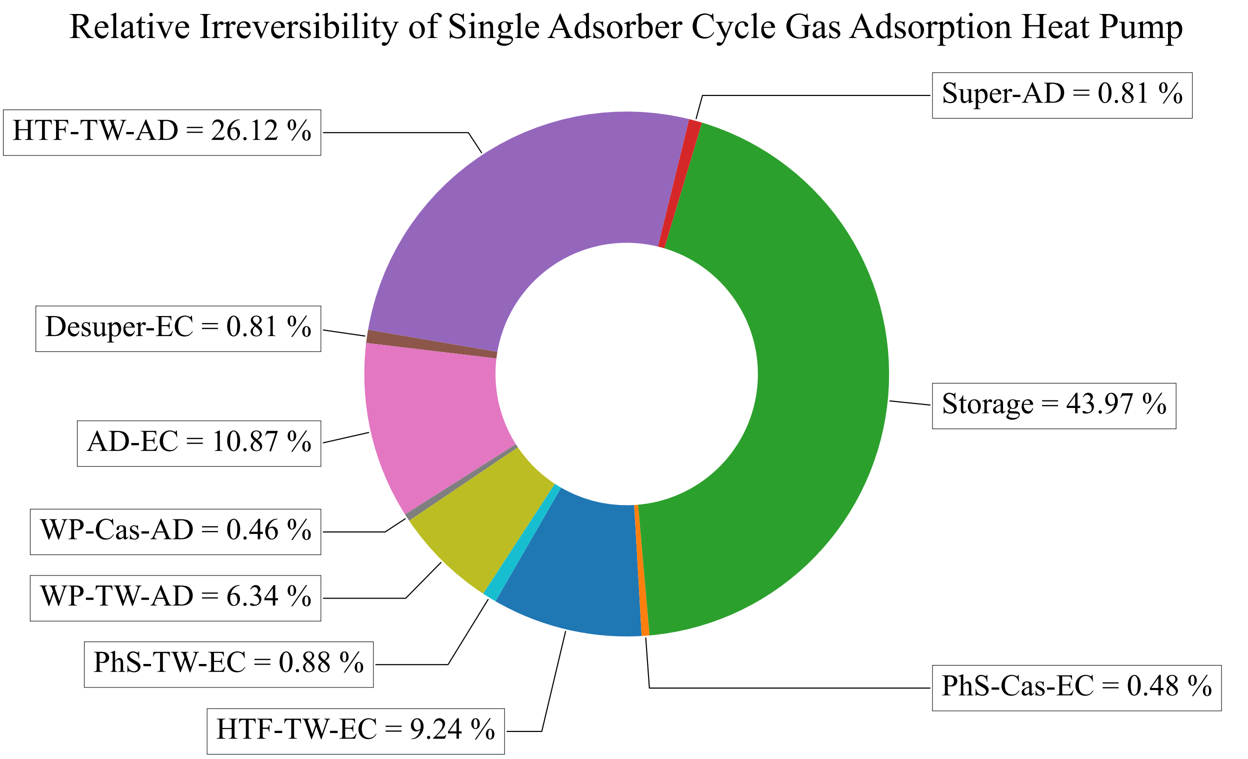

Figure 4.54.: 30 %.

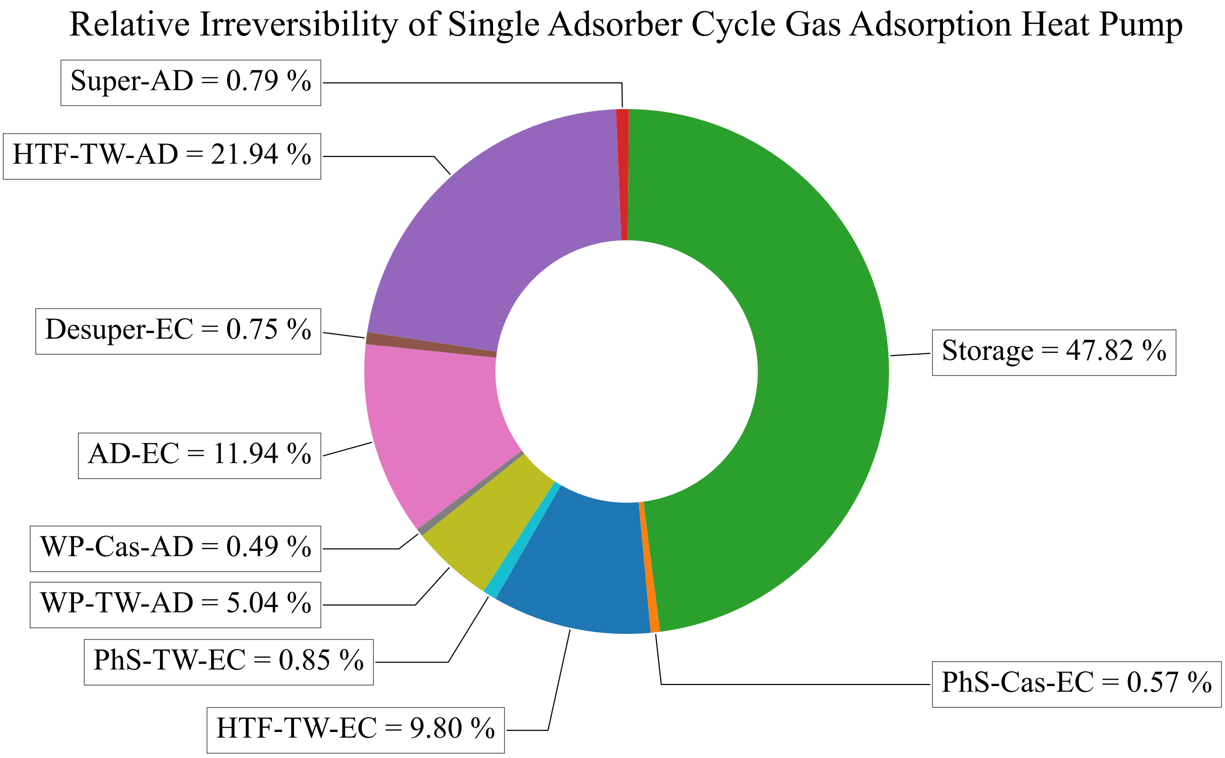

Figure 4.55.: 39 %.

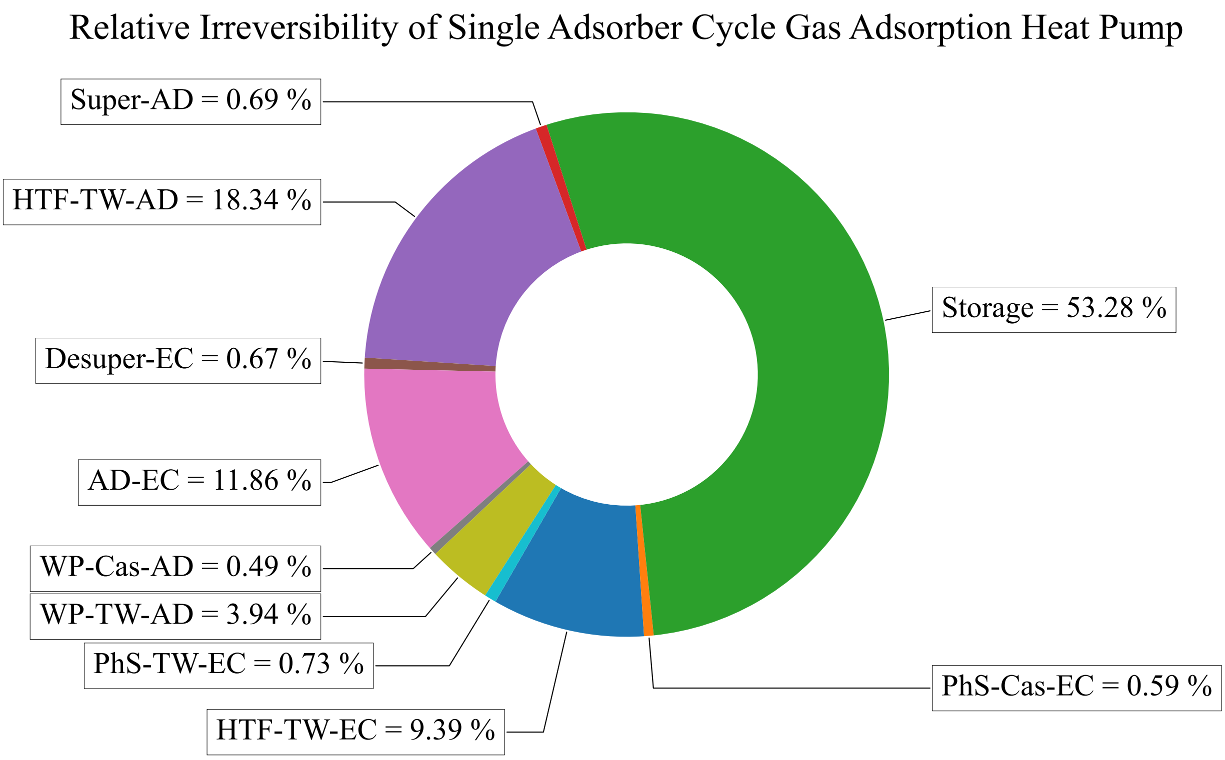

Figure 4.56.: 48 %.

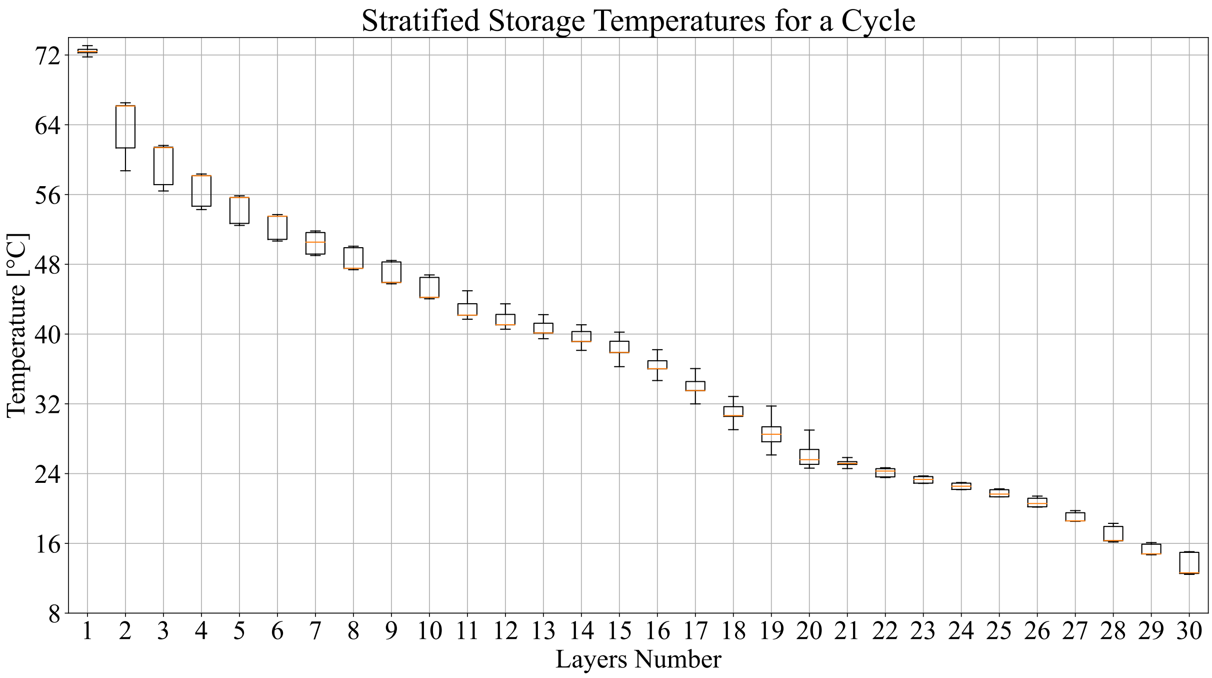

Figure 4.57.: Combi-Storage layers' temperatures for a heating system integrating with a single adsorber cycle GAHP operating at a 13 % part load ratio (refer to Table 2.4) for a cycle, with the maximum high-temperature source set at 90 °C.

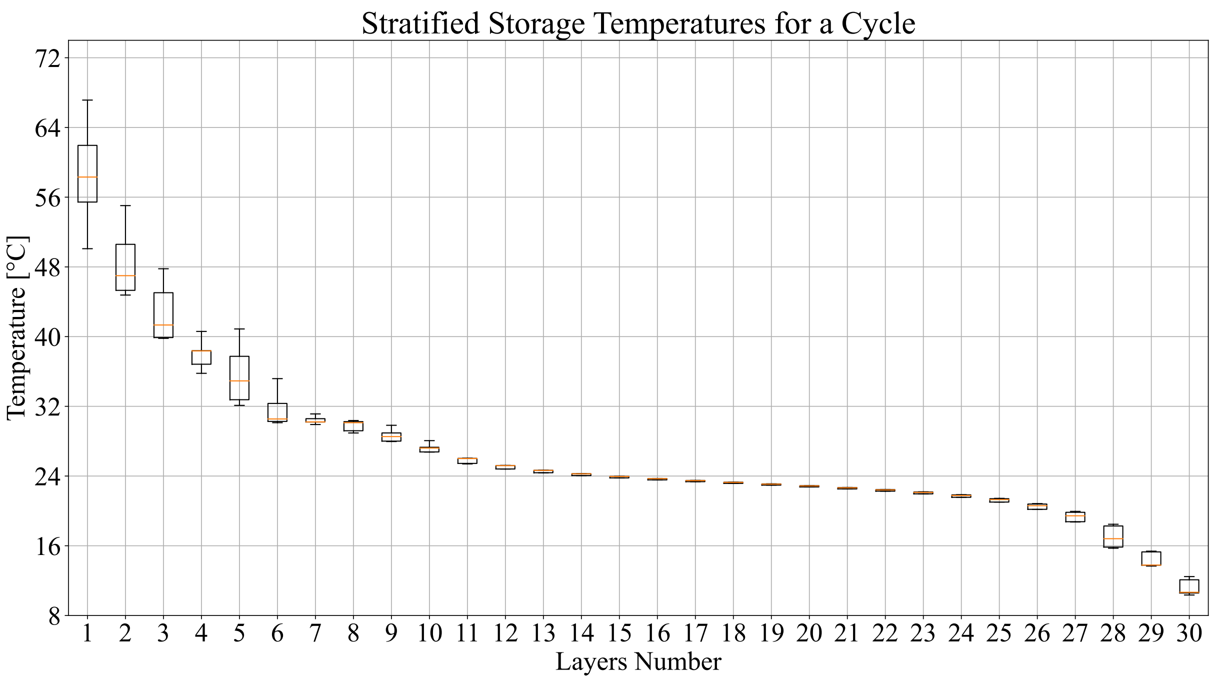

Figure 4.58.: 30 %.

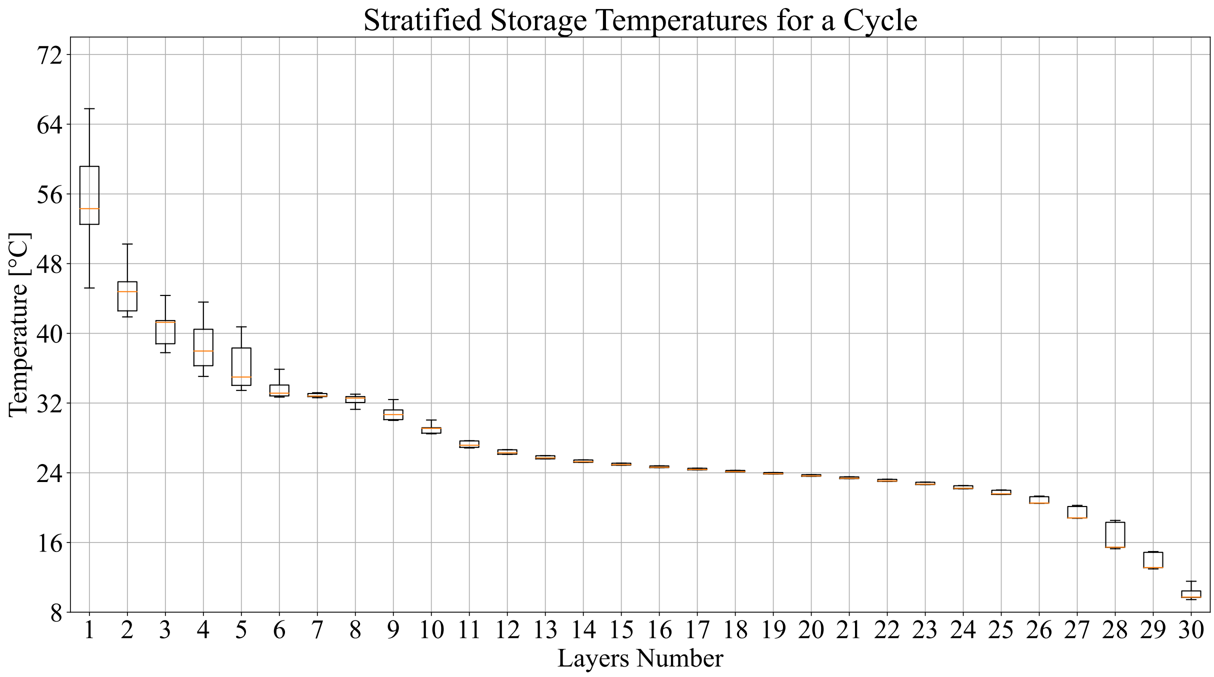

Figure 4.59.: 39 %.

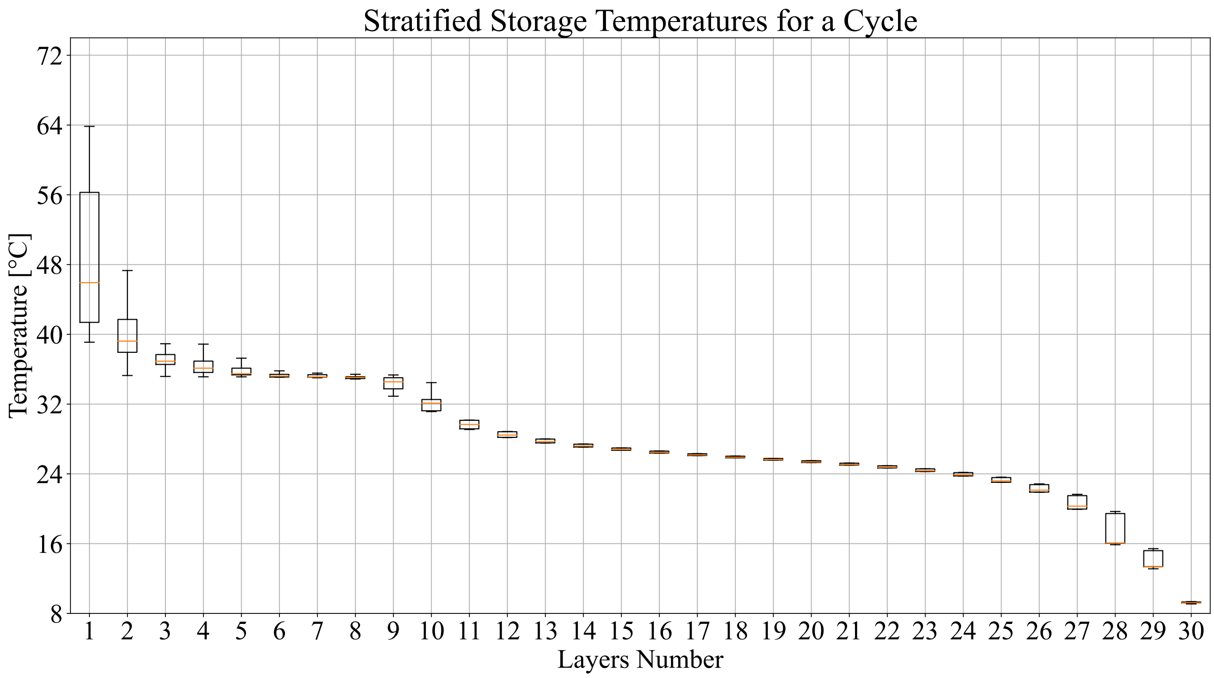

Figure 4.60.: 48 %.

Similar to the 13 % partial load presented in Figure 4.49, sensible heat recovery between the condenser and evaporator also occurs at other partial load conditions, as illustrated in Figure 4.49, Figure 4.61.

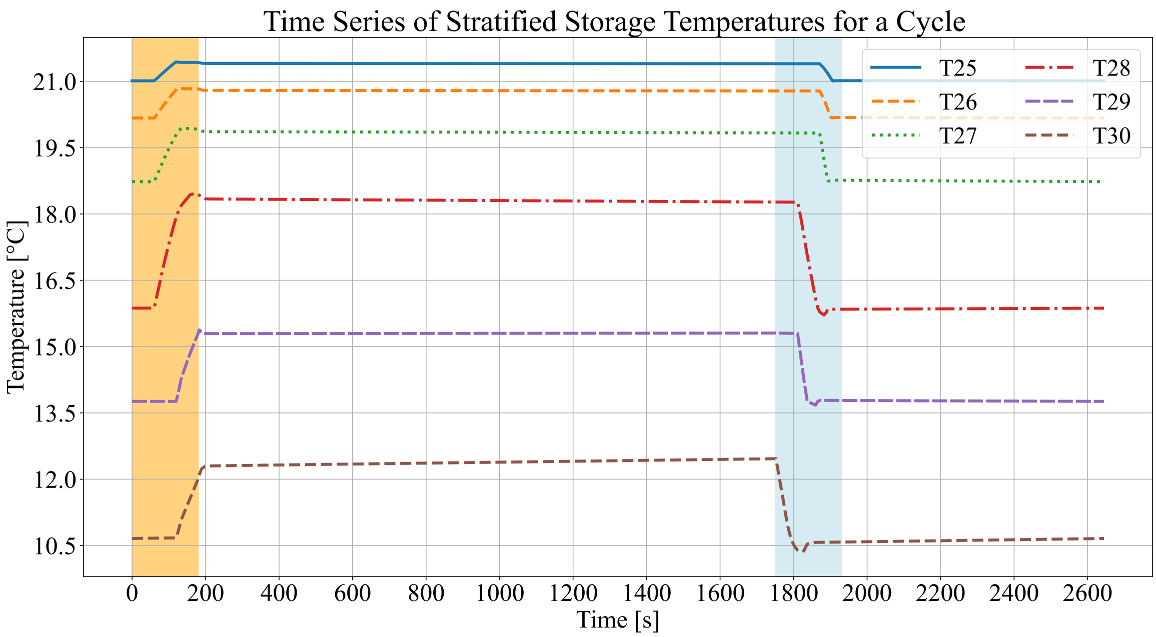

Figure 4.61.: Storage bottom layers temperature and transition mode from condenser to the evaporator (orange shaded area) and from evaporator to the condenser (light blue shaded area). This data corresponds to a heating system integrating with a single adsorber cycle GAHP operating at a 30 % part load ratio (refer to Table 2.4) for a cycle, with the maximum high-temperature source set at 90 °C.

Increasing the part load ratio, results in several consequences. Firstly, the minimum desorption loading increases, while the maximum adsorption loading decreases, namely in Figure 4.45, Figure 4.62, Figure 4.63, and Figure 4.64.

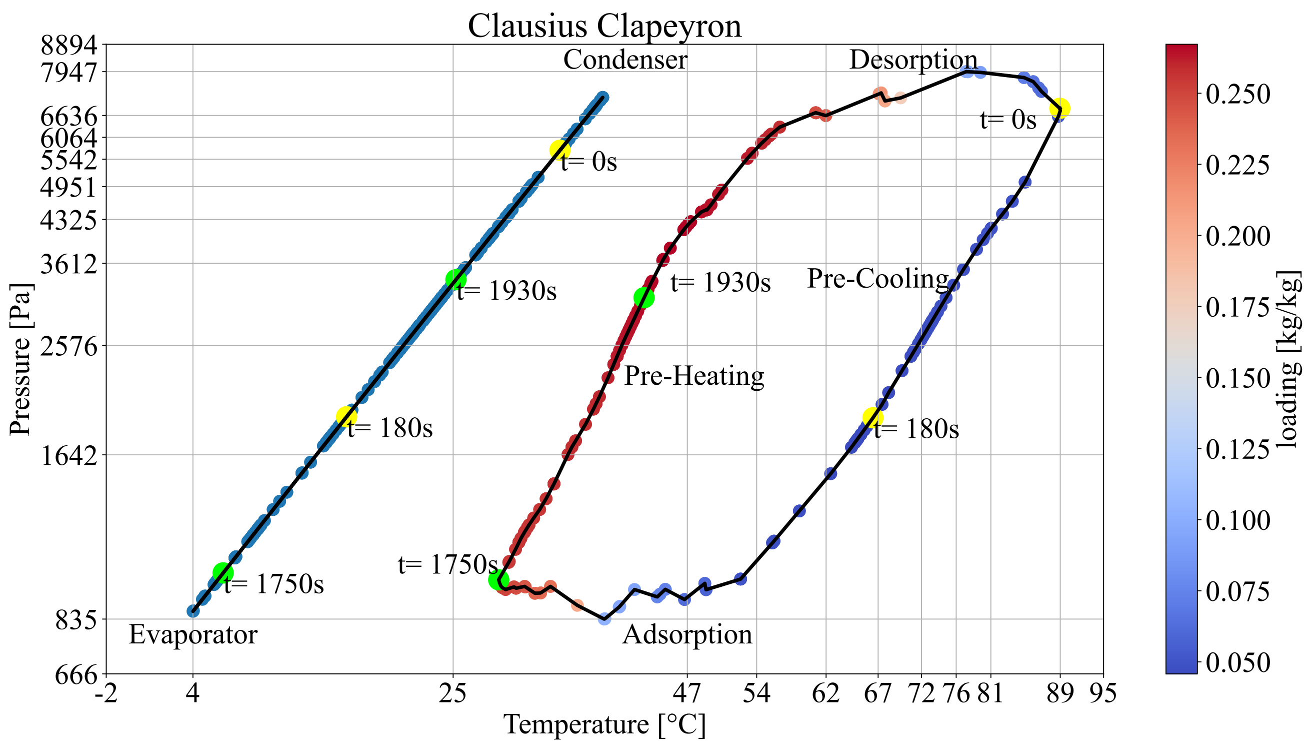

Figure 4.62.: 30 %.

Time Point	Desorber		Condenser	
	Temperature (°C)	Pressure (Pa)	Temperature (°C)	Pressure (Pa)
Start	89.7	6834	35.4	5750
End	67.3	1913	16.9	1920

Table 4.4.: Desorber and Condenser Conditions during 180 s Transition.

Time Point	Adsorber		Evaporator	
	Temperature (°C)	Pressure (Pa)	Temperature (°C)	Pressure (Pa)
Start	29.8	982	7.1	1010
End	43.4	3135	26.1	3377

Table 4.5.: Adsorber and Evaporator Conditions during 180 s Transition.

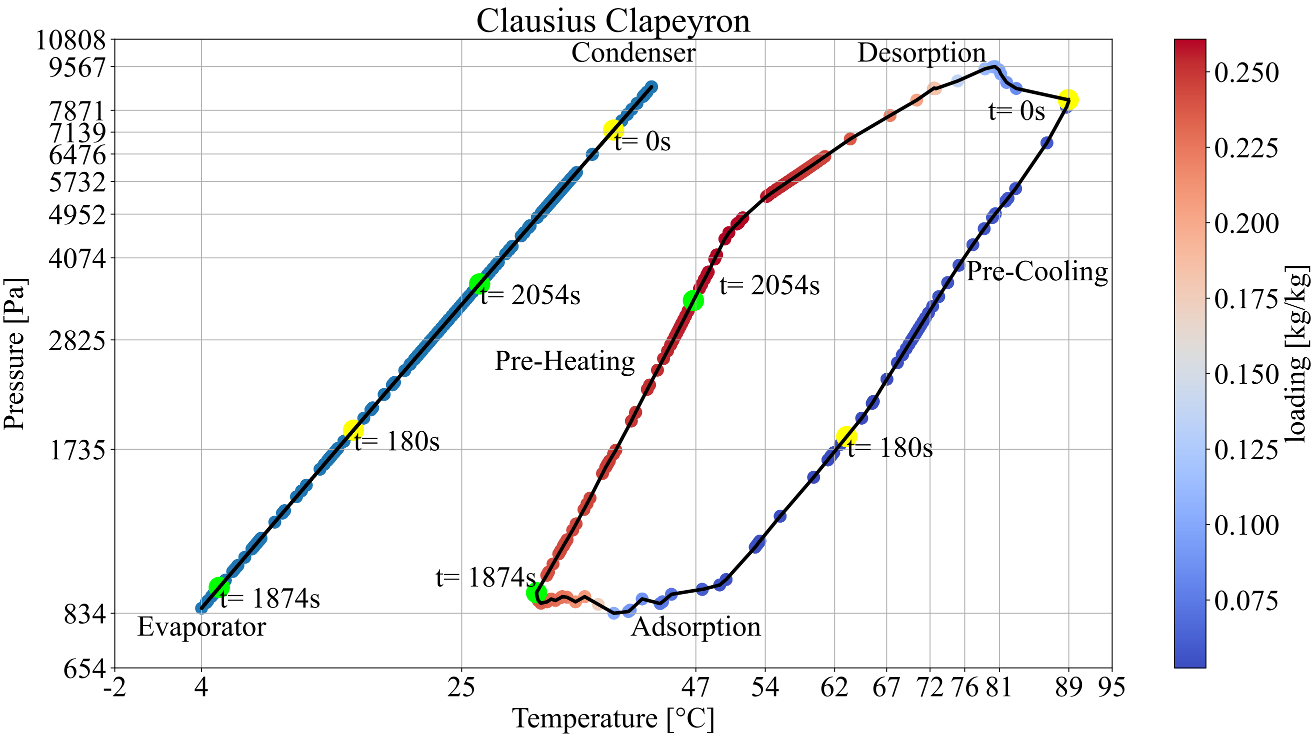

Figure 4.63.: 39 %.

Time Point	Desorber		Condenser	
	Temperature (°C)	Pressure (Pa)	Temperature (°C)	Pressure (Pa)
Start	89.9	8252	39.5	7206
End	63.4	1836	16.6	1889

Table 4.6.: Desorber and Condenser Conditions during 180 s Transition.

Time Point	Adsorber		Evaporator	
	Temperature (°C)	Pressure (Pa)	Temperature (°C)	Pressure (Pa)
Start	32.4	915	6.0	937
End	47.33	3368	27.3	3628

Table 4.7.: Adsorber and Evaporator Conditions during 180 s Transition.

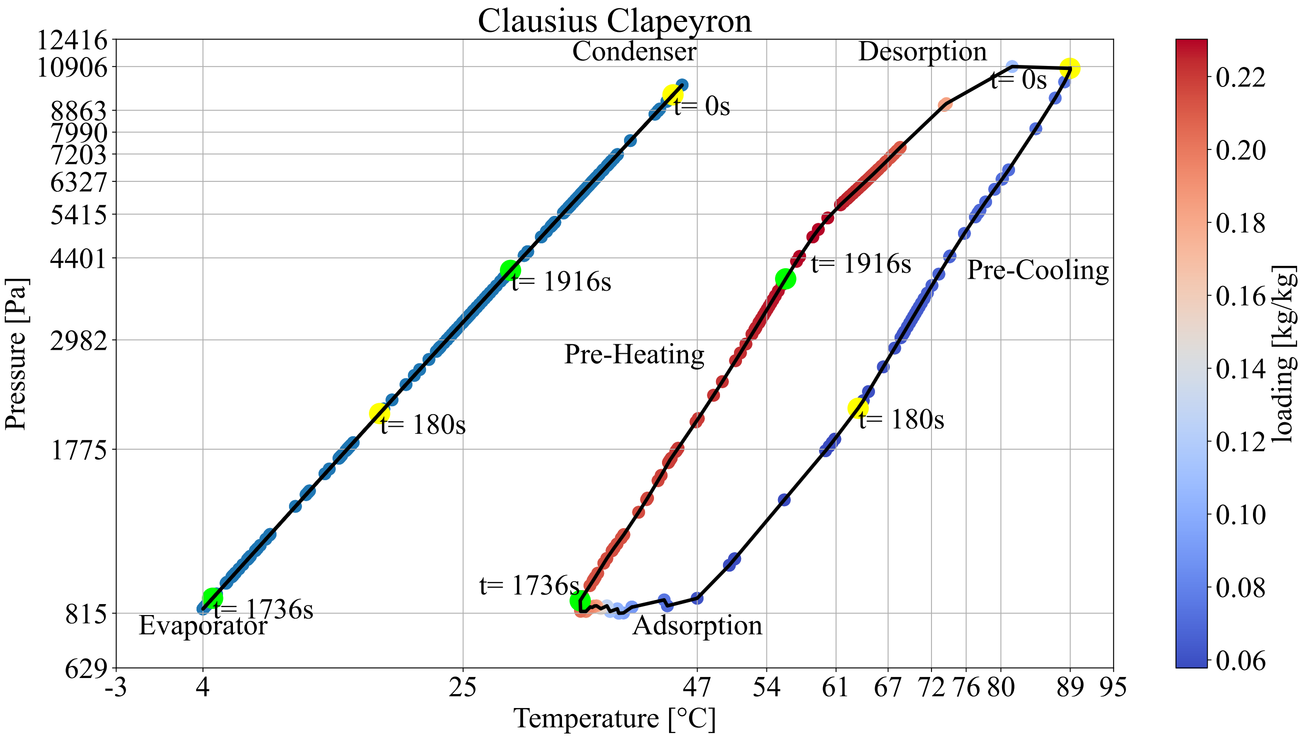

Figure 4.64.: 48 %.

Time Point	**Desorber**		**Condenser**	
	Temperature (°C)	**Pressure (Pa)**	**Temperature (°C)**	**Pressure (Pa)**
Start	89.7	10815	44.9	9538
End	64.3	2157	18.3	2103

Table 4.8.: Desorber and condenser conditions during 180 s transition.

Time Point	**Adsorber**		**Evaporator**	
	Temperature (°C)	**Pressure (Pa)**	**Temperature (°C)**	**Pressure (Pa)**
Start	36.0	866	5.1	876
End	56.4	3985	29.6	4148

Table 4.9.: Adsorber and evaporator conditions during 180 s transition.

Similar to the 13 % partial load shown in Figure 4.52, the entropy generation rate decreases with the reduction of mass flow rate in the adsorber/desorber during transitional phases in other partial load conditions, as depicted in Figure 4.52, Figure 4.65, Figure 4.66, and Figure 4.67.

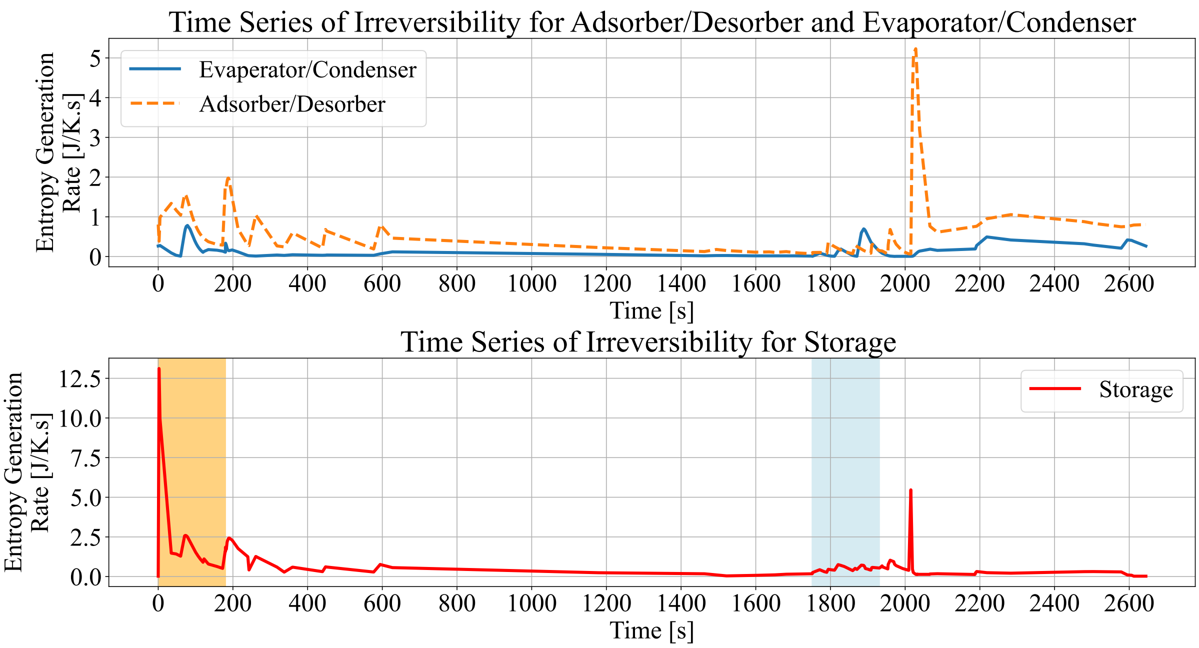

Figure 4.65.: Time series of entropy generation rate within module and storage as well as transition mode from condenser to the evaporator (orange shaded area) and vise versa (blue shaded area). This data corresponds to a heating system integrating with a single adsorber cycle GAHP operating at a 30 % part load ratio (refer to Table 2.4) for a cycle, with the maximum high-temperature source set at 90 °C.

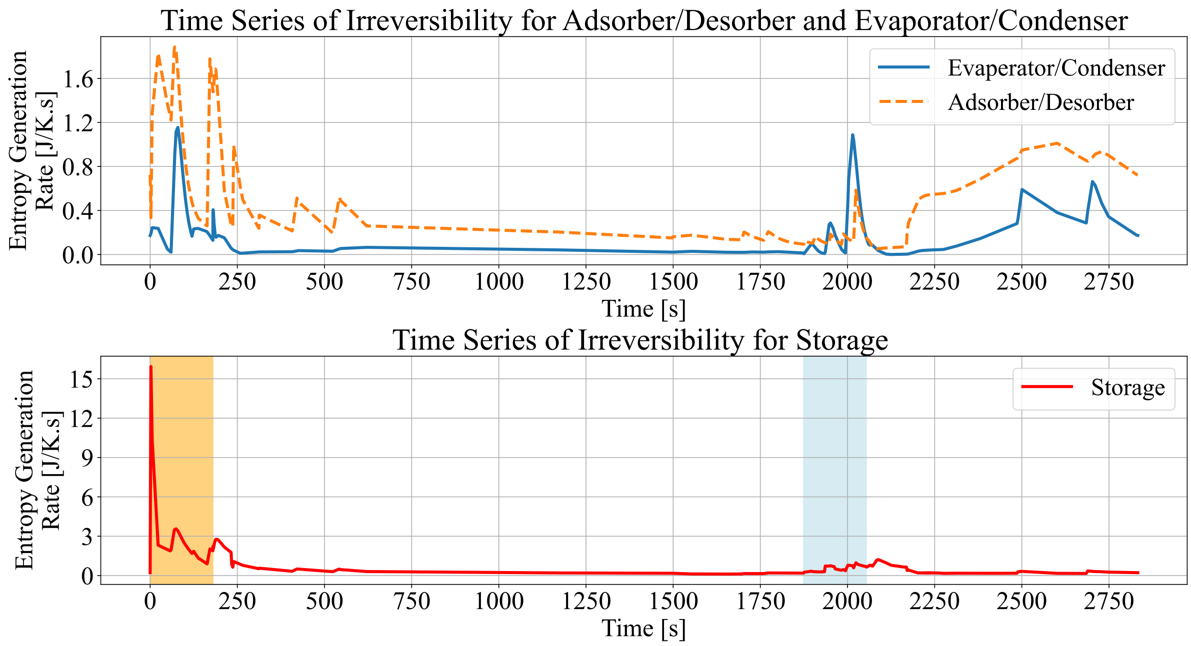

Figure 4.66.: 39 %.

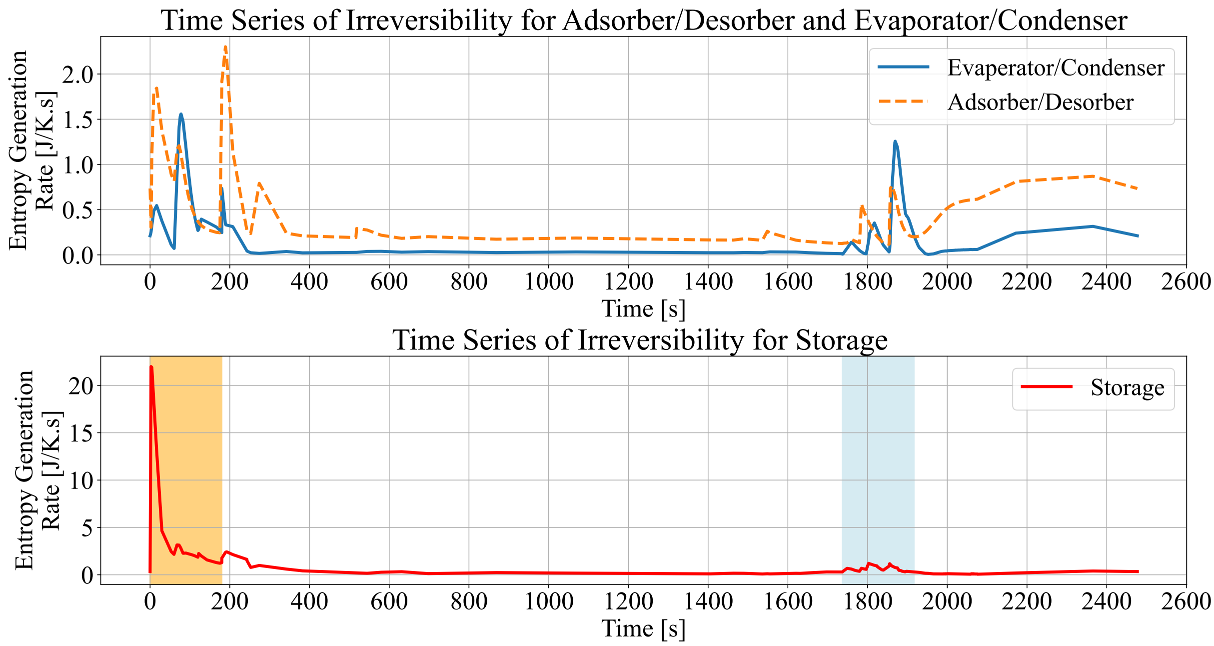

Figure 4.67.: 48 %.

Additionally, At higher part-load ratios, the burner activation period is extended to heat the upper section of the stratified storage and meet the space heating demand, as shown by the comparison of Figure 4.68, Figure 4.69, and Figure 4.70. While the overall cycle structure and switching conditions remain unchanged, additional system-level control is applied at partial loads of 39 % and 48 %. In these cases, both the burner power and mass flow rate are actively controlled to ensure sufficient storage temperatures. The temperature of storage layer one is used as the control variable, with a setpoint equal to the space heating supply temperature at 39 % part load and increased by 8 °C at 48 % part load. This combined adjustment of burner power and mass flow rate allows the system to satisfy higher thermal demand while preserving the same basic cycle operation.

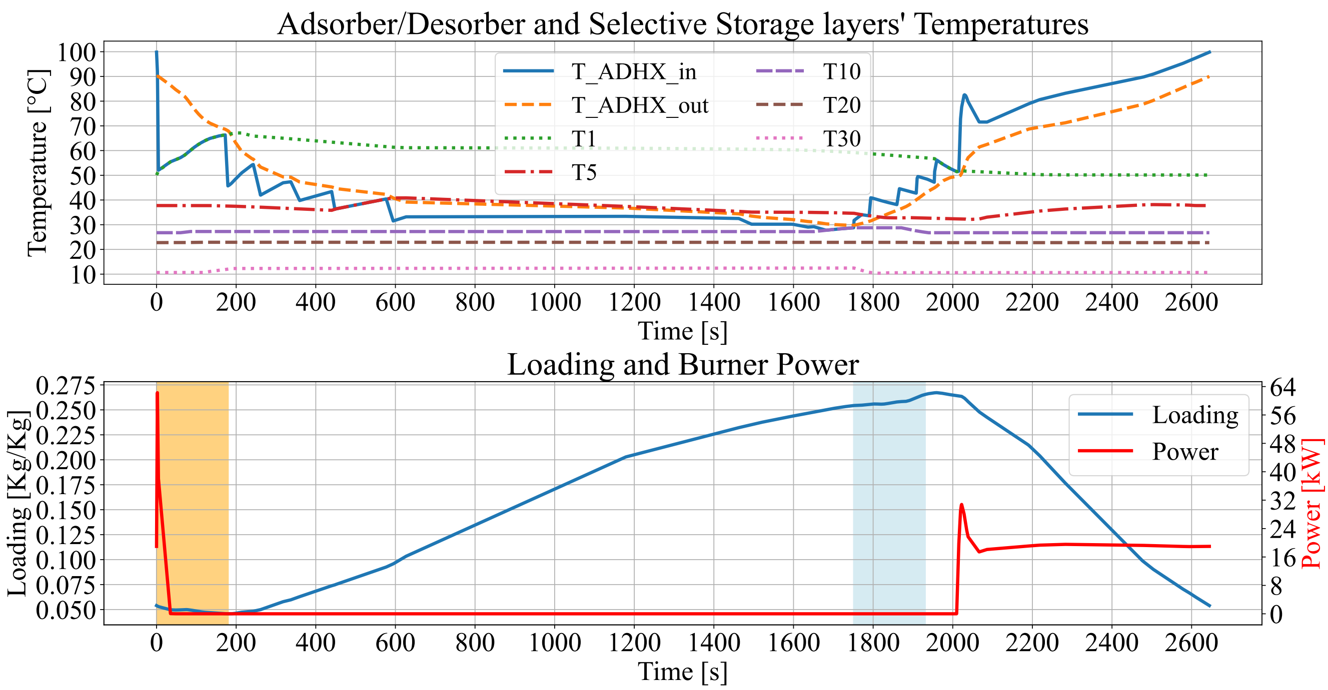

Figure 4.68.: Time series of heat transfer fluid supply and return temperatures for the adsorber, combi-storage representative layers' temperatures, loading, and burner power. This data corresponds to a heating system integrating with a single adsorber cycle GAHP operating at a 30 % part load ratio (refer to Table 2.4) for a cycle, with the maximum high-temperature source set at 90 °C. The orange and light blue shaded regions indicate two 180s transition phases.

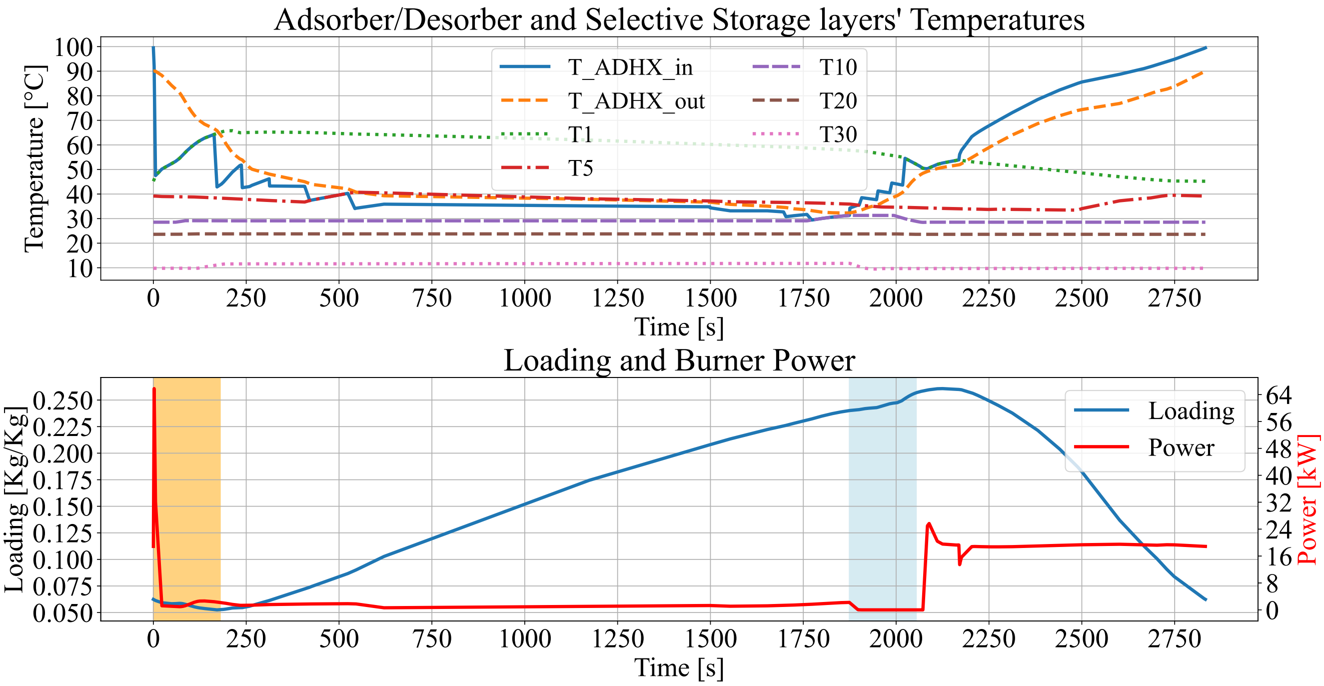

Figure 4.69.: 39 %.

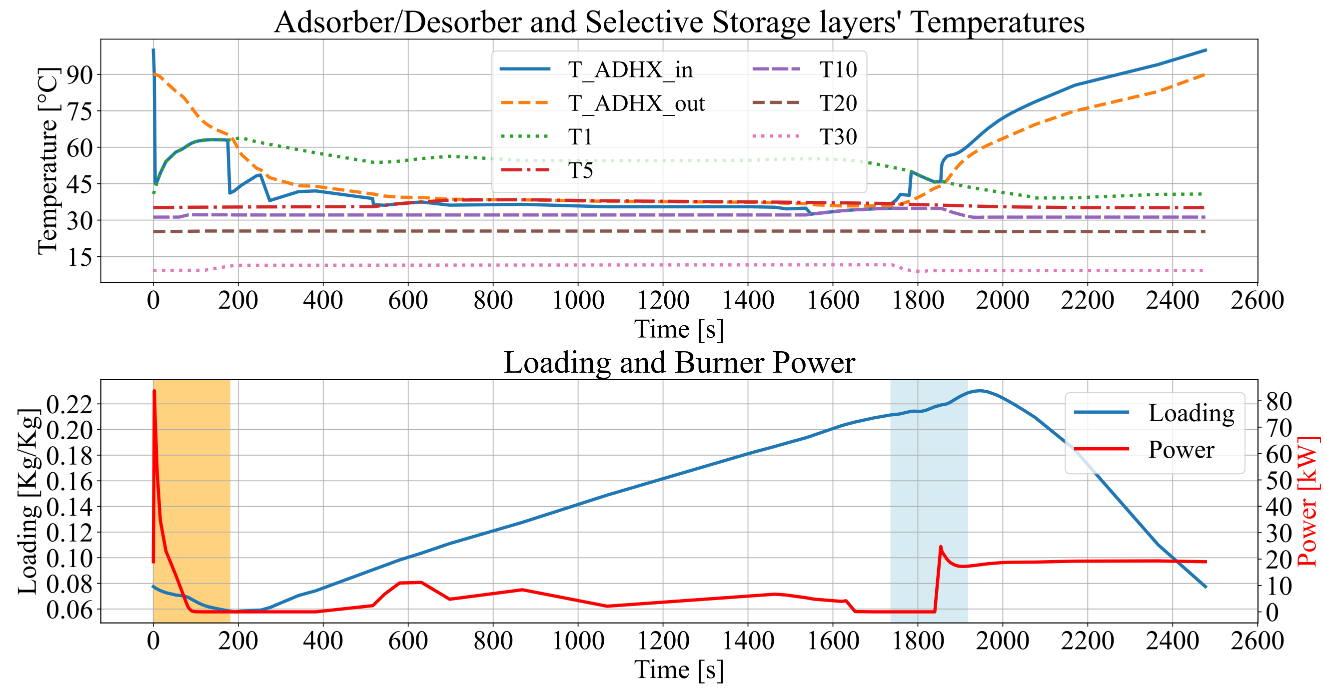

Figure 4.70.: 48 %.

Finally, according to the control strategy that is described in subsection 2.3.5, the power delivered to or from the adsorber/desorber and evaporator/condenser is depicted in Figure 4.71, Figure 4.72, and Figure 4.73. Additionally, the temperature of the supply and return water to each of these components is shown in the corresponding plots.

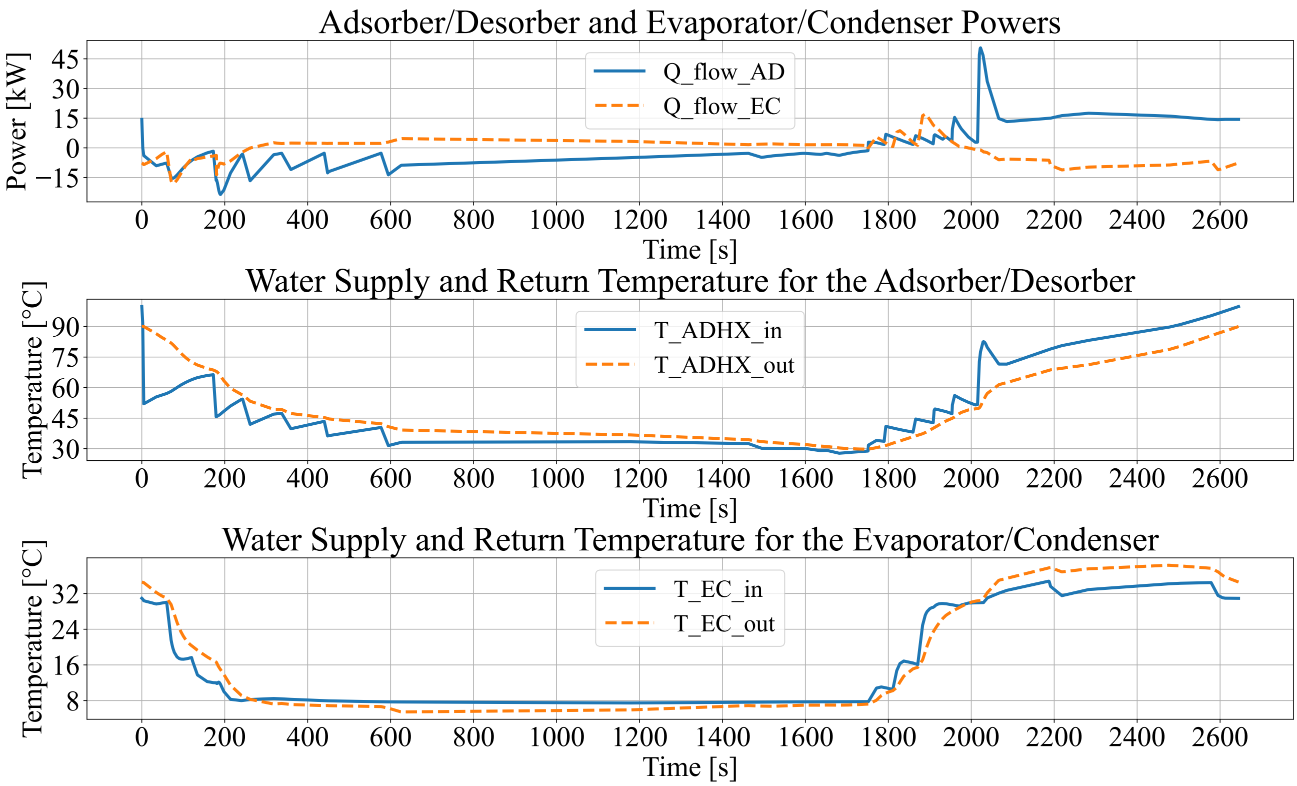

Figure 4.71.: Time series of power, supply, and return temperatures of heat transfer fluid for a module. This data corresponds to a heating system integrating with a single adsorber cycle GAHP operating at a 30 % part load ratio (refer to Table 2.4) for a cycle, with the maximum high-temperature source set at 90 °C [118].

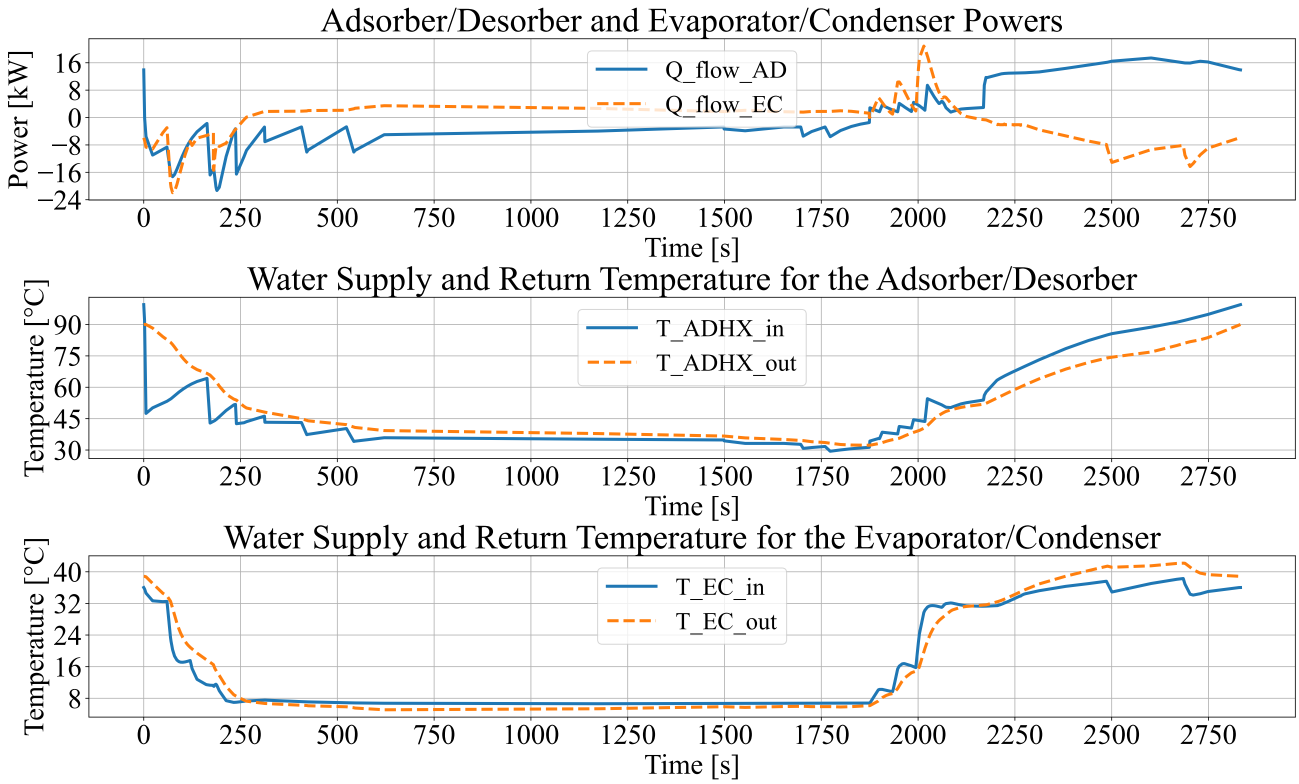

Figure 4.72.: 39 %.

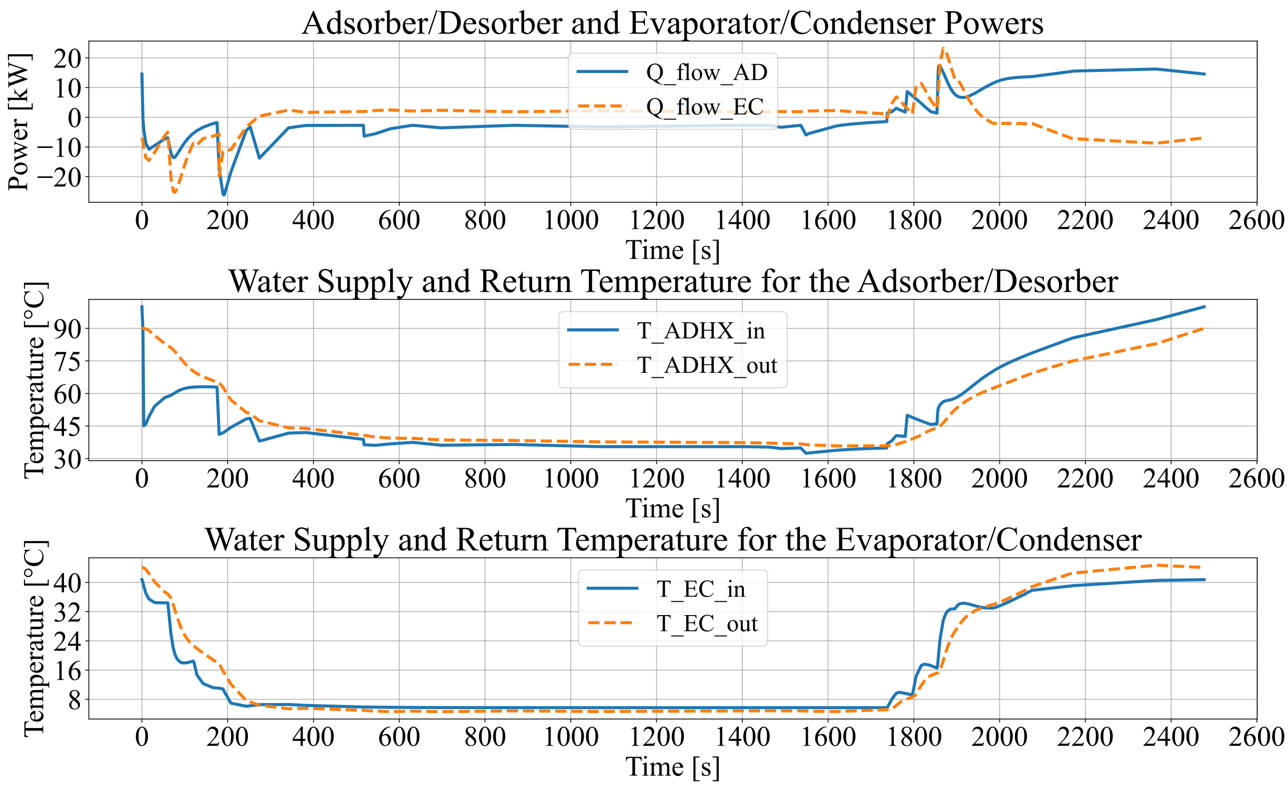

Figure 4.73.: 48 %.

The Seasonal Gas Utilization Efficiency (SGUE) of a heating system integrated with a single adsorber cycle GAHP and combi-storage has been computed according to two distinct standards, DIN EN 12309-6 [72] and VDI 4650 2 [73], based on the net calorific value (NCV). The results are then compared with the SGUE of a heating system integrated with a dual adsorber cycle Gas Adsorption Heat Pump and hydraulic separator in Figure 4.74. The variation in SGUE values for the same heating system, assessed under VDI 4650 2 [73] and DIN EN 12309-6 [72], can be attributed to the distinctive calculation methodologies employed in these two standards, as detailed in section A.2. VDI 4650 2 [73] considers five points, excluding 100 % from Table 2.4, and computes the harmonic mean value based on these five points. Conversely, DIN EN 12309-6 incorporates six points and determines efficiency through a weighted average, including 100 %. Consequently, VDI 4650 2 [73] tends to predict SGUE optimistically, while DIN EN 12309-6 [72] tends to predict it pessimistically. The observed differences arise from variations in the weighting or selection of different partial load points. Specifically, the weather data utilized for the Potsdam site results in a greater number of operating hours at lower part load points in VDI 4650 2 [73] compared to what is assumed in DIN EN 12309-6 [72].

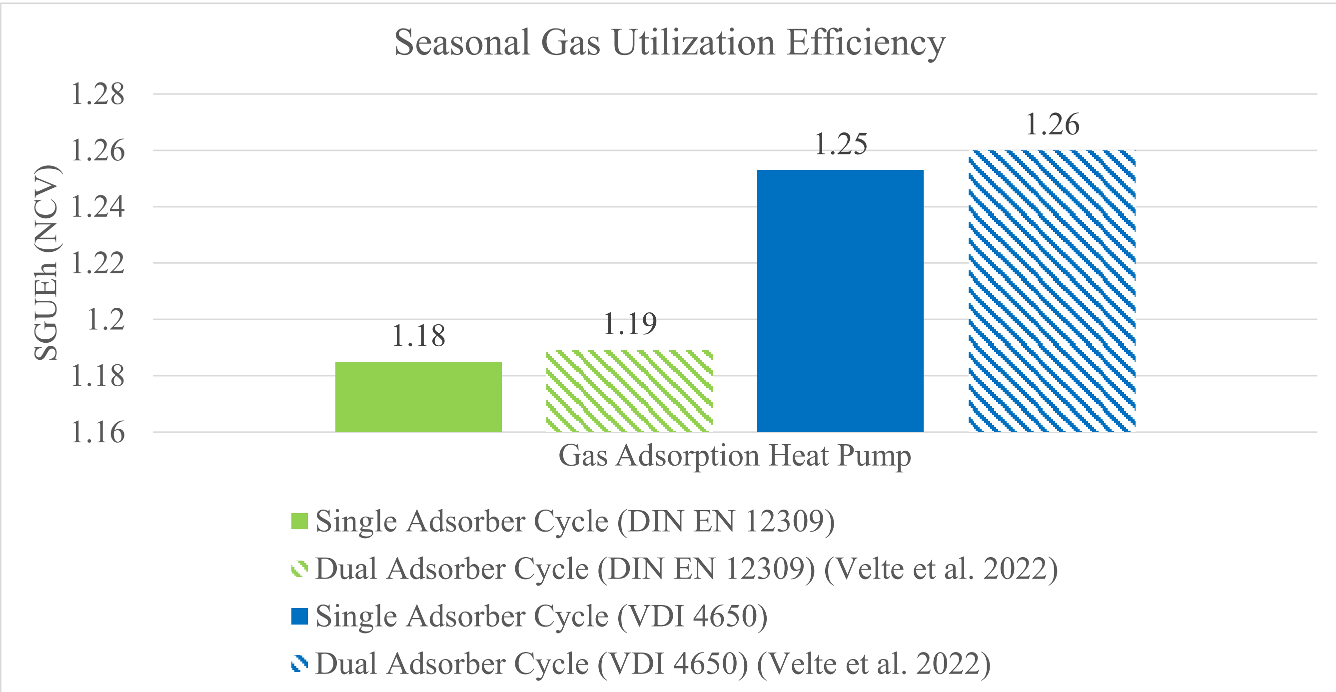

Figure 4.74.: Comparison of the seasonal gas utilization efficiency of a heating system with a single adsorber cycle GAHP [118], assessed by two standards: DIN EN 12309-6 [72] and VDI 4650-2 [73] .

4.3.1. Sensitivity Analysis of the Single Adsorber Cycle Gas Adsorption Heat Pump

The sensitivity analysis of the Single Adsorber Cycle Gas Adsorption Heat Pump consists of two parts. Firstly, the alteration of the high-temperature source from 90 °C to 110 °C. Secondly, doubling the mass flow rate of the burner and adsorber while keeping the high-temperature source at 90 °C. Figure 4.75 provides the results of the Gas Utilization Efficiency for each part load ratio mentioned in Table 2.4 for VDI 4650-2 [73].

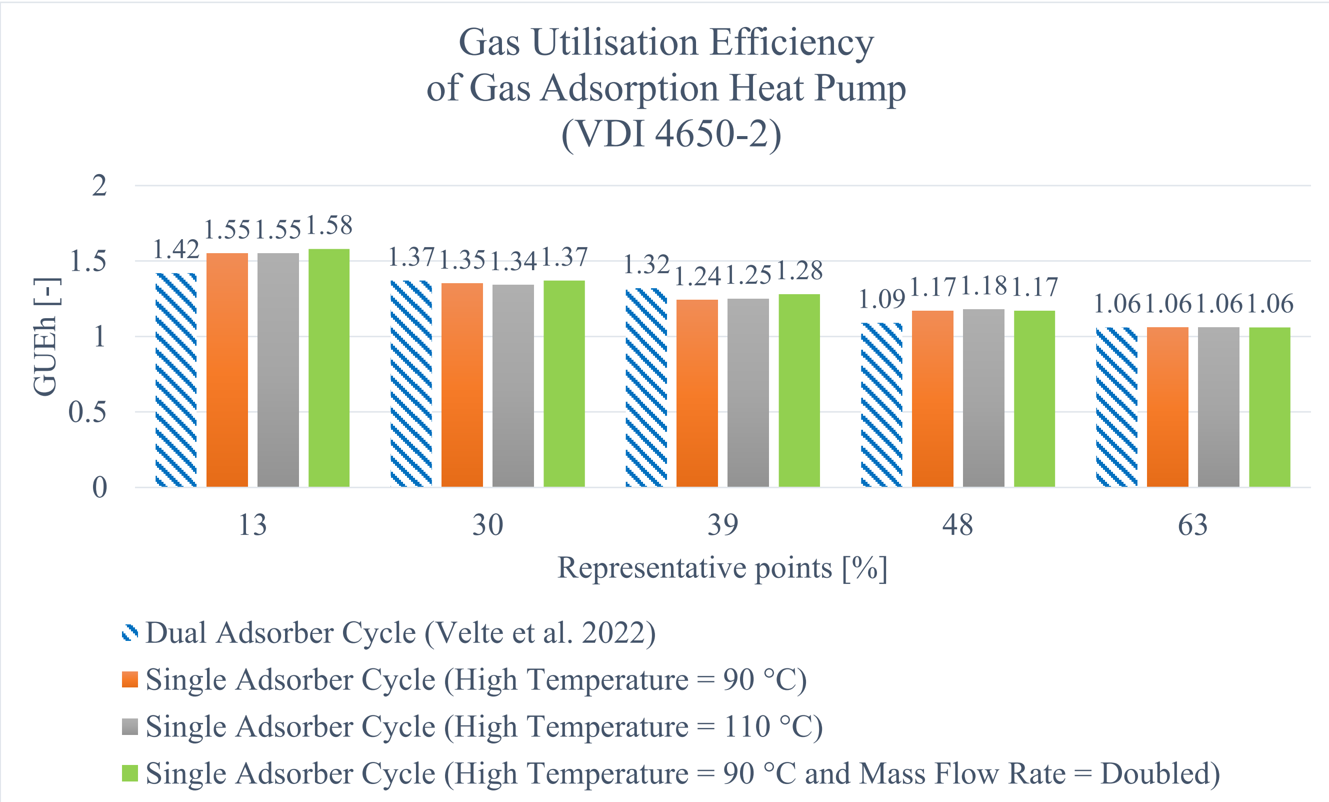

Figure 4.75.: Gas utilisation efficiency of a heating system [118]: sensitivity analysis with heat production involving a single adsorber cycle GAHP, and heat consumption is based on representative operating points specified in the VDI 4650-2 standard [73] .

Figure 4.76 illustrates the Seasonal Gas Utilization Efficiency in a heating system integrated with a single adsorber cycle GAHP and combi-storage under three different sensitivity analyses, comparing it with a heating system integrated with a validated dual adsorber cycle Gas Adsorption Heat Pump and hydraulic separator [63]. The results indicate that doubling the mass flow rate in the burner and adsorber leads to a higher Seasonal Gas Utilization Efficiency than the validated model. This improvement is primarily attributed to the increase in Gas Utilization Efficiency by 11.3 % for the 13 % part load ratio and 7.3 % for the 48 % part load ratio, while decreasing by 3 % for the 39 % part load ratio in Figure 4.75.

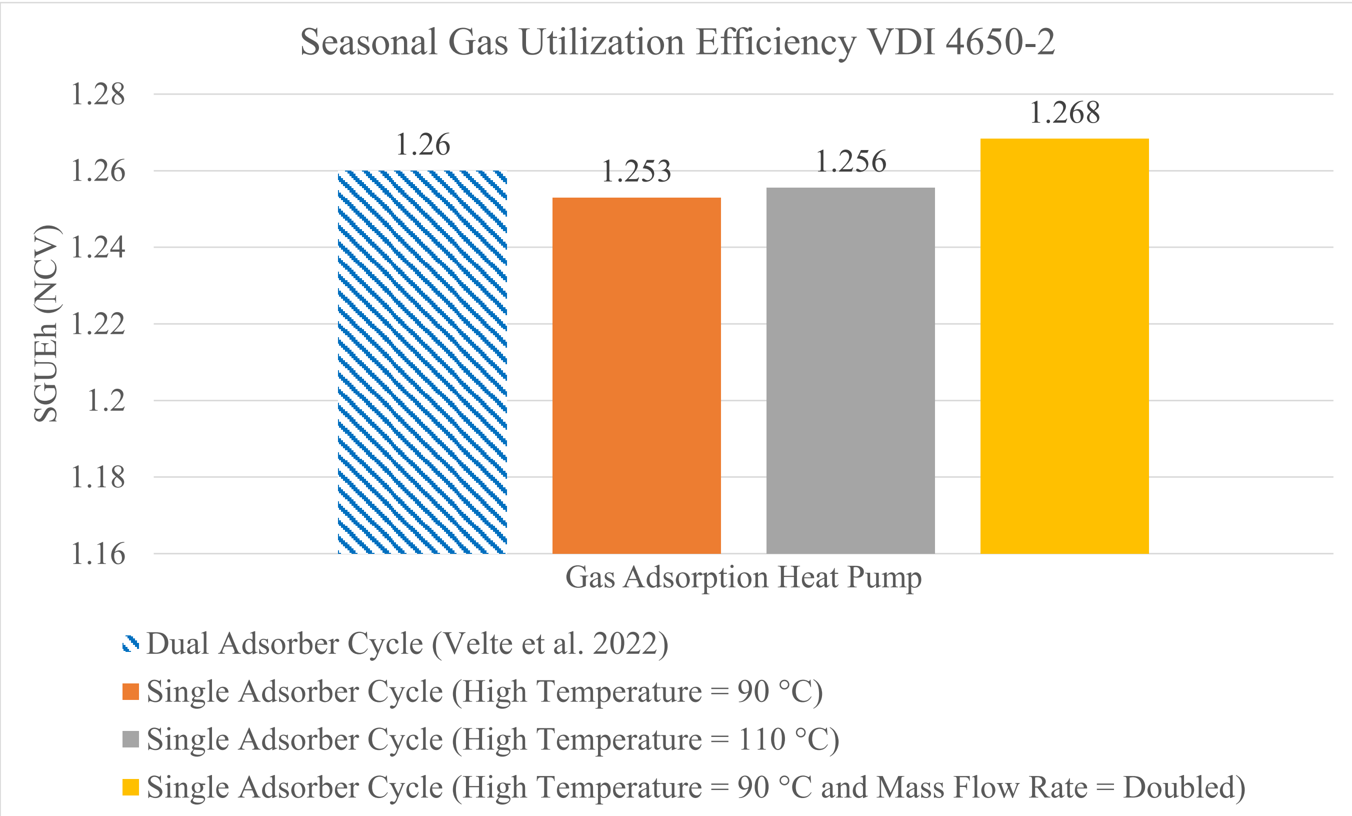

Figure 4.76.: Seasonal gas utilization efficiency of a heating system [118]: sensitivity analysis with heat production involving a single adsorber cycle GAHP and heat consumption based on representative operating points specified in the VDI 4650-2 standard [73].

5. Conclusion

This work confirms the potential of preheating domestic hot water (DHW) using condensing boiler effect and sorption process of a dual adsorber cycle Gas Adsorption Heat Pump (GAHP) through a numerical model developed in the Dymola environment. The research enhances AdoSan's heating system through two key approaches.

The first approach focuses on system design and required components to meet heating demands in a renovated multi-family house. The study evaluates the effectiveness of the GAHP in preheating DHW and supplying space heating, using one stratified storage tank. This configuration is compared to an alternative system with two stratified storage tanks–one dedicated to DHW preparation with a burner, and another for space heating with a GAHP–to analyze gas consumption differences between the one-tank and two-tank configurations. Additionally, for conditions that include a solar thermal circuit, the study assesses the impact of solar irradiation on reducing gas consumption while meeting both space heating and DHW demands, using both one- and two-tank configurations.

The second approach addresses the module level, assessing the thermodynamic performance of adsorber cycle GAHPs with different heat recovery strategies. The dual adsorber cycle employs storage in a secondary loop, situated on the opposite side of the heat exchanger. In contrast, the single adsorber cycle integrates stratified storage into the primary heat pump loop, with heat recovery occurring directly within the storage. The single adsorber cycle also offers greater operational flexibility compared to the dual adsorber cycle.

The control strategies employed in the aforementioned approaches are pivotal for the following reasons:

- Maintaining thermal comfort conditions in both the space heating and DHW circuits.
- Effectively utilizing the degrees of freedom in half-cycle durations in the single adsorber cycle, a goal achieved through the selected control strategy.
- Facilitating smooth switching between direct burner mode and GAHP mode as needed.
- Guaranteeing precise utilization of a strategically chosen section of the storage tank.
- Designing a hydraulic scheme and control hierarchy that extract fluid from the lower (coldest) section of the storage for supply to the collectors. The return of heated water is prioritized to meet space heating and domestic hot water demands within the storage.

Through the implementation of the control strategy, the research effectively limits temperature deviations from comfort ranges to negligible values and ensures the maintenance of sanitary conditions in the DHW circuit, including measures for Legionella prevention.

The AdoSan heating system, designed exclusively to meet space heating demands without addressing DHW needs, achieves a Seasonal Gas Utilization Efficiency (SGUE) of 1.21 [63]. In contrast, an improved configuration incorporating a solar thermal circuit to meet both DHW and space heating demands achieves a SGUE of 1.33. For AdoSan GAHP with a nominal output power of 40 kW, achieving the target SGUE of 1.3 is unattainable without integrating an additional non-fossil heat source. Nonetheless, achieving a 10 % solar fraction is feasible with a properly dimensioned solar thermal system. Challenges associated with hydraulic system integration have been addressed and resolved using the methodology outlined in [89]. However, the integration of control strategies constitutes a novel contribution of this research.

Furthermore, replacing the dual adsorber cycle with a single adsorber cycle not only enhances sensible heat recovery between the condenser and evaporator but also demonstrates, in preliminary system assessments, the potential to achieve a competitive SGUE relative to the AdoSan heating system.

5.1. Sensitivity Analysis of a Heating System with Dual Adsorber Cycle Gas Adsorption Heat Pump

The heat consumption of the reference heating system includes the space heating circuit under Potsdam weather conditions and DHW circuit, while heat production consists of a burner and the dual adsorber cycle GAHP, both of which are connected to a stratified storage. There is only one ideal inserter, which is located in the return line of DHW circuit to the stratified storage. Moreover, it is important to note that the burner fulfills two roles: first, it acts as the high-temperature source for the dual adsorber cycle GAHP, and second, it supplies power to the storage for DHW demands. Additionally, the exhaust gas is utilized to achieve a condensing boiler effect and to transfer heat from flue gas condensation to the stratified storage.

The sensitivity analysis of the reference heating system has provided valuable insights into the factors affecting DHW preheating with condensing boiler effect and the dual adsorber cycle GAHP. Additionally, it describes how these factors influence the system's SGUE. The annual energy difference between supply and demand for DHW preparation serves as an indicator of DHW preheating performance. Specifically, the annual energy delivered from the burner to the top of the storage in reference heating system is 24 % less than the annual energy delivered to the DHW circuit from stratified storage. This deficit is compensated by condensing boiler effect and the sorption heat of GAHP in the reference heating system.

Key findings from the annual simulation sensitivity analysis are as follows:

1. Different weather conditions serves as a test for robustness and flexibility of control strategy. Under the Karlsruhe weather conditions, the SGUE of the heating system improved by 1.6 %, indicating that control adapts to average lower temperature requirements with increased efficiency due to enhanced sorption effects. Although DHW demands are predominantly influenced by the user behavior rather than weather conditions, changes in weather conditions affect the power delivered from

GAHP to the stratified storage. Consequently, annual preheating DHW under Karlsruhe weather conditions is reduced by 14.1 % compared to preheating performance observed under Potsdam weather conditions.

2. Insertion of Ideal Components: The integration of three ideal inserters resulted in a 1.2 % increase in SGUE and a 20.8 % increase in annual DHW preheating compared to the reference heating system. This demonstrates that effective thermal stratification has a significant impact on DHW preheating performance. Therefore, It would appear worthwhile to undertake further development work on the storage side, both experimentally and numerically.

3. Maximum Desorption Temperature: Increasing the maximum desorption temperature to 110 °C without changing the control strategy led to a 0.8 % improvement in SGUE and a 5.7 % increase in annual DHW preheating compared to the reference heating system with maximum desorption temperature of 90 °C. Thus, the results indicate the robustness and flexibility of employed control strategy.

4. Storage Layers: Doubling the number of storage layers from 16 to 32 resulted in a 0.3 % increase in SGUE and a 11.9 % increase in annual DHW preheating compared to the reference heating system with 16 layers. The relatively small increase in SGUE indicates that the stratification requirements of the system are not particularly demanding, which is consistent with expectations. This provides a useful indication that achieving a comparable level of stratification in a laboratory system would not require excessive effort.

Conversely, certain factor negatively impacted SGUE:

1. DHW Demand: An increase in DHW demand by a factor of 2.5, driven by changes in user behavior, resulted in a 4.4 % reduction in SGUE and a 98.0 % increase in annual DHW preheating compared to the reference heating system. This is mainly because the annual activation time of the burner mode increased by 96.8 % and the GAHP's annual sorption time decreased by 27.2 % compared to the heating system. As a result, the annual condensing boiler effect to the combi-storage increased by 15.7 % compared to the reference heating system. This highlights the critical role of developers and researchers in designing hydraulic systems and control strategies that can effectively adapt to a wide range of user behaviors.

These findings underscore the importance of optimizing key parameters to improve the performance of the GAHP system and enhance overall system efficiency. Furthermore, the sensitivity analysis reveals opportunities for advancements beyond the current technological limitations of GAHP systems. Notably, the adsorber technology utilized in the AdoSan project employed a flat tube lamella heat exchanger for the adsorber/desorber heat exchanger. This represented a deviation from the original plan to use a flat tube fibrous structure heat exchanger, which was not included in the functional test bed due to production challenges.

5.2. Single Adsorber Cycle Gas Adsorption Heat Pump with Heat Recovery through Combi-Storage

To develop an advanced heating system, a single adsorber cycle has been integrated with a storage. This system is managed through three levels of control strategy.

First, consumption-side control: This level is concerned with regulating the mass flow rate of the pump on the consumption side.

Second, module-level control: This level involves extracting and inserting water from the storage system through ideal valves to operate the GAHP efficiently.

Third, system-level control: This level focuses on controlling the burner's power and managing its connection to either the single adsorber cycle or the storage.

These control strategies ensure that the system adheres to established temperature levels and heating loads, as specified by DIN EN 12309-6 [72] and VDI 4650-2 [73], thus maintaining the desired room temperature.

The integration of the single adsorber cycle with the storage offers two primary advantages:

Enhanced Heat Recovery: The system achieves effective heat recovery between the evaporator and condenser by carefully managing mass flow and temperature levels. At the end of the desorption phase, the condenser temperature can decrease from the space heating supply level to the lower temperature of the storage's bottom layer. This allows the remaining heat from the condenser to transfer into the storage. Additionally, by the end of the adsorption phase, the system can circulate cold water from the evaporator into storage while increasing the evaporator temperature to match the condenser temperature. This unique feature is unavailable in the dual adsorber cycle GAHP used in the AdoSan project.

Increased Operational Flexibility: by utilizing the additional degrees of freedom, such as adjusting the mass flow rate of the heat transfer fluid in both the burner and adsorber within the single adsorber cycle, its SGUE can be made comparable to that of the dual adsorber cycle.

Furthermore, as the single adsorber cycle GAHP utilizes only one adsorption module, it may offer a more cost-effective solution compared to the dual adsorber cycle GAHP.

It is important to note that the current technological snapshot of the adsorber cycle employs a flat tube lamella heat exchanger rather than a fibrous structure heat exchanger. This design choice appears to constrain the achievable heat recovery within the single adsorber cycle, limiting the insights provided by the sensitivity analysis conducted under the present technological conditions. As a result, transitioning to a fibrous structure heat exchanger would necessitate the development of a differently parameterized model. Consequently, the potential impacts of such a switch cannot be accurately predicted by adjusting the parameters of the existing model.

6. Outlook

6.1. Dual Adsorber Cycle Gas Adsorption Heat Pump

Building on the outcomes of the completed AdoSan project, a key direction beyond the scope of this research is the development of a system control strategy to optimize the integration of the gas adsorption heat pump, burner, and domestic hot water circuit [26]. To address this challenge, combining dynamic system models with specialized optimization algorithms to solve optimal control problems efficiently offers a promising approach to enhancing the energy efficiency of refrigeration systems [140].

For example, the advantage of the designed Nonlinear Model Predictive Control (NMPC) over a simple PI control lies not in setting energy-optimal steady points, but rather in significantly improving the response to disturbances. This means that under dynamic conditions, the refrigeration cycle operates much shorter in inefficient states [140]. Utilizing NMPC in the discontinuous adsorption refrigeration process has a distinct feature: the cycle duration serves as the control input to maximize the average cooling capacity. However, in our reference system, the cycle duration is automatically adjusted within the system-level control strategy, making it impractical to apply the NMPC approach.

However, integrating dynamic system models and specialized optimization algorithms presents a promising approach to improving energy efficiency in refrigeration systems. Therefore, future research should focus on the dynamic optimization of the heating system to achieve these potential improvements.

6.2. Single Adsorber Cycle Gas Adsorption Heat Pump

In this study, I demonstrated that a single adsorber cycle gas adsorption heat pump can achieve performance comparable to AdoSan's dual adsorber cycle gas adsorption heat pump by employing the standard cycle concept. Future research can proceed in two key areas. First, it can continue with the single adsorber cycle of AdoSan project. Second, it can focus on designing an optimal single adsorber cycle that integrates with the combi-storage to overcome the limitations of the evaporator/condenser identified in this research.

By considering one of these single adsorber approaches, it is possible to incorporate the double lift and double effect mechanisms proposed by Schmidt et al. [141] within the Stratisorp cycle, emphasizing their potential for effective application in heating systems utilizing low-temperature heat sources. Furthermore, the implementation of entropy balancing within the dynamic Modelica model provides a systematic framework for optimizing control strategies, particularly with respect to intra-cycle mass flows between the adsorber and evaporator/condenser. In this way, the developed model can be regarded as a flexible toolkit for further control optimization, enabling improved overall system efficiency while meeting space heating and domestic hot water demands.

This approach presents a promising path for future research and development in the field of adsorption heat pump technology.

7. List of Publications

1. Andersen, O., Dörr, H., Füldner, G., Groddeck, P., Herrmann, R., Herrmann, S., Kostmann, C., Sadeghlu, A., Schmalzried, H., Schmidt, F., Velte, A., Volmer, R., and Wittstadt, U. *AdoSan-LXB: LowEx-Konzepte für die Wärmeversorgung von Mehrfamilien-Bestandsgebäuden; Entwicklung einer Gas-Adsorptionswärmepumpe für die Bestandssanierung: gemeinsamer Abschlussbericht: Berichtszeitraum: 01.08.2018–28.02.2022 (FKZ 03ET1554A, B, C, E und F), 01.08.2018–30.06.2022 (FKZ 03ET1554D).* Freiburg, 2022. doi: `https://doi.org/10.2314/KXP:1860371825`.

2. Sadeghlu, A., and Schmidt, F. P. "Simulation Study of Single-Adsorber Heat Pump Cycle with Heat Recovery Through Stratified Storage in Both Adsorber and Evaporator/Condenser Loops". In: *Energies* 17.21 (2024). issn: 1996-1073. doi: `https://doi.org/10.3390/en17215472`.

3. Sadeghlu, A., and Schmidt, F. P. "Analysis of two bed adsorption heat pump with a stratified storage to supply heating demands in a house for retrofitting of multi-family buildings". In: *Heat Powered Cycles Conference*, 2023. doi: `https://doi.org/10.5281/zenodo.10245219`.

Bibliography

[1] Statistisches Bundesamt (Destatis). *Household consumption of housing energy down 0.9% in 2020.* URL: `https://www.destatis.de/EN/Press/2022/12/PE22_542_85.html`. Accessed: 15.05.2024.

[2] Bundesverband der Energie-und Wasserwirtschaft e.V. (BDEW). *Wie heizt Deutschland 2023? BDEW-Studie zum Heizungsmarkt.* 2023. URL: `https://www.bdew.de/media/documents/231221-BDEW-WHD2023.pdf`.

[3] Adolf, J., Schabla, U., Lücke, A., Breidenbach, L., Bräuninger, M., Leschus, L., Ehrlich, L., Otto, A., Oschatz, B., and Mallach, B. *Shell BDH Hauswärme-Studie: Klimaschutz im Wohnungssektor - Wie Heizen wir morgen? Fakten, Trends und Perspektiven für Heiztechniken bis 2030.* Bundesindustrieverband Deutschland Haus-, Energie- und Umwelttechnik e.V. (BDH), 2013. DOI: `10.13140/RG.2.2.32179.96801`.

[4] Slotyuk, L., Part, F., Schlegel, M.-C., and Akkerman, F. "Life cycle assessment of the domestic micro heat and power generation proton exchange membrane fuel cell in comparison with the gas condensing boiler plus electricity from the grid". In: *Sustainability* 16.6 (2024). DOI: `10.3390/su16062348`.

[5] Sterner, M. *Bioenergy and Renewable Power Methane in Integrated 100% Renewable Energy Systems. Limiting Global Warming by Transforming Energy Systems.* Vol. 14. Kassel University Press, 2009. ISBN: 978-3-89958-799-9. DOI: `10.17170/kobra-202210176997`.

[6] Henning, H.-M. and Palzer, A. "A comprehensive model for the German electricity and heat sector in a future energy system with a dominant contribution from renewable energy technologies—Part I: Methodology". In: *Renewable and Sustainable Energy Reviews* 30 (2014), pp. 1003–1018. DOI: `10.1016/j.rser.2013.09.012`.

[7] Palzer, A. "Sektorübergreifende Modellierung und Optimierung eines zukünftigen deutschen Energiesystems unter Berücksichtigung von Energieeffizienzmaßnahmen im Gebäudesektor". PhD thesis. Fakultät für Maschinenbau, Karlsruher Institut für Technologie, 2016. ISBN: 978-3-8396-1041-1.

[8] Palzer, A. and Henning, H.-M. "A comprehensive model for the German electricity and heat sector in a future energy system with a dominant contribution from renewable energy technologies–Part II: Results". In: *Renewable and Sustainable Energy Reviews* 30 (2014), pp. 1019–1034. DOI: `10.1016/j.rser.2013.11.032`.

[9] Stocker, T. et al. (ed.) *Climate change 2021: the physical science basis: Working Group I Contribution to the Sixth Assessment Report of the Intergovernmental Panel on Climate Change.* Cambridge university press, 2023. ISBN: 9781009157896. DOI: `10.1017/9781009157896`.

[10] Statistisches Bundesamt (Destatis). *Inflation rate at +2.2% in April 2024.* URL: https://www.destatis.de/EN/Press/2024/05/PE24_188_611.html#fussnote-1-1333462. Accessed: 22.05.2024.

[11] Cavagnoli, S., Bonanno, A., Fabiani, C., Palomba, V., Frazzica, A., Carminati, M., Hermann, R., and Pisello, A. "Revitalizing Heritage: Assessing the Viability of Geothermal Heat Pumps for Energy Retrofit in Historic Buildings-a Holistic Investigation Through Laboratory, Field, and Techno-Economic Analyses". In: *Field, and Techno-Economic Analyses* (2024). DOI: 10.2139/ssrn.4743256.

[12] Kühn, A. *Thermally driven heat pumps for heating and cooling.* Universitätsverlag der TU Berlin, 2013. ISBN: 978-3-7983-2686-6. DOI: 10.14279/depositonce-3726.

[13] Reay, D. A. and Macmichael, A. *Heat Pumps: Design and Applications.* 3rd. Oxford: Elsevier, 2013. ISBN: 9780080227160.

[14] Lämmle, M., Metz, J., Kropp, M., Wapler, J., Oltersdorf, T., Günther, D., Herkel, S., and Bongs, C. "Heat Pump Systems in Existing Multifamily Buildings: A Meta-Analysis of Field Measurement Data Focusing on the Relationship of Temperature and Performance of Heat Pump Systems". In: *Energy Technology* 11.12 (2023). DOI: 10.1002/ente.202300379.

[15] Henninger, S. K., Schmidt, F. P., and Henning, H.-M. "Water adsorption characteristics of novel materials for heat transformation applications". In: *Applied Thermal Engineering* 30.13 (2010), pp. 1692–1702. ISSN: 1359-4311. DOI: 10.1016/j.applthermaleng.2010.03.028.

[16] Schwamberger, V. "Thermodynamische und numerische Untersuchung eines neuartigen Sorptionszyklus zur Anwendung in Adsorptionswärmepumpen und -kältemaschinen". PhD thesis. Fakultät für Maschinenbau, Karlsruher Institut für Technologie, 2016. DOI: 10.5445/IR/1000059868.

[17] Velte, A. "Experimentelle Arbeiten und Entwicklung von numerischen Modellen zur Analyse und Optimierung von Erweiterten Adsorptionskreisläufen für die Wärmeversorgung von Gebäuden". PhD thesis. Technische Fakultät, Albert-Ludwigs-Universität Freiburg, 2018. DOI: 10.6094/UNIFR/154691.

[18] Pentchev, I., Paev, K., and Seikova, I. "Dynamics of non-isothermal adsorption in packed bed of biporous zeolites". In: *Chemical Engineering Journal* 85.2-3 (2002), pp. 245–257. DOI: 10.1016/S1385-8947(01)00160-7.

[19] Füldner, G. "Stofftransport und Adsorptionskinetik in porösen Adsorbenskompositen für Wärmetransformationsanwendungen". PhD thesis. Fakultät für Mathematik und Physik, Albert-Ludwigs-Universität Freiburg, 2015. DOI: 10.6094/UNIFR/10072.

[20] Critoph, R. E. "Activated carbon adsorption cycles for refrigeration and heat pumping". In: *Carbon* 27.1 (1989). Proceedings of the Conference on Porosity and Carbon materials: Measurements and applications, pp. 63–70. ISSN: 0008-6223. DOI: 10.1016/0008-6223(89)90157-7.

[21] Tamainot-Telto, Z., Metcalf, S. J., Critoph, R. E., Zhong, Y., and Thorpe, R. “Carbon–ammonia pairs for adsorption refrigeration applications: ice making, air conditioning and heat pumping”. In: *International Journal of Refrigeration* 32.6 (2009), pp. 1212–1229. ISSN: 0140-7007. DOI: 10.1016/j.ijrefrig.2009.01.008.

[22] Bauer, J., Herrmann, R., Mittelbach, W., and Schwieger, W. “Zeolite/aluminum composite adsorbents for application in adsorption refrigeration”. In: *International Journal of Energy Research* 33.13 (2009), pp. 1233–1249. DOI: 10.1002/er.1611.

[23] Wittstadt, U., Füldner, G., Andersen, O., Herrmann, R., and Schmidt, F. “A New Adsorbent Composite Material Based on Metal Fiber Technology and Its Application in Adsorption Heat Exchangers”. In: *Energies* 8.8 (2015), pp. 8431–8446. ISSN: 1996-1073. DOI: 10.3390/en8088431.

[24] Wittstadt, U., Füldner, G., Laurenz, E., Warlo, A., Große, A., Herrmann, R., Schnabel, L., and Mittelbach, W. “A novel adsorption module with fiber heat exchangers: Performance analysis based on driving temperature differences”. In: *Renewable Energy* 110 (2017). Increasing the renewable share for heating and cooling by the means of sorption heat pumps and chillers, pp. 154–161. ISSN: 0960-1481. DOI: 10.1016/j.renene.2016.08.061.

[25] Palomba, V., Lombardo, W., Große, A., Herrmann, R., Nitsch, B., Strehlow, A., Bastian, R., Sapienza, A., and Frazzica, A. “Evaluation of in-situ coated porous structures for hybrid heat pumps”. In: *Energy* 209 (2020), p. 118313. ISSN: 0360-5442. DOI: 10.1016/j.energy.2020.118313.

[26] Andersen, O., Dörr, H., Füldner, G., Groddeck, P., Herrmann, R., Herrmann, S., Kostmann, C., Sadeghlu, A., Schmalzried, H., Schmidt, F., Velte, A., Volmer, R., and Wittstadt, U. *AdoSan-LXB : LowEx-Konzepte für die Wärmeversorgung von Mehrfamilien-Bestandsgebäuden; Entwicklung einer Gas-Adsorptionswärmepumpe für die Bestandssanierung: gemeinsamer Abschlussbericht: Berichtszeitraum: 01.08.2018-28.02.2022 (FKZ 03ET1554A, B, C, E und F), 01.08.218-30.06.2022 (FKZ 03ET1554D)*. Freiburg, 2022. DOI: 10.2314/KXP:1860371825.

[27] Freni, A., Dawoud, B., Bonaccorsi, L., Chmielewski, S., Frazzica, A., Calabrese, L., and Restuccia, G. *Characterization of zeolite-based coatings for adsorption heat pumps*. Springer, 2015. ISBN: 9783319093260.

[28] Myers, A. L. “Thermodynamics of adsorption in porous materials”. In: *AIChE Journal* 48 (2004). DOI: 10.1002/aic.690480115.

[29] Langmuir, I. “The Adsorption of Gases on plane Surfaces of Glass, Mica and Platium”. In: *Journal of the American Chemical Society* 40.9 (1918). DOI: 10.1021/ja02242a004.

[30] Brunauer, S., Emmett, P. H., and Teller, E. “Adsorption of Gases in Multimolecular Layers”. In: *Journal of the American Chemical Society* 60.2 (1938). DOI: 10.1021/ja01269a023.

[31] Dubinin, M. M. “The Potential Theory of Adsorption of Gases and Vapors for Adsorbents with Energetically Nonuniform Surfaces”. In: *Journal of the American Chemical Society* 60.2 (1960). DOI: 10.1021/cr60204a006.

[32] Dubinin, M. M. “Adsorption in micropores”. In: *Journal of Colloid and Interface Science* 23.4 (1967), pp. 487–499. ISSN: 0021-9797. DOI: 10.1016/0021-9797(67)90195-6.

[33] Critoph, R. E. “Performance limitations of adsorption cycles for solar cooling”. In: *Solar energy* 41.1 (1988), pp. 21–31. DOI: 10.1016/0038-092X(88)90111-9.

[34] Ruthven, D. M. *Principles of adsorption and adsorption processes.* John Wiley & Sons, 1984. ISBN: 9780471866060.

[35] Critoph, R. E. “Evaluation of alternative refrigerant—adsorbent pairs for refrigeration cycles”. In: *Applied Thermal Engineering* 16.11 (1996), pp. 891–900. DOI: 10.1016/1359-4311(96)00008-7.

[36] Henninger, S. K. “Untersuchungen von neuen hochporösen Sorptionsmaterialien für Wärmetransformationsanwendungen”. PhD thesis. Fakultät für Mathematik und Physik, Albert-Ludwigs Universität Freiburg, 2007. URL: http://www.freidok.uni-freiburg.de/volltexte/5264/.

[37] Wang, L., Zhu, D., and Tan, Y. “Heat transfer enhancement on the adsorber of adsorption heat pump”. In: *Adsorption* 5 (1999), pp. 279–286. DOI: 10.1023/A:1008964013879.

[38] Ng, E. P. and Mintova, S. “Nanoporous materials with enhanced hydrophilicity and high water sorption capacity”. In: *Microporous and Mesoporous Materials* 114.1-3 (2008), pp. 1–26. DOI: 10.1016/j.micromeso.2007.12.022.

[39] Van Heyden, H., Munz, G., Schnabel, L., Schmidt, F., Mintova, S., and Bein, T. “Kinetics of water adsorption in microporous aluminophosphate layers for regenerative heat exchangers”. In: *Applied Thermal Engineering* 29.8-9 (2009), pp. 1514–1522. DOI: 10.1016/j.applthermaleng.2008.07.001.

[40] Newalkar, B. L., Jasra, R. V., Kamath, V., and Bhat, S. G. T. “Sorption of water in aluminophosphate molecular sieve AlPO4-5”. In: *Microporous and mesoporous materials* 20.1-3 (1998), pp. 129–137. DOI: 10.1016/S1387-1811(97)00021-8.

[41] Kakiuchi, H., Takewaki, T., Takumi, H., Yamazaki, M., and Watanabe, H. “Adsorption heat pump, and use of adsorption material as adsorption material for adsorption heat pump”. Patent. WO 02/066910 A1. 2003.

[42] Kakiuchi, H., Shimooka, S., Iwade, M., Oshima, K., Yamazaki, M., Terada, S., Watanabe, H., and Takewaki, T. “Novel water vapor adsorbent FAM-Z01 and its applicability to an adsorption heat pump”. In: *Kagaku Kogaku Ronbunshu* 31.5 (2005), pp. 361–364. DOI: 10.1252/kakoronbunshu.31.361.

[43] Kakiuchi, H., Shimooka, S., Iwade, M., Oshima, K., Yamazaki, M., Terada, S., Watanabe, H., and Takewaki, T. “Water vapor adsorbent FAM-Z02 and its applicability to adsorption heat pump”. In: *Kagaku Kogaku Ronbunshu* 31.4 (2005), pp. 273–277. DOI: 10.1252/kakoronbunshu.31.273.

[44] Dias, J. M. S. and Costa, V. A. F. "Adsorption heat pumps for heating applications: A review of current state, literature gaps and development challenges". In: *Renewable and Sustainable Energy Reviews* 98 (2018), pp. 317–327. ISSN: 1364-0321. DOI: 10.1016/j.rser.2018.09.026.

[45] Sharafian, A. and Bahrami, M. "Assessment of adsorber bed designs in waste-heat driven adsorption cooling systems for vehicle air conditioning and refrigeration". In: *Renewable and Sustainable Energy Reviews* 30 (2014), pp. 440–451. DOI: 10.1016/j.rser.2013.10.031.

[46] Ziegler, F. "Sorption heat pumping technologies: Comparisons and challenges". In: *International journal of refrigeration* 32.4 (2009), pp. 566–576. DOI: 10.1016/j.ijrefrig.2009.03.007.

[47] Van Benthem, G. H. W., Cacciola, G., and Restuccia, G. "Regenerative adsorption heat pumps: optimization of the design". In: *Heat Recovery Systems and CHP* 15.6 (1995), pp. 531–544. DOI: 10.1016/0890-4332(95)90063-2.

[48] Alam, K. C. A., Saha, B. B., Kang, Y. T., Akisawa, A., and Kashiwagi, T. "Heat exchanger design effect on the system performance of silica gel adsorption refrigeration systems". In: *International Journal of Heat and Mass Transfer* 43.24 (2000), pp. 4419–4431. DOI: 10.1016/S0017-9310(00)00072-7.

[49] Bujok, T., Boruta, P., Mika, L., and Sztekler, K. "Analysis of Designs of Heat Exchangers Used in Adsorption Chillers". In: *Energies* 14.23 (2021). ISSN: 1996-1073. DOI: 10.3390/en14238038.

[50] Núñez, T. "Charakterisierung und Bewertung von Adsorbentien für Wärmetransformationsanwendungen". PhD thesis. Fakultät für Physik, Albert-Ludwigs-Universität Freiburg, 2001.

[51] Bendix, P., Füldner, G., Möllers, M., Kummer, H., Schnabel, L., Henninger, S., and Henning, H.-M. "Optimization of power density and metal-to-adsorbent weight ratio in coated adsorbers for adsorptive heat transformation applications". In: *Applied Thermal Engineering* 124 (2017), pp. 83–90. DOI: 10.1016/j.applthermaleng.2017.05.165.

[52] Núñez, T., Mittelbach, W., and Henning, H.-M. "Development of an adsorption chiller and heat pump for domestic heating and air-conditioning applications". In: *Applied Thermal Engineering* 27.13 (2007), pp. 2205–2212. DOI: 10.1016/j.applthermaleng.2005.07.024.

[53] Rezk, A., Al-Dadah, R. K., Mahmoud, S., and Elsayed, A. "Effects of contact resistance and metal additives in finned-tube adsorbent beds on the performance of silica gel/water adsorption chiller". In: *Applied Thermal Engineering* 53.2 (2013), pp. 278–284. DOI: 10.1016/j.applthermaleng.2012.04.008.

[54] Demir, H., Mobedi, M., and Ülkü, S. "The use of metal piece additives to enhance heat transfer rate through an unconsolidated adsorbent bed". In: *international journal of refrigeration* 33.4 (2010), pp. 714–720. DOI: 10.1016/j.ijrefrig.2009.12.032.

[55] Zhang, L. Z. "Design and testing of an automobile waste heat adsorption cooling system". In: *Applied thermal engineering* 20.1 (2000), pp. 103–114. DOI: 10.1016/S1359-4311(99)00009-5.

[56] Freni, A., Frazzica, A., Dawoud, B., Chmielewski, S., Calabrese, L., and Bonaccorsi, L. "Adsorbent coatings for heat pumping applications: Verification of hydrothermal and mechanical stabilities". In: *Applied Thermal Engineering* 50.2 (2013), pp. 1658–1663. DOI: 10.1016/j.applthermaleng.2011.07.010.

[57] Lang, R., Westerfeld, T., Gerlich, A., and Knoche, K. F. "Enhancement of the heat and mass transfer in compact zeolite layers". In: *Adsorption* 2 (1996), pp. 121–132. DOI: 10.1007/BF00127042.

[58] Freni, A., Bonaccorsi, L., Proverbio, E., Maggio, G., and Restuccia, G. "Zeolite synthesised on copper foam for adsorption chillers: A mathematical model". In: *Microporous and Mesoporous Materials* 120.3 (2009), pp. 402–409. DOI: 10.1016/j.micromeso.2008.12.011.

[59] Guilleminot, J. J., Choisier, A., Chalfen, J. B., Nicolas, S., and Reymoney, J. L. "Heat transfer intensification in fixed bed adsorbers". In: *Heat Recovery Systems and CHP* 13.4 (1993), pp. 297–300. DOI: 10.1016/0890-4332(93)90052-W.

[60] Atakan, A., Fueldner, G., Munz, G., Henninger, S., and Tatlier, M. "Adsorption kinetics and isotherms of zeolite coatings directly crystallized on fibrous plates for heat pump applications". In: *Applied thermal engineering* 58.1-2 (2013), pp. 273–280. DOI: 10.1016/j.applthermaleng.2013.04.037.

[61] Velte, A., Joos, L., and Füldner, G. "Experimental Performance Analysis of Adsorption Modules with Sintered Aluminium Fiber Heat Exchangers and SAPO-34-Water Working Pair for Gas-Driven Heat Pumps: Influence of Evaporator Size, Temperatures, and Half Cycle Times". In: *Energies* 15.8 (2022). ISSN: 1996-1073. DOI: 10.3390/en15082823.

[62] Velte-Schäfer, A., Yannan, Z., Nonnen, T., Wittstadt, U., Frazzica, A., Füldner, G., and Palomba, V. "numerical modelling and evaluation of a novel sorption module for thermally driven heat pumps and chillers using open-source simulation library". In: *Energy Conversion and Management* 291 (2023), p. 117252. ISSN: 0196-8904. DOI: 10.1016/j.enconman.2023.117252.

[63] Velte, A., Laurenz, E., Leisner, S., Weber, J., Wittstadt, U., and Füldner, G. "Experimental Results of a Gas Fired Adsorption Heat Pump and Simulative Prediction of Annual Performance in a Multi-Family House". In: *Applied Thermal Engineering* 212 (2022), p. 118581. ISSN: 1359-4311. DOI: 10.1016/j.applthermaleng.2022.118581.

[64] Loga, T., Diefenbach, N., Stein, B., and Born, R. *Deutsche Wohngebäudetypologie. Beispielhafte Maßnahmen zur Verbesserung der Energieeffizienz von typischen Wohngebäuden.* Institut Wohnen und Umwelt, Darmstadt, Germany, Feb. 2015. URL: https://www.episcope.eu/downloads/public/docs/scientific/DE_TABULA_ScientificRepor_IWU.pdf.

[65] Loga, T., Diefenbach, N., Stein, B., and Born, R. *TABULA - Scientific Report Germany Further Development of the National Residential Building Typology*. Institute for Housing and Environment Darmstadt, Germany, Oct. 2012. URL: https://episcope.eu/fileadmin/tabula/public/docs/scientific/DE_TABULA_ScientificReport_IWU.pdf.

[66] Bongs, C., Wapler, J., Dinkel, A., Miara, M., Auerswald, S., Lämmle, M., Hess, S., Kropp, M., Eberle, R., Rodenbücher, B., Schmidt, F., Ruppert, M., Carbonare, N., and Wagner, A. *Projekt LowEx-Bestand Analyse Abschlussbericht LowEx-Konzepte für die Wärmeversorgung von Mehrfamilien-Bestandsgebäuden ("LowEx-Bestand Analyse")*. Fraunhofer-Institut für Solare Energiesysteme ISE, KIT - Die Forschungsuniversität in der Helmholtz- Gemeinschaft, and Albert-Ludwigs-Universität Freiburg Institut für Nachhaltige Technische Systeme (INATECH), Mar. 2023. URL: https://lowex-bestand.de/index.php/ergebnisse/?lang=en&download=1541.

[67] Walberg, D., Holz, A., Gniechwitz, T., and Schulze, T. "Wohnungsbau in Deutschland 2011 – Modernisierung oder Bestandsersatz". In: *Mauerwerk* 15 (Sept. 2011), pp. 294–300. DOI: 10.1002/dama.201100508.

[68] Cischinsky, H. and Diefenbach, N. "Datenerhebung wohngebäudebestand 2016". In: *Datenerhebung zu den Energetischen Merkmalen und Modernisierungsraten im Deutschen und Hessischen Wohngebäudebestand; Institut Wohnen und Umwelt (IWU): Darmstadt, Germany* (2018), p. 179. URL: https://wohngebaeudedaten2016.iwu.de/.

[69] Leisner, S. "Modellgestützte Entwicklung eines Regelungsalgorithmus für eine Gas-Adsorptionswärmepumpe mit experimenteller Validierung". MA thesis. Fakultät für Maschinenbau und Verfahrenstechnik, Technische Hochschule Augsburg, 2021.

[70] Lämmle, M., Bongs, C., Wapler, J., Günther, D., Hess, S., Kropp, M., and Herkel, S. "Performance of air and ground source heat pumps retrofitted to radiator heating systems and measures to reduce space heating temperatures in existing buildings". In: *Energy* 242 (2022), p. 122952. ISSN: 0360-5442. DOI: 10.1016/j.energy.2021.122952.

[71] Miara, M. et al. (ed.) *Heat Pumps in Multi-Family Buildings for Space Heating and Domestic Hot Water*. Heat Pump Centre c/o RISE – Research Institutes of Sweden, 2022. URL: https://heatpumpingtechnologies.org/annex62/.

[72] Deutsches Institut für Normung (DIN). *Gasbefeuerte Sorptions-Geräte für Heizung und/oder Kühlung mit einer Nennwärmebelastung nicht über 70 kW - Teil 6: Berechnung der saisonalen Effizienzkennzahlen*. EN 12309-6. Berlin, Germany, 2015.

[73] Verein Deutscher Ingenieure (VDI). *Kurzverfahren zur Berechnung der Jahresheizzahl und des Jahresnutzungsgrads von Sorptionswärmepumpenanlagen Gas-Wärmepumpen zur Raumheizung und Warmwasserbereitung*. 4650-2. Düsseldorf, Germany, 2013.

[74] Verein Deutscher Ingenieure (VDI). *Berechnung der Jahresarbeitszahl von Wärmepumpenanlagen Elektrowärmepumpen zur Raumheizung und Trinkwassererwärmung*. 4650-1. Düsseldorf, Germany, 2016.

[75] Shelton, S. V., Wepfer, W. J., and Miles, D. J. "Square wave analysis of the solid-vapor adsorption heat pump". In: *Heat Recovery Systems and CHP* 9.3 (1989), pp. 233–247. ISSN: 0890-4332. DOI: 10.1016/0890-4332(89)90007-0.

[76] Critoph, R. E. "Forced convection adsorption cycles". In: *Applied Thermal Engineering* 18.9 (1998), pp. 799–807. ISSN: 1359-4311. DOI: 10.1016/S1359-4311(97)00110-5.

[77] Schmidt, F. P., Füldner, G., Schnabel, L., and Henning, H.-M. "Novel cycle concept for adsorption chiller with advanced heat recovery utilising a stratified storage". In: *Proceedings of the 2nd International Conference on Solar Air-Conditioning*. Tarragona, Spain, Oct. 2007, pp. 618–623.

[78] Munz, G., Schmidt, F., Nunez, T., and Schnabel, L. "Adsorption heat pump with heat accumulator". U.S. pat. US008631667B2. Jan. 21, 2014.

[79] Vollmer, R., Köhler, B., Koch, L., Wapler, J., Scharf, K., Ebert, B., Bongs, C., and Hess, S. *LowEx-Bestand Referenzgebäude: Geometrie, Bauphysik, Last-Zeitreihen und Sanierungsszenarien*. Fraunhofer-Institut für Solare Energiesysteme ISE KIT - Die Forschungsuniversität in der Helmholtz- Gemeinschaft Albert-Ludwigs-Universität Freiburg, Institut für Nachhaltige Technische Systeme (INATECH), Apr. 2022. URL: https://www.lowex-bestand.de/wp-content/uploads/2022/04/2022-04-26_LiB_Bericht_AP_3.1_Referenzgeb%C3%A4ude_Parameter_FINAL.pdf.

[80] *Dymola: Dassault Systemes*. URL: https://www.3ds.com/products/catia/dymola. Accessed: 11.01.2024.

[81] *Modelica: Model complex system more efficiently*. URL: https://modelica.org/. Accessed: 11.01.2024.

[82] Brenan, K. E., Campbell, S. L., and Petzold, L. R. *Numerical solution of initial-value problems in differential-algebraic equations*. SIAM, 1995. ISBN: 9780444015112.

[83] Shah, R. K. and Sekulic, D. P. *Fundamentals of heat exchanger design*. John Wiley & Sons, 2003. ISBN: 9780470172605.

[84] Wetter, M., Zuo, W., Nouidui, T. S., and Pang, X. "Modelica Buildings library". In: *Journal of Building Performance Simulation* 7.4 (2014), pp. 253–270. DOI: 10.1080/19401493.2013.765506.

[85] Wetter, M. *Simulation model finned water-air-coil without condensation*. Lawrence Berkeley National Lab. (LBNL), Berkeley, California, United States, 1999. DOI: 10.2172/7353.

[86] Wetter, M. *Simulation model air-to-air plate heat exchanger*. Lawrence Berkeley National Lab. (LBNL), Berkeley, California, United States, 1999. DOI: 10.2172/7352.

[87] Kropp, M., Hörnle, O., Lämmle, M., Wapler, J., and Hess, S. *Einfluss der Trinkwarmwasser-Systemvariante auf die Performance von Wärmepumpen in Mehrfamilienhäusern*. Albert-Ludwigs-Universität Freiburg Institut für Nachhaltige Technische Systeme (INATECH), 2020. URL: https://www.lowex-bestand.de/wp-content/uploads/2021/01/AA-IV-07-DKV-2020-Manuskript-Kropp.pdf.

[88] Hadorn, J.-C. *Solar and heat pump systems for residential buildings.* John Wiley & Sons, 2015. ISBN: 9783433030400.

[89] Zaß, K. *Hydraulische Schaltungen für solarthermische Kombianlagen mit hohen Deckungsraten – theoretischer Vergleich und konstruktive Umsetzung.* Kassel University Press, 2012. DOI: 10.17170/kobra-202302167496.

[90] Jordan, U. and Vejen, K. "Einfluss verschiedener Beladeeinrichtungen auf den Ertrag eines Kombisystems". In: *Gleisdorf Solar 2002.* Oct. 16, 2002, pp. 111–119.

[91] Solar Rating and Certification Corporation. *OG-100 Solar Thermal Collector Certification.* Licence Holder= DIMAS SA, Licence Number= 2010019B. URL: https://secure.solar-rating.org/Certification/Ratings/RatingsSummaryPage.aspx?type=1. Accessed: 14.09.2022.

[92] TÜV Rheinland DIN CERTCO GmbH. *Annex to Solar Keymark Certificate.* Licence Holder= DIMAS SA, Licence Number= 011-751490 F. URL: https://solarkeymark.eu/database/. Accessed: 14.09.2022.

[93] Verein Deutscher Ingenieure (VDI). *Solare Trinkwassererwärmung - Allgemeine Grundlagen - Systemtechnik und Anwendung im Wohnungsbau.* 6002-1. Düsseldorf, Germany, 2004.

[94] Duffie, J. A. and Beckman, W. A. *Solar Engineering of Thermal Processes.* John Wiley & Sons, Inc, 2006. ISBN: 9780470873663.

[95] Weiss, W. *Solar Heating Systems for Houses: A Design Handbook for Solar Combisystems.* Taylor & Francis Group, 2003. ISBN: 9781902916460.

[96] Lawrie, L. K. and Crawley, D. B. *Development of Global Typical Meteorological Years (TMYx).* 2022. URL: https://climate.onebuilding.org.

[97] *Meteonorm: Global Meteorological Database.* URL: https://meteonorm.com/. Accessed: 17.01.2024.

[98] Verein Deutscher Ingenieure (VDI). *Reference Load Profiles of Single-family and Multi-family Houses for the Use of CHP Systems.* 4655. Düsseldorf, Germany, 2008.

[99] Deutsches Institut für Normung (DIN). *Berechnung des Energiebedarfs fuer Heizung und Kuehlung.* EN ISO 13790. Berlin, Germany, 2008.

[100] Burhenne, S. and Jacob, D. "Simulation models to optimize the energy consumption of buildings". In: *ICEBO - International Conference for Enhanced Building Operations.* Energy Systems Laboratory, 2008. URL: https://hdl.handle.net/1969.1/90803.

[101] Fischer, D. "Integrating heat pumps into smart grids". PhD thesis. Division of Applied Thermodynamics and Refrigeration Department of Energy Technology, KTH Royal Institute of Technology, 2017. ISBN: 978-91-7729-503-7.

[102] Eurostat. *Harmonised European time use surveys.* URL: https://ec.europa.eu/eurostat/web/microdata/harmonised-european-time-use-surveys. Accessed: 17.01.2024.

[103] Verein Deutscher Ingenieure (VDI). *Economic Efficiency of Building Installations - Effective Energy Requirements for Heating Service Water.* 2067-12. Düsseldorf, Germany, 2000.

[104] Baeten, B., Confrey, T., Pecceu, S., Rogiers, F., and Helsen, L. "A validated model for mixing and buoyancy in stratified hot water storage tanks for use in building energy simulations". In: *Applied Energy* 172 (2016), pp. 217–229. ISSN: 0306-2619. DOI: 10.1016/j.apenergy.2016.03.118.

[105] Prijić, E. "Untersuchung der Vermischungsvorgänge in einem Schichtspeicher mit aktiven Einschichteinrichtungen mittels eines 1D-Modells in der Modellierungssprache Modelica". MA thesis. Fakultät für Maschinenbau, Karlsruhe Institute für Technologie, 2019.

[106] Drück, H. and Pauschinger, T. "Multiport store–model for TRNSYS". In: *Type 340, Version 1.99 F* (2006). URL: https://www.trnsys.de/static/788c19e80e1b4e690b35e44b05c8b164/ts_type_340_de.pdf.

[107] Recknagel, H., Sprenger, E., and Schramek, E.-R. *Taschenbuch für Heizung+ Klimatechnik 2011/12.* Vol. 75. Oldenbourg Industrieverlag, 2011. ISBN: 9783835632004.

[108] Çengel, Y. A. and Boles, M. A. *Thermodynamics: An Engineering Approach.* 5th. New York: McGraw-Hill, 2011. ISBN: 9780072884951.

[109] Lanzerath, F. "Modellgestützte Entwicklung von Adsorptionswärmepumpen". PhD thesis. Fakultät für Maschinenwesen, Rheinisch-Westfälischen Technischen Hochschule Aachen, 2014. URL: https://publications.rwth-aachen.de/record/444649/files/5147.pdf.

[110] Lanzerath, F., Bau, U., Seiler, J., and Bardow, A. "Optimal design of adsorption chillers based on a validated dynamic object-oriented model". In: *Science and Technology for the Built Environment* 21.3 (2015), pp. 248–257. DOI: 10.1080/10789669.2014.990337.

[111] Velte, A., Füldner, G., Laurenz, E., and Schnabel, L. "Advanced Measurement and Simulation Procedure for the Identification of Heat and Mass Transfer Parameters in Dynamic Adsorption Experiments". In: *Energies* 10.8 (2017). ISSN: 1996-1073. DOI: 10.3390/en10081130.

[112] Laurenz, E., Füldner, G., Velte, A., Schnabel, L., and Schmitz, G. "Frequency response analysis for the determination of thermal conductivity and water transport in MOF adsorbent coatings for heat transformation". In: *International Journal of Heat and Mass Transfer* 169 (2021), p. 120921. ISSN: 0017-9310. DOI: 10.1016/j.ijheatmasstransfer.2021.120921.

[113] Schnabel, L. "Experimentelle und numerische Untersuchung der Adsorptionskinetik von Wasser an Adsorbens-Metallverbundstrukturen". PhD thesis. Fakultät III-Prozesswissenschaften, Technischen Universität Berlin, 2009. DOI: 10.14279/depositonce-2141.

[114] Schwamberger, V. and Schmidt, F. P. “Estimating the Heat Capacity of the Adsorbate–Adsorbent System from Adsorption Equilibria Regarding Thermodynamic Consistency”. In: *Industrial & Engineering Chemistry Research* 52.47 (2013), pp. 16958–16965. DOI: 10.1021/ie4011832.

[115] Alefeld, G. and Radermacher, R. *Heat Conversion Systems*. CRC-Press, 1993. ISBN: 9780849389283.

[116] Paulussen, S. “Adsorption Apparatus Comprising a Heat Recovery System”. U.S. pat. US 20110167842A1. July 14, 2011.

[117] Wang, R. Z. “Performance improvement of adsorption cooling by heat and mass recovery operation”. In: *International Journal of Refrigeration* 24.7 (2001), pp. 602–611. ISSN: 0140-7007. DOI: 10.1016/S0140-7007(01)00004-4.

[118] Sadeghlu, A. and Schmidt, F. P. “Simulation Study of Single-Adsorber Heat Pump Cycle with Heat Recovery Through Stratified Storage in Both Adsorber and Evaporator/Condenser Loops”. In: *Energies* 17.21 (2024). ISSN: 1996-1073. DOI: 10.3390/en17215472.

[119] Schwamberger, V., Desai, A., and Schmidt, F. P. “Novel Adsorption Cycle for High-Efficiency Adsorption Heat Pumps and Chillers: Modeling and Simulation Results”. In: *Energies* 13.1 (2020). ISSN: 1996-1073. DOI: 10.3390/en13010019.

[120] Yu, Z. J., Huang, G., Haghighat, F., Li, H., and Zhang, G. “Control strategies for integration of thermal energy storage into buildings: State-of-the-art review”. In: *Energy and Buildings* 106 (2015). SI: IEA-ECES Annex 31 Special Issue on Thermal Energy Storage, pp. 203–215. ISSN: 0378-7788. DOI: 10.1016/j.enbuild.2015.05.038.

[121] Müller, D., Lauster, M. R., Constantin, A., Fuchs, M., and Remmen, P. “AixLib - An Open-Source Modelica Library within the IEA-EBC Annex60 Framework”. In: Stuttgart: Fraunhofer IRB Verlag, Sept. 14, 2016, pp. 3–9. URL: https://publications.rwth-aachen.de/record/681852.

[122] Wetter, M., Blum, D., and Hu, J. *Modelica IBPSA Library v1*. May 2019. DOI: 10.11578/dc.20190520.1.

[123] Bau, U., Lanzerath, F., Gräber, M., Graf, S. W., Schreiber, H., Thielen, N., and Bardow, A. “Adsorption energy systems library - Modeling adsorption based chillers, heat pumps, thermal storages and desiccant systems”. In: vol. 96. Linkoping Electronic Conference Proceedings. Linköping: Modelica Association and Linkoping University Electronic Press, Mar. 10, 2014, pp. 875–883. DOI: 10.3384/ECP14096875.

[124] *Dezentrales Pumpensystem „Wilo-Geniax“TÜV-zertifizierte Heizenergie- und Stromeinsparungen*. URL: https://www.ikz.de/detail/news/detail/dezentrales-pumpensystem-wilo-geniaxtuev-zertifizierte-heizenergie-und-stromeinsparungen/. Accessed: 12.06.2024.

[125] Haller, M. Y., Haberl, R., Persdorf, P., and Reber, A. “Stratification Efficiency of Thermal Energy Storage Systems – A new KPI based on Dynamic Hardware in the Loop Testing - Part I: Test Procedure”. In: *Energy Procedia* 155 (2018). 12th International Renewable Energy Storage Conference, IRES 2018, 13-15 March 2018, Düsseldorf, Germany, pp. 188–208. ISSN: 1876-6102. DOI: 10.1016/j.egypro.2018.11.056.

[126] Haller, M. Y., Haberl, R., and Reber, A. “Stratification efficiency of thermal energy storage systems – A new KPI based on dynamic hardware in the loop testing - Part II: Test results”. In: *Energy and Buildings* 202 (2019), p. 109366. ISSN: 0378-7788. DOI: 10.1016/j.enbuild.2019.109366.

[127] Meunier, F., Poyelle, F., and LeVan, M. D. “Second-law analysis of adsorptive refrigeration cycles: The role of thermal coupling entropy production”. In: *Applied Thermal Engineering* 17.1 (1997), pp. 43–55. ISSN: 1359-4311. DOI: 10.1016/1359-4311(96)00019-1.

[128] MathWorks. *MATLAB Documentation*. 2020. URL: https://www.mathworks.com/help/matlab/.

[129] Tiller, M. *Introduction to Physical Modeling with Modelica*. Springer, 2001. ISBN: 9781461356158.

[130] Volmer, R., Eckert, J., Füldner, G., and Schnabel, L. “Evaporator development for adsorption heat transformation devices – Influencing factors on non-stationary evaporation with tube-fin heat exchangers at sub-atmospheric pressure”. In: *Renewable Energy* 110 (2017). Increasing the renewable share for heating and cooling by the means of sorption heat pumps and chillers, pp. 141–153. ISSN: 0960-1481. DOI: 10.1016/j.renene.2016.08.030.

[131] Dincer, I. and Rosen, M. A. *Exergy Energy, Environment and Sustainable Development*. Elsevier, 2007. ISBN: 9780080445298.

[132] Verein Deutscher Ingenieure (VDI). *Hygiene in Trinkwasser-Installationen - Anforderungen an Planung, Ausführung, Betrieb und Instandhaltung*. 6023. Düsseldorf, Germany, 2013.

[133] Deutsches Institut für Normung (DIN). *Technische Regeln für Trinkwasser-Installationen - Teil 2: Planung*. EN 806-2. Berlin, Germany, 2005.

[134] Darelid, J., Löfgren, S., and Malmvall, B.-E. “Control of nosocomial Legionnaires’ disease by keeping the circulating hot water temperature above 55 degrees C: experience from a 10-year surveillance programme in a district general hospital”. In: *Journal of Hospital Infection* 50.3 (Mar. 2002), pp. 213–219. DOI: 10.1053/jhin.2002.1185.

[135] Deutscher Verein des Gas- und Wasserfaches. *Energieeinsparungen im Warmwasserbereich in Trinkwasser-Installationen – geht das?* 2023. URL: https://www.dvgw.de/medien/dvgw/leistungen/publikationen/energiesparen-warmwasser-dvgw-langfassung.pdf.

[136] Zhang, F., Bales, C., and Fleyeh, H. “From time series to image analysis: A transfer learning approach for night setback identification of district heating substations”. In: *Journal of Building Engineering* 43 (2021), p. 102537. ISSN: 2352-7102. DOI: 10.1016/j.jobe.2021.102537.

[137] Moon, J. W. and Han, S.-H. “Thermostat strategies impact on energy consumption in residential buildings”. In: *Energy and Buildings* 43.2 (2011), pp. 338–346. ISSN: 0378-7788. DOI: 10.1016/j.enbuild.2010.09.024.

[138] Gadd, H. and Werner, S. “Daily heat load variations in Swedish district heating systems”. In: *Applied Energy* 106 (2013), pp. 47–55. ISSN: 0306-2619. DOI: 10.1016/j.apenergy.2013.01.030.

[139] Aristov, Yu. I., Sapienza, A., Ovoshchnikov, D. S., Freni, A., and Restuccia, G. “Reallocation of adsorption and desorption times for optimisation of cooling cycles”. In: *International Journal of Refrigeration* 35.3 (2012). Refrigeration and Heat Pumping with Sorption Processes, pp. 525–531. ISSN: 0140-7007. DOI: 10.1016/j.ijrefrig.2010.07.019.

[140] Varchmin, A. “Regelungstechnische Analyse von Kälteanlagen mit parallelen Verdampfern”. PhD thesis. Fakultät für Maschinenbau, Technischen Universität Carolo-Wilhelmina zu Braunschweig, 2017.

[141] Schmidt, F. and Desai, A. “Adsorptionswärmepumpe oder -kältemaschine und Verfahren zu ihrem Betrieb”. Deutsches Patent- und Markenamt DE102018109575A1. Oct. 2019. URL: https://register.dpma.de/DPMAregister/pat/register?AKZ=1020181095759&CURSOR=0.

[142] Deutsches Institut für Normung (DIN). *Heizkessel; Ermittlung des Norm-Nutzungsgrades und des Norm-Emissionsfaktors.* 4702-8. Berlin, Germany, 1990.

[143] Deutsches Institut für Normung (DIN). *Prüf Gase - Prüfdrücke - Geräteklassen.* EN 437. Berlin, Germany, 2003.

[144] *Anlage 8 zu den §§ 69 und 70 – Anforderungen an die Wärmedämmung von Rohrleitungen und Armaturen.* Gesetz zur Einsparung von Energie und zur Nutzung erneuerbarer Energien zur Wärme- und Kälteerzeugung in Gebäuden (Gebäudeenergiegesetz – GEG), Anlage 8. 2020. URL: https://www.gesetze-im-internet.de/geg/anlage_8.html.

A. Appendix

A.1. Dual Adsorber Cycle Gas Adsorption Heat pump Operation Modes in Reference System

The reference system at the module level comprises two Single Adsorber Cycles. The hydraulic scheme for Single Adsorber Cycle 1 is detailed as follows: the desorption process is depicted in Figure A.1, heat recovery is illustrated in Figure A.2, and the direct burner mode is shown in Figure A.3. Similarly, for Single Adsorber Cycle 2, the desorption process is represented in Figure A.4, heat recovery is outlined in Figure A.5, and the direct burner mode is described in Figure A.6. In each scheme, the red line indicates the high-temperature level, the orange line represents the middle temperature level, and the blue line denotes the low-temperature level. Additionally, the green line shows the heat recovery path, while the grey line indicates the inactive path.

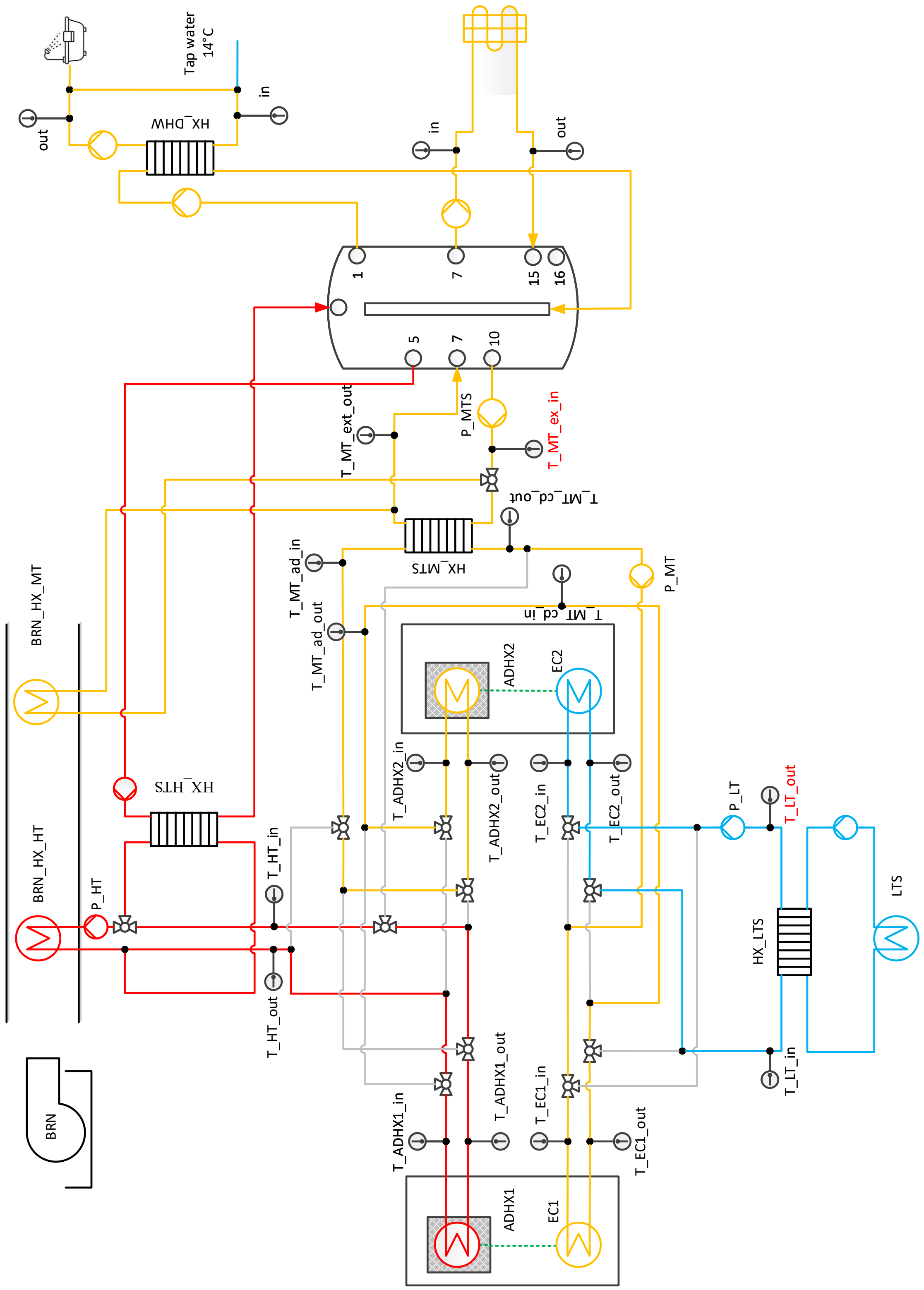

Figure A.1.: Desorption Mode in adsorber/desorber heat exchanger 1 in Dual Adsorber Cycle Gas Adsorption Heat pump

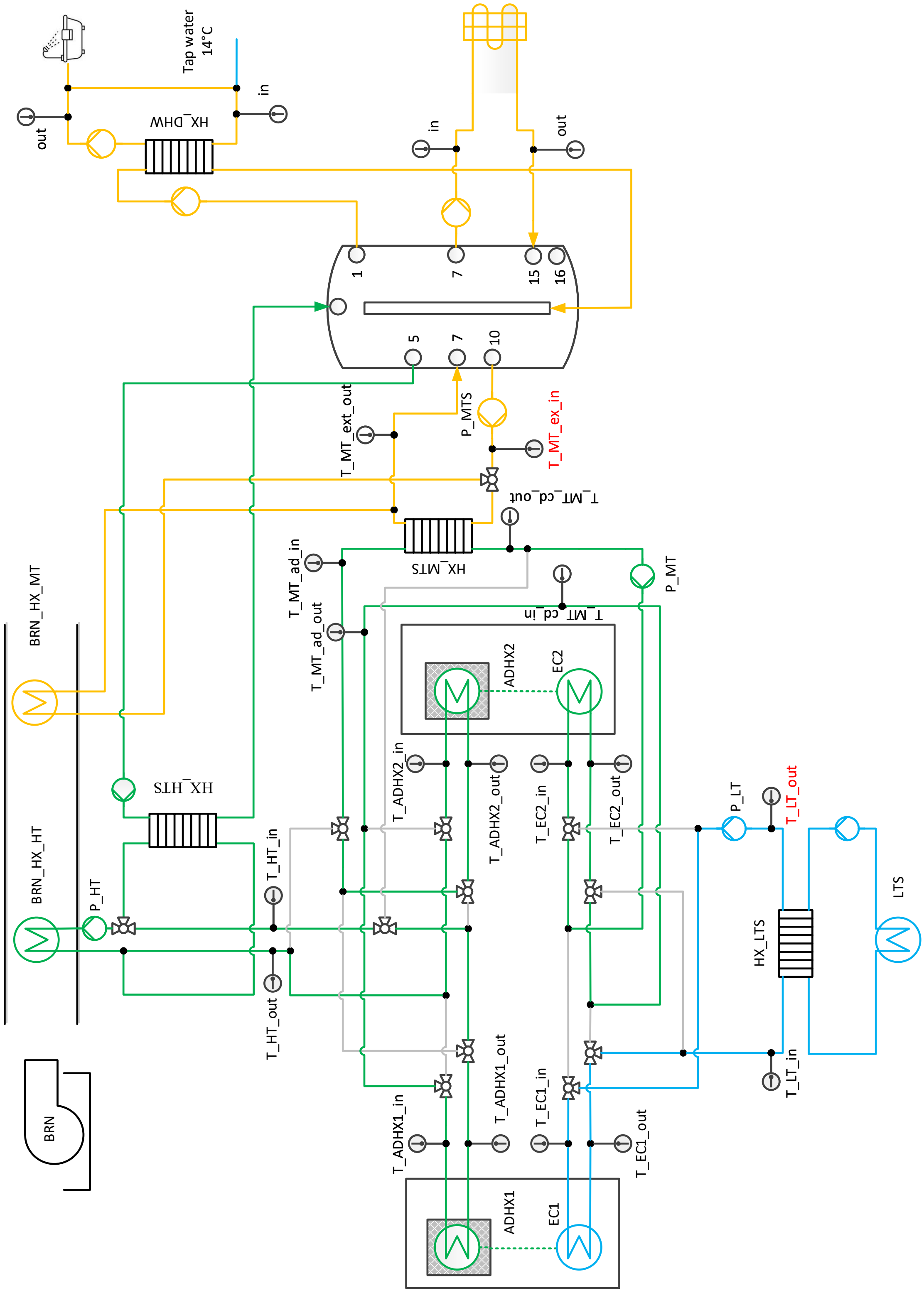

Figure A.2.: Heat Recovery Mode in adsorber/desorber heat exchanger 1 in Dual Adsorber Cycle Gas Adsorption Heat pump

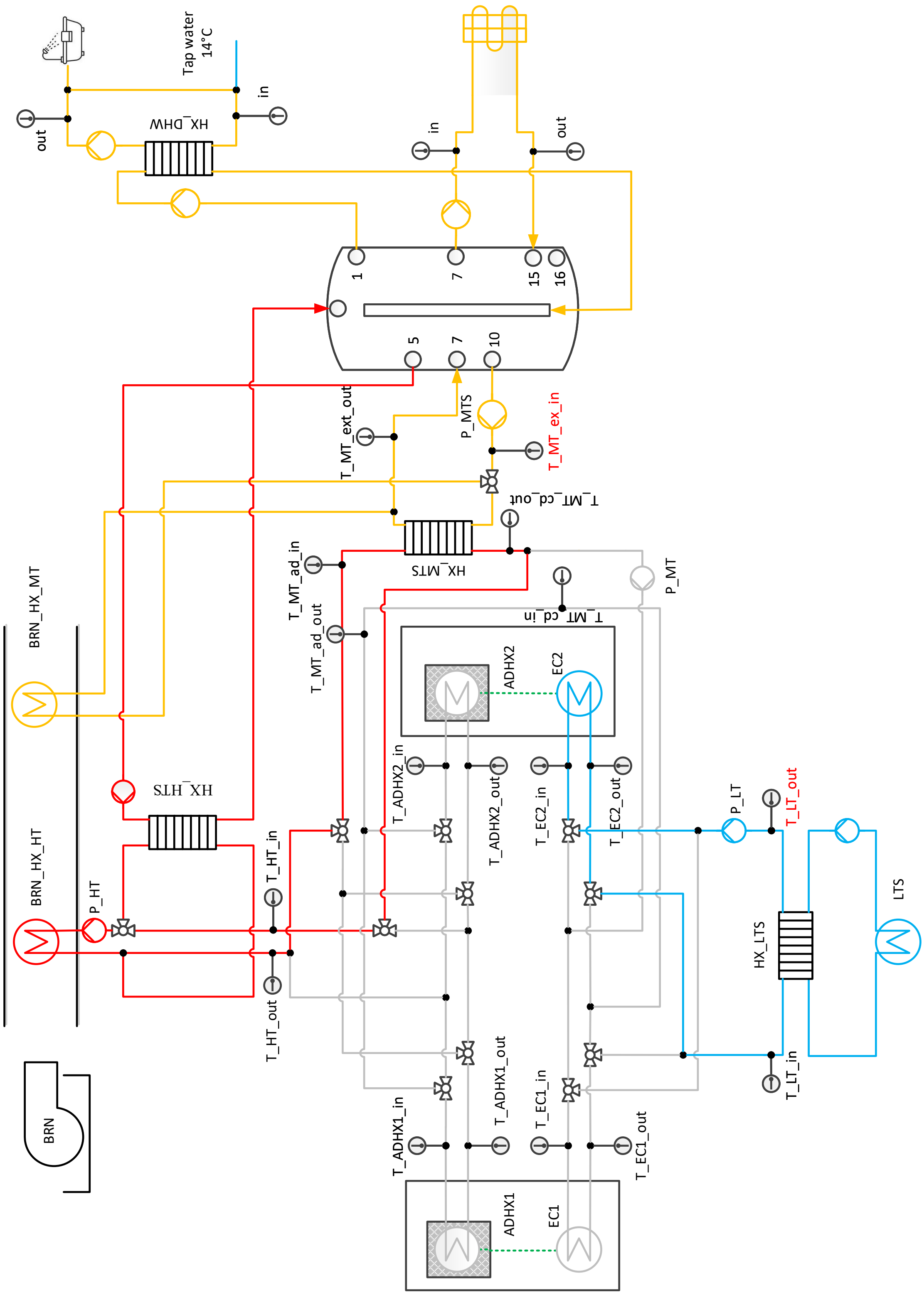

Figure A.3.: Direct Burner Mode in adsorber/desorber heat exchanger 1 in Dual Adsorber Cycle Gas Adsorption Heat pump

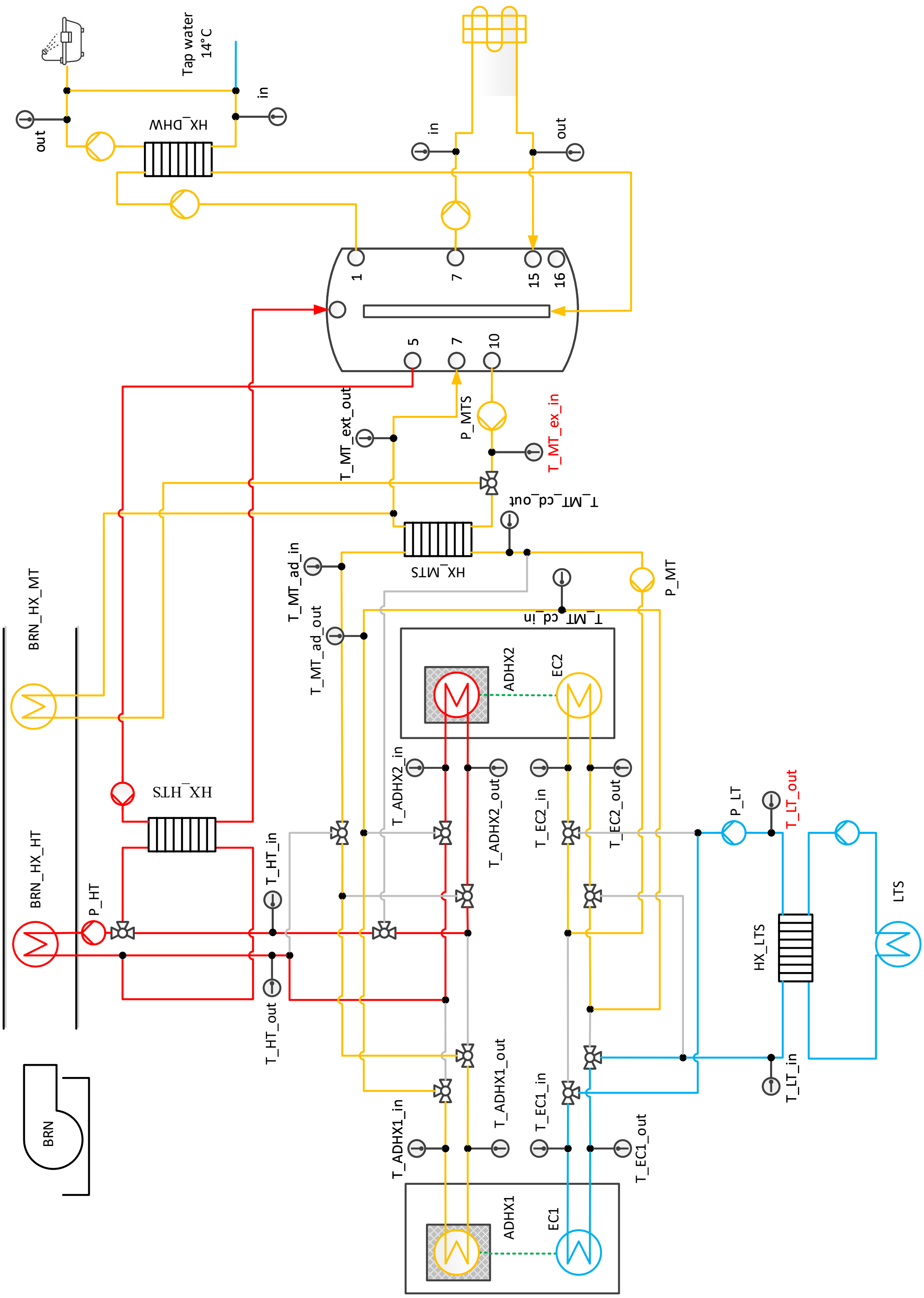

Figure A.4.: Desorption Mode in adsorber/desorber heat exchanger 2 in Dual Adsorber Cycle Gas Adsorption Heat pump

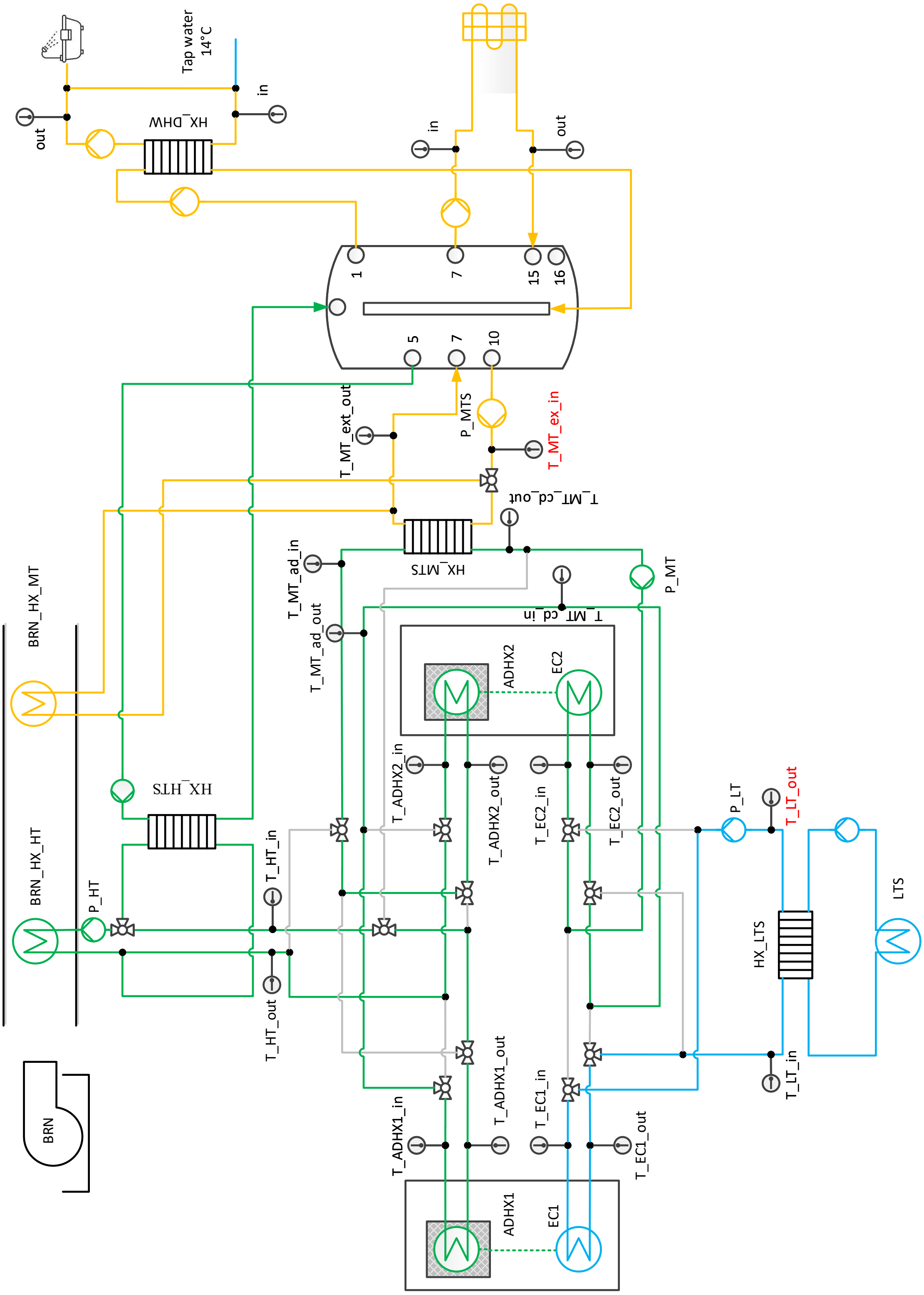

Figure A.5.: Heat Recovery Mode in adsorber/desorber heat exchanger 2 in Dual Adsorber Cycle Gas Adsorption Heat pump

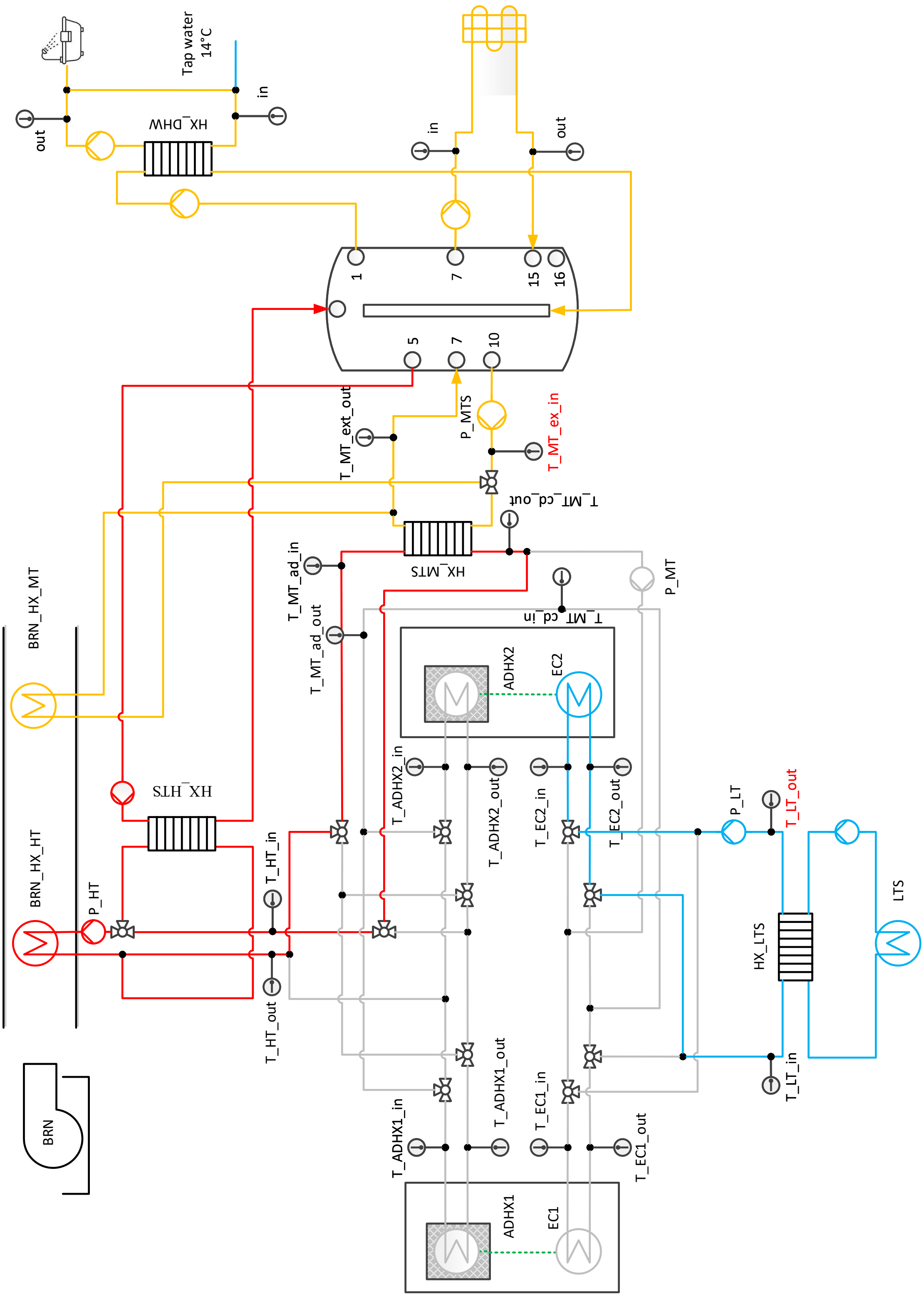

Figure A.6.: Direct Burner Mode in adsorber/desorber heat exchanger 2 in Dual Adsorber Cycle Gas Adsorption Heat pump

A.2. SGUE Calculation Approaches

To design a sorption heat pump system for heating, several factors must be considered, beginning with the selection of the heating system type and the ambient heat source temperature. It is essential to account for fluctuations in outdoor temperatures throughout the year when making these decisions. After defining the location, heating system, and ambient heat source, the primary variable influencing the design is the changing outdoor temperature.

This temperature variability is crucial because space heating energy demands are directly affected by factors like transmission heat losses, ventilation heat losses, and heat gains (e.g., from solar radiation and internal heat generated by occupants or animals). Transmission and ventilation losses increase as the outdoor temperature decreases, meaning that the heating system must compensate for these losses. Thus, the required heat output is proportional to the difference between indoor and outdoor temperatures.

To simplify the relationship between outdoor temperature and heating demand, previous standards, such as the now-outdated VDI Guideline 2067 Part 6, along with studies by Schwamberger [16], offer a practical approach. These methods involve using a frequency distribution of daily mean outdoor temperatures to generate an ordered annual duration curve. This curve correlates the heating system's power with the difference between indoor and outdoor temperatures. The curve is typically divided into five intervals, each representing a relative heating power. This approach serves as the foundation for calculating system efficiency parameters, as outlined in VDI Guideline 4650 Part 2.

Seasonal Gas Utilization Efficiency in DIN EN 12309-6 [72] is referred to as Annual Gas Utilization Efficiency in VDI-4650-2 [73]. In this context, the Annual Gas Utilization Efficiency for space heating, evaluated at the representative operating points specified by DIN 4702-8 [142] and detailed in Table 2.4, is calculated in accordance with the guidelines provided in VDI-4650-2 [73] as follow:

$$SGUE_{\mathrm{heat}} = \eta_{\mathrm{N,h}} = \frac{5}{\sum_{i=1}^{5} \frac{1}{\eta_{\mathrm{h,i}}}} \tag{A.1}$$

$$\eta_{\mathrm{h,i}} = \int_{0}^{EachCycle} \left(\frac{\dot{Q}_{HDS}}{\frac{\dot{Q}_{flueGas,HT}}{\eta_{NCV}(T_{flueGas,HT})}} \right) dt \tag{A.2}$$

In contrast, the European Standard EN 12309 Part 6 adopts a different methodology for calculating the seasonal efficiency of gas-fired sorption systems. It defines SGUE, which is determined by interpolating between six key outdoor temperature points and corresponding operating hours.

The DIN EN 12309-6 standard distinguishes between different reference heating periods (medium, warmer, colder) and multiple application temperatures (low, medium, high, very high). The simulation boundary conditions for the heating system considered in this research (55/41) and climate medium (A) are outlined in Table 2.4.

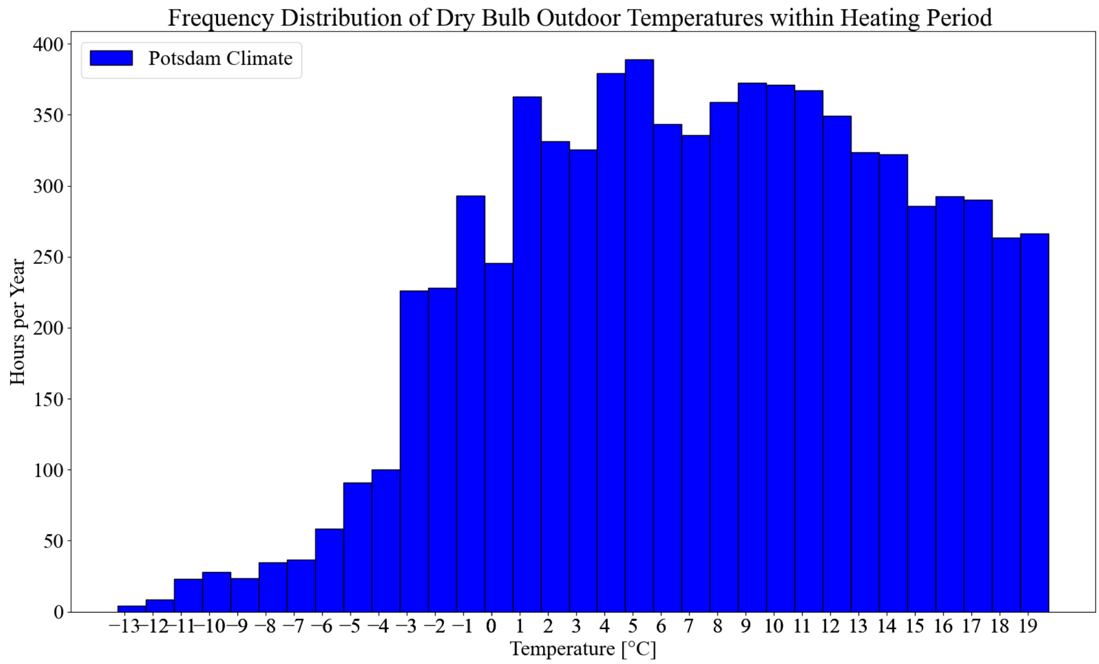

Figure A.7.: Frequency distribution of the dry bulb outdoor temperatures below 20 over one year into 1°C temperature bins

In this study, I employ the frequency distribution of dry bulb outdoor temperatures below 20 in Potsdam over the course of a year, categorized into 1°C temperature bins, as illustrated in Figure A.7. Using this temperature distribution, the procedure for calculating Seasonal Gas Utilization Efficiency is described as follows:

$$PLR_h(T_j) = \frac{T_j - 16}{T_{\text{design}h} - 16} \tag{A.3}$$

$$P_{\text{heat}}(T_j) = P_{\text{design}h} \times PLR_h(T_j) \tag{A.4}$$

$$GUE_{\text{heat}}(T_j) = \int_0^{EachCycle} \left(\frac{\dot{Q}_{HDS}}{\frac{\dot{Q}_{flueGas,HT}}{\eta_{NCV}(T_{flueGas,HT})}} \right) dt \tag{A.5}$$

$\dot{Q}_{HDS}$ in equation (A.5) is the heat delivered to the Heat Distribution System (HDS) in Figure 2.10

$$SGUE_{\text{heat}} = \frac{\sum_{j=1}^{n} \Delta t_j \cdot P_{\text{heat}}(T_j)}{\sum_{j=1}^{n} \Delta t_j \cdot \frac{P_{\text{heat}}(T_j)}{GUE_{\text{heat}}(T_j)}} \tag{A.6}$$

$T_{\text{design}h}$ is -12.8 °C and $PLR_h(T_j)$ is the partial load ratio detailed in Table 2.4. From these, it is possible to determine the temperature T_j. The corresponding Δt_j is then specified by Figure A.7.

A.3. Representative Operating Point

The Annual Load Duration Curve, illustrated in Figure A.8, is discretized into five segments of equal energy area in accordance with the DIN 4702-8 standard [142]. For each segment, a representative operating point (marked as "Middle Points") is identified. These points are used to evaluate the system's performance across its characteristic load spectrum. This energy-weighted approach ensures that the performance assessment of the reference system accounts for the frequency and magnitude of the actual thermal demand throughout the year.

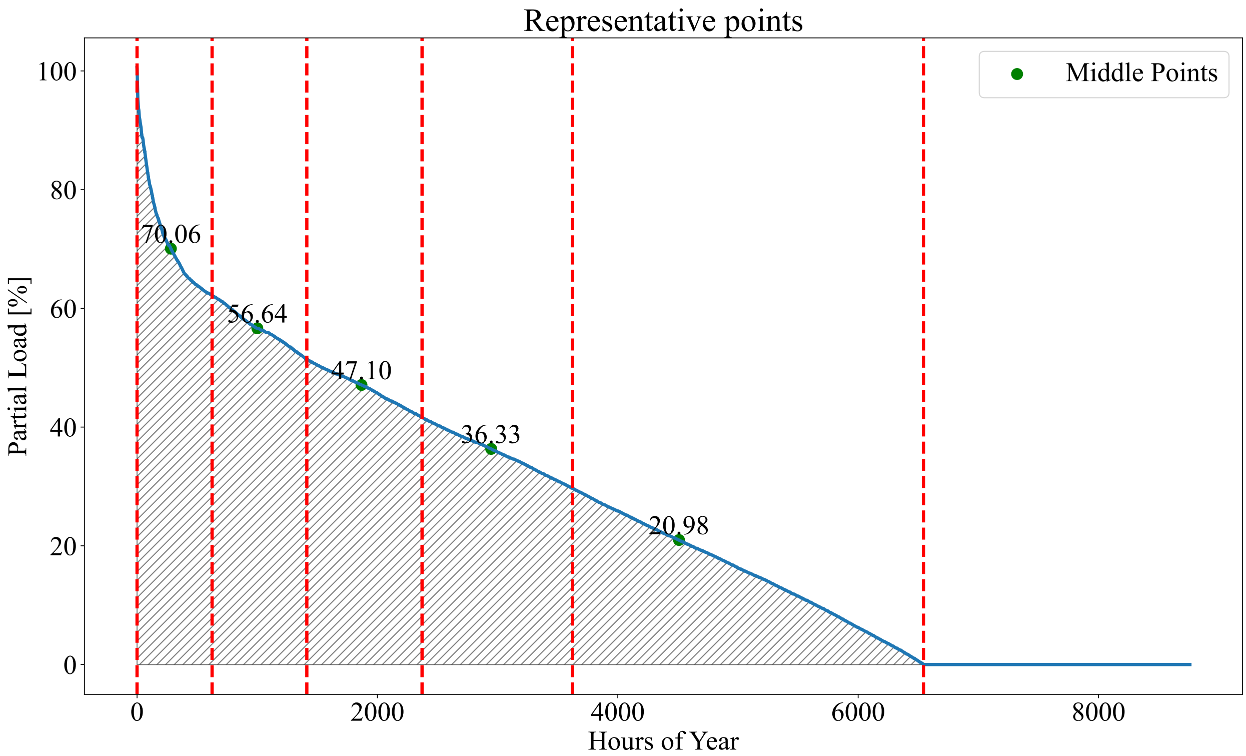

Figure A.8.: Annual Load Duration Curve: Representative Operating Points

A.4. Gas Consumption Efficiency Based on Net Calorific Value

The theoretical efficiency of the gas burner is calculated in Equation A.7. The numerator represents the actual thermal energy released by the gas under the given operating conditions, accounting for the gas temperature and excess air ratio. The denominator represents the chemical energy content of the fuel, expressed by its lower heating value (LHV) under standard reference conditions. The use of the LHV accounts only for the usable chemical energy of the fuel, excluding the latent heat of vaporization of the water formed during combustion, as specified by DIN EN 437 [143]. When calculating $q_{m,\text{flueGas}}$, the condensation of the exhaust gas is taken into account.

$$\eta(T_{\text{flueGas}}) = \frac{q_{m,\text{flueGas}}(T_{\text{flueGas}}, \lambda > 1)}{H_u(T = 15°\text{C}, \lambda = 1)} \tag{A.7}$$

For calculation of theoretical efficiency, the reaction equation in Equation A.8 for the combustion of pure Methane and the assumptions in Table A.1 are considered.

Parameter	Unit	Value
Excess Air-Fuel Ratio for Over Stoichiometric Combustion (λ)	-	1.3
Oxygen Content in Ambient Air	Vol %	0.21
Content of Inert Gas (Summarized as Nitrogen)	Vol %	0.79
Ambient Pressure	Pa	1.013×10^5
Ambient Temperature During Combustion (DIN EN 437)	°C	15

Table A.1.: Parameters and assumption for calculating the gas burner theoretical efficiency

First, there is ideal heat transfer between the gas and the heat exchanger, with no heat losses from the components.

Second, the reaction proceeds to complete conversion and exhibits ideal gas behavior.

Third, the amount of water condensing on the heat exchanger is determined using the saturation vapor pressure of water.

$$CH_4\ (g) + 2O_2\ (g) \rightarrow CO_2\ (g) + 2H_2O\ (g) \tag{A.8}$$

$$\Delta_R H^0 = \sum \Delta H_f^\circ(\text{products}) - \sum \Delta H_f^\circ(\text{reactants}) \tag{A.9}$$

Standard reaction Enthalpy $\Delta_R H^0$ should be calculated with Equation A.9 at $T_0 = 25\,°\text{C}$ and $P_0 = 1.013 \times 10^5$ Pa.

$$\Delta_R H = \Delta_R H^0 + \sum (H_{m,i}(T_{Product}) - H_{m,i}(T_{Reactants})) \cdot \nu_i \tag{A.10}$$

$T_{Reactants} = 15\,°\text{C}$ and ν_i is the stoichiometric coefficient for each products and reactants.

$$q_{m,\text{flueGas}} = \frac{\Delta_R H}{M_{CH_4}} + q_{m,\text{condense}} \tag{A.11}$$

$$q_{m,\text{condense}} = \frac{n_{\text{condense}}(T_{\text{flueGas}}) \cdot M_{H_2O}}{M_{CH_4}} \cdot \Delta H_{v,H_2O}(T_{\text{flueGas}}) \tag{A.12}$$

The specific mass energy of the combustion gas is calculated according to Equation Equation A.11. $q_{m,\text{condense}}$ is the specific mass energy released during the condensation of water vapor in the exhaust gas. The amount of condensing water $n_{\text{condense}}(T_{\text{flueGas}})$ and the enthalpy of vaporization of water, $\Delta H_{v,H_2O}(T_{\text{flueGas}})$, both depend on the temperature of the exhaust gas.

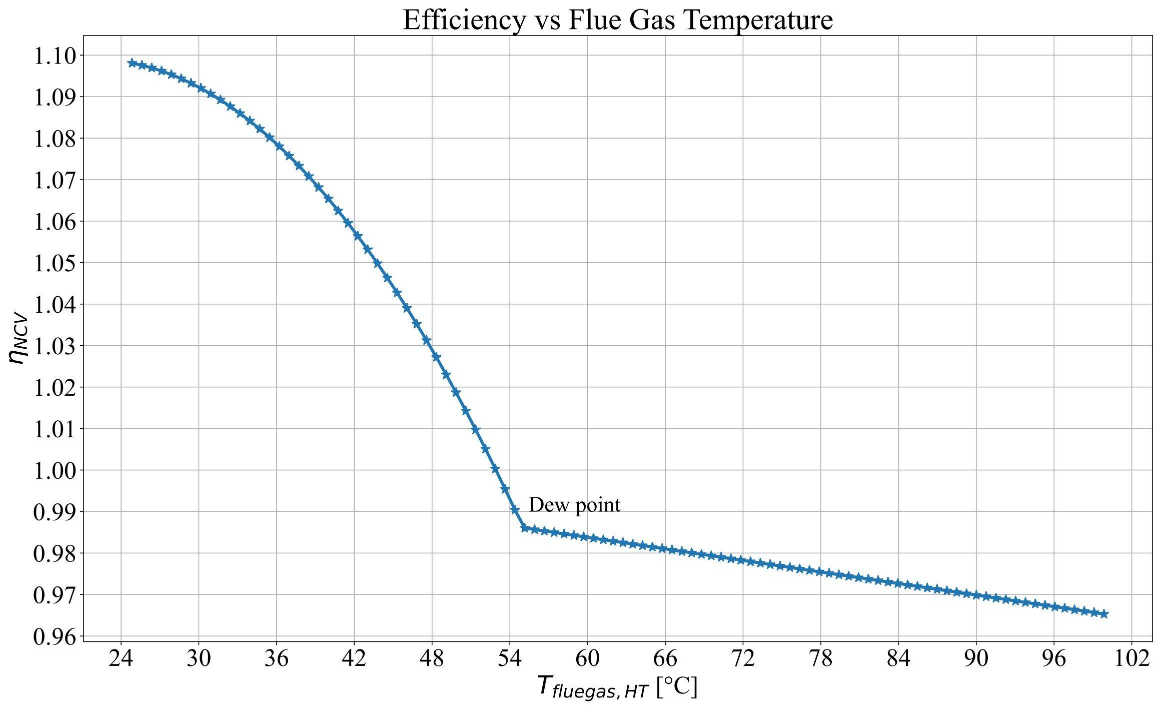

Figure A.9.: Variation of Efficiency with Flue Gas Temperature

Therefore, theoretical efficiency of gas burner based on net calorific value are shown in Figure A.9. The calculation points are approximated by linear regression for heat transfer without condensation for $T_{\text{flueGas}} \geq 55\,°\text{C}$:

$$\eta(T_{\text{flueGas}}) = -4.6368 \times 10^{-4} \cdot T_{\text{flueGas}} + 1.13824575 \tag{A.13}$$

and by a second-degree polynomial regression for heat transfer with condensation for $T_{\text{flueGas}} < 55\,°\text{C}$:

$$\eta(T_{\text{flueGas}}) = -1.03284 \times 10^{-4} \cdot T_{\text{flueGas}}^2 + 0.006096407 \cdot T_{\text{flueGas}} + 0.7897193051 \tag{A.14}$$

A.5. Two-Storage System

The annual temperature profiles for the Two-Storage system, with labeled specified storage layers connected to the components, are depicted in Figure A.10. Water is extracted from layer 9, heated with the HX-HTS, and the return hot water is directed to the top of the storage. Although, return DHW consumption, as shown in Figure 2.15 in subsection 2.3.2, is distributed across storage layers with an ideal inserter, the two bottom layers exhibit minimal temperature variation. This minimal variation is likely due to the over-sizing of the storage unit based on the technical recommendations in Equation 2.15.

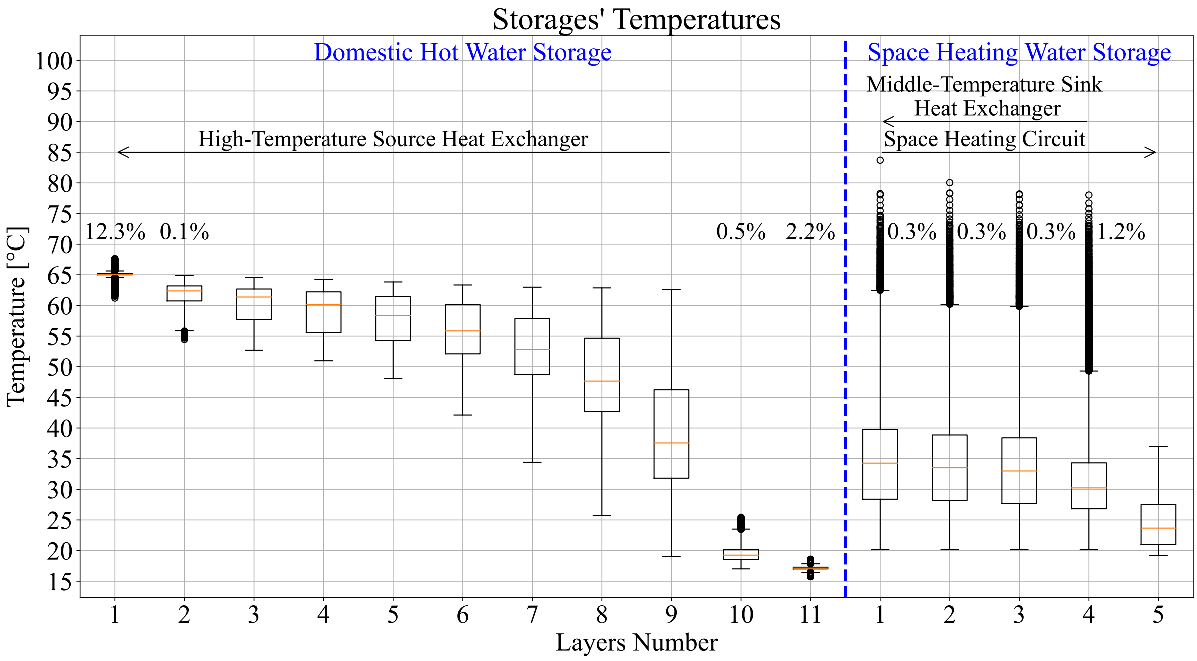

Figure A.10.: Annual temperatures of storage layers for space heating and water heating storage in the two-storage system (supply water to the HX-HTS from layer 9). Outliers percentage represents the share of transient temperature deviations relative to the total dataset for each layer.

The comfort temperature range and sanitation conditions in the DHW circuit are maintained with the hydraulic configuration of the two-storage system, as shown in Figure A.11 and Figure A.12. However, the two-storage system slightly degrades the comfort temperature levels in both the SHC and DHW circuits compared with the reference system. This effect becomes evident when comparing Figure A.11 with Figure 4.13, where a higher occurrence of temperatures below 20.4 °C is observed, and when comparing Figure A.12 with Figure 4.11, where temperatures below 60 °C occur more.

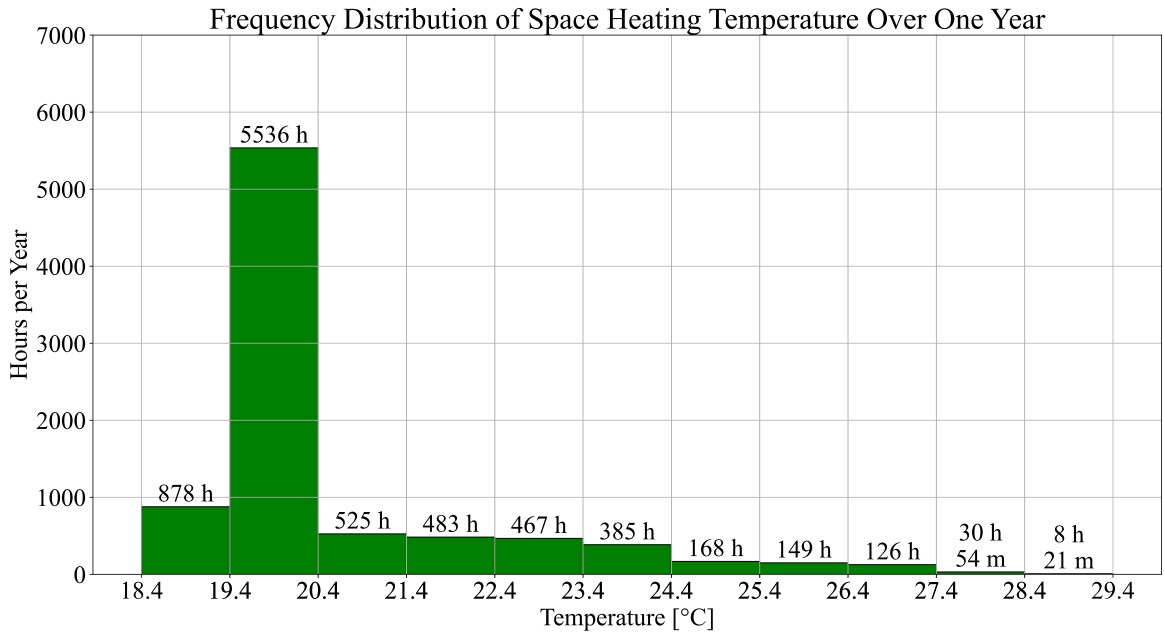

Figure A.11.: Frequency distribution of room temperature in 1 °C temperature bins in system with two-storage.

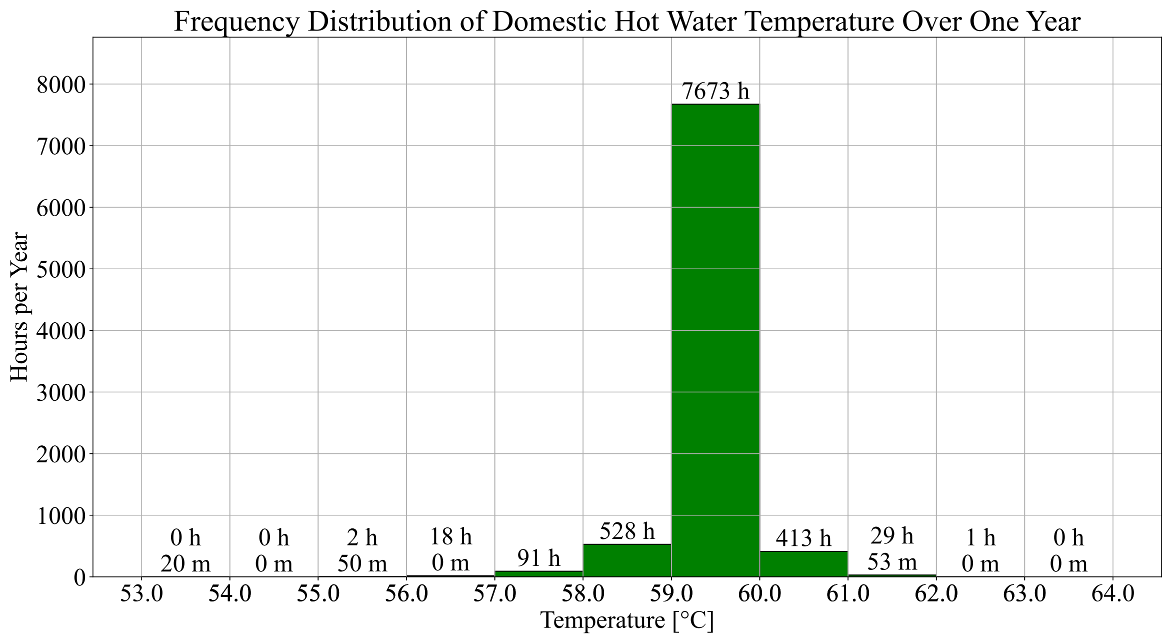

Figure A.12.: Frequency distribution of DHW temperature in 1 °C temperature bins in system with two-storage.

A.6. Monthly Irradiation and Yields

Notably, the annual solar gross yield of the system with a combi-storage reaches 0.29 (29 %), whereas the system with two separate storage units achieves 0.23 (23 %). As shown in Figure A.13, a considerable difference exists between the irradiation on the tilted collector surface and the thermal energy delivered to the solar heat exchanger, reflecting thermal and hydraulic losses along the path from the solar collector to the heat exchanger (As details described in Table A.2). In addition, a discrepancy can be observed between the energy transferred from HX_Solar to the combi-storage and to the two-storage configuration. This difference is primarily driven by the collector inlet temperature, which is determined by the respective control strategies.

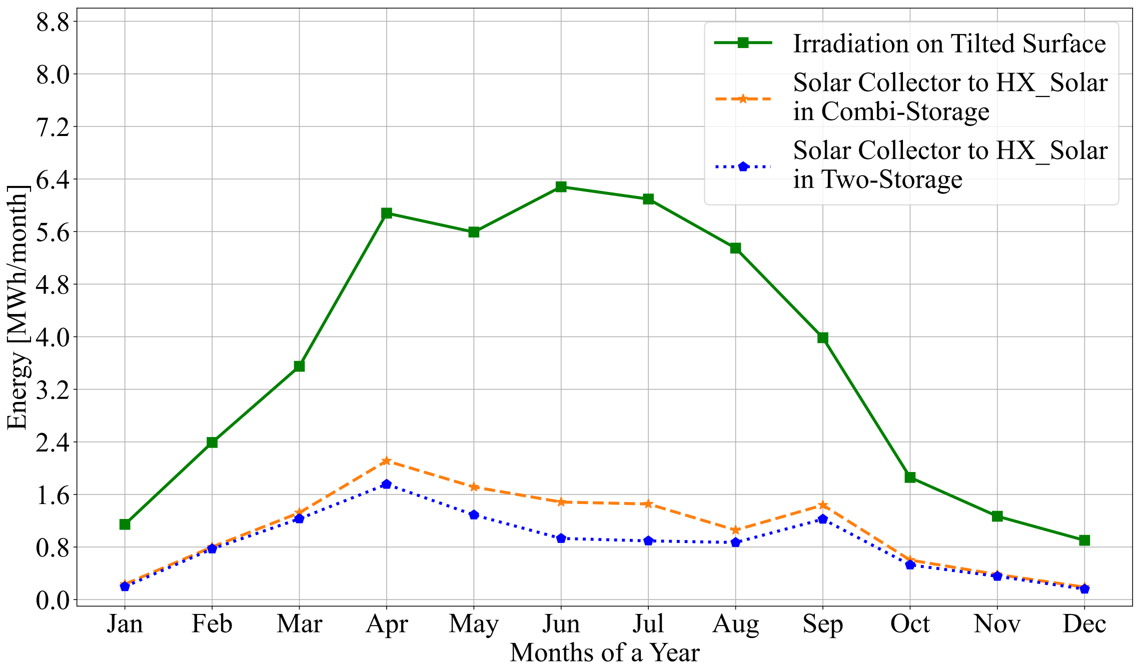

Figure A.13.: Monthly irradiation on tilted surface and monthly energy delivered to the solar heat exchanger in systems with combi-storage and solar thermal collector, and with two-storage and solar thermal collector.

In the two-storage configuration, the control strategy (subsection 2.3.4) prioritizes charging the space heating (SHC) storage because it typically operates at a lower temperature level, which supports higher collector efficiency. However, the annual results reveal limitations associated with this discrete switching control. Once the SHC demand is satisfied or the storage reaches its setpoint temperature, the controller redirects the solar heat to the domestic hot water (DHW) storage. As illustrated by the solar yield distribution between SHC and DHW storage (Figure A.14), this switching occurs repeatedly throughout the year. Since the DHW storage is maintained at significantly higher temperature levels than the

Parameter	unit	Value
length of Supply line	m	15
length of return line	m	15
Insulation Specific Heat Conductivity	$W/m \cdot K$	0.01
Insulation Thickness[a]	mm	10
Pipe Diameter	mm	29.2

Table A.2.: Solar thermal collector parameters.

[a] An insulation thickness of 10 mm was assumed for the pipes. Due to the very low thermal conductivity of the insulation material (λ = 0.01 W/(m·K)), this corresponds approximately to an equivalent insulation thickness of about 35 mm when compared with the reference conductivity λ = 0.035 W/(m·K) commonly used in German insulation recommendations [144].

SHC storage (Figure A.15), the solar loop must extract warmer return water during these phases. This increases the collector inlet temperature and therefore the temperature difference (ΔT) between the collector fluid and the ambient air, leading to increased radiative and convective losses and reducing the collector efficiency [1]. Consequently, these periods of high-temperature operation contribute to the lower annual solar gross yield of 0.23 observed in the two-storage system. In contrast, the combi-storage configuration benefits from the stratified structure of the 16-layer tank, which provides a continuous range of temperature levels within a single storage volume. While the upper layers (TStor[1–2] in Figure A.16) operate near the domestic hot water setpoints above 60 °C, the lower layers (TStor[15–16]) maintain consistently low temperatures with a narrow distribution throughout the year. This continuous stratification enables the solar loop to draw return water from the coldest available layer at the bottom of the storage. Unlike the two-storage configuration, where the controller alternates between two discrete temperature levels, the combi-storage allows the collector loop to operate consistently with a low inlet temperature. As a result, the collector field operates with a smaller temperature difference relative to the ambient environment, which improves thermal efficiency and effectively decouples the solar harvesting process from the high-temperature requirements of the DHW zone.

Overall, the comparison indicates that the 16-layer combi-storage provides a more robust hydraulic interface than the discrete switching strategy used in the two-storage configuration. The greater temperature resolution within the stratified storage allows the system to maintain a low collector return temperature even when high-temperature DHW

[1]

$$\eta_{\text{coll}} = \eta_0 - a_1 \frac{(T_m - T_a)}{G} - a_2 \frac{(T_m - T_a)^2}{G} \tag{A.15}$$

where η_{coll} is the collector efficiency [-], η_0 is the optical efficiency [-], a_1 and a_2 are the first and second order heat loss coefficients, T_m is the mean collector temperature, T_a is the ambient temperature, and G is the solar irradiance on the collector plane [94].

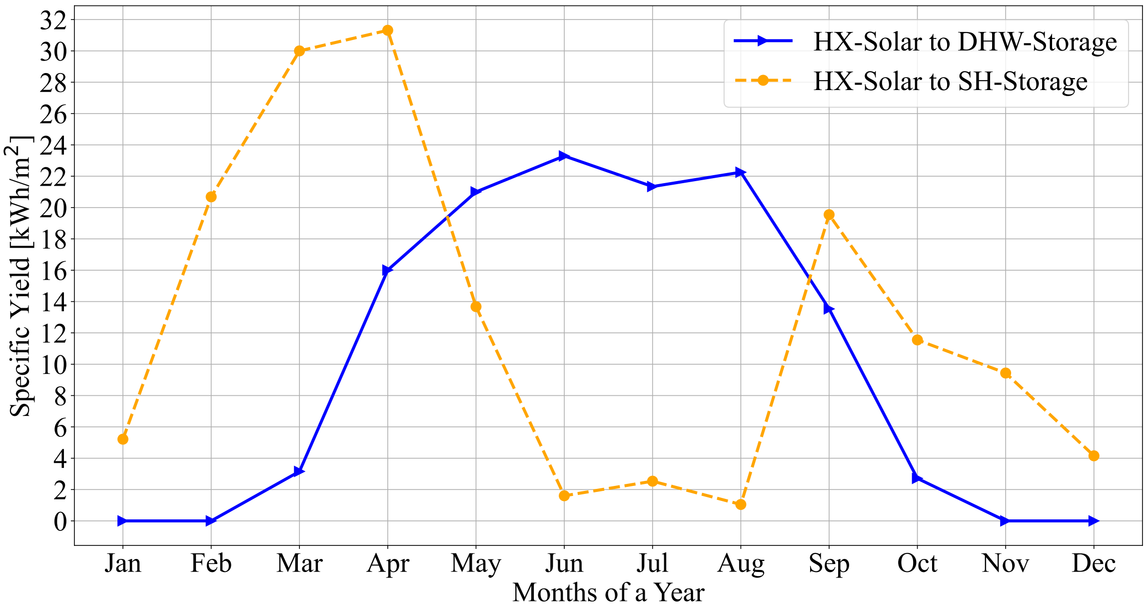

Figure A.14.: Monthly specific solar yield for the Two-storage system with a 37 m^2 collector area.

demands are present. Consequently, the annual solar gross yield increases from 0.23 to 0.29, representing an improvement of approximately 26 %.

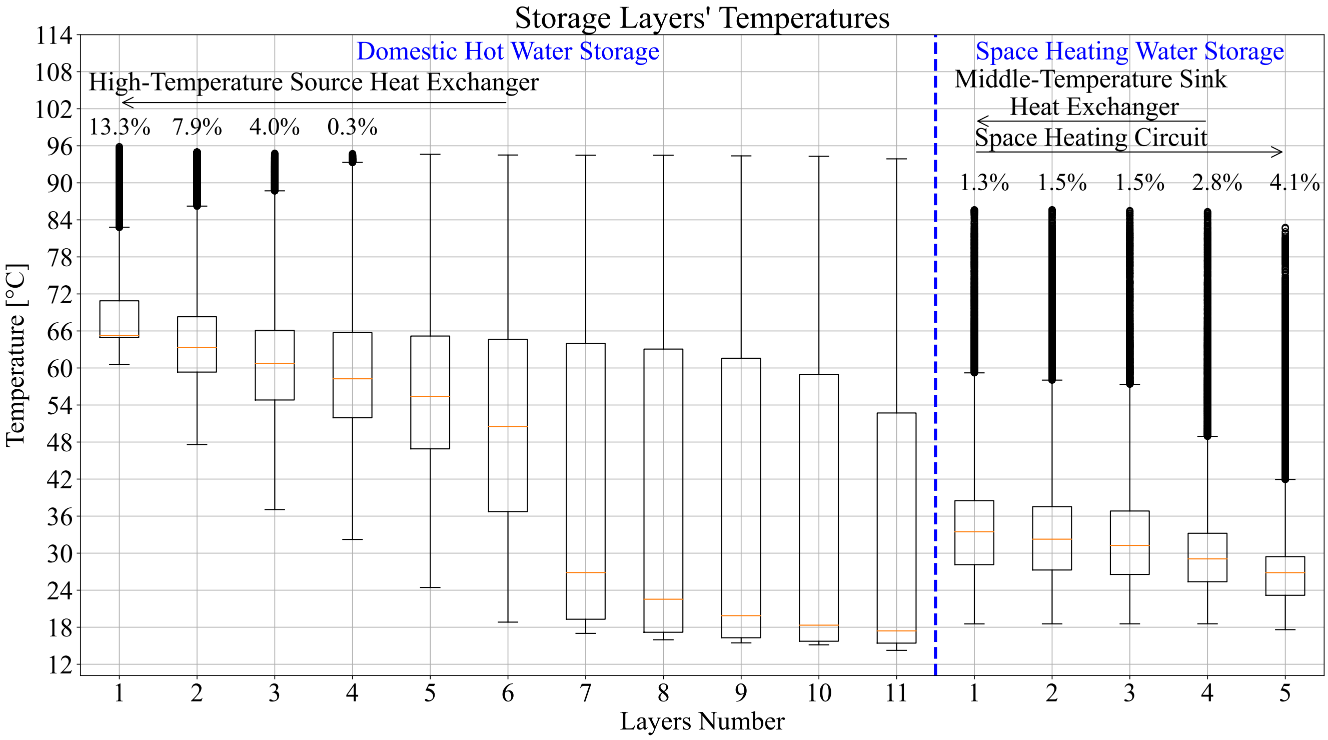

Figure A.15.: Annual temperatures of storage layers for space heating and water heating storage in two-storage with solar thermal circuit system. Outliers percentage represents the share of transient temperature deviations relative to the total dataset for each layer.

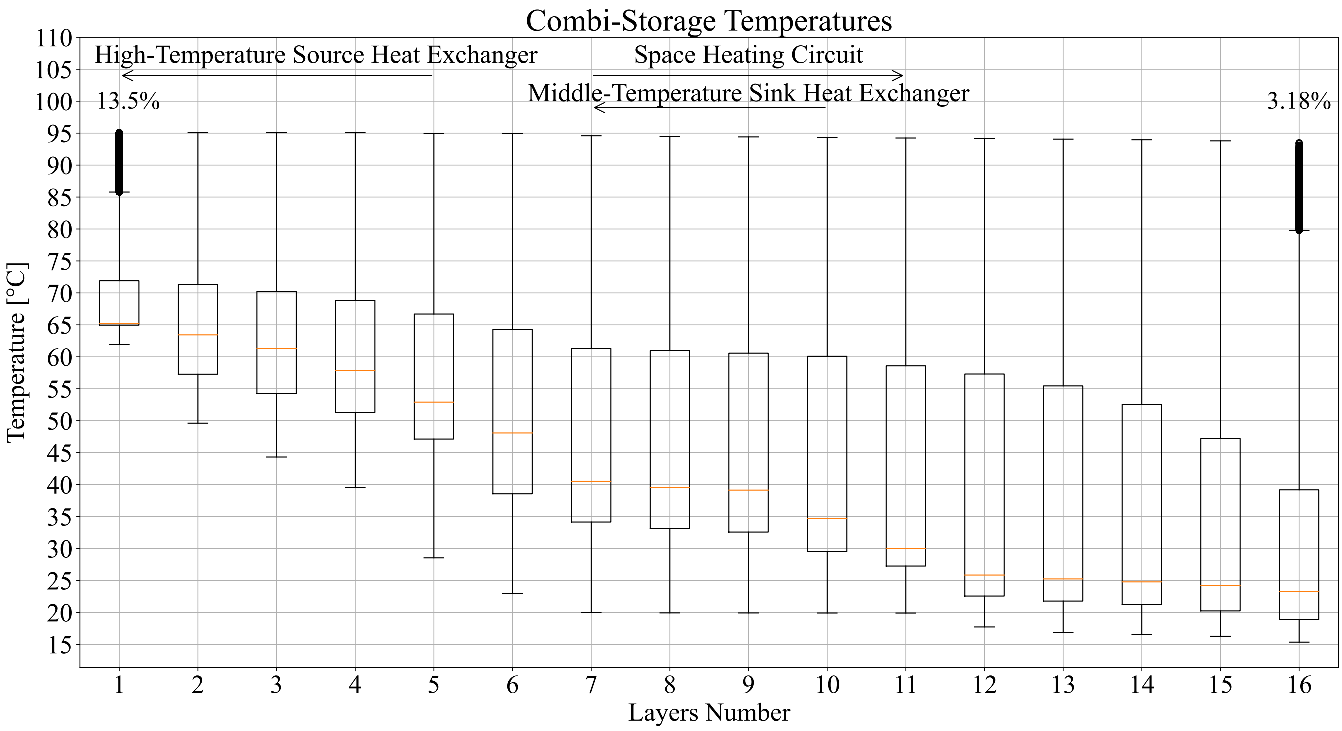

Figure A.16.: Annual temperatures of storage layers for combi-storage in combi-storage with solar thermal circuit system. Outliers percentage represents the share of transient temperature deviations relative to the total dataset for each layer.

A.7. Preheating DHW in Karlsruhe and Potsdam

High density areas with the pattern /// in Figure A.17 illustrate that the monthly energy delivered from the High-Temperature Source heat exchanger to the combi-storage is higher in the reference system under Karlsruhe weather conditions. In contrast, monthly delivered energy from combi-storage to the DHW circuit and the monthly demand energy within the DHW circuit remain consistent under both weather conditions. This consistency is mainly because DHW demand profile depends on user behavior, as described in subsubsection 2.1.2.2.

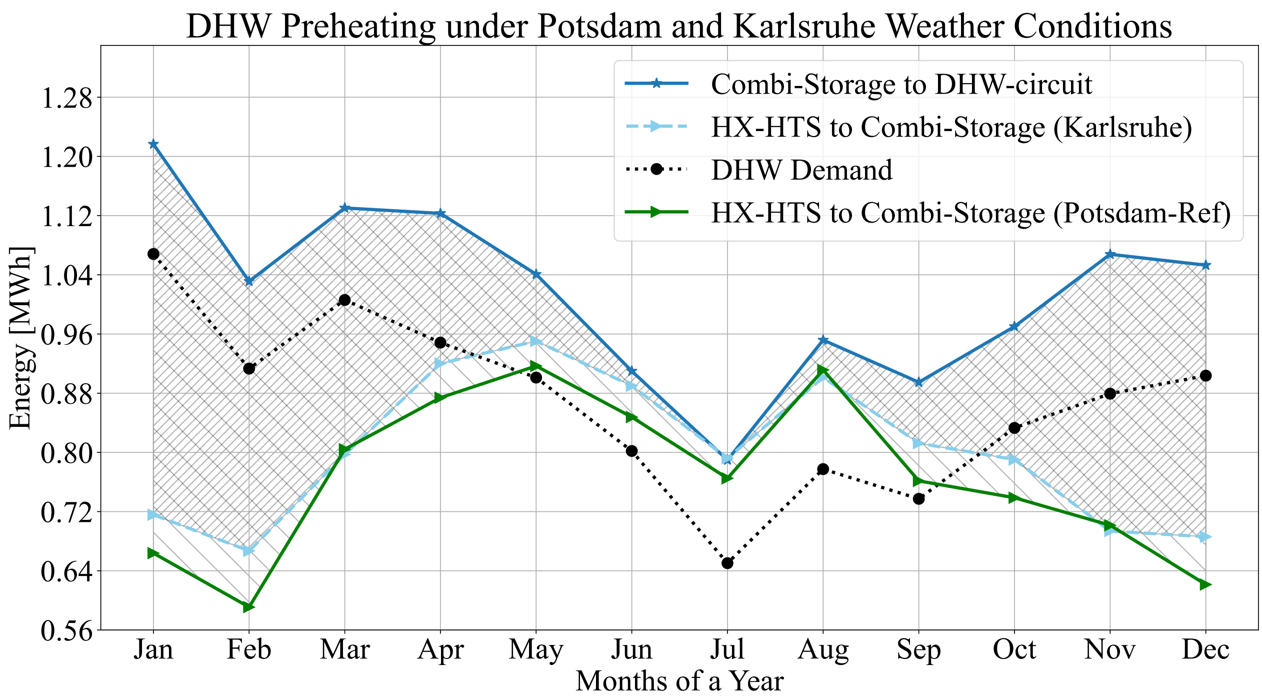

Figure A.17.: Preheating DHW in reference system under Potsdam and Karlsruhe weather conditions.

A.8. Scaled DHW Consumption

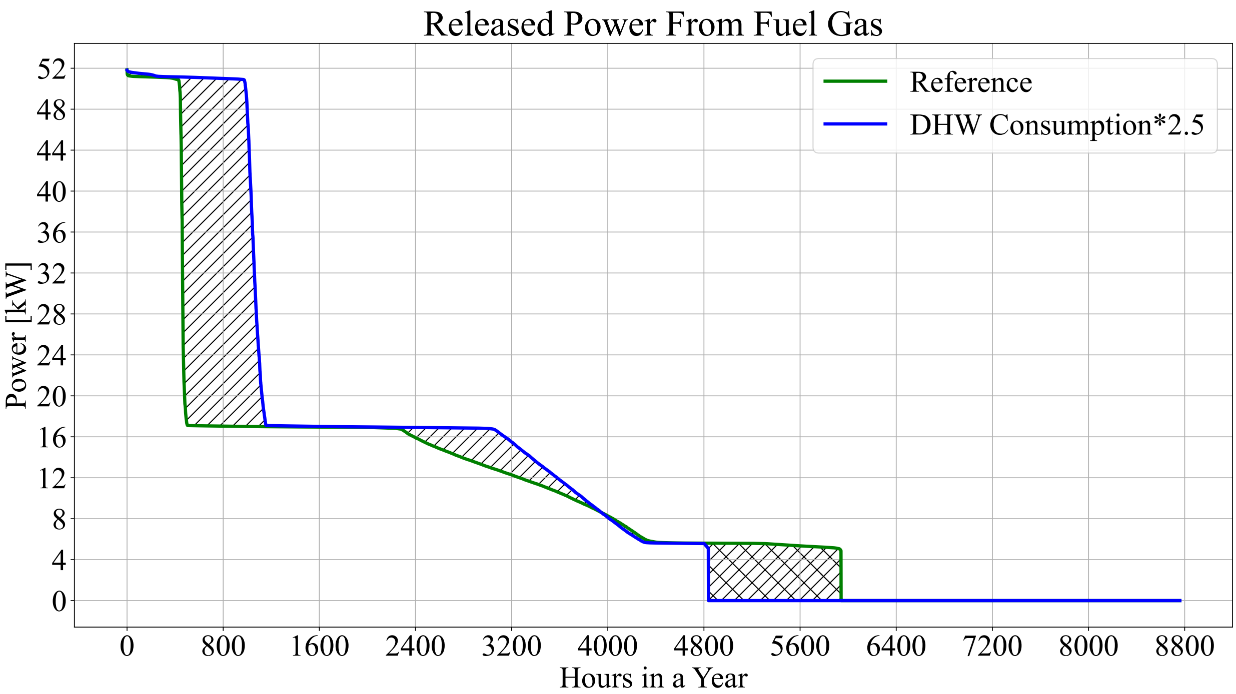

Figure A.18.: Annual power duration curves for the reference system: comparison of defined DHW profile vs. scaled consumption (factor of 2.5).

Figure A.18 shows that gas burner in reference system with scaled consumption, operates more frequently than in the reference system with defined DHW load profile. This finding is also depicted in monthly energy released from fuel gas in plot A of Figure A.19 and the monthly energy released from burner second heat exchanger (BRN-HX-MT in Figure 2.7) in plot C of Figure A.19. Additionally, the monthly energy delivered from the borehole heat exchanger (Plot B in Figure A.19) in the reference system with scaled consumption is less than that in the reference system without scaling. This reduction is due to the lower operation mode of the GAHP in sorption mode. Consequently, the SGUE of the system with scaled consumption is reduced 3.5 % compare to the reference system with defined DHW profile.

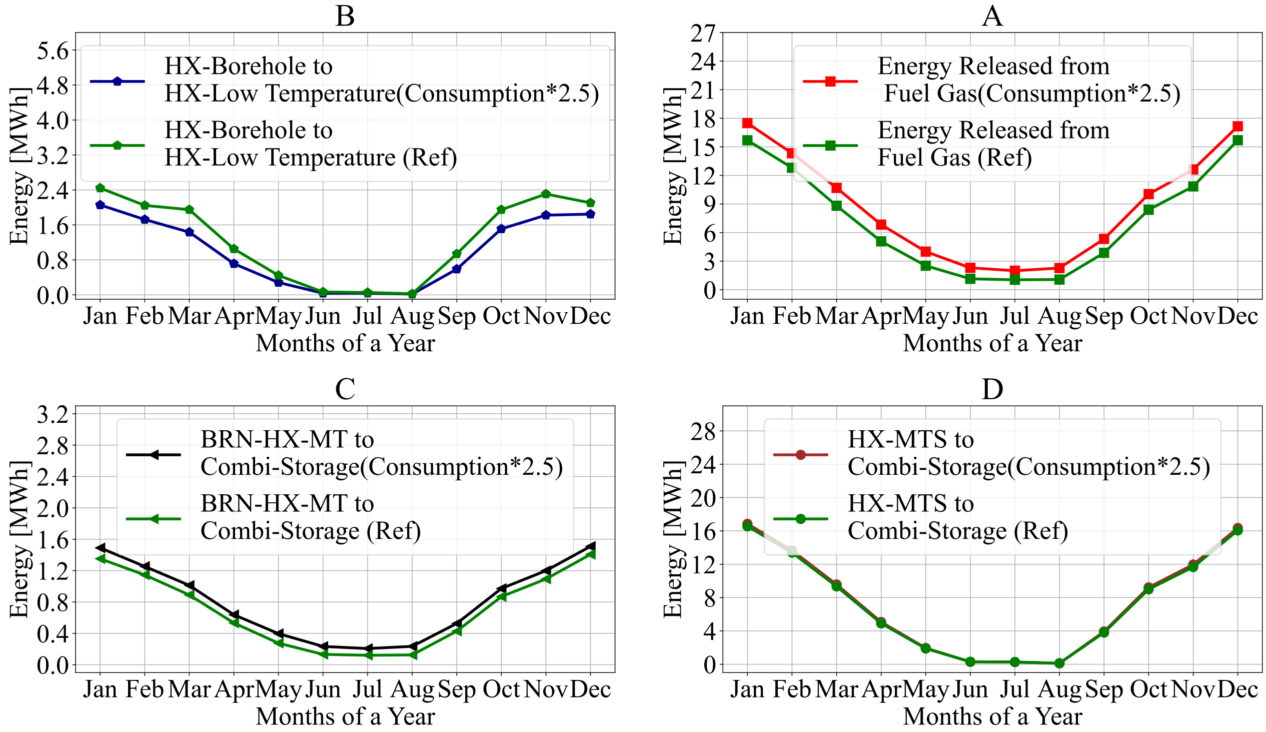

Figure A.19.: Monthly energy released from fuel gas and monthly energy delivered from various components in reference system: comparison of defined DHW profile vs. scaled consumption (factor of 2.5).

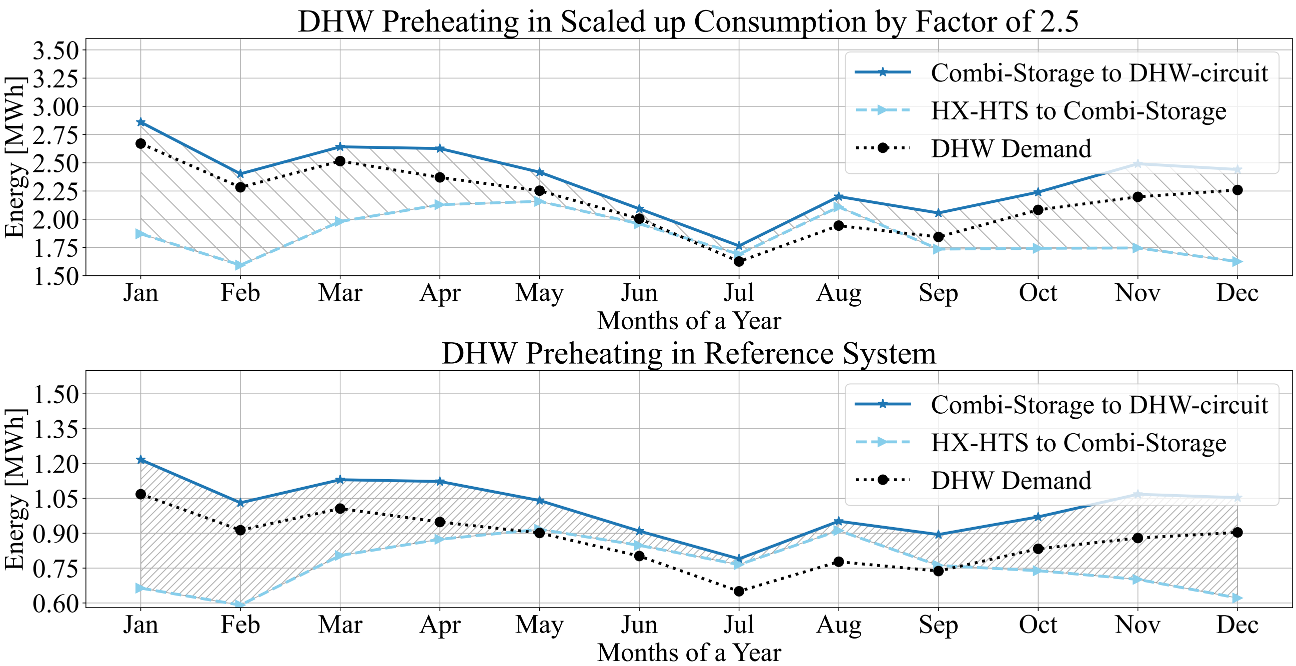

Figure A.20.: Preheating DHW in reference system: comparison of defined DHW profile vs. scaled consumption (factor of 2.5).

The sensitivity analysis with a DHW demand increased by a factor of 2.5 serves as a parametric stress test for the reference system. It is important to note that under standard engineering design principles, a demand of this magnitude would necessitate a significantly larger DHW storage volume to buffer the load. By maintaining the original small tank size—where the hydraulic configuration already limits the effective volume available for high-temperature DHW—the scaled draw-offs frequently result in high-intensity peak power demands.

Because the scaling increases the instantaneous mass flow rate rather than the duration of events, the heating demand often occurs at power levels that the GAHP cannot supply. This forces a shift away from the efficient adsorption cycle toward the burner operation to maintain the setpoint. Consequently, these results demonstrate that the current control strategy and hydraulic design are not robust toward significant shifts in consumption patterns. The system's performance is highly sensitive to the alignment between storage capacity and the peak power of the demand profile; without an appropriately sized buffer, the efficiency gains of the GAHP are largely bypassed.

Figure A.20 illustrates the effect of preheating domestic hot water (DHW) in the reference system under conditions of scaled consumption (low density hatch pattern) and the defined DHW load profile (high density hatch pattern).

The temperature deviation from target temperatures in reference system with scaled consumption are represented in Figure A.21 and Figure A.22. As the system prioritizes supplying the DHW in the reference system with scaled consumption, room temperature reaches the range of 17.4 °C to 18.4 °C for 16 hours per year. Additionally, the DHW circuit exhibits temperature variations, ranging between 51 °C and 52 °C for 10 minutes per year, and 52 °C and 53 °C for 20 minutes per year. These temperature ranges are reasonable based on scaled DHW consumption.

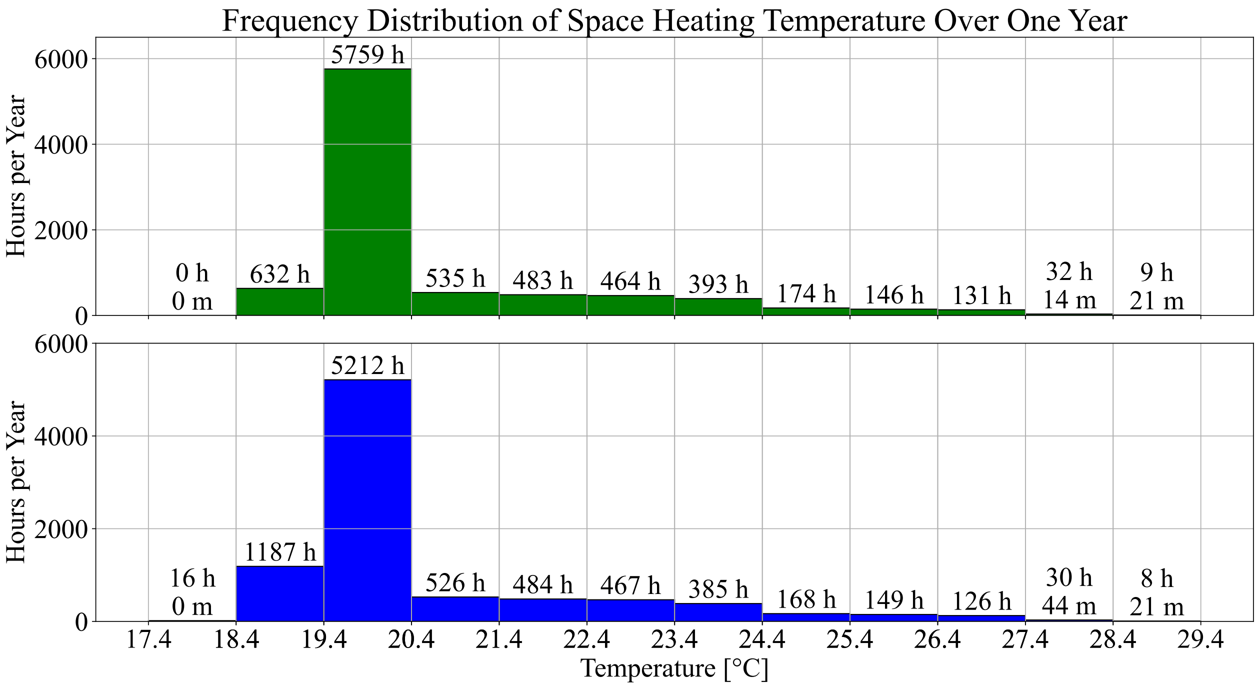

Figure A.21.: Frequency distribution of room temperature in 1 °C temperature bins in the reference system (green) and reference with scaled consumption (blue).

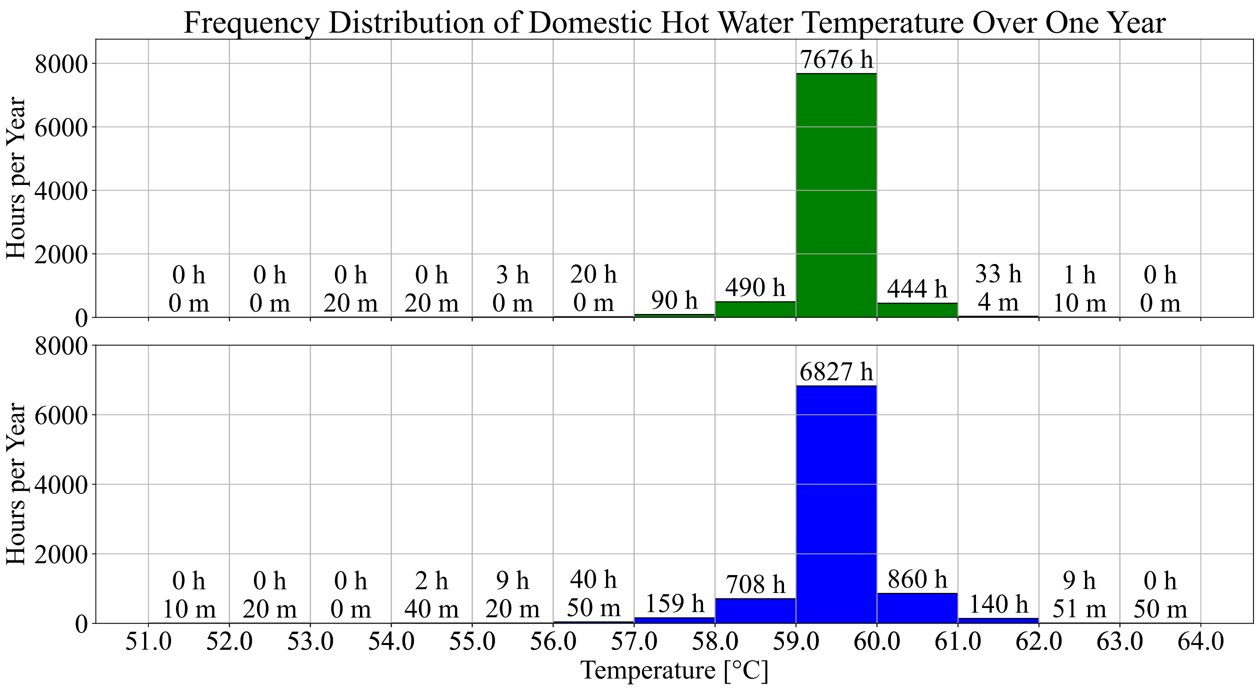

Figure A.22.: Frequency distribution of DHW temperature in 1 °C temperature bins in the reference system (green) and reference with scaled consumption (blue).

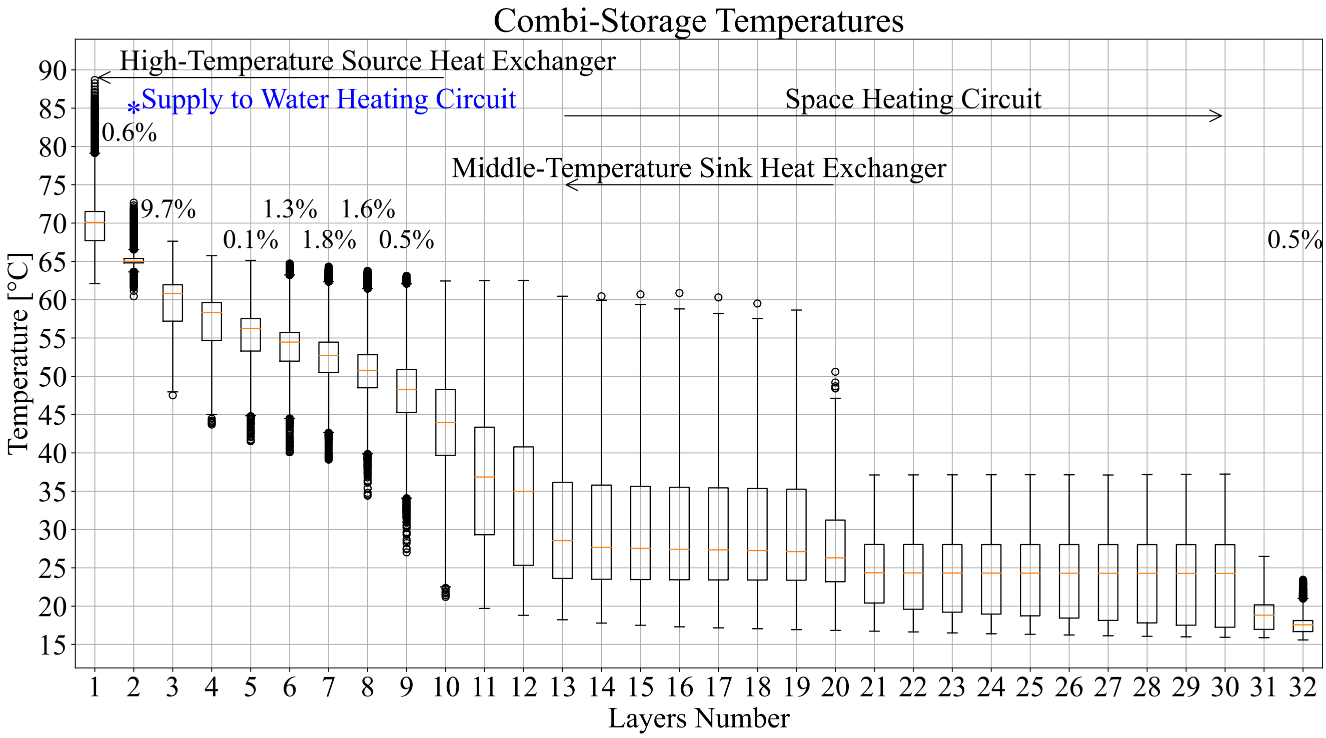

Figure A.23.: Annual temperatures of storage with 32 layers. Outliers percentage represents the share of transient temperature deviations relative to the total dataset for each layer.

A.9. Storage Properties

Considering the changes in hydraulic connections and system-level control of a reference system with 32 layers (Figure A.23), comfort temperature range are shown in Figure A.24 for Space Heating Circuit and in Figure A.25 for Water Heating Circuit. Figure A.26 demonstrates that the GAHP operates less frequently than the reference system with 16 layers. Additionally, Figure A.27 illustrates an improvement in DHW preheating compared to the reference system.

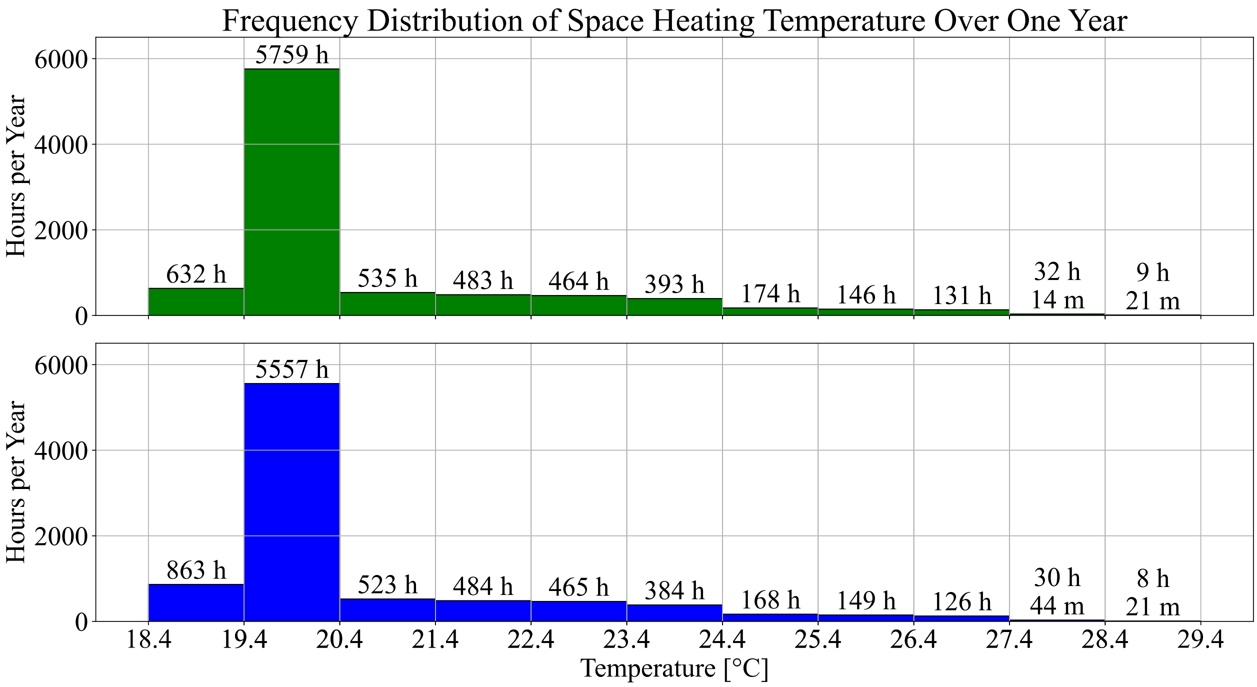

Figure A.24.: Frequency distribution of room temperature in 1 °C temperature bins in reference system (green) and reference with 32 storage layers (blue).

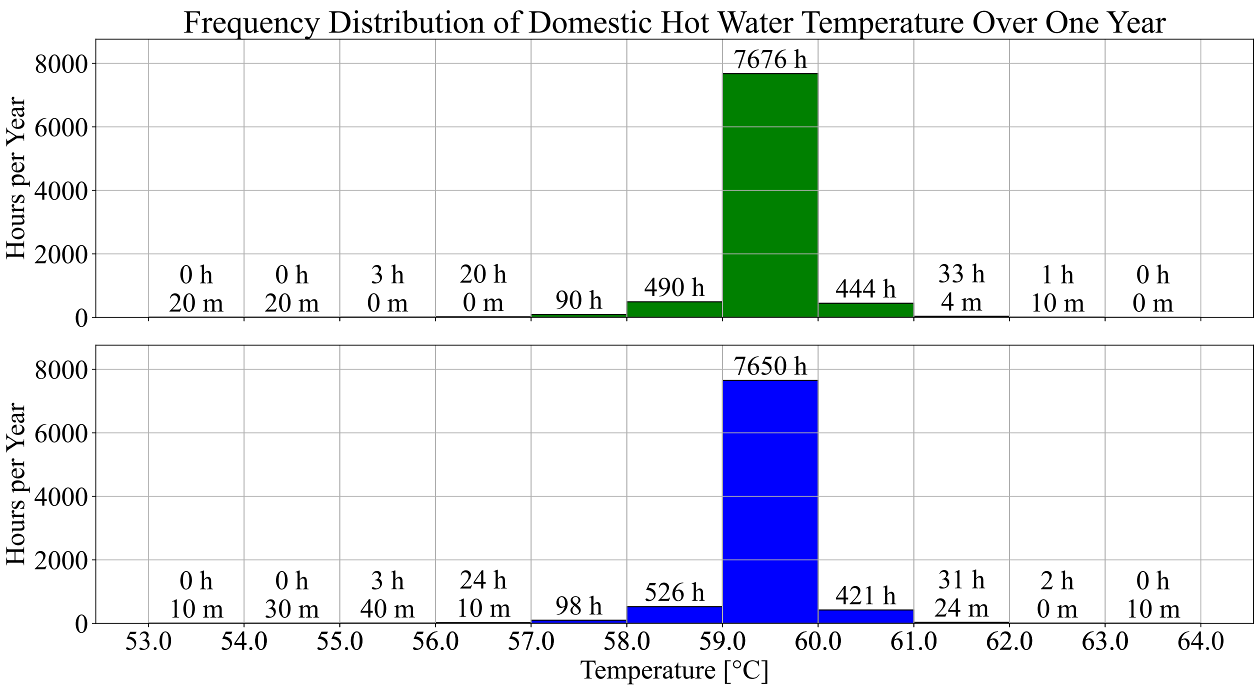

Figure A.25.: Frequency distribution of DHW temperature in 1 °C temperature bins in reference system (green) and reference with 32 storage layers (blue).

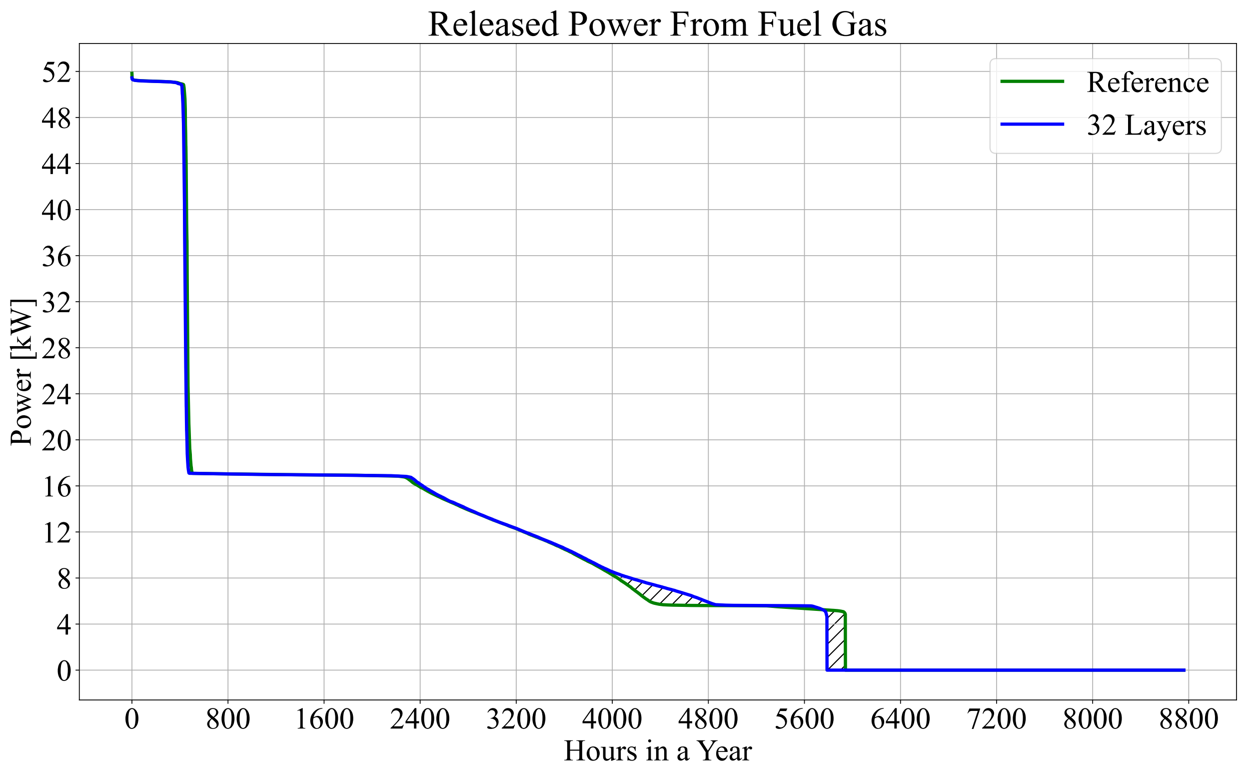

Figure A.26.: Annual power duration curves with 32 storage layers.

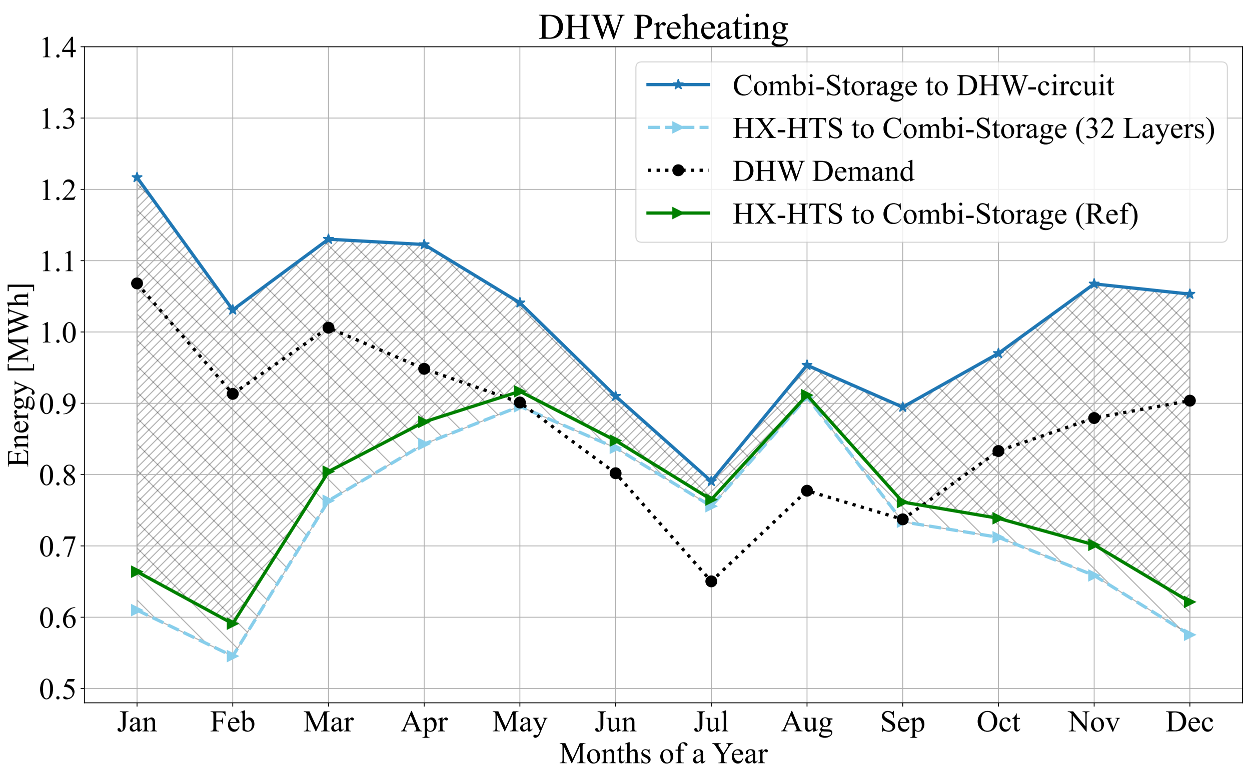

Figure A.27.: Preheating DHW in reference system with 32 storage Layers.

A.10. Sensitivity Analysis of Dual Adsorber cycle GAHP with Combi-Storage and Solar Circuit System

I conducted a sensitivity analysis by varying the UA value and mass flow rate of pumps on both sides of the solar heat exchanger, as illustrated in Figure 2.6, to assess the impact on solar gross yield and domestic hot water (DHW) preheating in a configuration with a solar thermal collector (Figure 2.16). The heat transfer area of the exchanger is assumed to be fixed; therefore, variations in UA represent changes in the overall heat transfer coefficient resulting from different flow conditions, such as altered flow velocities, Reynolds numbers, and convective heat transfer coefficients, rather than changes in surface area. Mass flow rates are varied independently to explicitly capture flow-dependent effects, such as changes in Reynolds and Nusselt numbers, allowing geometric and convective influences on heat transfer performance to be distinguished. According to subsubsection 2.1.1.2, the UA value for the solar heat exchanger is 5151 W/K, and the mass flow rate ranges from 0.16 kg/s to 0.32 kg/s. and 0.32 is only active when the storage top layer temperature exceeds 70 °C.

In the first scenario, I set the minimum mass flow rate to 0.05 kg/s and the maximum to 0.1 kg/s, maintaining these rates to reduce the mixing effect of the solar mass flow rate within the storage. Additionally, the UA value was reduced to 4790 W/K. As shown in Figure A.28, the monthly solar gross yield decreased between January and May and between September and December. Conversely, the DHW preheating increased during these periods (Figure A.29). Furthermore, the Seasonal Gas Utilization Efficiency (SGUE) and annual solar gross yield decreased by 0.15 % and 4.01 %, respectively, compared to a UA value of 5151 W/K and a mass flow rate of 0.16-0.32 kg/s (represented by the green line plots). The observed minimum of the solar gross yield during summer (Figure A.28) is caused by the finite thermal storage capacity of the system. During periods of high solar irradiation and low domestic hot water demand, the storage reaches its maximum temperature, leading to stagnation of the solar collector and reduced heat production. Consequently, the simulated "solar gross yield" reflects system-limited energy utilization rather than the theoretical collector output under an infinite heat sink assumption. In contrast to the classical definition of gross yield in solar thermal literature, which assumes an unlimited heat sink, the term (as described in Equation 2.12) is used here to denote the heat actually transferred from the collector loop to the storage within the modeled system boundaries.

In the second scenario, I considered a UA value of 12000 W/K based on Zaß's findings [89], which indicated the highest energy savings with a UA value of 12000 W/K. The results in Figure A.30 and Figure A.31 mirrored the changes observed in the first scenario. Additionally, the SGUE and annual solar gross yield decreased slightly by 0.01 % and 2.74 %, respectively, which is considered negligible and not statistically meaningful. Consequently, this variation does not indicate a significant sensitivity of system performance to the selected UA value within the investigated range.

In the third scenario, I increased the mass flow rate while maintaining a UA value of 12000 W/K. As shown in Figure A.32, there was a slight reduction in solar gross yield in February and November, but a small increase in September. The DHW preheating, as depicted in Figure A.33, was less effective than in the second scenario when the mass flow rate was half. Nonetheless, the SGUE and annual solar gross yield increased slightly by 0.15 % and 0.43 %, respectively, compared to a UA value of 5151 W/K and a mass flow rate of 0.16-0.32 kg/s.

In the fourth scenario, we maintained a UA value of 12000 W/K and a constant mass flow rate of 0.05 kg/s during periods of sufficient solar irradiation. As depicted in Figure A.34, the monthly solar gross yield decreased, except between August and September. However, the DHW preheating area in Figure A.35 was the highest compared to the other scenarios. The SGUE and annual solar gross yield decreased by 5 %, with a slight increase of 0.06 % compared to a UA value of 5151 W/K and a mass flow rate of 0.16-0.32 kg/s.

Therefore, based on the requirements of a multi-family house, a trade-off is necessary between achieving high solar gross yield and maximizing the DHW preheating area when designing the external solar heat exchanger and selecting the mass flow rate of pumps on both sides.

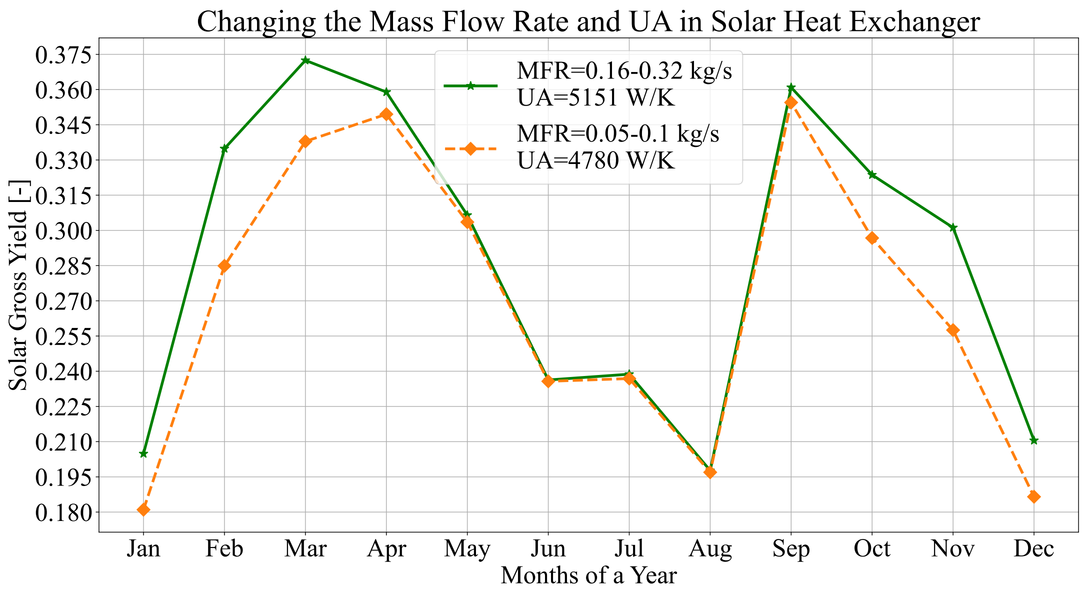

Figure A.28.: Monthly solar gross yield for systems with different UA values: 5151 W/K (mass flow rates: 0.16 kg/s and 0.32 kg/s, indicated in green line) and 4780 W/K (mass flow rates: 0.05 kg/s and 0.1 kg/s). Mass flow rates are adjusted between these values based on storage top layer temperature.

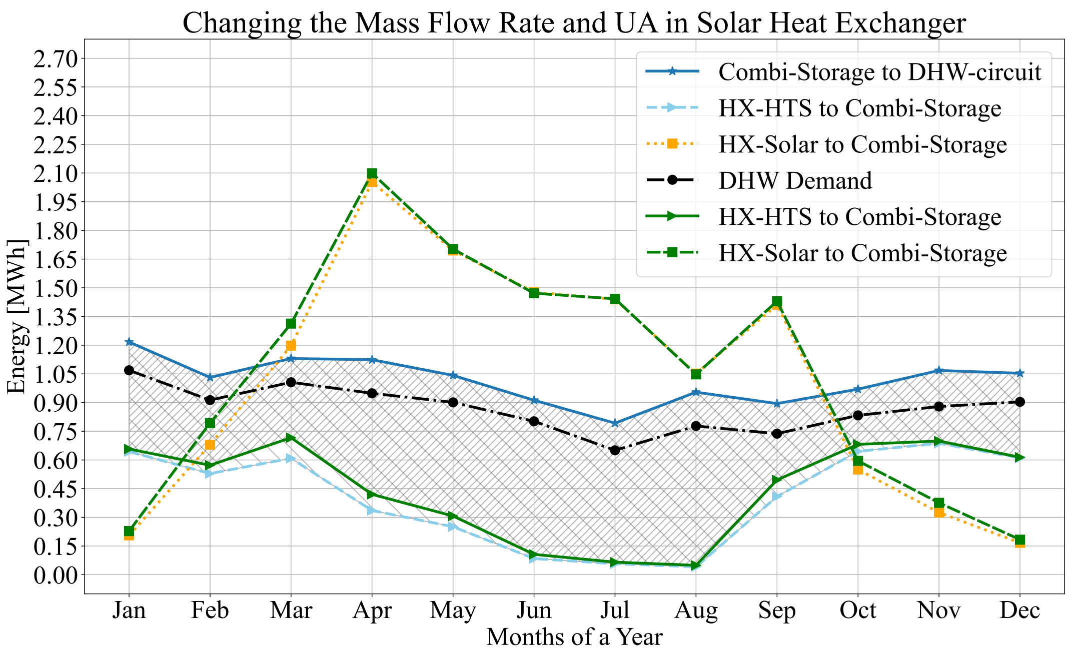

Figure A.29.: Monthly DHW preheating variations for systems with different UA values: 5151 W/K (mass flow rates: 0.16 kg/s and 0.32 kg/s, indicated in green line) and 4780 W/K (mass flow rates: 0.05 kg/s and 0.1 kg/s). Mass flow rates are adjusted between these values based on storage top layer temperature.

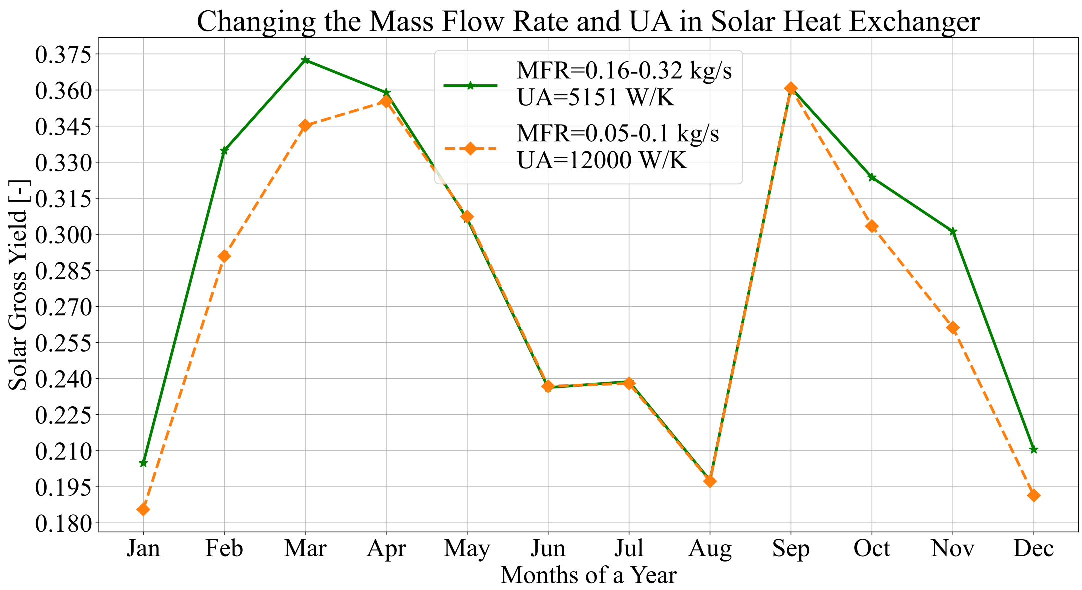

Figure A.30.: Monthly solar gross yield for systems with different UA values: 5151 W/K (mass flow rates: 0.16 kg/s and 0.32 kg/s, indicated in green line) and UA=12000 W/K (mass flow rates: 0.05 kg/s and 0.1 kg/s). Mass flow rates are adjusted between these values based on storage top layer temperature.

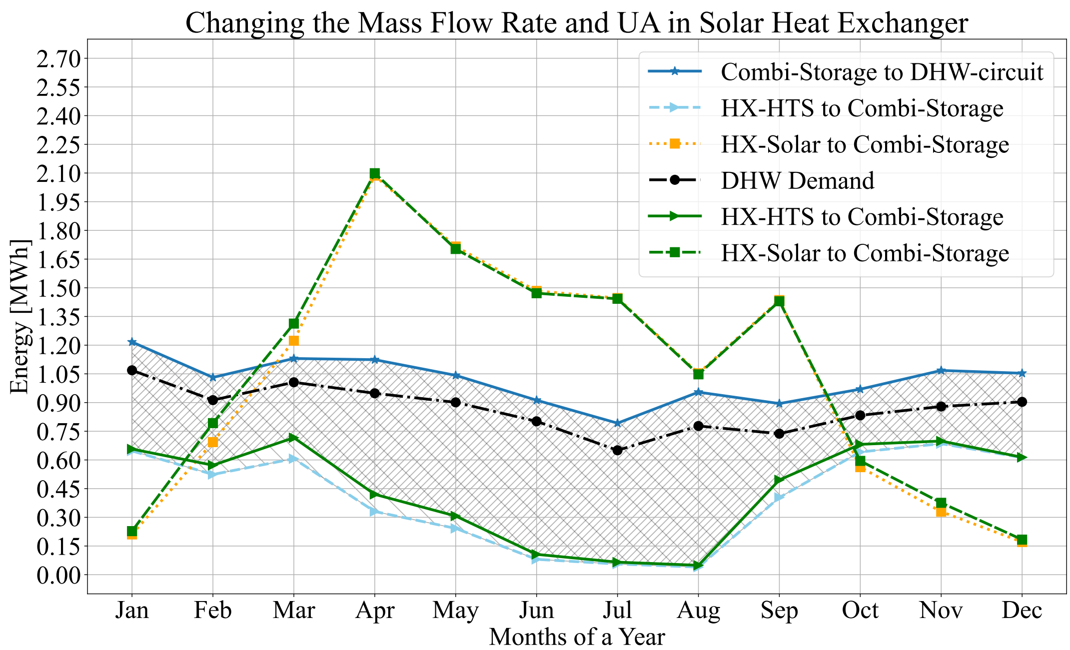

Figure A.31.: Monthly DHW preheating changes for systems with different UA values: 5151 W/K (mass flow rates: 0.16 kg/s and 0.32 kg/s, indicated in green line) and UA=12000 W/K (mass flow rates: 0.05 kg/s and 0.1 kg/s). Mass flow rates are adjusted between these values based on storage top layer temperature.

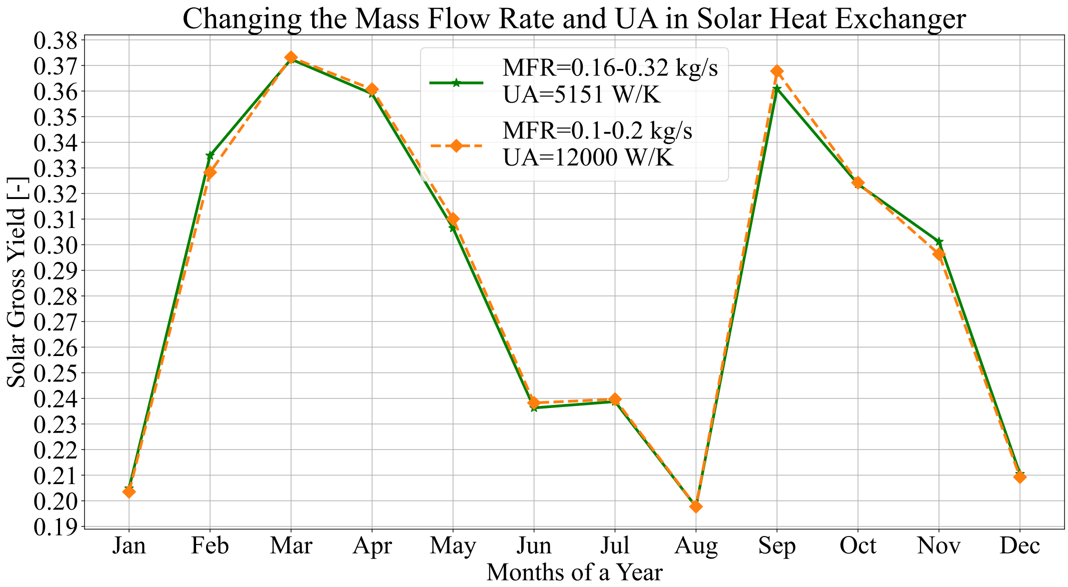

Figure A.32.: Monthly solar gross yield for systems with different UA values: 5151 W/K (mass flow rates: 0.16 kg/s and 0.32 kg/s, indicated in green line) and UA=12000 W/K (mass flow rates: 0.1 kg/s and 0.2 kg/s). Mass flow rates are adjusted between these values based on storage top layer temperature.

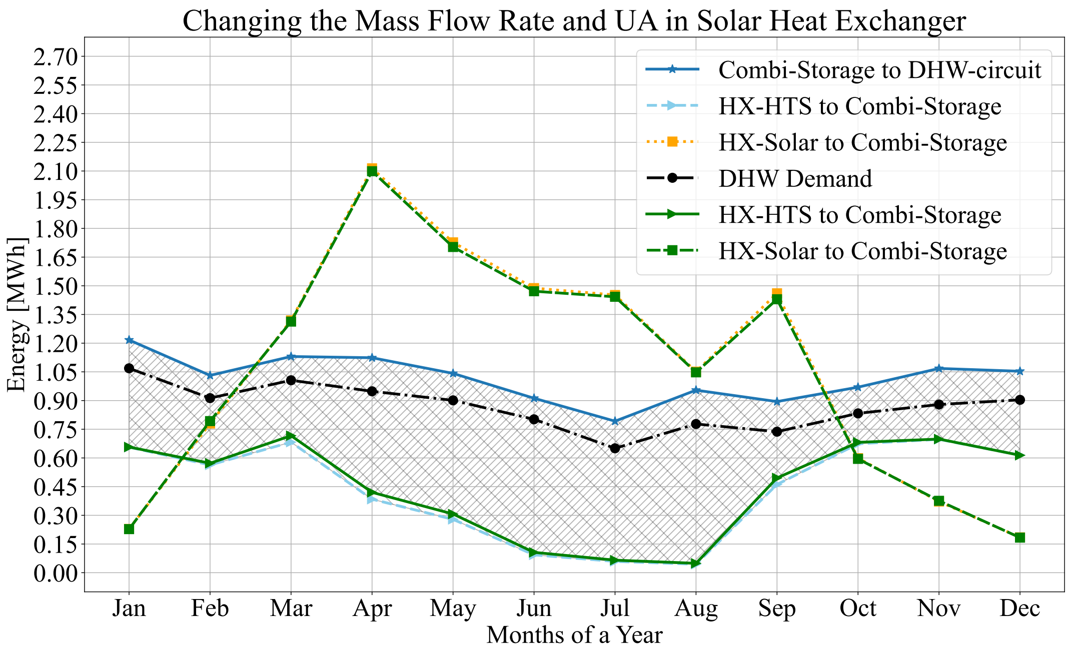

Figure A.33.: Monthly DHW preheating changes for systems with different UA values: 5151 W/K (mass flow rates: 0.16 kg/s and 0.32 kg/s, indicated in green line) and UA=12000 W/K (mass flow rates: 0.1 kg/s and 0.2 kg/s). Mass flow rates are adjusted between these values based on storage top layer temperature.

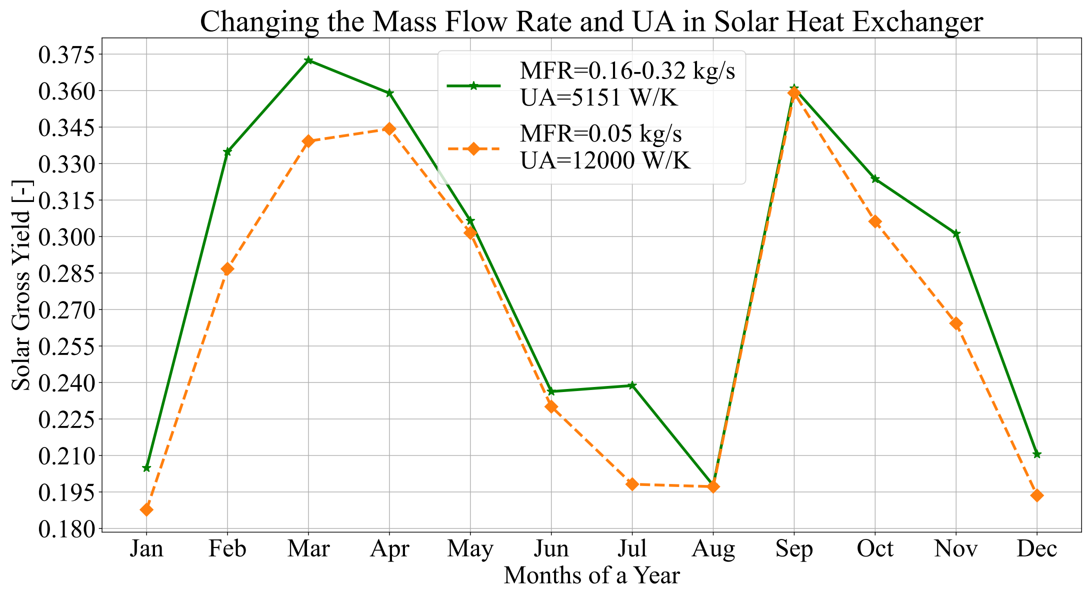

Figure A.34.: Monthly solar gross yield for systems with different UA values: 5151 W/K (mass flow rates: 0.16 kg/s and 0.32 kg/s, controlled between these values based on storage top layer temperature, indicated in green line) and 12000 W/K (mass flow rate: 0.05 kg/s).

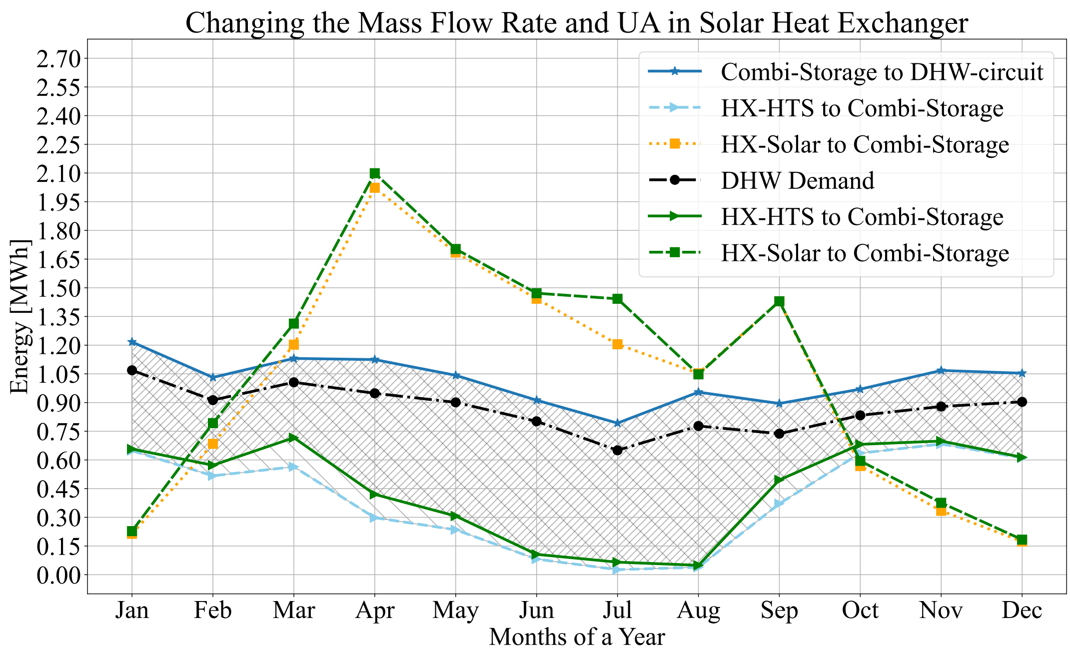

Figure A.35.: Monthly DHW preheating changes for systems with different UA values: 5151 W/K (mass flow rates: 0.16 kg/s and 0.32 kg/s, controlled between these values based on storage top layer temperature, indicated in green line) and 12000 W/K (mass flow rate: 0.05 kg/s).